University of Cape Town

Submitted in fulfilment of the requirements for the degree of

Master of Science

Department of Geological Sciences

Thermobarometry and geochemistry of peridotite xenoliths from the southwestern margin of the Kaapvaal craton, South Africa

---

Author

Fiona Clark

Supervisor

Dr. Philip E. Janney

October 2020

Abstract

Globally, there are significant contrasts, both thermally and chemically, between peridotite xenoliths exhumed from Archean, and post-Archean terranes. Studies of the thermal structure of the lithosphere, in combination with surface heat flow data, suggest that thermal gradients beneath cratonic regions (Archean blocks which stabilized > 2.5 Ga) are lower than those in off-craton regions, commonly attributed to thinner lithosphere in Proterozoic domains. Although this is true to an extent for southern Africa, the contrasts appear less distinct than Archean-Proterozoic lithosphere contrasts elsewhere, and the thermal structure reflects a regional, Mesozoic, disturbances which has been temporally linked to large-scale tectonic processes. Major element P-T results from peridotite xenoliths sampled during Group II kimberlite magmatism (~ 150 Ma), that erupted through the southwestern Proterozoic Namaqua-Natal Province record geothermal gradients akin to those of cratonic terranes. In contrast, xenoliths sampled during the younger Group I kimberlite magmatism (~ 80 Ma) within the Namaqua-Natal Province record equilibration temperatures which are displaced to higher values throughout the pressure ranges. This study reports results from peridotite xenolith samples from seven kimberlites and related rocks which erupted within the Eastern Namaqualand and Namaqualand-Bushmanland-Warmbad area. Two of the localities studied here (Melton Wold and Markt) erupted during Group II kimberlite magmatism, and five localities (Hebron, Uintjiesberg, Gansfontein, Hoedkop and Schuitdrift) erupted during the younger Group I kimberlite magmatism. The results build on prior work, which focused on mineral and whole rock major element chemistry, platinum group elements and Re-Os isotope data, and provide an insight into lithosphere formation and modification in the Namaqua-Natal lithospheric mantle through mineral trace element analysis. These samples also provide an opportunity to further investigate the Mesozoic thermal

evolution of the Namaqua-Natal lithosphere through application of a REE-based thermobarometer. REE diffusion rates are typically 2 – 3 orders of magnitude lower than divalent major elements, making the REE-based thermobarometer a potentially useful tool for probing the contrasting thermal profiles exhibited in samples from the Group II and Group I kimberlites studied here.

Major element-based thermobarometry results and the resulting FITPLOT paleogeotherms indicate that at the time of Grp II kimberlite magmatism the Namaqua-Natal lithosphere was ~ 200 km thick, with a 60 km "diamond window", and had a geothermal gradient of 40 mW/m^2. In contrast, at the time of Grp I kimberlite magmatism ~ 60 km of lithospheric erosion may have occurred, accompanied by a shift in the thermal regime of the Namaqua-Natal lithosphere to a 45 mW/m^2 geotherm. REE-based thermobarometry results produce a large amount of scatter in P-T space, even after a rigorous attempt at identifying well equilibrated clinopyroxene and garnet pairs. The presence of carbonatitic and silico-carbonate metasomatic signatures in these samples necessitates caution in the use of the REE-based thermobarometer when applied to xenoliths entrained by kimberlites. It is likely that the scatter observed in the results presented here is due to differing REE partitioning controls in systems containing carbonate in the melt to those of carbonate-free, silicate melts.

HREE concentrations in reconstructed whole-rocks and olivine Mg-numbers are consistent with 30% melt extraction in a shallow melting regime. Garnet and clinopyroxene trace element signatures indicate a shift in the style of metasomatism in the Namaqua-Natal lithosphere between Group II and Group I kimberlite magmatism. Zr/Hf versus Ti/Eu systematics reflect kimberlitic/silicate style metasomatism in the samples exhumed during Group II magmatism, whereas samples exhumed during Group I kimberlite magmatism reflect a carbonatitic style of metasomatism.

Acknowledgements

First and foremost, I would like to thank my supervisor, Phil Janney, for allowing me the opportunity to work on this project. I am grateful for the opportunities which he has afforded me and the criticisms he has provided which improved my capabilities as a researcher and helped bring this work to completion.

I would like to acknowledge the DSI-NRF Centre of Excellence for Integrated Mineral and Energy Resource Analysis (CIMERA) and the Department of Geological Sciences at UCT for student funding. CIMERA is thanked for generous funding toward the research costs of this project.

Christel Tinguely (UCT), the late Roger Dixon (UP), Nic Laidler (UCT), Rene van der Merwe (UCT) and Jonathan van Rooyen (UCT) are thanked for technical assistance and sample preparation. Nathalie Barends and Noluthando Sintsili, whose presence and smiles truly enhanced my experience at UCT (Additionally, I am forever indebted to Thandi for relentlessly caring for the "geophysics" office plants every time I went away).

Emotionally, I am certain I could not have gotten through the last few years without the support and companionship of my friends and family (who will never read this, but I'll thank them anyway). Musiegh, Tam, Kelly, Kirstie, Gen, Andrea, Martin, Megz, Christel, Tara, Jess, Chad and Guy, thank you for the comfort and love that you provided when my father passed away, but beyond that, I wish to acknowledge the strength that you all share with me every day. Merci pour cette danse qu'on a partagé ensemble. Jess, thanks for looking after me and housing me after surgery number one. Kelly, thank you for taking care of me after surgery number two.

I would like to sincerely thank my family – Mom, Struan and Daryn, for always being there for me (financially and emotionally), for being a source of

inspiration and for always picking me up when I fall. Mom, I am so proud of you and eternally grateful for the opportunities you have given me and for emphasizing the importance of who I am, rather than what I am.

This thesis is dedicated to my dad. Who was the epitome of a believer, constantly convincing me that I was capable of taking on any task, no matter how much doubt existed in my mind and the minds of others.

Table of contents

List of Figures

List of Tables

1. Introduction

Our understanding of the lithospheric mantle's structure and evolution is greatly obstructed by its isolated nature. Geochemical studies of the continental lithospheric mantle largely rely on xenolith samples which have been entrained by deep-seated, volatile-rich magmas such as kimberlites and alkali basalts. Data from xenoliths and xenocrysts entrained by kimberlites have provided insights into the formation of Earths ore reserves, the chemical and thermal structure and evolution of continents, and the long-term geochemical cycling of elements between the surface and the Earth's interior (Boyd and Gurney, 1986; Doucouré and de Wit, 2003; Broecker, 2012; Ashwal et al., 2017). These xenoliths are likely sampled from the walls of magma conduits and may reflect metasomatic influence from such. Therefore, although xenoliths provide a rare insight into the underlying mantle, it should be noted that they most likely provide a biased sample which may not be representative of the continental lithospheric mantle as a whole. Nevertheless, xenolith samples have provided essential information on lithospheric origins, specifically discerning Archean and post-Archean lithospheric terranes (Griffin et al., 2003a, 2009; Pearson and Wittig, 2008; Wittig et al., 2008).

Archean cratons (continental blocks which stabilized prior to 2.5 Ga; de Wit and Linol, 2015) represent the first robust continental terranes and form the integral cores of present-day continents. The long-lived stability of cratons is commonly attributed to the cold, thick (150 – 200km; Rudnick et al., 1998), and melt-depleted nature of Archean lithospheric mantle (Boyd and Mertzman, 1987; Griffin and O'Reilly, 2007). High degrees of melt extraction, resulting in depletion of Al and Ca, produce buoyant and predominantly infertile harzburgitic and dunitic residues which are relatively resistant to convective asthenospheric erosion (Carlson et al., 2005). Of major economic and industrial importance, is the fact that the majority of the Earth's

diamond resources are derived from cratonic settings. Although generally restricted to Archean terranes, diamond forming events have occurred throughout geologic time and their formation appears largely controlled by pressure, temperature and the composition and redox state of infiltrating fluids or melts (Stachel and Luth, 2015). The close association of diamondiferous kimberlites with depleted harzburgitic garnets and Archean cratons has driven exploration targeting for several decades (Clifford, 1966; Gurney, 1984) resulting in widespread study of cratonic regions.

In contrast, global Proterozoic mantle is considered less favourable as a diamond forming substrate. Proterozoic mantle is typically more fertile (expressed by higher modal garnet and clinopyroxene (hereafter cpx) and displays lower degrees of melt extraction (lower olivine forsterite content) than Archean mantle (e.g. Boyd and Mertzman, 1987; Griffin et al., 2003a, 2009). Present-day surface heat flow measurements for Proterozoic terranes are typically higher than those recorded in Archean cratons, commonly interpreted to indicate a thinner lithosphere (Nyblade and Pollack, 1993). The dominantly lherzolitic lithology and high surface heat flow observed in Proterozoic regions has resulted in the assumption that these regions are of low diamond potential. Because of this, and the relative lack of xenoliths available from non-diamondiferous (and hence unmined) off-craton kimberlites, the lithosphere of Proterozoic regions has been far less extensively characterized than that of the Archean.

The restriction of a thick, depleted, diamond forming substrate to lithosphere below Archean crustal regions has recently been questioned. Re-depletion model ages (T_{RD}; Intersection of the mantle evolution curve with measured $^{187}Os/^{188}Os$ in the sample, taken as a minimum estimate of the true melt depletion age) for peridotite xenoliths from Siberian diamondiferous kimberlites suggest a post-Archean lithosphere forming and reworking event around 2 Ga (Ionov et al., 2015). Although Archean T_{RD} (2.8 to 3.5 Ga) ages are present within the data, the presence of a major lithosphere

formation event during the Paleoproterozoic suggests major lithospheric reworking and addition. Recent Re-Os work on peridotites from the diamondiferous Fort a la Corne kimberlites, which erupted through the Sask craton in Canada which exhibits Archean crustal ages, display no evidence for the presence of Archean lithosphere (Czas, 2018). T_{RD} ages predominantly cluster around 2.0 to 2.3 Ga, suggesting a decoupling of crustal and lithospheric ages, and Proterozoic lithosphere, therefore, appears to be suitable for diamond growth (Czas, 2018). Notwithstanding that harzburgitic Archean lithosphere appears to be the dominant source region for diamonds overall (see Fig. 6. in Stachel and Harris, 2008), the presence of several unconventional deposits derived from lithosphere of more fertile character (e.g. Victor mine, Canada; Stachel et al., 2018) and Proterozoic age (e.g. Siberian and Sask cratons; Ionov et al., 2015; Czas, 2018) suggests that the widely adopted diamond exploration model of Clifford (1966) and Gurney (1984) may be an oversimplification of global diamond distribution.

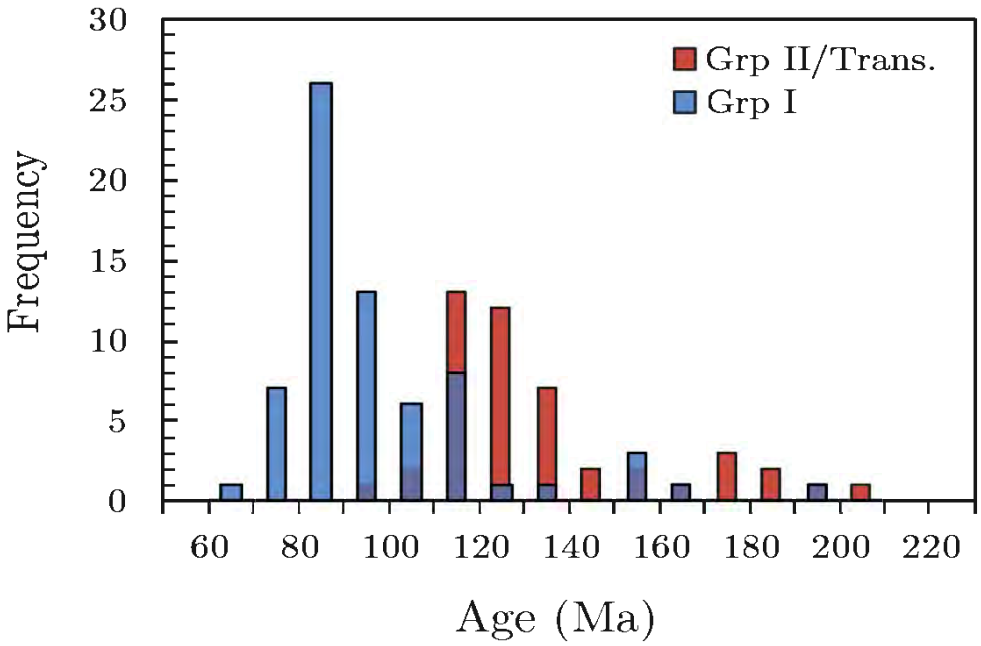

Figure 1.1: Histogram showing the age distribution of Group II and transitional (red) and Group I (blue) kimberlites in southern Africa. The peak Group II/transitional kimberlite activity was from 145 – 115 Ma and the peak Group I kimberlite activity was between 100 – 80 Ma. Source for kimberlite age data is Tappe et al. (2018) and Janney; University of Cape Town.

In southern Africa, Mesozoic kimberlite emplacement occurred in two main pulses at ca. 145 – 115 Ma and 100 – 80 Ma (Figure 1.1; Smith, 1983a; b; Smith et al., 1985; Field et al., 2008; Tappe et al., 2018). The former being chemically classified as Group II kimberlites (micaceous, high εSr and low εNd) and the latter as Group I kimberlites (basaltic, primitive mantle source with a HIMU component, slightly positive εNd). Data obtained from xenoliths and xenocrysts entrained by off-craton kimberlites suggest that there was a distinct change in the thermal structure of the off-craton lithosphere southwest of the Kaapvaal craton between the emplacement of the Group II and the Group I kimberlites at 115 – 100 Ma (Bell et al., 2003; Kobussen et al., 2008, 2009; Janney et al., 2010).

Xenoliths derived from Mesozoic Group II, 145 - 115 Ma, and Group I, 100 – 80 Ma, kimberlites suggest contrasting thermal gradients and lithospheric architecture between these eruption pulses (Bell et al., 2003; Janney et al., 2010). At the time of Group II kimberlite magmatism, the geothermal gradient recorded by xenolith and xenocryst thermobarometry in off-craton kimberlites is similar to that of the Kaapvaal craton. However, in the younger (Group I) pulse of kimberlite magmatism the geothermal gradient recorded by xenolith and xenocryst thermobarometry is displaced to higher temperatures for a given pressure associated with a thinner lithosphere which is more consistent with present-day geophysics estimates (~ 150 km; Fouch et al., 2004; Priestley et al., 2006; Globig et al., 2016). A similar observation was made for cratonic kimberlites from the southwestern Kaapvaal, however, the displacement to warmer geotherms is less pronounced than that noted off-craton (Mather et al., 2011). Fingerprinting the chemical signature of the Mesozoic lithosphere-scale heating and/or thinning remains contentious as there is a variety of evidence for metasomatism by

different agents occurring from 180 Ma to 80 Ma along the southwestern margins of the Kaapvaal craton and surrounding Proterozoic lithosphere (Griffin et al., 2003b, 2009; Kobussen et al., 2008, 2009; le Roex and Class, 2016; Weiss et al., 2018). The evidence for a relatively thick, cool lithosphere sampled by the Group II kimberlites suggests that the Proterozoic mantle in this region may have been a suitable host for diamonds prior to the prevailing thermal disturbance during the Mesozoic.

Historically, pressure and temperature estimates of mantle xenoliths have utilised major element mineral chemistry. I apply a new rare earth element (REE) based thermobarometer which is based in REE exchange between garnet and cpx (Sun and Liang, 2015). The slower inter-mineral diffusion of the trivalent REE (typically two to three orders of magnitude lower) in comparison to divalent major elements (Van Orman et al., 2001, 2002), offers the opportunity to investigate the recent thermal disturbances, where present. The accuracy of the REE-based thermobarometer of Sun and Liang (2015) has been evaluated, with application to the aforementioned peridotite xenolith suite, by comparison to more commonly used major element based thermobarometers.

This study focuses on characterizing the evolution of the Proterozoic lithospheric mantle southwest of the Kaapvaal craton, focusing on the temporal framework around the eruptions of Group II and Group I kimberlites within southern Africa. It builds on prior work, which focused on mineral and whole rock major element chemistry, platinum group elements (PGE) and Re-Os isotopes (Janney et al., 2010). A mineral trace element dataset is presented for a suite of peridotite xenoliths from 7 kimberlites which erupted through the Namaqua-Natal Province. An integrated geochemical and thermodynamic approach is applied to examine the net effect of metasomatism, melt extraction and the thermal evolution of the lithosphere.

Aims and Objectives

- To characterize the Eastern Namaqualand peridotite xenolith suite for mineral major and trace element chemistry.
- Constrain the extent of melt depletion in the off-craton lithospheric mantle using reconstructed whole rock trace element results.
- Examine the thermal evolution of the off-craton lithospheric mantle sampled by the eastern Namaqualand kimberlites using major and trace element-based thermobarometers.
- Examine the extent of metasomatism and the nature of the metasomatic agents which have affected the lithospheric mantle below eastern Namaqualand.

2. Geology, prior work and samples

The interior of southern Africa is dominated by the Archean Kaapvaal and Zimbabwe cratons and the flanking Proterozoic Namaqua Natal Province (NNP). The NNP forms a ~1400km long and up to 400km wide Proterozoic amalgamation of several crustal terranes situated along the southern margin of the Kaapvaal craton (Nicolaysen and Burger, 1965; Eglington and Armstrong, 2004), which were accreted to the Kaapvaal craton at ~1.2 – 1.0 Ga (Eglington and Armstrong, 2004; Eglington, 2006; Jacobs et al., 2008; Macey et al., 2018). Crustal basement exposures occur in two sectors, the eastern Natal sector and the western Namaqua sector. Exposures in the eastern Natal sector reveal juvenile crustal rocks of Mesoproterozoic arc sequences (McCourt et al., 2006). In the western Namaqua sector, the crustal basement consists of granulite and amphibolite facies rocks which were extensively reworked during the Paleo- and Mesoproterozoic (Eglington, 2006; Macey et al., 2018). The central region is poorly defined, being largely obscured by Phanerozoic Karoo supergroup sediments. The peridotites which form the focus of this study were recovered from kimberlites which erupted through the Namaqua sector of the NNP.

The Namaqua sector is subdivided into several tectonostratigraphic terranes representing a stack of fault-bound thrust sheets (Macey et al., 2017, 2018). Geographically, from west to east the terranes constituting the Namaqua sector are the Bushmanland Subprovince, Richterveld Subprovince, Kakamas (or Gordonia) Domain, Aus Domain, Areachap Domain and Kaaien Domain. Intrusions of kimberlite, ultramafic lamprophyres and related alkaline rocks within the Namaqua sector are prevalent in two main clusters: (i) the Eastern Namaqualand cluster, and (ii) the Namaqualand-Bushmanland-Warmbad (NBW) megalineament (Figure 2.1).

Several of the NBW kimberlites erupted through the Bushmanland Subprovince, the largest crustal block within the Namaqua sector. Two suites of pre-

and post-tectonic felsic gneisses represented by the Little Namaqualand Suite (1.212 – 1.191 Ga) and the Spektakel Suite (1.098 – 1.033 Ga) dominate the Bushmanland Subprovince (Clifford et al., 2004; Macey et al., 2018). The former host Paleoproterozoic (~2.0 – 1.7 Ga) zircon xenocrysts with ages overlapping Sm-Nd mantle model ages of 2.0 Ga (T_{CHUR}; Clifford et al., 2004). Whilst the latter Spektakel Suite hosts coarse-grained megacrystic granite and charnockites (Macey et al., 2018). Supracrustal rocks record peak metamorphism around 1.03 Ga which postdates the Namaquan Orogeny, the cause of which remains contentious (Schmitz and Bowring, 2004; Macey et al., 2018).

The Eastern Namaqualand kimberlite cluster erupted through a portion of the NNP where Karoo sediment cover obscures basement exposure. Granitic gneisses entrained by the Markt kimberlite record U-Pb zircon ages of ~1.1 Ga consistent with eruption through the Kakamas Domain (Schmitz and Bowring, 2004). The Kakamas Domain consists of granulite-facies metasediments of ~1.2 Ga age which were intruded by voluminous granites between 1.21 -1.08 Ga (Pettersson et al., 2007; Bial et al., 2015).

Chemically, the Proterozoic lithospheric mantle beneath the NNP displays chemical compositions intermediate between global off-craton and Archean lithospheric peridotite (Boyd et al., 2004; Janney et al., 2010). Re-Os T_{RD} ages suggest that lithosphere formation occurred in two principal stages, spanning from 2.5 to 1.0 Ga, and resulted in high degrees of melt extraction, producing a moderately infertile mantle residue (Janney et al., 2010). Garnets in these xenoliths are almost entirely chemically classified as G9 (lherzolitic) after Grütter et al. (2004) and the median olivine forsterite content is 91.5, slightly lower than that in Kaapvaal peridotites (Janney et al., 2010; Shiimi, 2017). Xenolith and xenocryst studies suggest that the lithosphere sampled by the kimberlites has experienced varied, localised degrees of metasomatism and re-enrichment, following partial melting, by melts and fluids

relating to Mesozoic kimberlites and Karoo magmatism (Kobussen et al., 2008, 2009; Janney et al., 2010; le Roex and Class, 2016; Shiimi, 2017).

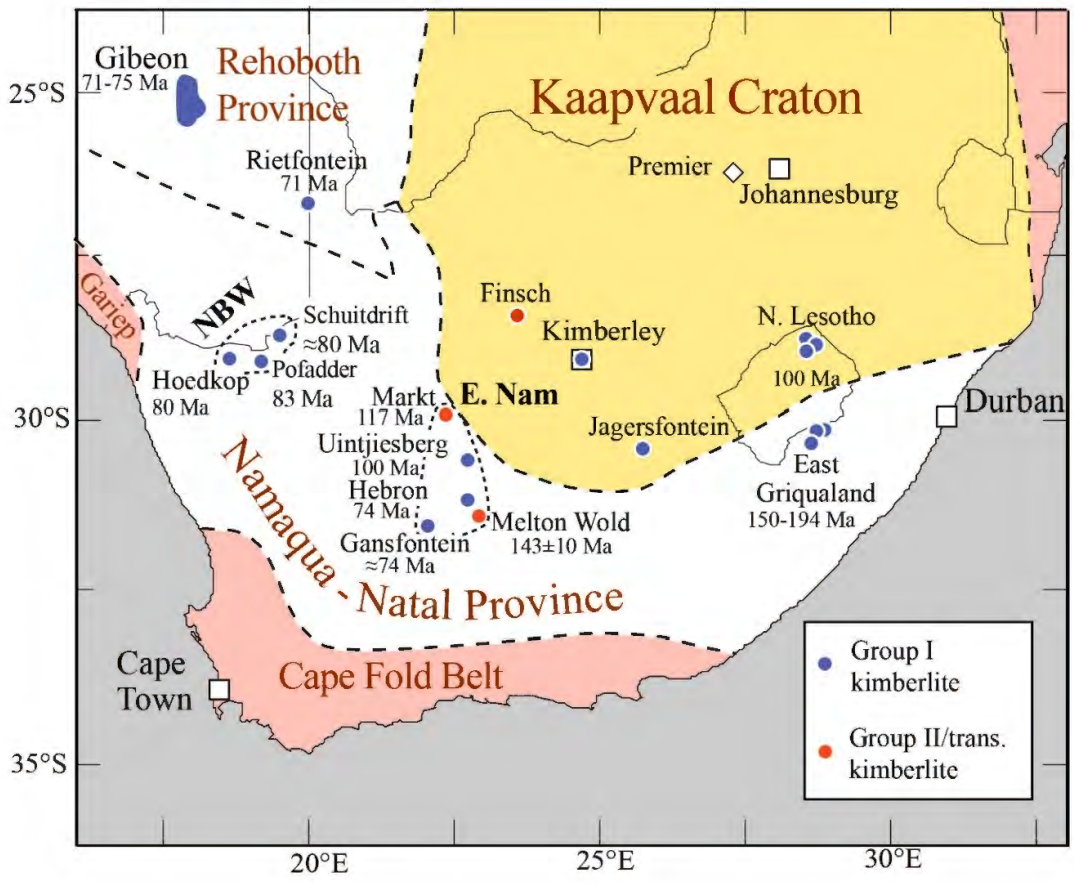

Figure 2.1: Schematic map of simplified tectonic boundaries of southern Africa showing locations of xenolith localities investigated in this study outlined by dotted line. The localities investigated are from the Namaqua-Bushmanland-Warmbad kimberlite province (marked as NBW on the map; Hoedkop and Schuitdrift), and the Eastern Namaqualand kimberlite province (marked as E. Nam on the map; Melton Wold, Markt, Hebron, Uintjiesberg and Gansfontein). Note that only a small subset of the better known on-craton kimberlites are shown on the map. Modified after Janney et al. (2010).

The samples investigated here were obtained from seven kimberlites (Figure 2.1); five erupted within the Eastern Namaqualand kimberlite cluster (Melton Wold, Markt, Hebron, Uintjiesberg, and Gansfontein) and two erupted within the NBW cluster (Hoedkop and Schuitdrift). Both Melton Wold and Markt erupted during the earlier Group II kimberlite pulse and contain minor and uneconomical microdiamonds,

whilst the remainder of the kimberlites erupted during the later Group I kimberlite pulse. The peridotites were selected based on the presence of both garnet and cpx, The suite of peridotites are a subset of those described by Janney et al. (2010). The samples predominantly classify as granular lherzolites (n = 23), with several classifying as deformed lherzolites (n = 3; Hoedkop), and a small number of orthopyroxene-rich pyroxenites and websterites. A detailed description of the sample petrography is provided in the Electronic Appendix 1 of Janney et al. (2010) (available online at http://www.petrology.oxfordjournals.org) and a summary of the rock types and mineral assemblages has been provided in the appendix.

3. Analytical techniques

3.1 Sample preparation

3.1.1 SELFRAG

Cpx and garnet grains were liberated from peridotite samples using SelFrag high voltage pulse power fragmentation technology, housed in the Department of Geology, Stoneman Geochemical Laboratory and Analytical Facilities at the University of Pretoria. The system works as a Faraday cage, with nitrogen-controlled voltage and a pulse control design which is based on a Marx generator. Charge is emitted from the electrode to impact the counter electrode positioned at the bottom of the process vessel. Samples are placed on top of the counter electrode and immersed in water, which acts as an insulator - attracting the discharge to the relatively more conducting solid. The selective fragmentation technique works by exploiting different chemical potentials between minerals. Discharge travels from the electrode through the sample, following the path of least resistance toward the counter electrode, producing a non-contact breakage of the relative minerals. System voltages were set between 90 – 120 kV, depending on the sample size and mineral assemblage, and a built-in sieve of 1 mm mesh size was used to collect the liberated materials.

3.1.2 Mounts and thin sections

Depending on the amount of material available and the size of the xenolith, samples were prepared for trace element analysis as polished 25 x 45 mm thin sections or 25 mm diameter epoxy grain mounts, both at the Department of Geological Sciences, University of Cape Town, although in some cases polished thin sections prepared in the USA for the study of Janney et al. (2010) were also used. In some cases, both thin sections and grain mounts were prepared. Thin sections were either prepared in 30 µm (USA) or 100µm (UCT) thicknesses. Clean and fresh mineral grains, liberated through SelFrag technology, were handpicked under a binocular microscope and mounted on to 25mm epoxy discs.

Grain mounts were preferentially used for laser ablation work to maximise sampling yield as the thickness of the thin sections curtailed the integration times for spot analysis.

3.2 Trace element analysis

Laser ablation inductively coupled plasma mass spectrometry (LA-ICP-MS) allows for in-situ simultaneous high precision and high sensitivity analysis of a large number of elements in individual minerals, as well as analysis of within-grain compositional variation, with a spatial resolution down to 50 µm in favourable cases.

Samples were analysed on the Thermo-Fisher X-Series II quadrupole ICP-MS housed in the Department of Geological Sciences at the University of Cape Town. A New-Wave UP-213 laser ablation system was used to ablate the samples, with a 75 – 100 µm beam diameter at a 10 Hz repeat rate. This is a frequency quintupled Nd-YAG laser, operating at 213 nm, in the deep ultraviolet range of the electromagnetic spectrum. Ablation was conducted using helium as the ablation gas, which was mixed with argon, used as a carrier gas, prior to entering the ICP-MS torch.

Analytical calibration of element sensitivities was achieved by external standardization using synthetic reference materials NIST-610 and NIST-612. NIST-610 and -612 are silicate glasses produced by the United States National Institute of Standards and Technology. In-house cpx, CPX JJG-1424, and garnet, GT JJG-1424, (JJG-1424 is a well-equilibrated websterite xenolith from the Thaba Putsoa kimberlite in northern Lesotho) were analysed at regular intervals of every ten unknowns to account for instrumental drift. To adjust each analysis for sensitivity variations over time and between samples, the trace element count rates were normalized to those of Si obtained from previously collected electron probe micro-analysis (EPMA) data.

Data for each spot analysis was acquired through three replicates of one hundred sweeps across the mass range for a total counting time of 140 seconds. Three to ten grains of each mineral were analysed per sample and depending on the grain size two to four spots were analysed on each grain. Reported concentrations are average values, unless

otherwise stated. Ablation positions were carefully selected to avoid ablation of microfractures or secondary minerals. If ablated, such material can result in high concentrations overwhelming the very low intrinsic values of many incompatible elements, particularly Ba. Where spikes in the Ba signal were observed, analyses were discarded.

3.3 Assessment of data quality

One of the goals of this study is to compare major-element and trace-element based thermobarometry results to assess the rates of lithospheric heating or cooling within the study area. Several uncertainties exist in thermobarometry, which impede certainty in the interpretation of results. Reducing the uncertainty in thermobarometry pertaining to analytical work requires paying careful attention to analytical details in order to generate precise and accurate data. In order to minimise this error a detailed assessment of the quality of the data obtained from LA-ICP-MS as well as published EPMA data is required.

3.3.1 Major element data quality

The major element database utilized throughout this study, previously published in Janney et al. (2010), was obtained between 1999 and 2008 at three different labs – Carnegie Institute of Washington (CIW), Arizona State University (ASU), and the University of Chicago (UC) on a JEOL JXA-8900, JEOL JXA-8600 and Cameca SX50 wavelength-dispersive EPMA instruments, respectively. In attempt to cross-calibrate data between labs we undertook a pilot study analysing cpx, opx and garnet in four samples, at the University of Cape Town on a JEOL JXA-8100 during Sept. 2018. The reruns and thermobarometry results have been compared to previously reported values to assess the quality of the published dataset.

Major element compositions were determined using a JEOL JXA-8100 electron microprobe housed in the Department of Geological Sciences at the University of Cape Town. A 15kV accelerating voltage was used, operating at a 20 nA beam current with a 3 µm beam size. 10 second counting times at peak, and background positions, were used for all elements, and natural and synthetic minerals were used as standards. All analyses

were performed at the cores of mineral grains. In-house cpx (CPX JJG-1424), and orthopyroxene (OPX JJG-1424), and international standard Kakanui Pyrope (K-P), issued by the Smithsonian Institute, were analysed at regular intervals of every ten unknowns to account for instrumental drift.

In-house standards

EPMA results for in-house CPX JJG-1424, OPX JJG-1424 and K-P standards, along with recommended values are reported in Table 3.1 – 3.4, respectively. For in-house standards CPX JJG-1424 and OPX JJG-1424, recommended values are an average of EPMA and XRF values. The recommended values for K-P are those reported by the Smithsonian National Museum of Natural History.

CPX JJG-1424

All major elementsare within 10 – 15% of the recommended values (Table 3.1). Minor elements, Although minor differences are noted throughout the lab session, particularly in TiO_2, MnO and CaO, at the count times and beam currents utilized it is not possible to scrutinize the data to a higher degree.

OPX JJG-1424

For those elements which are in high concentration in orthopyroxene (SiO_2, FeO and MgO) the data are within 10% of the recommended values (Table 3.2). However, for elements present in minor abundances (TiO_2, Al_2O_3, Cr_2O_3, MnO, CaO and Na_2O) the results obtained during this study indicate both low precision and accuracy (up to 60% below recommended values). Precision of probe data is a function of the count rate, and therefore the beam current. Elements with a high atomic number (e.g. Fe and Mn) have low count weights per weight percent, and it is often favourable to count for longer than the standard times on these elements to increase the accuracy and precision when they are in present in low abundance. A probable explanation for the large variation in low abundance elements is the specific analytical conditions applied (10s count times and 20nA cup currents).

Kakanui Pyrope

Garnet data for all elements are within 10 – 15% of the recommended values (Table 3.3).

Table 3.1: EPMA results obtained for in-house cpx standard CPX JJG-1424 during this study (a – z). n.d. denotes not detected. Recommended values are an average of EPMA and XRF results obtained from the lab.

	Date	wt.%	SiO_2	TiO_2	Al_2O_3	Cr_2O_3	FeO	MgO	MnO	CaO	Na_2O	K_2O	Total
Recommended			54.64	0.28	3.13	0.81	1.71	16.44	0.14	21.40	1.66		99.05
a.	18/09/2018		54.1	0.27	3.08	0.76	1.6	16.7	0.04	21.5	1.6	n.d.	99.66
b.	18/09/2018		54.4	0.29	3.11	0.78	1.6	16.6	0.03	21.0	1.5	n.d.	99.35
c.	18/09/2018		54.7	0.27	3.05	0.75	1.7	16.5	0.03	21.6	1.5	0.003	100.09
d.	18/09/2018		54.5	0.28	3.10	0.79	1.6	16.9	n.d.	21.5	1.5	0.004	100.23
e.	18/09/2018		54.2	0.19	3.17	0.70	1.7	16.6	0.07	21.5	1.5	0.003	99.64
f.	19/09/2018		54.5	0.29	3.05	0.78	1.5	16.6	0.05	22.0	1.5	0.005	100.28
g.	19/09/2018		54.3	0.29	3.12	0.72	1.6	16.5	0.05	20.7	1.6	n.d.	98.73
h.	19/09/2018		54.4	0.29	3.16	0.80	1.6	16.4	0.04	20.6	1.5	0.003	98.81
i.	19/09/2018		54.9	0.27	3.08	0.77	1.6	16.5	0.06	20.7	1.7	n.d.	99.53
j.	19/09/2018		54.8	0.30	3.08	0.82	1.7	16.9	0.04	21.3	1.6	n.d.	100.56
k.	19/09/2018		54.1	0.29	3.08	0.75	1.7	16.6	0.06	21.5	1.5	n.d.	99.59
l.	19/09/2018		54.5	0.24	3.09	0.78	1.8	16.5	0.05	21.4	1.5	n.d.	99.75
m.	19/09/2018		54.4	0.33	3.05	0.79	1.7	16.8	0.05	21.8	1.6	n.d.	100.38
n.	19/09/2018		54.2	0.26	3.05	0.77	1.6	16.5	0.02	21.7	1.6	n.d.	99.61
o.	19/09/2018		54.4	0.32	3.06	0.74	1.5	16.7	0.08	21.6	1.7	n.d.	100.02
p.	19/09/2018		54.5	0.30	3.09	0.84	1.7	16.7	0.04	21.6	1.6	n.d.	100.47
q.	19/09/2018		54.4	0.26	3.18	0.70	1.8	16.5	0.04	21.6	1.6	0.009	100.08
r.	19/09/2018		54.3	0.25	3.14	0.75	1.6	16.7	0.02	21.7	1.5	n.d.	100.00
s.	19/09/2018		53.9	0.29	3.09	0.78	1.7	16.6	0.06	21.7	1.5	n.d.	99.73
t.	19/09/2018		54.3	0.24	3.17	0.75	1.7	16.8	0.01	21.6	1.6	n.d.	100.03
u.	19/09/2018		54.6	0.27	3.14	0.75	1.6	16.5	0.08	21.7	1.6	0.001	100.35
v.	19/09/2018		54.3	0.28	3.10	0.75	1.6	16.7	0.03	21.5	1.6	n.d.	99.89
w.	19/09/2018		54.4	0.23	3.08	0.78	1.6	16.4	0.03	21.7	1.6	0.008	99.90
x.	19/09/2018		54.5	0.27	3.04	0.73	1.6	16.6	0.05	21.4	1.6	0.005	99.72
y.	21/09/2018		54.7	0.25	3.13	0.70	1.7	16.7	0.05	21.6	1.6	n.d.	100.42
z.	21/09/2018		54.5	0.27	3.15	0.76	1.7	16.7	0.03	21.5	1.6	0.006	100.20

Table 3.2: EPMA results for in-house orthopyroxene standard OPX JJG-1424 obtained during this study (a – g). Recommended values are an average of EPMA and XRF results obtained from the lab.

	Date	wt.%	SiO_2	TiO_2	Al_2O_3	Cr_2O_3	FeO	MgO	MnO	CaO	Na_2O	Total
Recommended			57.01	0.13	1.27	0.23	5.07	36.33	0.11	0.23	0.07	99.24
a.	20/09/2018		57.7	0.11	0.97	0.18	5.1	35.8	0.12	0.24	n.d.	100.19
b.	20/09/2018		57.2	0.08	0.94	0.17	4.9	35.8	0.06	0.25	0.03	99.39
c.	20/09/2018		57.3	0.10	1.02	0.16	5.2	36.0	0.13	0.26	0.03	100.23
d.	20/09/2018		56.5	0.09	1.05	0.12	4.9	35.8	0.06	0.23	0.03	98.79
e.	20/09/2018		57.7	0.08	0.99	0.19	5.1	35.9	0.08	0.25	0.04	100.32
f.	21/09/2018		57.7	0.05	0.95	0.20	5.0	35.7	0.05	0.27	0.04	99.94
g.	21/09/2018		57.2	0.05	0.98	0.17	5.0	35.9	0.09	0.24	0.05	99.64

Table 3.3: EPMA result for pyrope standard K-P (Kakanui pyrope) obtained during this study (a – j). n.d. denotes not detected. Recommended values are from the Smithsonian National Museum of National History microbeam standards datasheet.

		Wt.%	SiO_2	TiO_2	Al_2O_3	Cr_2O_3	FeO	MgO	MnO	CaO	Na_2O	K_2O	Total
Recommended			41.46	0.47	23.73		10.68	18.51	0.28	5.17			100.30
a.	20/09/2018		41.5	0.45	23.8	0.10	10.8	18.7	0.31	5.28	0.01	n.d.	100.94
b.	20/09/2018		41.7	0.43	24.4	0.08	10.7	18.6	0.29	5.18	0.01	0.013	101.31
c.	20/09/2018		41.4	0.40	24.1	0.04	10.5	18.4	0.31	5.17	n.d.	0.007	100.31
d.	20/09/2018		41.6	0.41	23.7	0.09	10.5	18.5	0.33	5.22	0.04	n.d.	100.44
e.	21/09/2018		41.7	0.44	24.1	0.05	10.5	18.1	0.31	5.27	0.06	n.d.	100.60
f.	21/09/2018		41.5	0.43	23.7	0.10	10.6	18.8	0.34	5.06	0.01	0.011	100.64
g.	21/09/2018		41.3	0.38	24.0	0.10	10.7	18.6	0.33	5.19	0.07	n.d.	100.61
h.	21/09/2018		41.4	0.43	23.8	0.12	10.2	18.7	0.31	5.18	0.04	n.d.	100.21
i.	21/09/2018		41.9	0.41	24.1	0.06	10.0	18.0	0.29	5.33	0.05	0.008	100.02
j.	21/09/2018		41.5	0.41	23.6	0.06	10.8	18.5	0.28	5.32	0.03	0.013	100.39

Comparison to mineral chemistry and thermobarometry data from Janney et al. (2010)

Concentrations of major elements obtained from EPMA during this study and those reported in Janney et al. (2010) are reported in Table 10.1 – 10.3 of the appendix and illustrated in Figure 3.1 & 3.2. For the purposes of this section, data published in Janney et al. (2010) are referred to as PEJ, and data obtained in this study are referred to as FC. Illustrations are displayed as PEJ dataset normalized to FC dataset. Note that the y-axis of the graphs does not remain constant. For all the samples and constituent minerals, the greatest discrepancies between the two datasets are noted between minor elements.

Results for UINT-4 display large variation in TiO_2, MnO and Na_2O across the FC dataset, as evidenced by the large error bars (Figure 3.1a – c). All major elements agree within analytical uncertainty with results reported in PEJ. Al_2O_3, Cr_2O_3 and Na_2O in cpx disagree across labs, but remain within 20% of the PEJ dataset. The misfit for opx results reflects low precision of minor elements in the FC dataset, this is particularly evident in CaO (Figure 3.1c).

The data for garnet and opx in UINT-8 are in general agreement with those of PEJ (Figure 3.1e & f), however, variation is noted in the cpx results (Figure 3.1d). TiO_2 and FeO are higher and Al_2O_3, Cr_2O_3 and Na_2O are lower in cpx from the FC data, in comparison to the PEJ data. Nine cpx spots were analysed on this sample in this study, all of which display consistent deviation from the PEJ data (note error bars calculated from repeat analysis).

The largest misfit noted between the labs is evident in GANS-2. For CaO, MgO, FeO and Na_2O, which were run at longer count times in cpx, the results agree well with the PEJ dataset (Figure 3.2a). TiO_2, Cr_2O_3 and Na_2O in both cpx and garnet

(Figure 3.2a – c) disagree across dataset. Opx results are in general agreement across labs, however, large variation is noted in elements of low abundance (Figure 3.2d).

The majority of the oxides in GANS-9 cpx, garnet and opx agree, within analytical uncertainty, across the labs (Figure 3.2e – g). Abundances of Cr_2O_3 are high, in comparison to the PEJ data, across all minerals analysed in GANS-9.

It is apparent that for elements present in high abundance, greater agreement is noted across the labs. Although minor variation is evident for major elements, the range in variability noted here has often been observed in interlaboratory comparisons (c.f. Figure 2 Kuehn et al. (2011)) and is largely dependent on the methodologies used (e.g. count times, beam currents, equipment, calibration standards and correction methods). Interlaboratory variations noted for minor elements, particularly those with high atomic numbers, suggests that analytical conditions could be adapted for these elements to improve precision and accuracy. The disagreement observed in Cr_2O_3 results for several minerals in the samples analysed here is alarming. Although minor variation is noted in minor element concentrations of the in-house standards in comparison to the recommended values, it is not to the order of magnitude observed when comparing the data analysed here to the published data.

To assess the influence of the observed interlaboratory variation on thermobarometry results, pressures and temperatures of last equilibration were calculated for both FC and PEJ datasets. Four thermobarometer combinations were used: (i) The two-pyroxene thermometer and garnet-opx barometer of Brey and Kohler (1990) (T_BKN & P_BKN), (ii) the single cpx thermobarometer of Nimis and Taylor (2000) (T_NT & P_NT), (iii) the two-pyroxene thermometer of Taylor (1998) (T_TA98) in combination with the garnet-opx barometer of Nickel and Green (1985) (P_NG85) and (iv) the cpx-garnet thermometer of Krogh (1988) (T_KR88) in combination with the garnet-opx BKN barometer (P_BKN).

Thermobarometry results are reported in Table 3.4 and illustrated in Figure 3.3a – h. The figures present P-T results calculated for the FC dataset subtracted from those calculated from the PEJ dataset. Filters applied to assess whether samples were within the calibration range for T_NT and P_NT are those recommended in Ziberna et al. (2016). All samples apart from GANS-2 are in reasonable agreement when applying the BKN thermobarometer (Figure 3.3a &b). Results for GANS-2 show that when using cpx data obtained using longer count times on selected elements, the results are pulled closer to those of PEJ. However, temperature results still disagree by 150°C, and 8kbar. The results obtained using the T_NT thermobarometer are all in good agreement (Figure 3.3c & d). When applying the compositional filters of Ziberna et al. (2016), both GANS-2 and GANS-9 cpx data calculated from PEJ data do not fall within the calibration range of the thermobarometer as Cr_2O_3 values are too low.

Similar to what was found when applying the BKN thermobarometer, results calculated for T_TA98-P_NG85 show reasonable agreement for all samples apart from GANS-2 (Figure 3.3e & f). Temperatures disagree by up 200°C and pressures by 10 kbar in GANS-2. Unlike all other thermobarometer combinations discussed above, when applying T_KR88-P_BKN to GANS-2, the results show reasonable agreement across labs. Temperatures calculated using T_KR88 suggest good agreement for all samples apart from UINT-8 (Figure 3.3g & h). This sample displays minor interlaboratory disagreement across minor element results, particularly for cpx. A similar result is observed for the pressure results.

It is evident from the results discussed above that the data collected during this study using the EPMA at the University of Cape Town disagree, to varying degrees, with those published by Janney et al. (2010) and emphasize the importance of analytical conditions and internal consistency with regards to thermobarometry calculations of individual samples. These errors may be the result of systematic errors

relating to EPMA setup or random errors resulting from operator inconsistency, the condition of the samples surface, and random instrumental instability. The disagreement in Cr_2O_3 regardless of the sample or mineral being analysed (see Figure 3.1 and 3.2 for results for cpx in UINT-8, GANS-2 & GANS-9, garnet in GANS-9 and orthopyroxene in GANS-9) and the high precision in Cr_2O_3 analyses (calculated from repeat analysis) preclude error resulting from surface irregularities in the samples. The underlying cause of the discrepancies in the two datasets may be due to any number of systematic errors or differences in analytical calibration and require a rigorous assessment of standards and the microprobe setup. However, technical difficulties with the electron microprobe at the University of Cape Town following these analyses meant that no further analyses could be performed throughout the course of this study and a closer look at the abovementioned issues could not be performed. For this reason, the published dataset (PEJ) was utilised for this study.

Table 3.4: Pressure (kbar) and temperature (° C) estimates calculated for samples analysed in interlaboratory comparison pilot study as well as previously published major element data of Janney et al. (2010). Details pertaining to thermobarometers utilised are discussed in the text.

Sample	UINT-4 (PEJ)	UINT-4 (FC)	UINT-8 (PEJ)	UINT-8 (FC)	GANS-2 (PEJ)	GANS-2 (FC LONG)	GANS-2 (FC SHORT)	GANS-9 (PEJ)	GANS-9 (FC)
Locality	Uintjiesberg	Uintjiesberg	Uintjiesberg	Uintjiesberg	Gansfontein	Gansfontein	Gansfontein	Gansfontein	Gansfontein
Type	Garnet websterite	Garnet websterite	Garnet spinel lherzolite	Garnet spinel lherzolite	Garnet spinel lherzolite	Garnet spinel lherzolite	Garnet spinel lherzolite	Garnet websterite	Garnet websterite
Paragenesis	opx-cpx-gt	opx-cpx-gt	ol-opx-cpx-gt-sp	ol-opx-cpx-gt-sp	ol-opx-cpx-gt-sp	ol-opx-cpx-gt-sp	ol-opx-cpx-gt-sp	opx-cpx-gt	opx-cpx-gt
T_{BKN}	894	874	1015	1062	820	968	1012	976	994
P_{BKN}	28	27	34	36	25	33	36	35	33
T_{NT}	840	831	946	962	Not suitable	974	1021	Not suitable	961
P_{NT}	30	29	41	34	Not suitable	37	38	Not suitable	30
T_{TA98}	843	835	942	972	822	974	1020	943	973
P_{NG85}	27	26	33	34	27	35	37	33	34
T_{KR88}	884	882	1192	1040	848	811	785	814	803
P_{BKN}	27	27	43	35	27	24	23	25	20

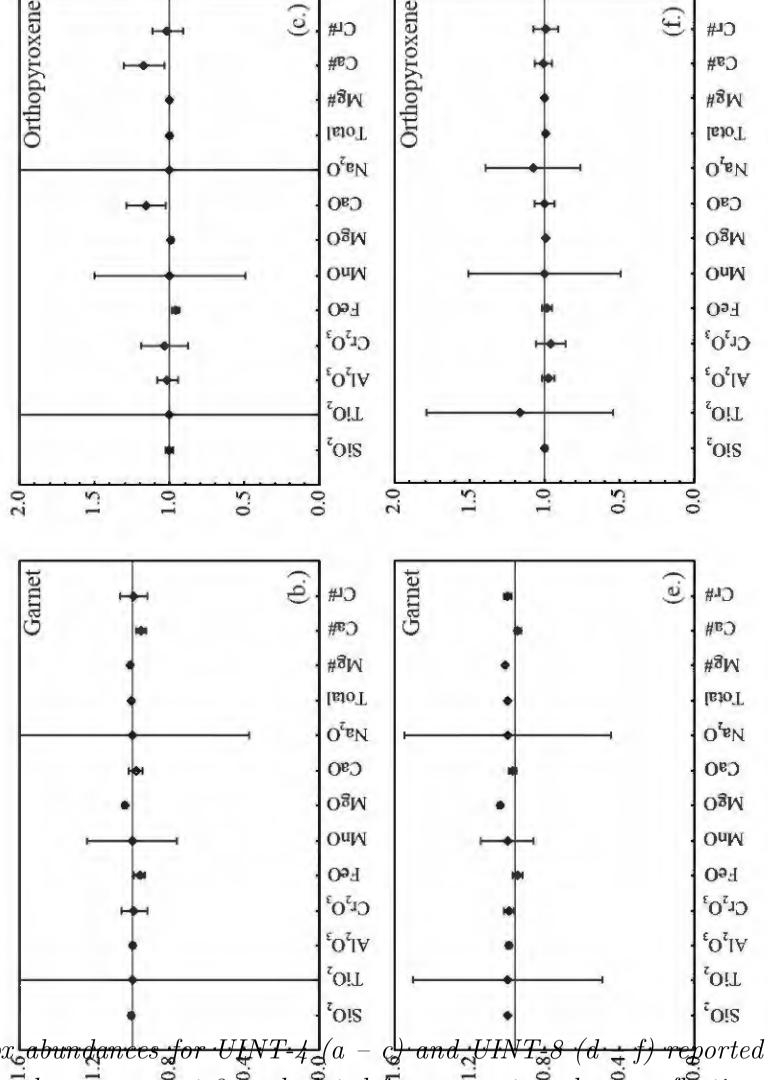

Figure 3.1: Cpx, garnet and opx abundances for UINT-4 (a – c) and UINT-8 (d – f) reported in (Janney et al., 2010) divided by mean abundances obtained during this study. Error bars represent 2σ calculated from repeat analyses, reflecting low precision in elements of low abundance. Note that the scale of the y-axis does not remain constant throughout the figures.

Figure 3.2 (following page): Cpx, garnet and opx abundances for GANS-2 (a – d) and GANS-9 (e – g) reported in (Janney et al., 2010) divided by mean abundances obtained during this study. Error bars represent 2σ calculated from repeat analyses, reflecting low precision in elements of low abundance. Note that the scale of the y-axis does not remain constant throughout the figures. Cpx in GANS-2 (a & b) was run at two separate analytical conditions. Results reported in (a) refer to results obtained with 30s count times on Ca, Mg, Fe, Na and Al.

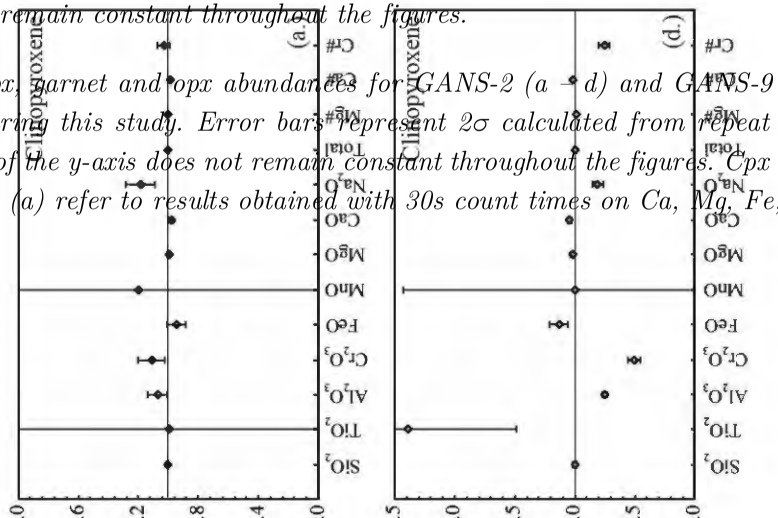

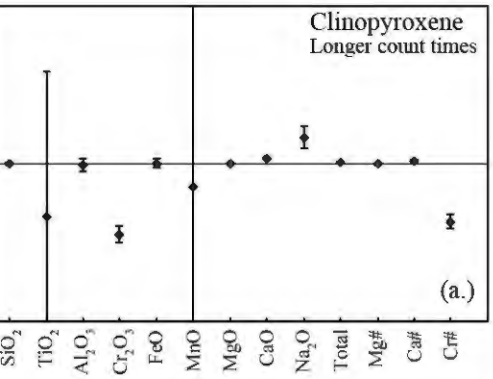
Clinopyroxene
Longer count times
(a.)
SiO2
TiO2
Al2O3
Cr2O3
FeO
MnO
MgO
CaO
Na2O
Total
Mg#
Ca#
Cr#

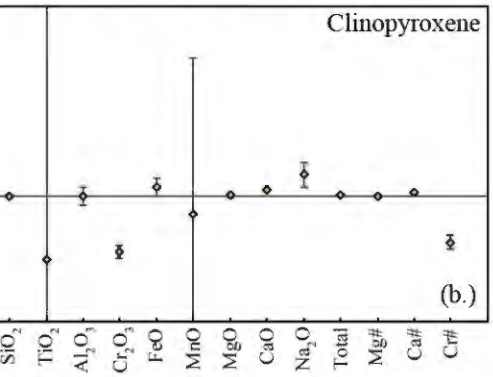
Clinopyroxene
(b.)
SiO2
TiO2
Al2O3
Cr2O3
FeO
MnO
MgO
CaO
Na2O
Total
Mg#
Ca#
Cr#

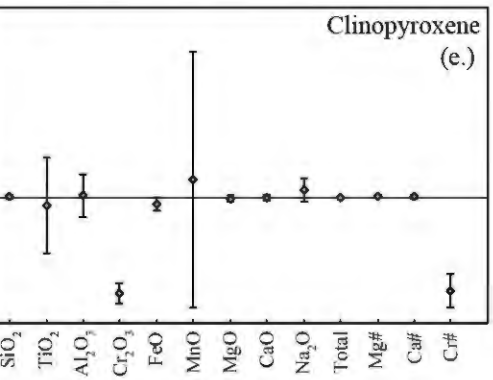
Clinopyroxene
(e.)
SiO2
TiO2
Al2O3
Cr2O3
FeO
MnO
MgO
CaO
Na2O
Total
Mg#
Ca#
Cr#

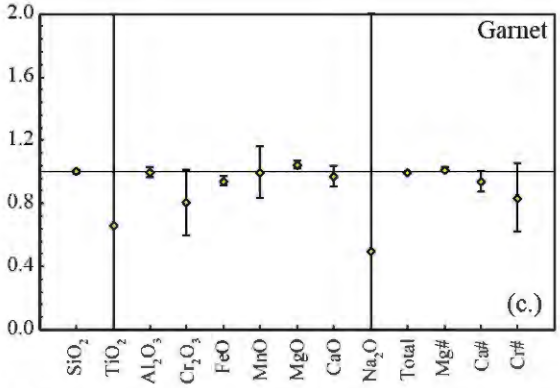
Garnet
(c.)
2.0
1.6
1.2
0.8
0.4
0.0
SiO2
TiO2
Al2O3
Cr2O3
FeO
MnO
MgO
CaO
Na2O
Total
Mg#
Ca#
Cr#

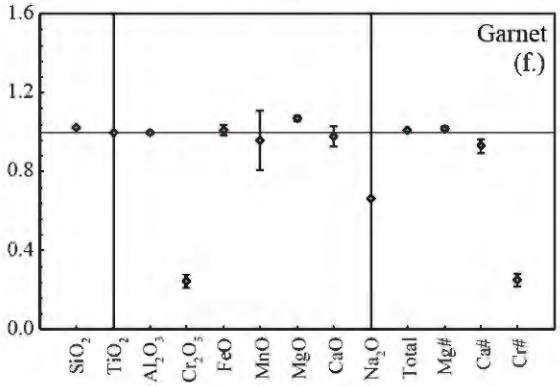
Garnet
(f.)
1.6
1.2
0.8
0.4
0.0
SiO2
TiO2
Al2O3
Cr2O3
FeO
MnO
MgO
CaO
Na2O
Total
Mg#
Ca#
Cr#

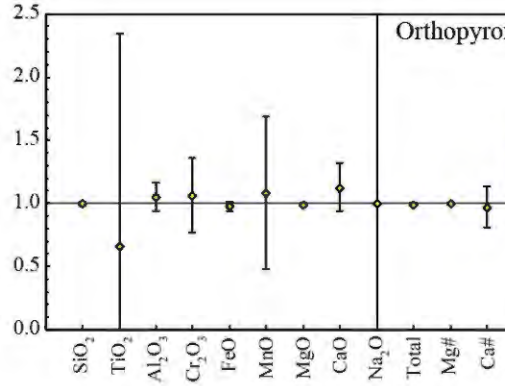
Orthopyro
2.5
2.0
1.5
1.0
0.5
0.0
SiO2
TiO2
Al2O3
Cr2O3
FeO
MnO
MgO
CaO
Na2O
Total
Mg#
Ca#

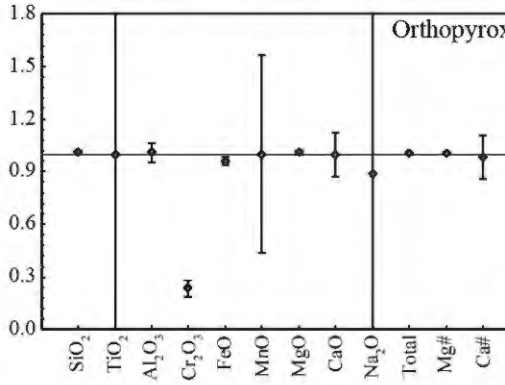
Orthopyrox
1.8
1.5
1.2
0.9
0.6
0.3
0.0
SiO2
TiO2
Al2O3
Cr2O3
FeO
MnO
MgO
CaO
Na2O
Total
Mg#
Ca#

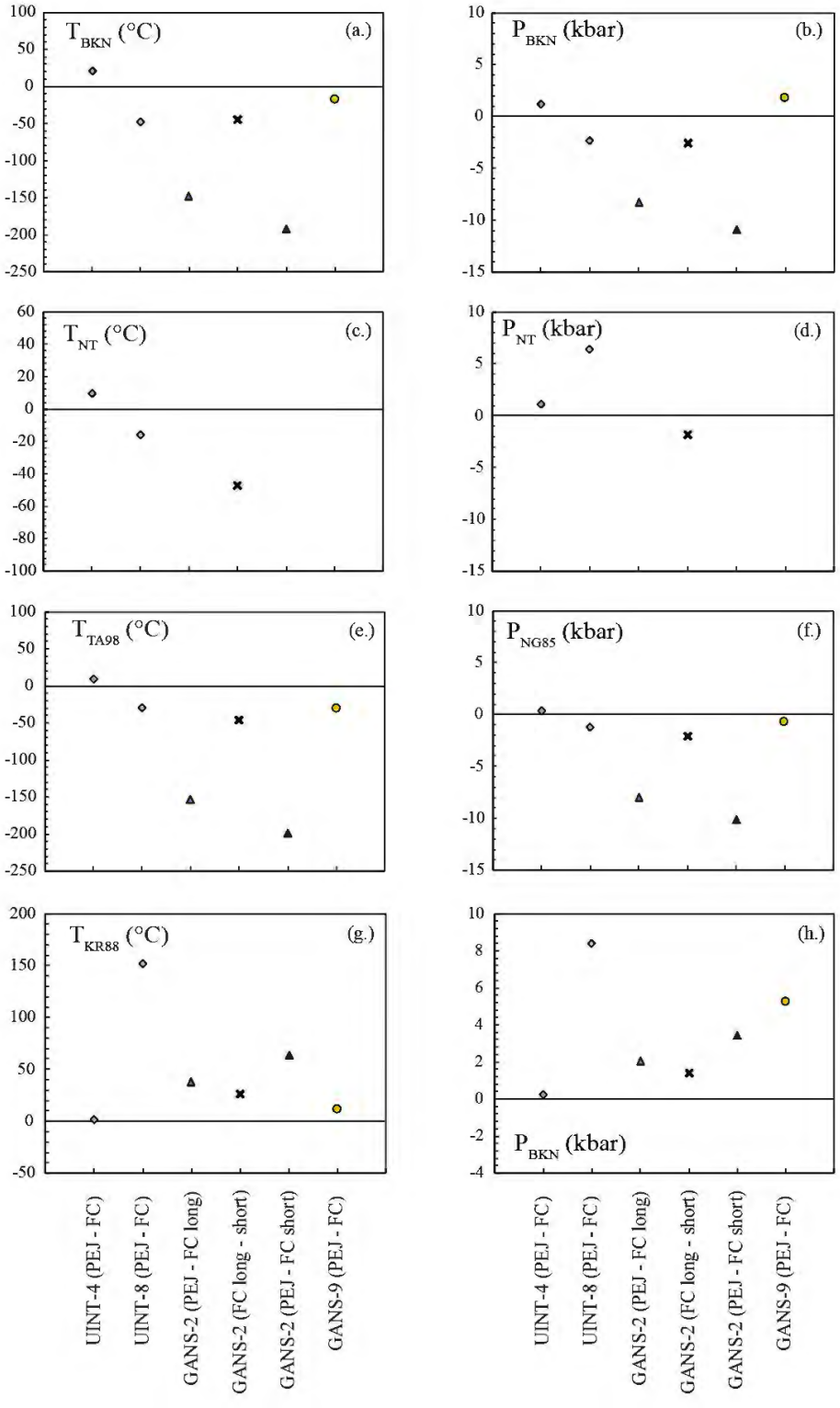

Figure 3.3:Thermobarometry results calculated from FC dataset subtracted from those calculated from PEJ dataset. Details pertaining to thermobarometers utilised are discussed in the text. Note that the y-axis does not remain constant across the figures.

3.3.2 Trace element data quality

LA-ICP-MS data were collected over several months in three main analytical sessions, (i) August 2018, (ii) October/November 2018 and (iii) August 2019.

NIST-610 & -612

Measured concentrations for NIST-610 and -612 as unknowns are reported in Table 11.1 – 11.4 of the appendix, and presented in Figure 3.4. Values plotted in the figures represent mean concentrations per session normalized to the recommended values of Pearce et al. (1997). The NIST-610 and -612 glasses are fused silicate glasses composed of high purity quartz sand, soda ash, alumina and calcium carbonate. Both glasses are doped with sixty-one trace elements. These trace elements were doped at concentrations of approximately 500µg g^{-1} for NIST-610, and 50 µg g^{-1} for NIST-612.

The mean trace element measurements for all elements apart from Zn from both August 2018 and August 2019 datasets are within 5 – 10% of the recommended values reported by Pearce et al. (1997). Concentrations for Zn in this study range from 481 – 690 ppm, it is apparent from the large error bars present across both lab sessions (Figure 3.4a & b), that the variability is not restricted to one session. Jochum et al. (2011) list Zn as a moderately inhomogeneous element in NIST silicate glasses. Homogeneities noted in chalcophile and siderophile elements within NIST glasses have been ascribed to volatile loss during high temperature fusion when being manufactured (Eggins and Shelley, 2002). Concentrations of Zn in NIST-612 obtained during October 2018 show minor deviation from recommended values, however it is apparent in results obtained during August 2019 (Figure 3.4c) that the large variation noted in NIST-610 is also present in NIST-612 results (Figure 3.4d). Low precision in Zn suggest that concentrations within the samples may be due to inhomogeneity within the NIST glasses.

Measured concentrations for NIST-612 during October 2018 and Aug 2019 are predominantly within 10 – 15% and 10 – 20%, respectively, of the recommended values of Pearce et al. (1997). The measured concentrations from LA-ICP-MS for Ti and Ta are low by 20 – 30% in relation to the recommended values. Jochum et al. (2011) report concentrations of Ti which are 10% lower than those reported in Pearce et al. (1997) and concentrations of Ta which disagree by up to 7% with those reported in Pearce et al. (1997), which may suggest heterogeneity in Ti and Ta in NIST samples or inaccuracy in the recommended values. To validate the accuracy of Ti results from LA-ICP-MS, garnet TiO_2 concentrations measured by EPMA were converted to Ti and plotted against LA-ICP-MS results (Figure 3.5). The data are within reasonable agreement, suggesting that Ti results from measure by laser ablation are of acceptable quality.

CPX and GT JJG-1424

Measured concentrations for the in-house cpx and garnet standards (CPX JJG-1424 & GT JJG-1424) are reported in Table 11.5 – 11.10 of the Appendix and presented in Figure 3.6 as normalized ratios to the recommended values. The recommended values used here for the in-house standard represent a mean concentration obtained through solution ICP-MS. The in-house standards have not been extensively quantified for trace elements, thus results illustrated and reported here should not be weighted heavily but do emphasize the importance of quantifying standards.

The majority of elements which are present in concentrations > 1 ppm are with 15 – 20% of the recommended values. Those elements which are present at concentrations below 1 ppm and fall toward the lower limits of detection (e.g. heavy rare earth elements in cpx and light rare earth elements in garnet) display large disagreement with the recommended values.

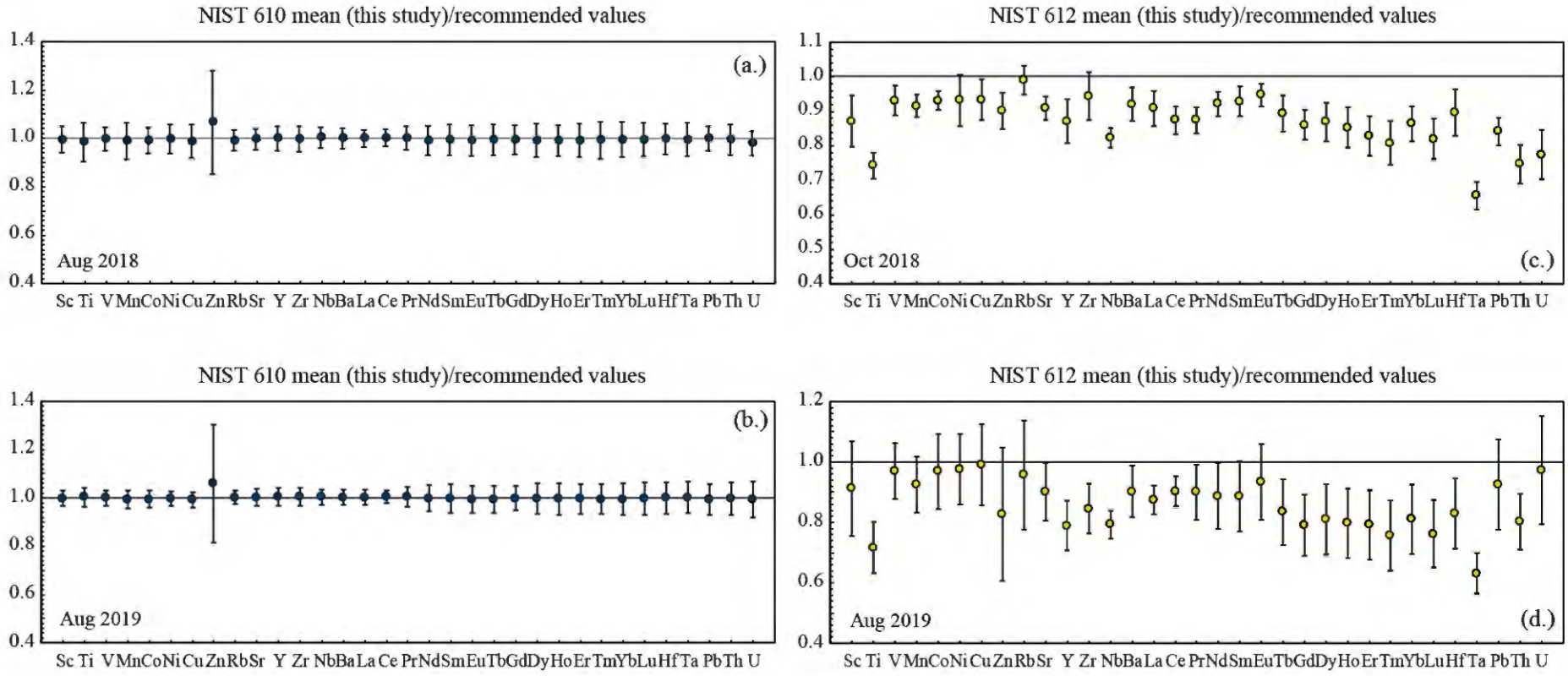

Figure 3.4: Mean NIST-610 (a & b) and NIST-612 concentrations from this study over various lab sessions divided by recommended values reported by Pearce et al. (1997). Error bars are 2σ calculated from repeat analysis.

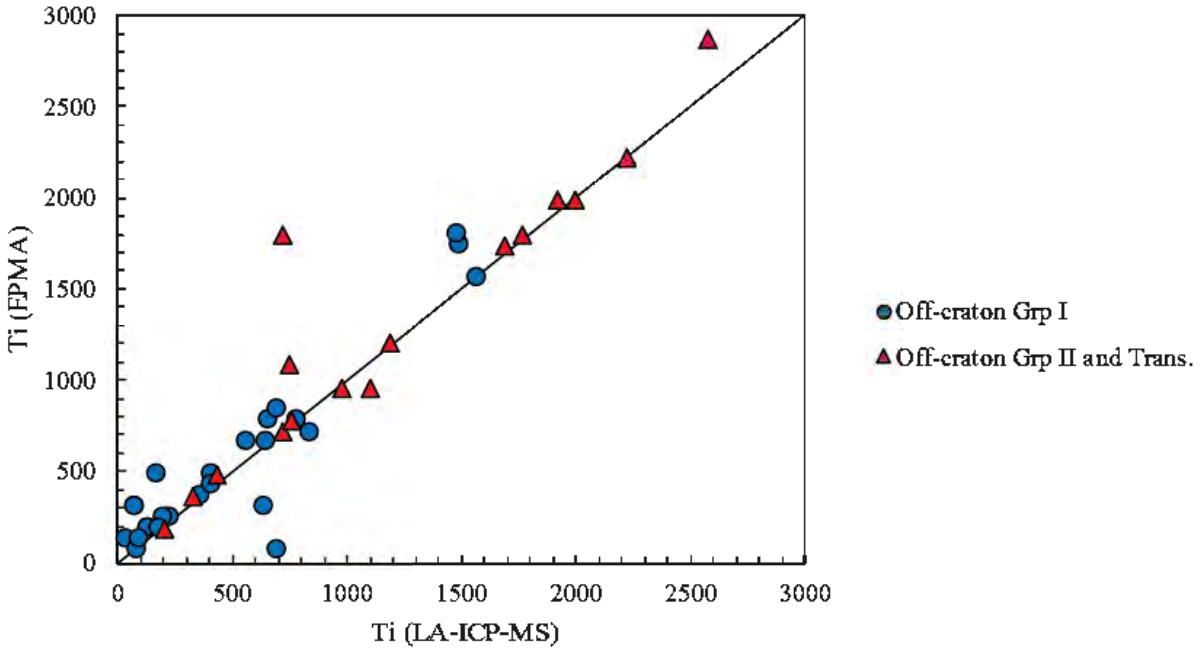

Figure 3.5: Ti (ppm) concentrations in garnet from off-craton peridotites measured by EPMA (y-axis) vs Ti measured by LA-ICP-MS (x-axis) displaying reasonable agreement between the datasets.

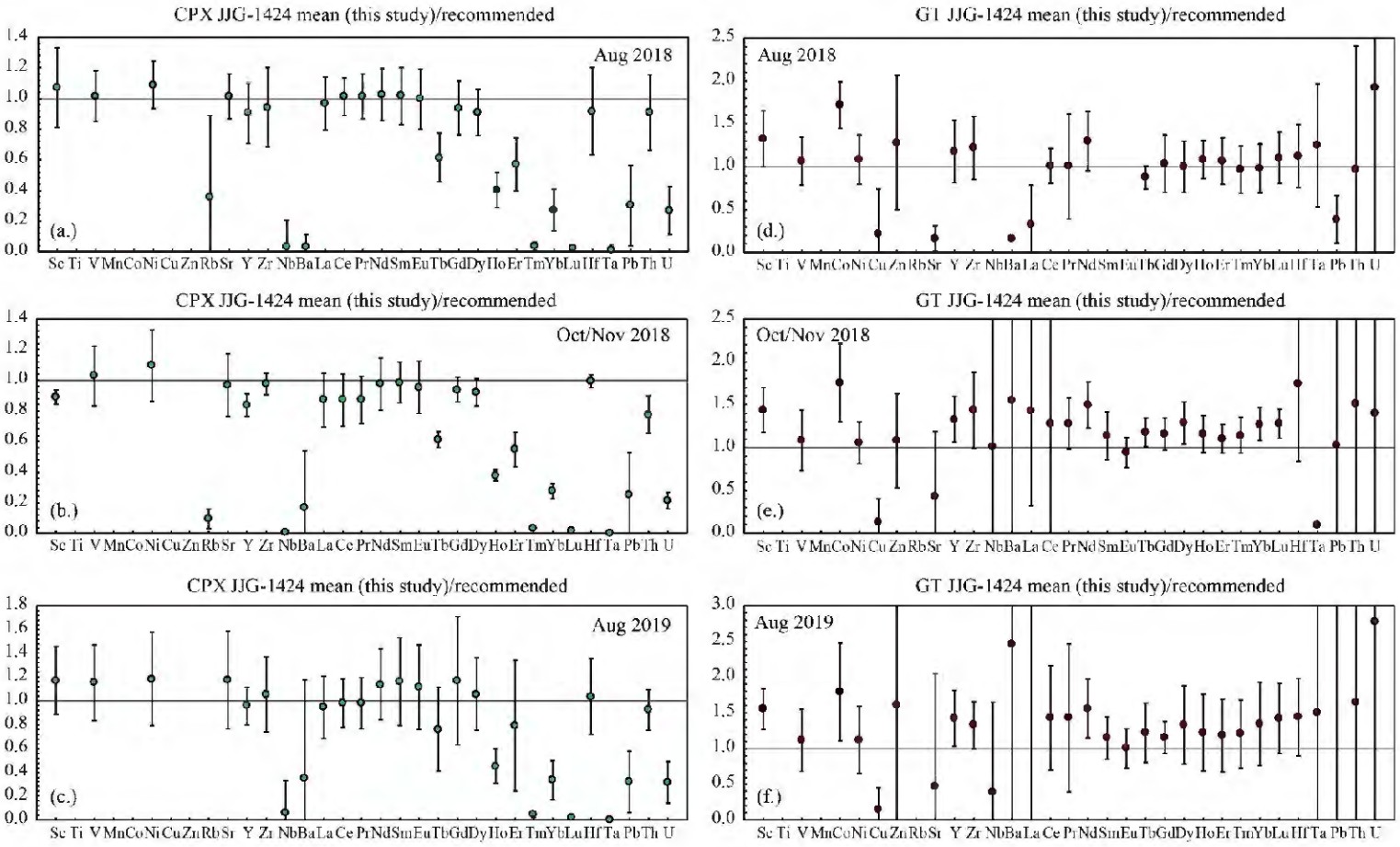

Figure 3.6: Mean CPX JJG-1424 (a – c) and Gt JJG-1424 (d – f) concentrations from this study obtained over various lab sessions, divided by recommended values. Error bars are 2σ calculated from repeat analysis.

4. Trace element results

LA-ICP-MS analyses results for garnet and cpx in off-craton peridotite xenoliths are reported in Table 4.1 & Table 4.2 and illustrated as CI chondrite and primitive mantle normalized (McDonough and Sun, 1995) graphs in Figure 4.1 – 4.5. Due to the fact that xenoliths from kimberlites of the same age from the Eastern Namaqualand and NBW clusters show similar characteristics, the samples are divided by age rather than geographic position.

It should be noted that the word "anomaly" in the context of this section, refers to any element with abundances significantly lower, or higher, than that interpolated between elements of neighbouring incompatibility on the primitive mantle normalized incompatible element diagrams. Crystal-chemical controls within minerals play a large role in the incorporation of trace elements, such that some specific elements are expected to be depleted or enriched in specific minerals (e.g. enrichment in heavy REEs in garnet). The ordering of elements in incompatible element plots are based on increasing bulk partition coefficients between basaltic melts and typical mantle peridotite rather than individual mantle minerals. Therefore, elements may appear "anomalously" low or high in these plots due to crystallographic structure effects (i.e., size and coordination of cation sites) as well as reflecting the composition of the melts/fluids that may have equilibrated with the minerals.

4.1 Garnet

Garnets were subdivided into groups based on the position of the maxima within the light REE (LREE; La – Nd) and by the slopes within the medium REE (MREE; Sm – Ho) to heavy REE (HREE; Er – Lu).

"Normal" REE garnets display positive slopes within the LREE, followed by flat or gently positive slopes between the MREE and HREE. They display large variations in Ti (80 – 2600 ppm), Y (7 – 24 ppm) and Zr (8 -143 ppm; Figure 4.3a &b).

Sinusoidal patterns are those identified as having a positive slope within the LREE with a local maximum between Sm and Gd, a local minimum located within the MREE to HREE and a positive slope in the heaviest REE. The precise location of the minima of the trough does vary across the sample suite and within individual localities (e.g. see patterns for Melton Wold garnets, Figure 4.2f). Samples with sinusoidal REE have Ti contents of less than 1200 ppm and Zr of less than 42 ppm with Y contents between 2 and 24 ppm (Figure 4.3a & b).

Sloped patterns are characterized by a positive slope within the LREE with maxima between Gd and Tb, followed by negative slopes toward Lu. Sloped garnets are restricted having to higher Zr contents (60 – 90 ppm), Y between 18 and 22 ppm and Ti between 140 and 845 ppm (Figure 4.3a & b).

Chondrite-normalized REE patterns in garnet most frequently exhibit "normal" patterns (n = 24); 14 samples display sinusoidal REE and 7 samples display sloped REE patterns (Figure 4.1 – 4.2). The presence of a REE style (i.e., "normal", sinusoidal or sloped) is not mutually exclusive across individual localities nor across a temporal framework (i.e. Group I vs Group II kimberlites). All of the localities studied here, apart from Schuitdrift for which only one sample was analysed, display at least two garnet REE styles.

Primitive mantle-normalized incompatible element diagrams show that all garnets exhibit negative Sr and Ti anomalies (Figure 4.1 – 4.2). Garnets exhumed by Group I kimberlites within the Eastern Namaqualand cluster (Hebron, Gansfontein and Uintjiesberg) and Hoedkop (NBW cluster) also display negative Hf anomalies. The garnet from the one garnet-bearing Schuitdrift peridotite (NBW cluster) displays pronounced

positive Zr and Hf anomalies (Figure 4.2c), whereas garnets exhumed by Group II and transitional Eastern Namaqualand kimberlites (Melton Wold and Markt) lack pronounced Zr and Hf anomalies (Figure 4.2e & g).

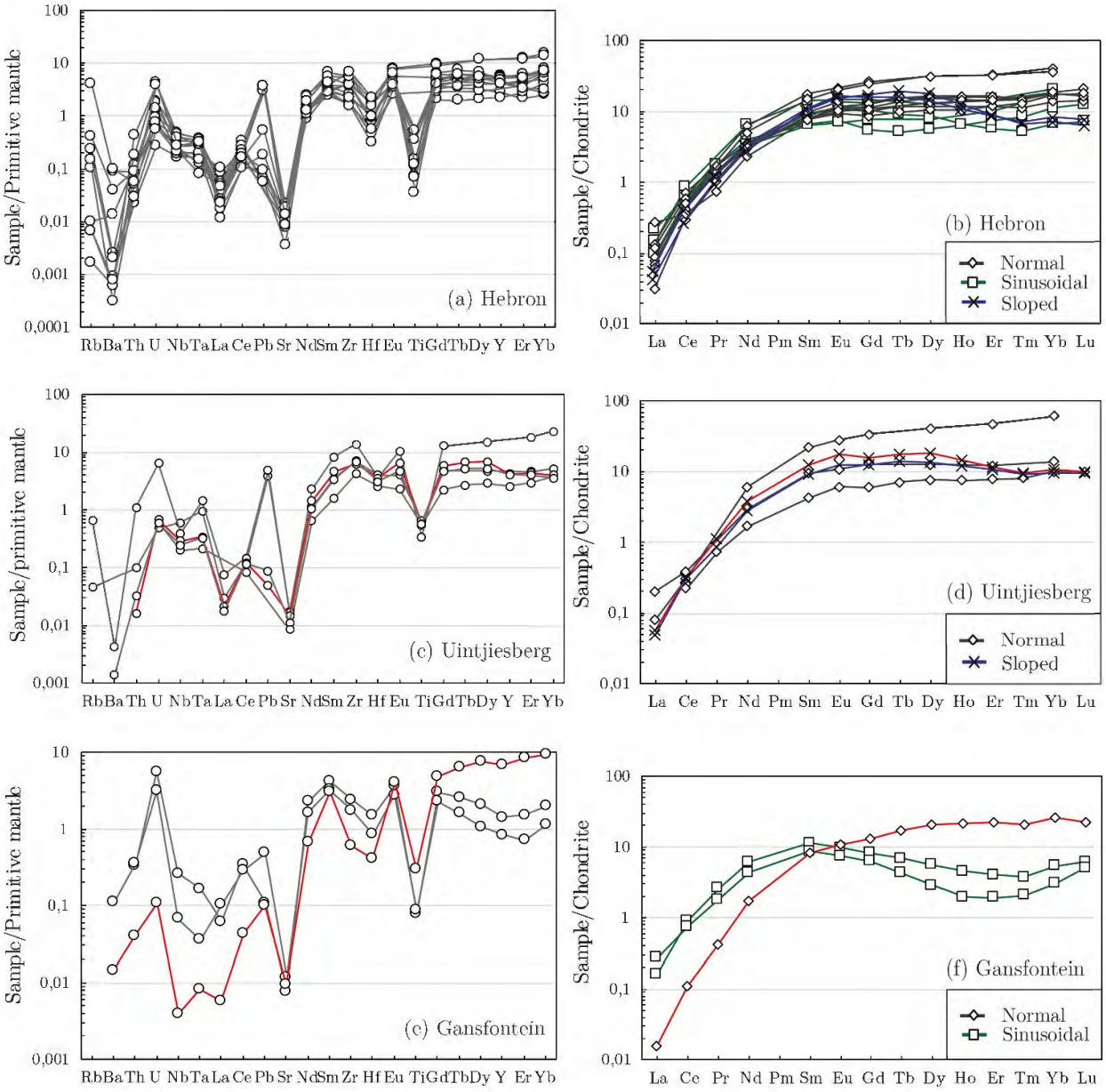

Figure 4.1: Primitive mantle normalized incompatible element and CI chondrite normalized REE diagrams for garnet from Eastern Namaqualand Group I kimberlites (a – f). Normalizing values from McDonough & Sun (1995). Data for Eastern Namaqualand peridotites with fewer than 14 REE shown are from le Roex and Class (2016). Samples illustrated in red represent websterite samples, UINT-4 (c & d) and GANS-9 (e & f).

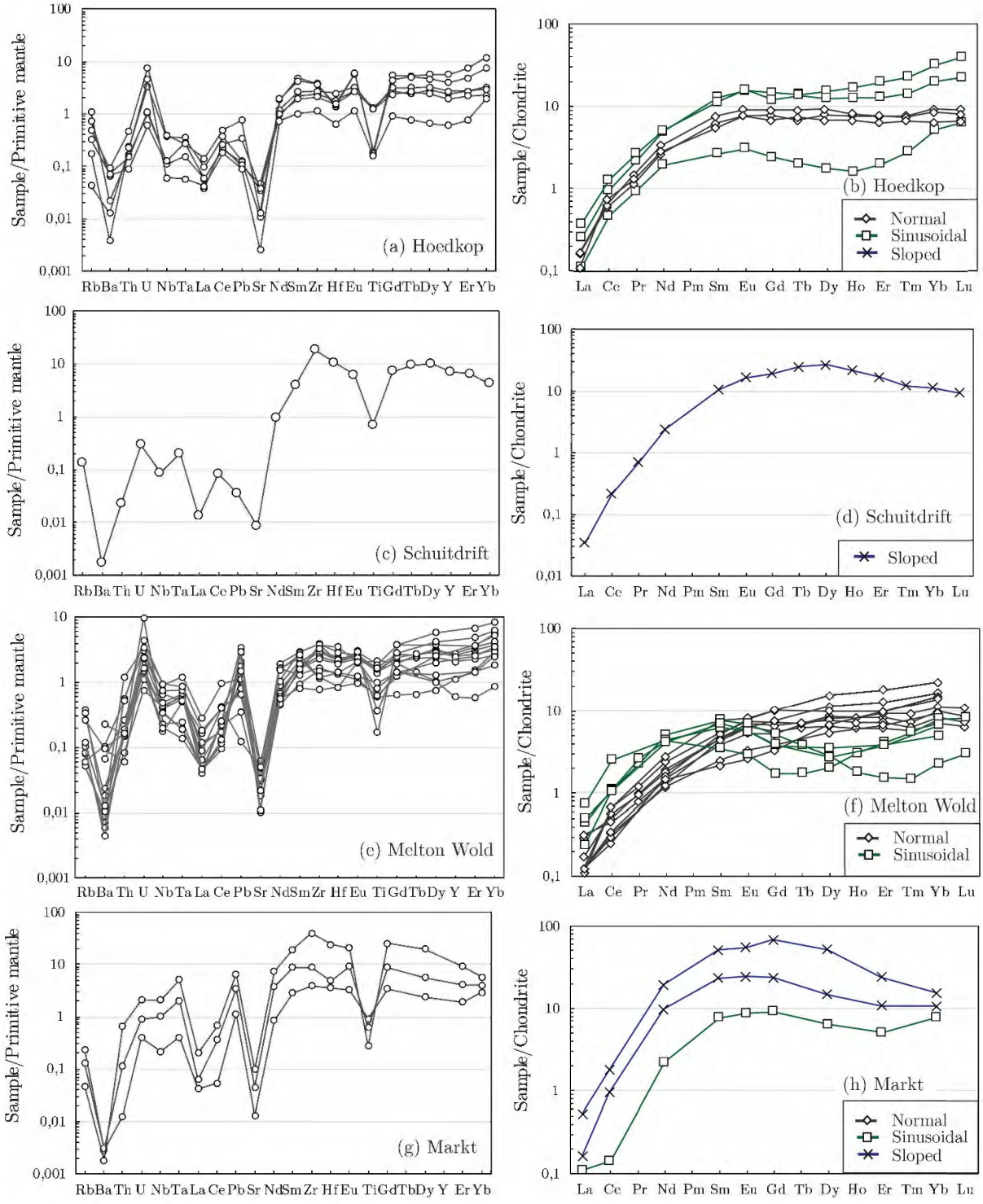

Figure 4.2: Primitive mantle normalized incompatible element and CI chondrite normalized REE diagrams for garnet from NBW (a - d) ultramafic lamprophyre (Hoedkop) and Schuitdrift kimberlite which erupted during the Group I kimberlite pulse and Eastern Namaqualand (e – h) Group II/transitional kimberlites. Normalizing values from McDonough & Sun (1995). Data sources as for Figure 4.1.

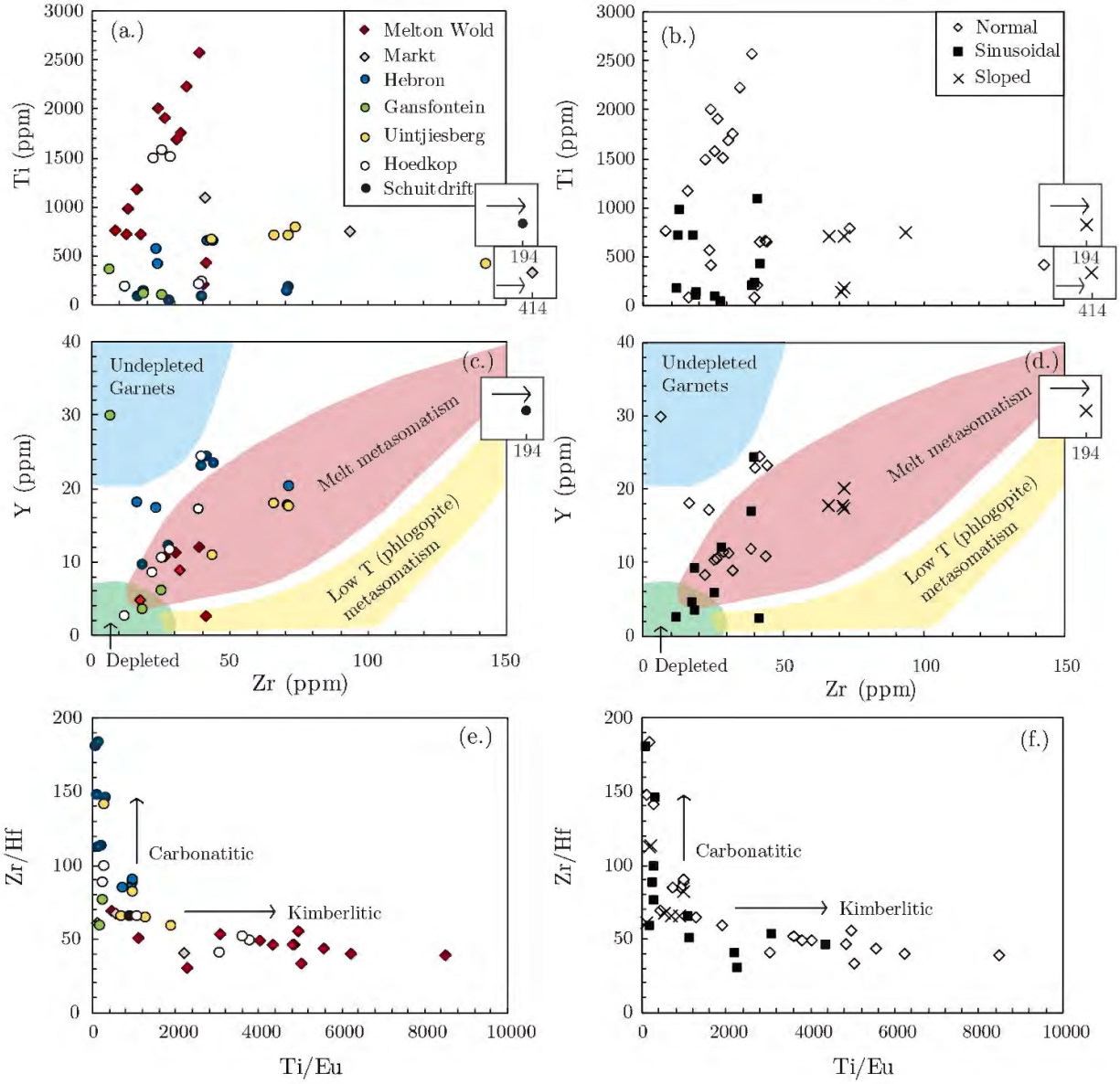

Figure 4.3: Zr (ppm) versus (a & b) Ti (ppm) and (c & d) Y (ppm) and (e & f) Ti/Eu versus Zr/Hf. Samples exhumed during the Group II kimberlite pulse (~140 – 120 Ma) are plotted as diamonds in figures a, c and e and samples exhumed during the Group I kimberlite pulse (100 – 80 Ma) are plotted as circles in figures a, c and e. Compositional fields for garnet xenocrysts in (c) and (d) are from Griffin et al. (1999). Carbonatitic and kimberlitic composition trends in (e) and (f) are from Shu and Brey (2015). Data sources as for Figure 4.1.

Table 4.1: LA-ICP-MS results for garnet in off-craton peridotites.

Locality	Hebron							
Sample	HBR-1	HBR-2	HBR-3	HBR-4	HBR-5	HBR-10	HBR-11	HBR-12
REE Type	S	N	S	HS	N	HS	N	N
ppm								
Sc	193	108	116	183	91	194	92	145
Ti	43	652	139	174	569	143	646	82
V	105	121	124	84	127	106	120	69
Mn	3155	2805	3004	2803	2870	3235	2762	3217
Co	38	38	41	37	38	42	39	36
Ni	27	33	32	35	31	38	31	23
Cu	0.13	0.24	0.26	0.07	<d.l.	0.06	<d.l.	0.13
Zn	9	10	8	6	8	7	9	6
Rb	2.5	<d.l.	0.24	0.09	<d.l.	<d.l.	<d.l.	0.14
Sr	0.25	0.25	0.19	0.17	0.20	0.27	0.33	0.07
Y	12	24	10	20	17	18	23	18
Zr	28	42	18	71	23	71	44	16
Nb	0.17	0.11	0.17	0.18	0.14	0.18	0.126	0.14
Ba	0.59	0.01	0.26	0.01	<d.l.	0.65	<d.l.	0.02
La	0.03	0.01	0.02	0.01	0.02	0.01	0.07	0.03
Ce	0.31	0.19	0.37	0.18	0.26	0.27	0.23	0.45
Pr	0.13	0.10	0.17	0.09	0.13	0.12	0.07	0.16
Nd	1.6	1.4	1.9	1.3	1.5	1.6	1.1	1.6
Sm	1.4	1.3	1.0	1.6	1.2	1.7	1.2	1.2
Eu	0.66	0.67	0.43	0.91	0.62	0.99	0.67	0.55
Tb	0.34	0.52	0.19	0.73	0.44	0.61	0.58	0.37
Gd	2.1	2.3	1.1	3.5	2.0	3.2	2.5	1.7
Dy	2.2	3.9	1.4	4.6	3.0	3.7	4.2	2.7
Ho	0.37	0.89	0.36	0.72	0.67	0.62	0.93	0.59
Er	0.94	2.63	1.23	1.51	1.96	1.45	2.68	1.97
Tm	0.13	0.38	0.22	0.17	0.29	0.18	0.38	0.34
Yb	1.1	2.9	1.9	1.2	2.3	1.4	3.0	2.9
Lu	0.18	0.41	0.31	0.16	0.35	0.20	0.41	0.46
Hf	0.15	0.47	0.13	0.63	0.28	0.62	0.49	0.09
Ta	0.00	0.01	0.01	0.01	0.01	0.01	0.01	<d.l.
Pb	0.01	0.03	0.01	0.01	<d.l.	0.08	0.01	0.01
Th	0.01	0.00	0.01	<d.l.	<d.l.	<d.l.	<d.l.	0.01
U	0.04	0.01	0.01	0.01	0.01	0.08	0.01	0.09

< d.l. denotes below detection limits, n.a. denotes not analysed and sample names ending with * denote published data from le Roex and Class (2016). S denotes sinusoidal, N denotes normal and HS denotes sloped garnet REE patterns.

Table 4.1 continued.

Locality					Uintjiesberg			
Sample	HBX-1*	HBX-2*	HBX-4*	HBX-6*	HBX-12*	UINT-micro	UINT-4	UINT-8
REE Type	N	S	S	N	N	N	HS	HS
ppm								
Sc	109	230	208	272	222	80	116	107
Ti	420	n.a.	n.a.	n.a.	n.a.	668	701	701
V	n.a.	n.a.	n.a.	n.a.	n.a.	143	147	130
Mn	n.a.	n.a.	n.a.	n.a.	n.a.	2471	3146	2398
Co	n.a.	n.a.	n.a.	n.a.	n.a.	42	49	39
Ni	25	39	29	39	40	47	53	45
Cu	n.a.	n.a.	n.a.	n.a.	n.a.	<d.l.	0,10	<d.l.
Zn	n.a.	n.a.	n.a.	n.a.	n.a.	9	3	10
Rb	0.061	0.006	0.004	0.001	0.004	<d.l.	<d.l.	<d.l.
Sr	0.31	0.42	0.18	0.35	0.36	0.17	0.30	0.23
Y	n.a.	n.a.	n.a.	n.a.	n.a.	11	18	17
Zr	24	39	18	59	57	44	66	71
Nb	0.22	0.31	0.28	0.30	0.26	0.13	0.20	0.16
Ba	0.002	0.087	0.004	0.004	0.005	<d.l.	<d.l.	0.01
La	0.017	0.037	0.054	0.029	0.015	<d.l.	0.01	0.01
Ce	0.32	0.55	0.41	0.38	0.32	0.14	0.21	0.20
Pr	n.a.	n.a.	n.a.	n.a.	n.a.	0.07	0.11	0.08
Nd	1.5	3.1	1.6	3.0	2.4	0.8	1.8	1.3
Sm	1.2	2.1	1.0	2.7	2.3	0.65	1.9	1.4
Eu	0.59	0.85	0.40	1.23	1.16	0.35	1.00	0.72
Tb	n.a.	n.a.	n.a.	n.a.	n.a.	0.26	0.67	0.52
Gd	2.2	2.9	1.6	5.3	5.0	1.2	3.2	2.5
Dy	3.4	3.3	2.0	8.0	7.9	1.9	4.6	3.4
Ho	n.a.	n.a.	n.a.	n.a.	n.a.	0.43	0.81	0.68
Er	2.35	2.46	1.66	5.49	5.32	1.30	1.91	1.75
Tm	n.a.	n.a.	n.a.	n.a.	n.a.	0.21	0.25	0.23
Yb	3.1	3.4	2.8	6.7	6.0	1.6	1.8	1.6
Lu	n.a.	n.a.	n.a.	n.a.	n.a.	0.25	0.25	0.24
Hf	0.28	0.22	0.16	0.55	0.43	0.73	1.00	0.87
Ta	0.012	0.014	0.010	0.014	0.013	0.01	0.01	0.01
Pb	0.45	0.56	0.55	0.44	0.54	<d.l.	0.01	0.01
Th	0.003	0.009	0.034	0.007	0.004	<d.l.	<d.l.	<d.l.
U	0.028	0.037	0.081	0.019	0.015	0.01	0.01	0.01

< d.l. denotes below detection limits, n.a. denotes not analysed and sample names ending with * denote published data from le Roex and Class (2016). S denotes sinusoidal, N denotes normal and HS denotes sloped garnet REE patterns.

Table 4.1 continued.

Locality			Gansfontein			Hoedkop		
Sample	UBX-1*	UBX-18*	GANS-1	GANS-2	GANS-9	HOD-1	HOD-2	HOD-3
REE Type	N	N	S	S	N	S	N	N
ppm								
Sc	212	136	206	269	62	368	106	97
Ti	420	790	95	105	366	234	1577	1503
V	n.a.	n.a.	144	122	103	163	216	225
Mn	n.a.	n.a.	3970	3370	4213	3395	2163	2002
Co	n.a.	n.a.	41	34	65	38	40	40
Ni	43	45	29	25	47	33	85	85
Cu	n.a.	n.a.	0.20	0.44	0.24	0.11	0.68	0.36
Zn	n.a.	n.a.	5	13	22	7	10	9
Rb	0.027	0.40	<d.l.	<d.l.	<d.l.	0.105	0.642	0.435
Sr	0.36	0.35	0.15	0.24	0.19	0.21	0.70	0.94
Y	n.a.	n.a.	6	4	30	24	10	12
Zr	143	74	25	18	6	40	25	28
Nb	0.400	0.260	0.172	0.045	0.003	0.243	0.084	0.072
Ba	<d.l.	0.028	<d.l.	0.737	0.097	0.026	0.145	0.430
La	0.020	0.050	0.040	0.067	0.004	0.062	0.038	0.038
Ce	0.20	0.25	0.57	0.48	0.07	0.61	0.35	0.38
Pr	n.a.	n.a.	0.25	0.17	0.04	0.21	0.10	0.13
Nd	2.9	1.4	2.9	2.0	0.8	2.3	1.2	1.5
Sm	3.4	1.5	1.7	1.3	1.2	2.0	0.89	1.1
Eu	1.60	0.62	0.55	0.42	0.61	0.89	0.42	0.49
Tb	n.a.	n.a.	0.26	0.16	0.62	0.52	0.24	0.32
Gd	6.9	2.6	1.6	1.2	2.6	3.0	1.5	1.7
Dy	10	3.2	1.4	0.73	5.1	3.9	1.9	2.2
Ho	n.a.	n.a.	0.25	0.11	1.19	0.94	0.41	0.43
Er	7.90	2.00	0.66	0.31	3.64	3.22	1.18	1.19
Tm	n.a.	n.a.	0.10	0.05	0.51	0.58	0.18	0.18
Yb	10.0	2.3	0.9	0.5	4.2	5.3	1.4	1.3
Lu	n.a.	n.a.	0.15	0.13	0.55	0.99	0.22	0.19
Hf	1.01	1.13	0.43	0.24	0.12	0.40	0.52	0.70
Ta	0.036	0.053	0.006	0.001	0.000	0.013	0.011	0.006
Pb	0.59	0.72	0.02	0.07	0.02	0.02	0.02	0.02
Th	0.008	0.088	0.026	0.028	0.003	0.019	0.014	0.007
U	0.010	0.130	0.112	0.063	0.002	0.068	0.021	0.012

< d.l. denotes below detection limits, n.a. denotes not analysed and sample names ending with * denote published data from le Roex and Class (2016). S denotes sinusoidal, N denotes normal and HS denotes sloped garnet REE patterns.

Table 4.1 continued.

Locality				Schuitdrift	Melton Wold			
Sample	HOD-4	HOD-5	HOD-11	SD-1	MW-1	XMW-7	XMW-8	XMW-13
REE Type	N	S	S	HS	N	N	N	N
ppm								
Sc	86	277	198	172	95	100	77	93
Ti	1496	210	188	845	1764	1692	2578	1916
V	226	140	109	148	284	263	231	296
Mn	2064	3348	3514	2832	2532	3098	2110	2830
Co	39	33	37	42	44	46	41	40
Ni	84	30	25	52	83	60	80	55
Cu	0.43	0.12	0.12	0.14	0.23	0.56	0.70	0.54
Zn	12	8	10	8	10	8	9	15
Rb	0.192	0.296	0.026	0.080	0.228	<d.l.	<d.l.	<d.l.
Sr	0.74	0.26	0.05	0.17	0.63	0.40	1.23	0.40
Y	8	17	2.6	31	9	11	12	11
Zr	22	38	12	194	32	30	39	26
Nb	0.083	0.258	0.040	0.057	0.269	0.265	0.116	0.291
Ba	0.478	0.606	0.085	0.011	0.069	0.632	0.436	1.493
La	0.025	0.092	0.027	0.008	0.071	0.027	0.078	0.042
Ce	0.44	0.82	0.30	0.14	0.32	0.43	0.29	0.36
Pr	0.12	0.26	0.09	0.07	0.09	0.12	0.08	0.09
Nd	1.3	2.4	0.9	1.2	0.9	1.1	0.7	0.8
Sm	0.79	1.7	0.41	1.6	0.70	0.84	0.58	0.69
Eu	0.42	0.92	0.18	0.96	0.36	0.42	0.30	0.40
Tb	0.26	0.51	0.08	0.93	0.23	0.26	0.25	0.27
Gd	1.3	2.4	0.49	3.9	1.12	1.46	1.06	1.33
Dy	1.6	3.1	0.44	6.8	1.6	2.2	2.0	1.9
Ho	0.36	0.72	0.09	1.24	0.34	0.47	0.46	0.40
Er	0.98	2.11	0.33	2.81	1.00	1.35	1.52	1.20
Tm	0.16	0.36	0.07	0.32	0.14	0.19	0.23	0.16
Yb	1.0	3.3	0.9	1.9	1.2	1.6	1.8	1.4
Lu	0.16	0.56	0.16	0.24	0.16	0.22	0.27	0.18
Hf	0.43	0.44	0.18	2.96	0.68	0.62	1.0	0.56
Ta	<d.l.	0.010	0.002	0.008	0.024	0.021	0.019	0.022
Pb	0.05	0.11	0.01	0.01	0.16	0.12	0.31	0.05
Th	0.012	0.037	0.018	0.002	0.006	0.005	0.021	0.013
U	0.022	0.154	0.093	0.006	0.015	0.047	0.027	0.064

< d.l. denotes below detection limits, n.a. denotes not analysed and sample names ending with * denote published data from le Roex and Class (2016). S denotes sinusoidal, N denotes normal and HS denotes sloped garnet REE patterns.

Table 4.1 continued.

Locality	Melton Wold							
Sample	XMW-19	XMW-22	MWX-5*	MWX-10*	MWX-15*	MWX-18*	MWX-19*	MWX 20*
REE Type	S	S	N	N	N	S	N	N
ppm								
Sc	157	115	337	94	75	98	71	88
Ti	436	722	203	2228	1183	720	2000	755
V	354	260	n.a.	n.a.	n.a.	n.a.	n.a.	n.a.
Mn	3271	2147	n.a.	n.a.	n.a.	n.a.	n.a.	n.a.
Co	40	39	n.a.	n.a.	n.a.	n.a.	n.a.	n.a.
Ni	39	75	15	39	30	28	29	33
Cu	0.14	0.24	n.a.	n.a.	n.a.	n.a.	n.a.	n.a.
Zn	9	11	n.a.	n.a.	n.a.	n.a.	n.a.	n.a.
Rb	0.048	<d.l.	0.20	0.05	0.031	0.036	0.062	0.16
Sr	0.66	0.97	0.36	0.20	0.43	1.00	0.22	0.22
Y	2.6	4.7	n.a.	n.a.	n.a.	n.a.	n.a.	n.a.
Zr	41	17	40	34	16	12	24	8
Nb	0.430	0.323	0.150	0.130	0.230	0.610	0.220	0.490
Ba	0.047	0.155	0.120	0.039	0.069	0.690	0.029	0.636
La	0.108	0.058	0.030	0.030	0.030	0.180	0.030	0.030
Ce	0.70	0.68	0.43	0.16	0.21	1.60	0.19	0.22
Pr	0.22	0.25	n.a.	n.a.	n.a.	n.a.	n.a.	n.a.
Nd	2.4	2.0	1.3	0.8	0.6	2.1	0.6	0.7
Sm	1.2	0.53	1.2	0.79	0.38	1.0	0.66	0.33
Eu	0.40	0.17	0.47	0.45	0.19	0.32	0.36	0.15
Tb	0.14	0.07	n.a.	n.a.	n.a.	n.a.	n.a.	n.a.
Gd	1.04	0.35	2.06	2.05	0.77	0.76	1.53	0.67
Dy	0.70	0.51	2.5	3.9	1.4	0.88	2.8	1.7
Ho	0.10	0.17	n.a.	n.a.	n.a.	n.a.	n.a.	n.a.
Er	0.25	0.67	1.60	2.98	1.10	0.63	2.12	1.62
Tm	0.04	0.14	n.a.	n.a.	n.a.	n.a.	n.a.	n.a.
Yb	0.4	1.3	2.5	3.7	1.6	0.8	2.7	2.3
Lu	0.08	0.21	n.a.	n.a.	n.a.	n.a.	n.a.	n.a.
Hf	0.82	0.38	0.58	0.62	0.40	0.40	0.55	0.24
Ta	0.019	0.025	0.009	0.005	0.007	0.045	0.007	0.028
Pb	0.10	0.02	0.52	0.42	0.27	0.17	0.45	0.44
Th	0.044	0.012	0.013	0.012	0.015	0.041	0.013	0.013
U	0.062	0.023	0.200	0.030	0.030	0.088	0.034	0.048

< d.l. denotes below detection limits, n.a. denotes not analysed and sample names ending with * denote published data from le Roex and Class (2016). S denotes sinusoidal, N denotes normal and HS denotes sloped garnet REE patterns.

Table 4.1 continued.

Locality	Melton Wold	Markt		
Sample	MWX-32*	JAR12013*	JAR12033*	MRK-1*
REE Type	S	S	HS	HS
ppm				
Sc	229	148	187	370
Ti	977	1097	750	330
V	n.a.	n.a.	n.a.	n.a.
Mn	n.a.	n.a.	n.a.	n.a.
Co	n.a.	n.a.	n.a.	n.a.
Ni	43	48	51	55
Cu	n.a.	n.a.	n.a.	n.a.
Zn	n.a.	n.a.	n.a.	n.a.
Rb	0.072	0.14	0.076	0.028
Sr	0.43	0.26	0.89	1.94
Y	n.a.	n.a.	n.a.	n.a.
Zr	13	41	93	414
Nb	0.620	0.140	0.660	1.380
Ba	0.084	0.019	0.020	0.012
La	0.120	0.027	0.040	0.130
Ce	0.67	0.09	0.60	1.14
Pr	n.a.	n.a.	n.a.	n.a.
Nd	2.0	1.1	4.6	9.2
Sm	1.1	1.2	3.6	7.9
Eu	0.32	0.50	1.41	3.17
Tb	n.a.	n.a.	n.a.	n.a.
Gd	0.78	1.9	4.8	14
Dy	0.68	1.6	3.7	13
Ho	n.a.	n.a.	n.a.	n.a.
Er	0.62	0.84	1.78	3.98
Tm	n.a.	n.a.	n.a.	n.a.
Yb	1.1	1.3	1.8	2.6
Lu	n.a.	n.a.	n.a.	n.a.
Hf	0.24	1.0	1.38	6.8
Ta	0.032	0.015	0.076	0.190
Pb	0.22	0.17	0.51	0.99
Th	0.094	0.001	0.009	0.052
U	0.068	0.008	0.018	0.042

< d.l. denotes below detection limits, n.a. denotes not analysed and sample names ending with * denote published data from le Roex and Class (2016). S denotes sinusoidal, N denotes normal and HS denotes sloped garnet REE patterns.

4.2 Clinopyroxene

The peridotitic cpx exhibit REE patterns which are enriched in the LREE with systematically decreasing abundances from Sm to Lu (Figure 4.4 - 4.5). The majority of the samples display a positive slope in the lightest REE with maxima at Nd, and have $(Nd/Yb)_N$ ranging from 5.1 to 310. One websteritic cpx from Uintjiesberg (Figure 4.4d) has a high $(Nd/Yb)_N$ of 710. When classified by cluster and eruption age, trace element concentrations of cpx from Group I Eastern Namaqualand kimberlites typically mirror those cpx from Group II and transitional kimberlites but fall at higher Ca#. Trace and major element concentrations for cpx from Group I NBW kimberlites overlap the range of both Group I and Group II Eastern Namaqualand samples.

Primitive mantle-normalized incompatible element patterns for cpx are correlated with increasing element incompatibility (Figure 4.4 – 4.5). Prominent negative Ti and Pb anomalies are present across the majority (80%) of the samples. Zr and Hf abundances display large variation within individual localities.

The clinopyroxenes from the two spinel lherzolites from Gansfontein have high MREE and HREE abundances which likely reflect the absence of garnet in these samples (Figure 4.4f).

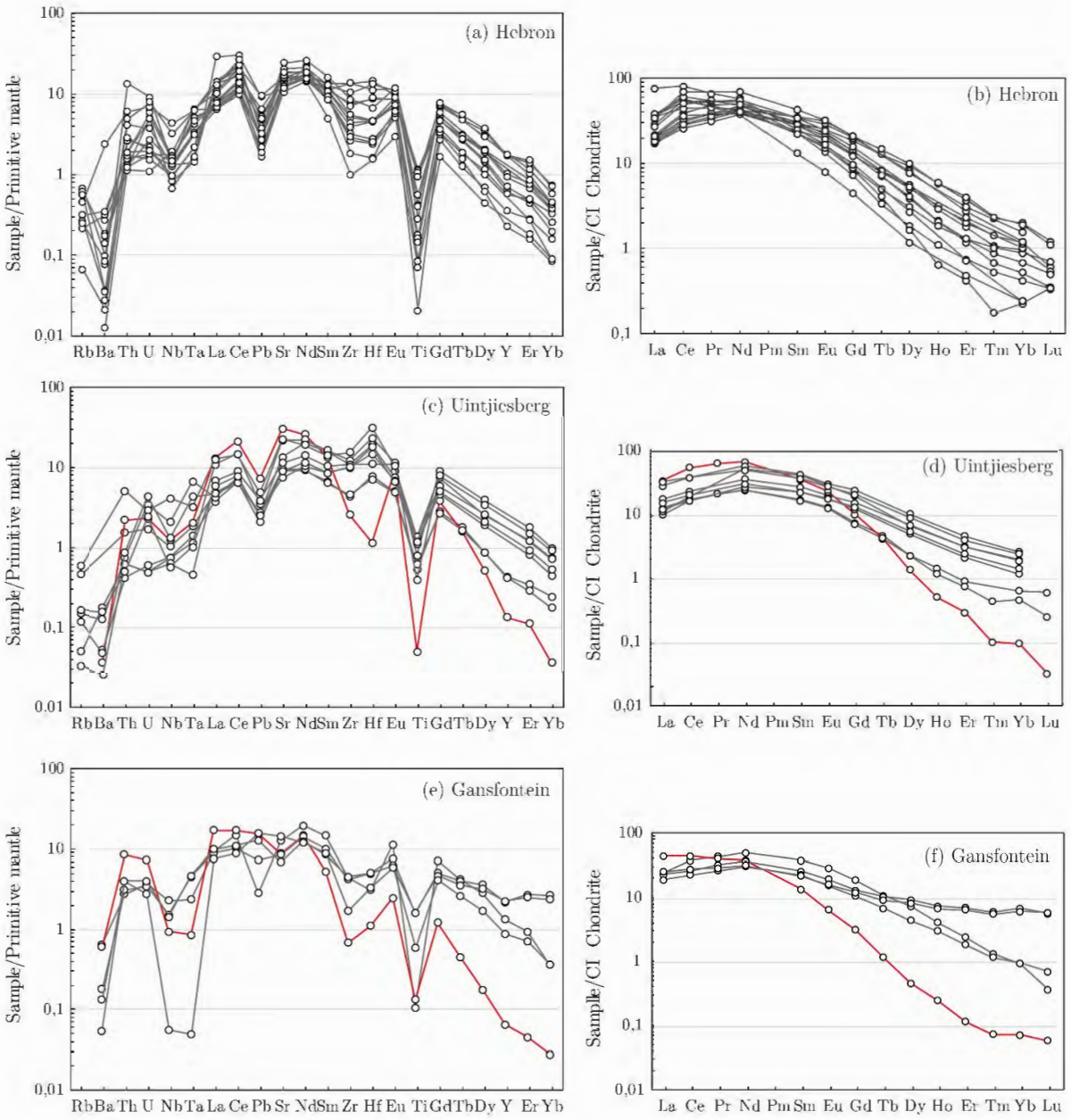

Figure 4.4: Primitive mantle normalized incompatible element and CI chondrite normalized REE diagrams for cpx from Group I Eastern Namaqualand kimberlites (a - f). Normalizing values from McDonough & Sun (1995). Data for Eastern Namaqualand peridotites with fewer than 14 REE shown are from le Roex and Class (2016). Samples illustrated in red represent websterite samples, UINT-4 (c & d) and GANS-9 (e & f).

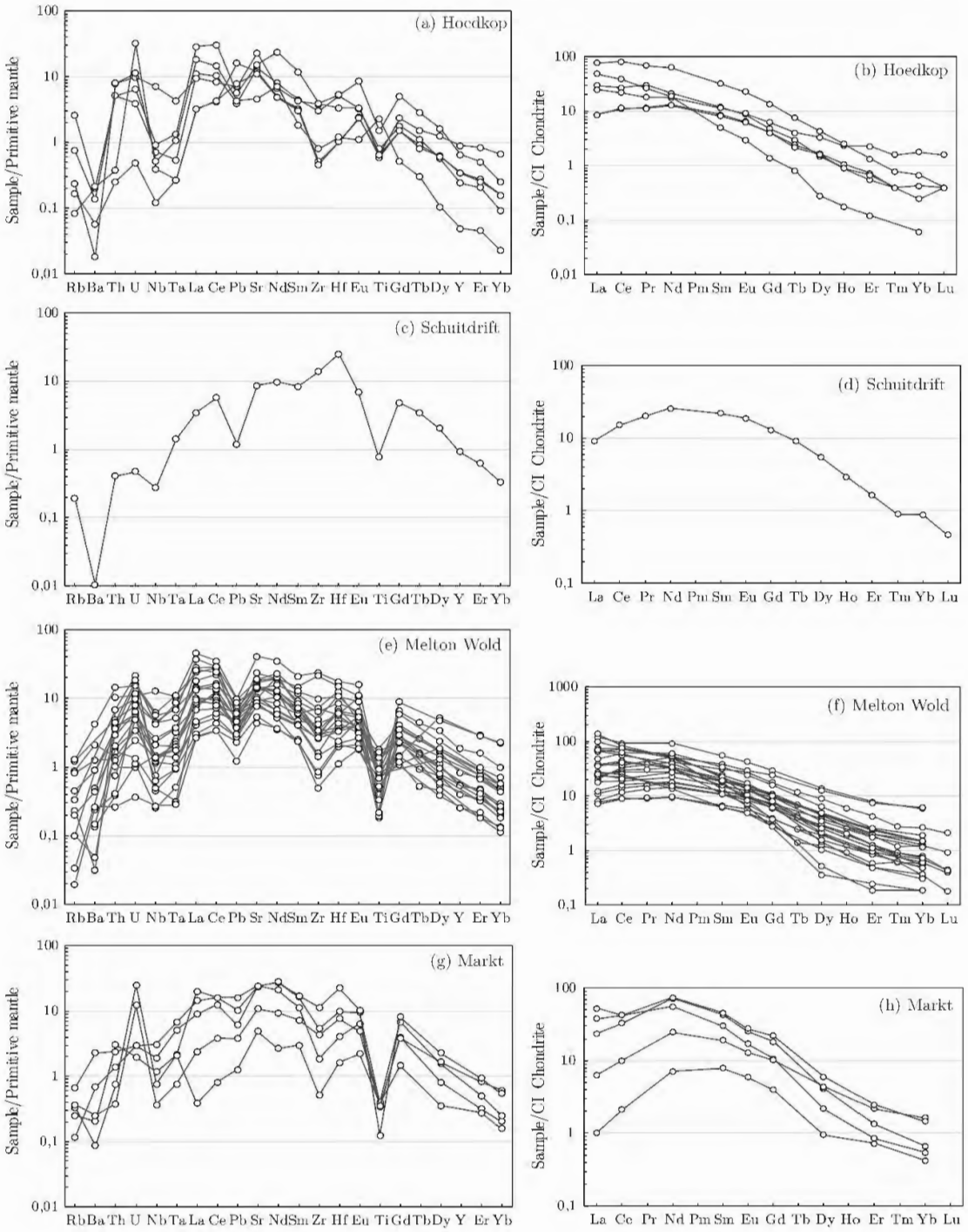

Figure 4.5: Primitive mantle normalized incompatible element and CI chondrite normalized REE diagrams for clinopyroxene from NBW (a - d) ultramafic lamprophyre (Hoedkop) and Schuitdrift kimberlite which erupted during the Group I kimberlite pulse and Eastern Namaqualand (e – h) Group II/transitional kimberlites. Normalizing values from McDonough & Sun (1995). Data for Eastern Namaqualand peridotites with fewer than 14 REE shown are from le Roex and Class (2016) and data for Hoedkop cpx are from Shiimi (2017).

Table 4.2: LA-ICP-MS data for clinopyroxene in off-craton peridotites.

Locality	Hebron							
Sample	HBR-1	HBR-2	HBR-3	HBR-4	HBR-5	HBR-10	HBR-11	HBR-12
ppm								
Sc	32	36	31	55	31	59	56	29
Ti	1390	1351	215	504	1149	344	199	177
V	327	331	287	237	316	307	190	168
Mn	497	526	520	526	477	620	586	519
Co	17	18	20	17	17	20	19	18
Ni	309	340	348	310	304	370	348	322
Cu	2.0	9.7	0.8	5.0	1.1	1.0	0.6	0.3
Zn	8.2	10	8.0	5.5	9.0	5.2	7.0	5.8
Rb	<d.l.	<d.l.	0.41	<d.l.	0.37	<d.l.	0.34	<d.l.
Sr	238	279	360	212	247	253	310	233
Y	4.4	4.0	1.5	7.3	2.7	7.6	3.0	2.5
Zr	80	75	28	143	54	144	46	19
Nb	0.85	0.94	0.83	1.26	1.15	0.98	0.55	0.88
Ba	0.08	0.93	0.66	1.22	1.14	1.78	0.24	0.52
La	4.2	4.6	5.3	4.3	4.9	4.4	9.0	19
Ce	18	20	25	16	21	18	33	51
Pr	3.2	3.7	4.7	3.0	3.7	3.5	5.3	6.4
Nd	19	22	24	18	20	20	25	28
Sm	4.4	4.7	3.5	4.5	4.3	5.4	4.3	3.8
Eu	1.33	1.31	0.78	1.47	1.21	1.80	1.12	0.96
Tb	0.31	0.31	0.13	0.48	0.27	0.55	0.27	0.19
Gd	2.8	2.8	1.5	3.7	2.6	4.2	2.6	1.8
Dy	1.41	1.31	0.47	2.36	0.97	2.52	1.03	0.77
Ho	0.18	0.16	0.06	0.33	0.12	0.33	0.12	0.10
Er	0.34	0.30	0.12	0.61	0.19	0.66	0.22	0.22
Tm	0.036	0.027	0.014	0.058	0.017	0.060	0.022	0.026
Yb	0.19	0.16	0.07	0.33	0.09	0.32	0.11	0.15
Lu	0.015	0.014	0.008	0.031	0.009	0.028	0.013	0.018
Hf	2.46	2.54	0.68	4.09	1.31	3.16	1.28	0.45
Ta	0.12	0.12	0.11	0.24	0.15	0.19	0.05	0.05
Pb	0.32	0.44	0.45	0.25	0.28	0.42	0.80	1.38
Th	0.10	0.10	0.33	0.09	0.13	0.10	0.21	1.07
U	0.04	0.06	0.08	0.02	0.04	0.10	0.04	0.18

< d.l. denotes below detection limits, n.a. denotes not analysed and sample names ending with * denote published data from le Roex and Class (2016) and sample names ending with ** denote data from Shiimi (2017).

Table 4.2 continued.

Locality	Hebron						Uintjiesberg	
Sample	HBX-1*	HBX-1*	HBX-4*	HBX-6*	HBX-10*	HBX-12*	UINT-micro	UINT-4
ppm								
Sc	28	24	24	45	59	43	23	24
Ti	1287	85	25	670	490	1120	648	61
V	n.a.	n.a.	n.a.	n.a.	n.a.	n.a.	266	256
Mn	n.a.	n.a.	n.a.	n.a.	n.a.	n.a.	687	468
Co	n.a.	n.a.	n.a.	n.a.	n.a.	n.a.	20	20
Ni	252	263	269	265	270	253	388	405
Cu	n.a.	n.a.	n.a.	n.a.	n.a.	n.a.	2.6	0.6
Zn	n.a.	n.a.	n.a.	n.a.	n.a.	n.a.	9.5	6.3
Rb	0.13	0.19	0.04	0.16	0.27	0.15	0.27	1.69
Sr	331	322	333	410	371	482	182	618
Y	n.a.	n.a.	n.a.	n.a.	n.a.	n.a.	1.9	0.58
Zr	41	10	31	58	110	90	46	27
Nb	1.08	0.45	0.64	0.96	2.87	2.11	0.69	0.82
Ba	2.08	2.32	0.14	0.23	15.7	0.56	16	0.25
La	5.1	9.0	7.1	6.6	9.2	8.4	3.2	8.6
Ce	23	36	34	32	39	45	11	36
Pr	n.a.	n.a.	n.a.	n.a.	n.a.	n.a.	2.1	6.3
Nd	19	18	19	26	23	33	12	33
Sm	3.8	2.0	3.4	5.3	5.2	6.5	2.7	5.5
Eu	1.12	0.46	0.95	1.40	1.68	1.84	0.78	1.38
Tb	n.a.	n.a.	n.a.	n.a.	n.a.	n.a.	0.18	0.16
Gd	2.5	0.9	2.0	3.2	4.0	4.3	1.6	2.1
Dy	1.28	0.30	0.68	1.35	2.04	1.97	0.59	0.36
Ho	n.a.	n.a.	n.a.	n.a.	n.a.	n.a.	0.08	0.03
Er	0.33	0.08	0.12	0.38	0.45	0.51	0.15	0.05
Tm	n.a.	n.a.	n.a.	n.a.	n.a.	n.a.	0.008	0.003
Yb	0.17	0.04	0.04	0.19	0.20	0.26	0.11	0.02
Lu	n.a.	n.a.	n.a.	n.a.	n.a.	n.a.	0.016	0.001
Hf	1.31	0.44	0.72	1.32	3.75	1.89	2.24	0.33
Ta	0.17	0.06	0.08	0.24	0.23	0.23	0.07	0.08
Pb	0.71	1.43	0.75	0.40	0.56	0.49	0.31	1.09
Th	0.15	0.15	0.15	0.23	0.48	0.39	0.12	0.18
U	0.12	0.10	0.04	0.04	0.14	0.16	0.04	0.05

< d.l. denotes below detection limits, n.a. denotes not analysed and sample names ending with * denote published data from le Roex and Class (2016) and sample names ending with ** denote data from Shiimi (2017).

Table 4.2 continued.

Locality	Uintjiesberg							Gansfontein
Sample	UINT-8	UBX-1*	UBX-5*	UBX-6*	UBX-14*	UBX-18*	JJG2199*	GANS-1
ppm								
Sc	29	44	149	128	90	41	85	40
Ti	755	482	977	1650	1660	1365	1440	124
V	285	n.a.	n.a.	n.a.	n.a.	n.a.	n.a.	245
Mn	531	n.a.	n.a.	n.a.	n.a.	n.a.	n.a.	532
Co	18	n.a.	n.a.	n.a.	n.a.	n.a.	n.a.	18
Ni	357	287	279	333	208	291	169	317
Cu	1.0	n.a.	n.a.	n.a.	n.a.	n.a.	n.a.	0.7
Zn	11	n.a.	n.a.	n.a.	n.a.	n.a.	n.a.	6.8
Rb	<d.l.	0.09	0.03	0.35	0.02	0.07	0.10	<d.l.
Sr	192	272	442	452	229	149	179	249
Y	1.8	n.a.	n.a.	n.a.	n.a.	n.a.	n.a.	5.7
Zr	49	117	130	164	116	105	107	47
Nb	0.50	1.38	0.49	2.75	0.42	0.88	0.38	1.52
Ba	0.35	0.85	1.2	46	0.17	0.32	1.04	4.3
La	2.5	2.8	7.1	8.3	4.4	3.1	3.8	6.0
Ce	11	13	25	25	15	11	13	25
Pr	2.1	n.a.	n.a.	n.a.	n.a.	n.a.	n.a.	4.3
Nd	12	26	28	24	18	13	15	24
Sm	2.6	6.4	6.7	5.8	4.3	3.5	3.5	6.0
Eu	0.75	1.71	1.81	1.63	1.18	1.08	1.03	1.75
Tb	0.16	n.a.	n.a.	n.a.	n.a.	n.a.	n.a.	0.42
Gd	1.5	4.1	5.0	4.4	3.2	2.6	2.7	3.9
Dy	0.59	1.73	2.68	2.32	1.78	1.29	1.44	1.93
Ho	0.07	n.a.	n.a.	n.a.	n.a.	n.a.	n.a.	0.24
Er	0.13	0.54	0.79	0.67	0.53	0.36	0.41	0.41
Tm	0.012	n.a.	n.a.	n.a.	n.a.	n.a.	n.a.	0.035
Yb	0.08	0.33	0.44	0.41	0.32	0.20	0.24	0.16
Lu	0.007	n.a.	n.a.	n.a.	n.a.	n.a.	n.a.	0.010
Hf	2.04	3.15	6.70	9.04	5.48	4.24	5.15	0.88
Ta	0.05	0.25	0.04	0.12	0.02	0.16	0.04	0.09
Pb	0.40	0.40	0.54	0.74	0.59	0.42	0.38	0.43
Th	0.03	0.06	0.05	0.41	0.05	0.07	0.04	0.22
U	0.01	0.07	0.01	0.06	0.01	0.09	0.05	0.08

< d.l. denotes below detection limits, n.a. denotes not analysed and sample names ending with * denote published data from le Roex and Class (2016) and sample names ending with ** denote data from Shiimi (2017).

Table 4.2 continued.

Locality	Gansfontein				Hoedkop			
Sample	GANS-2	GANS-3	GANS-9	GSF-4*	HOD-1**	HOD-2**	HOD-3**	HOD-4**
ppm								
Sc	48	81	27	77	22	17	16	16
Ti	160	1928	713	1952	959	719	779	779
V	174	319	290	281	449	234	240	228
Mn	528	613	640	463	n.a.	n.a.	n.a.	n.a.
Co	18	18	30	13	n.a.	n.a.	n.a.	n.a.
Ni	335	296	629	250	358	492	415	480
Cu	4.0	2.9	6.6	4.8	n.a.	n.a.	n.a.	n.a.
Zn	6.3	3.3	36	9.3	n.a.	n.a.	n.a.	n.a.
Rb	<d.l.	<d.l.	<d.l.	<d.l.	0.05	1.55	8.0	0.10
Sr	175	169	285	138	272	236	461	221
Y	0.28	9.4	3.8	9.8	1.03	1.5	3.9	1.5
Zr	7.2	44	18	48	32	5.4	40	4.8
Nb	0.62	1.00	0.04	0.95	0.47	0.26	4.65	0.08
Ba	4.1	1.19	0.35	0.89	1.34	1.41	55	0.38
La	11	5.8	4.9	6.4	7.18	2.11	6.12	2.08
Ce	29	17	15	18	17	7.0	14	7.2
Pr	4.0	3.2	2.6	2.9	2.9	1.1	1.7	1.1
Nd	19	18	15	16	10	6.1	8	6.0
Sm	2.2	4.1	3.6	3.5	1.8	1.3	1.7	1.3
Eu	0.38	1.17	0.92	0.96	0.50	0.37	0.52	0.36
Tb	0.05	0.40	0.26	0.35	0.11	0.09	0.15	0.08
Gd	0.7	2.8	2.2	2.6	1.0	0.8	1.3	0.8
Dy	0.12	2.43	1.15	2.16	0.38	0.42	0.84	0.41
Ho	0.01	0.43	0.18	0.40	0.05	0.06	0.13	0.05
Er	0.02	1.19	0.31	1.11	0.09	0.12	0.37	0.11
Tm	0.002	0.158	0.031	0.147	0.010	0.010	0.040	0.010
Yb	0.01	1.17	0.16	1.05	0.04	0.07	0.29	0.07
Lu	0.002	0.147	0.018	0.155	0.010	0.010	0.040	0.010
Hf	0.31	1.41	0.96	1.43	1.45	0.29	0.95	0.29
Ta	0.03	0.17	0.00	0.18	0.02	0.01	0.16	0.01
Pb	2.30	1.10	2.39	1.93	0.59	2.40	1.06	1.19
Th	0.68	0.25	0.32	0.32	0.41	0.03	0.63	0.02
U	0.15	0.07	0.06	0.08	0.08	0.65	0.2	0.01

< d.l. denotes below detection limits, n.a. denotes not analysed and sample names ending with * denote published data from le Roex and Class (2016) and sample names ending with ** denote data from Shiimi (2017).

Table 4.2 continued.

Locality	Hoedkop		Schuitdrift	Melton Wold				
Sample	HOD-5**	HOD-11**	SD-1	XMW-7	XMW-8	XMW-13	XMW-19	MW-1
ppm								
Sc	59	36	50	32	19	27	62	36
Ti	1798	2758	938	1533	1142	1537	220	629
V	186	150	318	339	238	302	254	226
Mn	n.a.	n.a.	621	836	751	728	572	776
Co	n.a.	n.a.	19	29	27	25	18	26
Ni	353	313	362	518	471	447	328	465
Cu	n.a.	n.a.	1.1	2.8	2.7	3.0	3.5	3.3
Zn	n.a.	n.a.	8.9	7.8	11	10	11	15
Rb	0.45	0.14	0.12	<d.l.	<d.l.	<d.l.	<d.l.	0.01
Sr	306	92	172	210	108	160	278	87
Y	2.8	0.21	4.0	2.4	1.7	2.3	7.9	1.1
Zr	41	8.5	145	27	7.9	28	74	5.2
Nb	0.61	0.34	0.18	0.97	0.16	0.30	1.55	0.18
Ba	0.9	0.12	0.07	12	0.89	1.57	3.24	1.74
La	19	12	2.3	2.7	1.8	2.0	4.9	1.7
Ce	51	24	10	9	6	7	21	6
Pr	6.6	2.5	2.0	1.5	0.9	1.3	3.6	0.9
Nd	30	9	12	8.2	4.5	6.7	20	4.5
Sm	4.8	0.8	3.4	1.9	1.0	1.6	4.8	1.0
Eu	1.31	0.17	1.08	0.60	0.33	0.54	1.58	0.28
Tb	0.28	0.03	0.34	0.16	0.09	0.15	0.44	0.05
Gd	2.7	0.3	2.6	1.4	0.8	1.2	3.6	0.6
Dy	1.09	0.07	1.37	0.72	0.49	0.75	2.27	0.31
Ho	0.14	0.01	0.17	0.11	0.07	0.12	0.34	0.05
Er	0.22	0.02	0.27	0.21	0.15	0.21	0.69	0.09
Tm	0.020	<d.l.	0.023	0.021	0.015	0.023	0.070	0.016
Yb	0.11	0.01	0.15	0.11	0.10	0.13	0.44	0.06
Lu	0.010	<d.l.	0.012	0.011	0.010	0.011	0.053	0.005
Hf	1.50	0.34	7.09	1.41	0.55	2.01	1.61	0.31
Ta	0.05	0.04	0.05	0.05	0.02	0.03	0.14	0.01
Pb	0.85	0.65	0.18	0.41	0.35	0.41	0.45	0.18
Th	0.41	0.64	0.03	0.08	0.03	0.03	0.15	0.021
U	0.13	0.23	0.01	0.02	0.02	0.17	0.07	0.01

< d.l. denotes below detection limits, n.a. denotes not analysed and sample names ending with * denote published data from le Roex and Class (2016) and sample names ending with ** denote data from Shiimi (2017).

Table 4.2 continued.

Locality	Melton Wold							
Sample	MW-2	MWX-2*	MWX-5*	MWX-10*	MWX-15*	MWX-18*	MWX-19*	MWX 20*
ppm								
Sc	44	24	82	29	17	17	18	17
Ti	1401	820	230	2204	847	475	1995	595
V	267	n.a.	n.a.	n.a.	n.a.	n.a.	n.a.	n.a.
Mn	691	n.a.	n.a.	n.a.	n.a.	n.a.	n.a.	n.a.
Co	20	n.a.	n.a.	n.a.	n.a.	n.a.	n.a.	n.a.
Ni	294	316	291	369	294	248	233	341
Cu	1.5	n.a.	n.a.	n.a.	n.a.	n.a.	n.a.	n.a.
Zn	10	n.a.	n.a.	n.a.	n.a.	n.a.	n.a.	n.a.
Rb	<d.l.	0.02	0.14	0.27	1.05	0.20	0.06	0.12
Sr	271	293	197	180	172	283	153	305
Y	3.6	n.a.	n.a.	n.a.	n.a.	n.a.	n.a.	n.a.
Zr	52	28	34	35	8.9	32	17	15
Nb	0.32	0.91	0.50	0.80	1.37	2.87	0.41	1.73
Ba	0.97	48	0.21	5.89	36	36	0.32	2.91
La	5.6	8.5	18	6.2	6.7	9.3	5.7	12
Ce	19	26	48	17	16	28	14	38
Pr	3.0	n.a.	n.a.	n.a.	n.a.	n.a.	n.a.	n.a.
Nd	16	16	26	13	6	15	7	16
Sm	3.3	2.9	3.4	2.9	1.0	2.4	1.7	1.7
Eu	0.90	0.83	0.60	0.89	0.28	0.60	0.48	0.41
Tb	0.26	n.a.	n.a.	n.a.	n.a.	n.a.	n.a.	n.a.
Gd	2.1	1.6	1.4	2.2	0.6	1.2	1.3	0.8
Dy	1.12	0.65	0.36	1.19	0.26	0.50	0.65	0.40
Ho	0.15	n.a.	n.a.	n.a.	n.a.	n.a.	n.a.	n.a.
Er	0.30	0.18	0.08	0.33	0.08	0.14	0.18	0.14
Tm	0.030	n.a.	n.a.	n.a.	n.a.	n.a.	n.a.	n.a.
Yb	0.20	0.12	0.06	0.21	0.05	0.08	0.09	0.08
Lu	0.023	n.a.	n.a.	n.a.	n.a.	n.a.	n.a.	n.a.
Hf	3.06	0.93	1.08	1.82	0.61	0.95	1.24	0.62
Ta	0.01	0.07	0.12	0.09	0.07	0.19	0.04	0.14
Pb	0.77	1.29	0.92	0.83	0.60	0.96	0.56	1.11
Th	0.13	0.23	0.55	0.23	0.31	0.54	0.16	0.32
U	0.03	0.13	0.44	0.24	0.12	0.20	0.10	0.10

< d.l. denotes below detection limits, n.a. denotes not analysed and sample names ending with * denote published data from le Roex and Class (2016) and sample names ending with ** denote data from Shiimi (2017).

Table 4.2 continued.

Locality	Melton Wold							
Sample	MWX-32*	MWX-2*	MWX-4*	MWX-12*	MWX-17*	MWX-21*	MWX 28*	MWX-29*
ppm								
Sc	30	37	53	48	41	41	98	26
Ti	397	1680	n.a.	1010	n.a.	n.a.	262	n.a.
V	n.a.	n.a.	n.a.	n.a.	n.a.	n.a.	n.a.	n.a.
Mn	n.a.	n.a.	n.a.	n.a.	n.a.	n.a.	n.a.	n.a.
Co	n.a.	n.a.	n.a.	n.a.	n.a.	n.a.	n.a.	n.a.
Ni	375	210	316	260	291	299	260	293
Cu	n.a.	n.a.	n.a.	n.a.	n.a.	n.a.	n.a.	n.a.
Zn	n.a.	n.a.	n.a.	n.a.	n.a.	n.a.	n.a.	n.a.
Rb	0.77	0.53	8.43	0.49	0.22	0.27	0.74	0.06
Sr	363	181	813	198	614	186	343	466
Y	n.a.	n.a.	n.a.	n.a.	n.a.	n.a.	n.a.	n.a.
Zr	36	44	248	76	11	10	225	67
Nb	3.70	0.76	8.39	0.91	0.60	0.82	2.98	4.10
Ba	28	14	284	8.35	179	8.69	24	5.91
La	24	3.0	29	4.4	33.5	17	9.2	16
Ce	48	10	59	12	54	36	23	47
Pr	n.a.	n.a.	n.a.	n.a.	n.a.	n.a.	n.a.	n.a.
Nd	25	8.4	44	11	24	19	24	24
Sm	3.4	1.9	8.5	2.4	2.1	2.7	5.9	3.7
Eu	0.75	0.57	2.43	0.73	0.38	0.49	1.69	1.00
Tb	n.a.	n.a.	n.a.	n.a.	n.a.	n.a.	n.a.	n.a.
Gd	1.6	1.5	6.0	1.9	0.6	0.8	4.8	2.0
Dy	0.54	0.96	3.52	1.18	0.09	0.13	3.21	0.88
Ho	n.a.	n.a.	n.a.	n.a.	n.a.	n.a.	n.a.	n.a.
Er	0.16	0.33	1.28	0.39	0.04	0.03	1.25	0.29
Tm	n.a.	n.a.	n.a.	n.a.	n.a.	n.a.	n.a.	n.a.
Yb	0.10	0.24	0.97	0.24	0.03	0.03	1.00	0.19
Lu	n.a.	n.a.	n.a.	n.a.	n.a.	n.a.	n.a.	n.a.
Hf	0.68	1.59	4.94	3.58	0.40	0.24	4.27	2.39
Ta	0.25	0.04	0.39	0.08	0.06	0.12	0.27	0.41
Pb	1.46	0.72	1.49	0.60	2.25	2.73	0.73	0.96
Th	1.14	0.11	0.83	0.1	1.08	1.01	0.39	0.29
U	0.31	0.07	0.22	0.05	0.57	0.28	0.16	0.33

< d.l. denotes below detection limits, n.a. denotes not analysed and sample names ending with * denote published data from le Roex and Class (2016) and sample names ending with ** denote data from Shiimi (2017).

Table 4.2 continued.

Locality	Melton Wold		Markt				
Sample	MWX-31*	MWX-34*	JAR12013*	JAR12033*	MRK-1*	JAR12043*	JAR12083*
ppm							
Sc	51	68	42	22	60	40	83
Ti	n.a.	1134	405	453	150	477	420
V	n.a.	n.a.	n.a.	n.a.	n.a.	n.a.	n.a.
Mn	n.a.	n.a.	n.a.	n.a.	n.a.	n.a.	n.a.
Co	n.a.	n.a.	n.a.	n.a.	n.a.	n.a.	n.a.
Ni	399	470	435	325	401	376	385
Cu	n.a.	n.a.	n.a.	n.a.	n.a.	n.a.	n.a.
Zn	n.a.	n.a.	n.a.	n.a.	n.a.	n.a.	n.a.
Rb	4.73	12	0.15	0.20	0.40	0.07	0.22
Sr	307	375	484	97	473	468	215
Y	n.a.	n.a.	n.a.	n.a.	n.a.	n.a.	n.a.
Zr	31	104	20	5.4	119	56	45
Nb	0.87	2.75	0.77	0.5	2.01	1.26	0.24
Ba	113	86	1.34	0.57	15	4.47	1.66
La	6.2	17	13	0.3	9.3	5.8	1.6
Ce	13	40	27	1.4	27	21	6.4
Pr	n.a.	n.a.	n.a.	n.a.	n.a.	n.a.	n.a.
Nd	13	29	26	3.4	35	34	12
Sm	2.8	5.2	4.6	1.2	7.0	6.6	2.9
Eu	0.81	1.38	0.98	0.34	1.59	1.46	0.75
Tb	n.a.	n.a.	n.a.	n.a.	n.a.	n.a.	n.a.
Gd	2.0	3.2	2.2	0.8	4.4	3.7	2.1
Dy	1.26	1.60	0.55	0.24	1.53	1.05	1.11
Ho	n.a.	n.a.	n.a.	n.a.	n.a.	n.a.	n.a.
Er	0.40	0.43	0.14	0.12	0.41	0.22	0.36
Tm	n.a.	n.a.	n.a.	n.a.	n.a.	n.a.	n.a.
Yb	0.25	0.31	0.09	0.07	0.24	0.11	0.27
Lu	n.a.	n.a.	n.a.	n.a.	n.a.	n.a.	n.a.
Hf	1.72	3.00	1.15	0.46	6.37	2.79	2.15
Ta	0.07	0.32	0.08	0.08	0.25	0.19	0.03
Pb	0.90	0.69	2.40	0.19	1.55	0.91	0.57
Th	0.06	0.36	0.24	0.06	0.19	0.11	0.03
U	0.10	0.37	0.04	0.51	0.06	0.06	0.25

< d.l. denotes below detection limits, n.a. denotes not analysed and sample names ending with * denote published data from le Roex and Class (2016) and sample names ending with ** denote data from Shiimi (2017).

4.3 Reconstructed bulk rock REE compositions

Whole rock REE compositions were calculated from garnet and cpx compositions and their modal abundances reported in Janney et al. (2010). It was assumed that the incompatible element contents of olivine and orthopyroxene were zero, as analytically reliable data for these minerals was not available and their concentrations of REE are known to be very low (e.g. Gregoire et al., 2003). However, in light of this assumption, the reconstructed whole-rock concentrations reported here should be taken as minimum estimates.

Reconstructed whole rock trace element patterns are shown in Figure 4.6 and reported in Table 4.3. The majority of the samples have flat primitive mantle normalized REE patterns with a slight dip in the lightest REE. In contrast, several samples with sinusoidal REE patterns (e.g. HBR-1, HBR-3, GANS-1 & GANS-2) display greater sinuosity, with negative slopes in the middle (and, in some cases, heavy) REE and positive slopes in the LREE's.

Samples from Melton Wold and Hoedkop are on average slightly more depleted relative to those from the other localities (Figure 4.6d & e). The whole rock REE trend of XMW-22, a cpx-free harzburgite, mirrors the trend of the garnet in the sample. Several samples from Hebron and Uintjiesberg display minor enrichment relative to primitive mantle (Figure 4.6a & b). GANS-9, a garnet websterite, is most enriched relative to primitive mantle, reflecting the high modal abundance of garnet and cpx in the sample (Figure 4.6c).

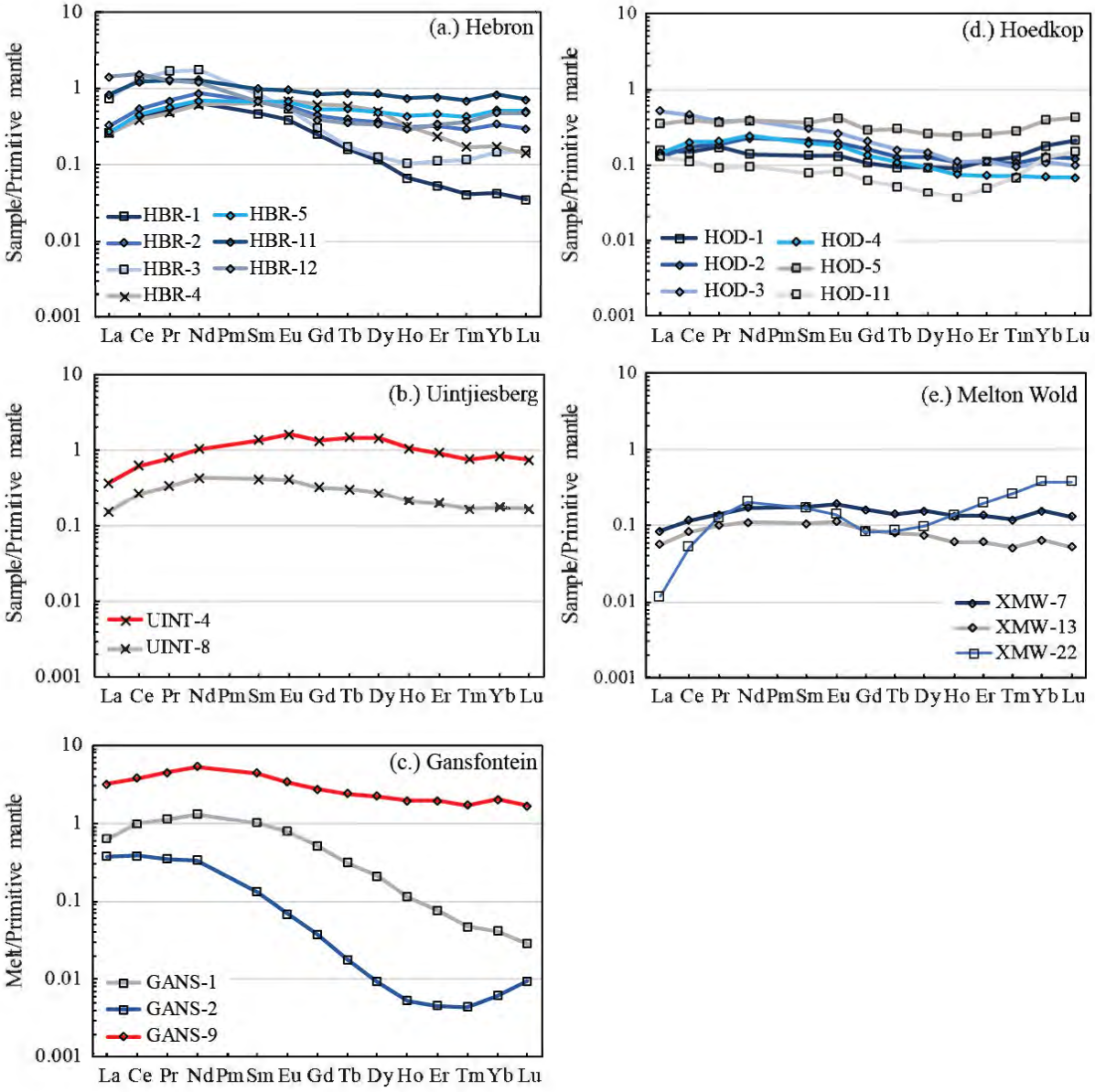

Figure 4.6: Reconstructed whole rock REE patterns normalized to primitive mantle (McDonough and Sun, 1995) for selected samples and localities from off-craton kimberlites (a – e). Samples associated with "normal" garnet REE patterns are indicated by diamond symbols, sinusoidal by square symbols and sloped by cross symbols. Samples illustrated in red are websterites UINT-4 (b) and GANS-9 (c).

Table 4.3: Reconstructed bulk rock REE concentrations for off-craton peridotites.

Sample	La	Ce	Pr	Nd	Sm	Eu	Gd	Tb	Dy	Ho	Er	Tm	Yb	Lu
	ppm	ppm	ppm	ppm	ppm	ppm	ppm	ppm	ppm	ppm	ppm	ppm	ppm	ppm
HBR-1	0.167	0.72	0.129	0.79	0.19	0.060	0.135	0.016	0.078	0.011	0.023	0.003	0.019	0.002
HBR-2	0.209	0.90	0.172	1.07	0.27	0.091	0.239	0.039	0.245	0.050	0.140	0.020	0.148	0.020
HBR-3	0.472	2.20	0.426	2.18	0.34	0.083	0.165	0.017	0.086	0.017	0.049	0.008	0.064	0.011
HBR-4	0.166	0.65	0.121	0.76	0.26	0.106	0.333	0.058	0.337	0.051	0.104	0.012	0.076	0.010
HBR-5	0.175	0.75	0.143	0.85	0.27	0.103	0.290	0.053	0.326	0.069	0.199	0.029	0.227	0.035
HBR-11	0.539	2.00	0.321	1.61	0.40	0.146	0.454	0.085	0.564	0.118	0.331	0.046	0.360	0.050
HBR-12	0.917	2.52	0.324	1.47	0.27	0.085	0.210	0.035	0.226	0.046	0.149	0.025	0.209	0.033
UINT-4	0.243	1.05	0.199	1.29	0.55	0.249	0.725	0.144	0.967	0.170	0.401	0.051	0.369	0.053
UINT-8	0.100	0.45	0.087	0.55	0.17	0.064	0.177	0.031	0.186	0.035	0.088	0.011	0.078	0.012
GANS-1	0.405	1.68	0.293	1.66	0.41	0.122	0.278	0.031	0.142	0.018	0.034	0.003	0.018	0.002
GANS-2	0.244	0.64	0.089	0.42	0.05	0.011	0.021	0.002	0.006	0.001	0.002	0.000	0.003	0.001
GANS-9	2.083	6.38	1.136	6.59	1.79	0.516	1.487	0.238	1.518	0.315	0.865	0.117	0.907	0.119
HOD-1	0.101	0.25	0.044	0.17	0.05	0.020	0.058	0.009	0.063	0.015	0.050	0.009	0.080	0.015
HOD-2	0.084	0.29	0.047	0.28	0.09	0.030	0.089	0.013	0.088	0.018	0.049	0.007	0.057	0.009
HOD-3	0.331	0.76	0.097	0.49	0.12	0.040	0.112	0.016	0.100	0.018	0.050	0.007	0.049	0.007
HOD-4	0.094	0.34	0.052	0.31	0.08	0.028	0.073	0.011	0.064	0.012	0.032	0.005	0.031	0.005
HOD-5	0.228	0.66	0.092	0.48	0.15	0.064	0.158	0.030	0.176	0.039	0.112	0.019	0.172	0.029
HOD-11	0.084	0.19	0.024	0.12	0.03	0.013	0.034	0.005	0.030	0.006	0.022	0.005	0.057	0.011
XMW-7	0.054	0.20	0.035	0.21	0.07	0.029	0.088	0.014	0.103	0.021	0.059	0.008	0.069	0.009
XMW-13	0.036	0.14	0.025	0.14	0.04	0.017	0.048	0.008	0.050	0.010	0.026	0.003	0.029	0.004
XMW-22	0.008	0.088	0.032	0.26	0.068	0.021	0.045	0.008	0.066	0.022	0.087	0.018	0.167	0.027

REE concentrations were calculated using garnet and cpx mineral compositions and reported modal abundances from Janney et al. (2010).

5. Thermobarometry

5.1 Introduction

The temperature and pressure of equilibration of mantle xenoliths has a significant effect on their mineral assemblage and mineral chemistry. Pressures and temperatures can be estimated using experimental data or thermodynamic models and such estimates rely on chemical exchange and reactions between coexisting mineral phases. By combining a pressure-dependent chemical exchange reaction with a temperature-dependent chemical exchange reaction, one can iteratively calculate a set of pressure and temperature estimates from which a palaeogeotherm at the time of kimberlite eruption can be inferred. This data can be used to make inferences on the structure of the lithosphere (e.g. thickness, thermal state, resource potential), which can be combined with present-day geophysical data to determine whether a region has experienced long-term stability or a lithosphere-scale perturbation as evidenced from mineral and thermal equilibrium.

The accuracy of thermobarometry results is influenced by the accuracy of measured mineral compositions, the accuracy of experimental calibration and the ability of the experimental system to be extrapolated to natural systems. Assessment of how applicable a given thermobarometer is to natural systems is hindered by a lack of absolute reference and the limited number of invariant reactions within the peridotite lithology that are applicable to thermobarometry (Finnerty and Boyd, 1984). Additionally, uncertainties can be exacerbated by analytical error and by extrapolation to compositions beyond the calibrated range (c.f. Ziberna et al., 2016).

When iteratively calculating pressures and temperatures from peridotite mineral data it is essential to first determine whether the minerals being utilised are in equilibrium (Nimis and Grütter, 2010). This can be assessed through textural relationships and consistent compositional differences. Traditionally, thermobarometers

used in mantle petrology have relied mainly on major element exchange between mantle minerals to estimate temperatures and pressures of final equilibration, assuming zero resetting during the kimberlite event. Thermometer formulations most frequently utilise the diopside-enstatite miscibility gap (opx ⇿ cpx) (Lindsley, 1983; Brey and Kohler, 1990), and Fe^{2+} - Mg exchange between garnet and olivine (O'Neill and Wood, 1979), garnet and cpx (Krogh, 1988), and garnet and orthopyroxene (Harley, 1984). Barometers are frequently based on Al and/or Cr solubility in orthopyroxene coexisting with garnet (Nickel and Green, 1985; Brey and Kohler, 1990). Additionally, several single mineral thermobarometers exist (e.g. the Ni-in-garnet thermometer (Ryan et al., 1996) and the enstatite-in-cpx thermometers and the Cr-in-cpx barometer (Nimis and Taylor, 2000)), which allow pressure and temperature results to be obtained from individual mantle xenocrysts. Such thermobarometers are widely used in diamond exploration, due to the far greater prevalence of mantle xenocrysts compared to xenoliths.

Temperature and pressure estimates from major element-based thermobarometers can be used to infer the thermal state of the lithosphere at the time of kimberlite eruption. Diffusion coefficients for divalent cations (Mg^{2+}, Ca^{2+}, Fe^{2+}, etc.) are typically large and diffusive "opening" temperatures (The temperature point a mineral must be heated to in order for diffusion to be effective; Watson and Cherniak, 2013) calculated for 50% retention of divalent cations in mantle minerals are generally reached by 677 – 801℃ (Sun and Liang, 2015). When a sample is heated for a period of time to temperatures above the defined diffusive "opening" temperature the mineral major element chemistry of the sample can be reset to reflect the most recent thermal conditions.

In contrast, diffusion coefficients for the trivalent REEs are typically two to three orders of magnitude lower than those of divalent cations, and their diffusive "opening" temperatures calculated for 50% retention are higher (1037 – 1049℃;Van Orman et al., 2001, 2002b; Sun and Liang, 2015). Hence, a given change in temperature will require a

greater amount of time to be reflected in REE-based thermobarometers than in major element-based thermobarometers. A recent study by Sun and Liang (2014) showed, via a lattice strain model calibrated against experimental mineral-melt partition coefficients, that REE partitioning in garnet and cpx is dependent on pressure, temperature and mineral composition. These authors developed a REE-based garnet-cpx thermobarometer which can be extrapolated to garnet peridotites, eclogites and granulites (Sun and Liang, 2015).

In developing the garnet-cpx REE-based thermobarometer, Sun and Liang (2015) modified the method developed by Liang et al. (2013) for their two-pyroxene-thermometer. The method is an adaptation of the temperature-, pressure- and composition-dependent partition coefficient, D, of trace elements which takes the form,

$$ln\,Di = \frac{\Delta S}{R} - \frac{\Delta H + P\Delta V}{RT} - ln\gamma_{Ri} \qquad (1)$$

where ΔS, ΔH and ΔV are changes in entropy, enthalpy and volume of the exchange reaction, respectively, i is the element or component, R is the ideal gas constant (8.3143 $Jmol^{-1}K^{-1}$), T is the temperature, P is the pressure and γR Which can be written in the general form,

$$lnD_i = A_i + \frac{Bi - f(P)}{T} \qquad (2)$$

where A_i and B_i are coefficients which can be determined through mineral-melt partitioning experiments and f(P) is a function of pressure. Equation (2), written in its linear form, for a group of geochemically similar elements (e.g. REEs) takes the form,

$$B_i = T(lnD_i - \mathrm{A}) + f(P) \qquad (3)$$

where the slope of a regression plotted in ($\ln D_i - A_i$) vs B_i space is the equilibrium temperature and the intercept, f(P), can be used to calculate the equilibrium pressure.

The garnet-cpx REE thermobarometer of Sun and Liang (2015) utilizes the garnet and cpx parameterized lattice strain model of Sun and Liang (2014), which takes the form,

$$D_{REE}^{gt-cpx} = \frac{D_0^{gt}}{D_0^{cpx}} exp\left[-\frac{4\pi N_A E^{gt}}{RT}\left(\frac{r_0^{gt}}{2}\left(r_0^{gt} - r_{REE}\right)^2 - \frac{1}{3}\left(r_0^{gt} - r_{REE}\right)^3\right) + \frac{4\pi N_A E^{cpx}}{RT}\left(\frac{r_0^{cpx}}{2}\left(r_0^{cpx} - r_{REE}\right)^2 - \frac{1}{3}\left(r_0^{cpx} - r_{REE}\right)^3\right)\right] \quad (4)$$

where $D^{gt\text{-}cpx}_{REE}$ is the partition coefficient for a given REE between garnet and cpx, D_0 is the partition coeffiencient for strain-free substitution, E is the apparent Young's modulus for the lattice site, r_0 is the size of the strain-free lattice site, r_{REE} is the ionic radius of the REE, N_A is Avogadro's number (6.02214×10^{23}) and the superscripts gt and cpx denote garnet and cpx, respectively. The mineral-mineral lattice strain model is derived from the parameterized cpx-melt and garnet-melt REE and Y lattice strain models of Sun and Liang (2012, 2013, 2014) which are based on cpx-basaltic melt partitioning experiments conducted at 1042 – 1470℃ and 1 atm – 4 GPa and garnet-basaltic melt partitioning experiments conducted at 1325 – 2300℃ and 2.4 – 25 GPa. The cpx-melt REE and Y lattice strain model of Sun and Liang (2012) is defined as,

$$lnD_0^{cpx} = -7.14(\pm 0.53) + \frac{7.19(\pm 0.73)\times 10^4}{RT} + 4.37(\pm 0.47)X_{Al}^{T} + 1.98(\pm 0.36)X_{Mg}^{M2} - 0.91(\pm 0.19)X_{H_2O}^{melt} \quad (5)$$

$$r_0^{cpx} = 1.066(\pm 0.007) - 0.104(\pm 0.035)X_{Al}^{M1} - 0.212(\pm 0.033)X_{Mg}^{M2} \quad (6)$$

$$E^{cpx}(GPa) = \left[2.27(\pm 0.44)r_0^{cpx} - 2.00(\pm 0.44)\right] \times 10^3 \quad (7)$$

where X^{T}_{Al} is the cation content of Al in the tetrahedral site, X^{M2}_{Mg} is the cation content of Mg in the M2 site and X^{M1}_{Al} is the cation content of Al in the M1 site in pyroxene per six-oxygen, X^{melt}_{H2O} is the molar fraction of H_2O in the melt which is set to 0 (Sun and Liang 2015). Cpx formulae are calculated assuming a random distribution of Fe^{2+} and Mg^{2+} over the M1 and M2 sites, with all iron present as ferrous iron (Sun and Liang 2012).

The garnet-melt REE and Y lattice strain model of Sun and Liang (2014) is defined as,

$$lnD_0^{gt} = -2.01(\pm 0.70) + \frac{9.03(\pm 0.98)\times 10^4 - 93.02(\pm 17.06)P(37.78-P)}{RT} - 1.04(\pm 0.44)X_{Ca} \quad (8)$$

$$r_0^{gt} = 0.785(\pm 0.031) + 0.153(\pm 0.029)X_{Ca} \quad (9)$$

$$E^{gt} = [-1.67(\pm 0.45) + 2.35(\pm 0.51)r_0] \times 10^3 \quad (10)$$

where X_{Ca} is the cation content of Ca in garnet per 12-oxygen. Given equations (4) to (10), equation (4) is rewritten in the linear form of equation (3) which takes on the expressions,

$$A = 5.13 - 1.04X_{Ca} - 4.37X_{Al}^{T} - 1.98X_{Mg}^{cpx} \quad (11)$$

$$B_i = 2.21 \times 10^3 + 909.85G(r_{REE}) \quad (12)$$

$$f(P) = -11.19P^2 + 422.66P \quad (13)$$

$$G(r_{REE}) = E^{cpx}\left(\frac{r_0^{cpx}}{2}\left(r_0^{cpx} - r_{REE}\right)^2 - \frac{1}{3}\left(r_0^{cpx} - r_{REE}\right)^3\right) - E^{gt}\left(\frac{r_0^{gt}}{2}\left(r_0^{gt} - r_{REE}\right)^2 - \frac{1}{3}\left(r_0^{gt} - r_{REE}\right)^3\right) \quad (14)$$

To calculate temperature and pressure for the REE-based thermobarometer, terms A and B_i are calculated through equation 11, 12 and 14 and cpx and garnet major and trace element data for each of the REEs and Y. The results are then plotted as a scatter plot in ($\ln D_i$ – A; i.e. x-term) vs B_i (i.e. y-term) space and a linear regression is fitted to the data in order to obtain the equilibrium temperature (i.e. slope of the regression equation) of the sample, and the intercept, *f*(P), is used to calculate equilibrium pressure of the sample through equation 14. Theoretically, a well equilibrated sample should define a straight, positively correlated line in the lnD – A vs B temperature inversion plot.

The regression line passing through the points on the temperature inversion diagrams is calculated using robust regression, as recommended by Sun and Liang (2015). In ordinary linear regression, the residuals for each data point are weighted equally. Because of this, when an outlier is present it can substantially skew the regression line. The premise of robust regression is to down weight the outliers which have high residuals,

such that the fitted regression is more robust. The REE-based thermobarometer uses a bi-weight function for robust regression. In a bi-weight, the residuals associated with data points have a maximum value (i.e., beyond a certain point, this residual for an outlying data point has a constant weighting that does not increase no matter how large its distance from the regression). This maximum residual value (termed the "tuning constant") can be adjusted, but Sun and Liang (2015) found that it worked best with a value of 2.5. This method allows for efficient reduction of the influence of outliers. It should be noted that although it can handle a large deviation of the dependent variable (y), it is not robust against a large deviation in the independent variable (x).

The strength of the REE-thermobarometry method is that it allows thermal histories to be assessed through comparison with major element-based thermobarometers. Additionally, in treating the REE and Y as a group, the analytical uncertainty associated with low concentration elements is minimised. However, the accuracy of the technique is largely dependent on the existence of trace element equilibrium between garnet and cpx in a sample. Metasomatism is commonly associated with kimberlite magmatism and the highly enriched nature of kimberlite melts trapped at the base of the lithosphere often results in a disturbance of incompatible elements, such as the LREE. Therefore, kimberlite melt-mantle wall-rock interaction, shortly prior to entrainment, has the potential to introduce significant bias. Thus, it is important to select a suitable dataset of well-equilibrated samples when applying the method in order to maximise the accuracy of the results.

This chapter provides an overview of the results obtained through REE-based thermobarometry in comparison to those obtained from major element-based thermobarometry. This data is used to assess the thermal contrasts noted between the two main kimberlite pulses along the south western margin of the Kaapvaal craton by Bell et al., (2003), Kobussen et al., (2008, 2009), Janney et al., (2010) and Mather et al., (2011). Paleogeotherms were quantitatively fitted to the data using the FITPLOT

program (McKenzie et al., 2005; McKenzie and Priestley, 2008; Mather et al., 2011), allowing the evaluation of lithospheric thickness and resource potential along the south western margin of the Kaapvaal craton during the Mesozoic.

5.2 FITPLOT

Paleogeotherms were calculated from pressure and temperature data using FITPLOT (McKenzie et al., 2005; McKenzie and Priestley, 2008; Mather et al., 2011), a quantitative paleogeotherm fitting program. The geotherm is fitted using a series of thermal equations and input parameters which describe the thermal properties of the crust and mantle in the region of interest. Geotherms are iteratively calculated and a unique geotherm is numerically fitted by root mean square distribution to a set of pressure and temperature estimates. Lithospheric thickness is calculated as the intersection of the mechanical boundary layer (conductive lithosphere) and the isentrope (i.e., adiabatic thermal gradient of the asthenosphere). The method allows unique geotherms to be fitted to the input pressure and temperature results. Hence it can be used to assess lithosphere scale disturbances such as those proposed to have occurred along the south western margin of the Kaapvaal craton.

5.3 Equilibrium

It is important to ensure that samples used for pressure and temperature estimation do not show petrographic or chemical signs of inter-mineral disequilibrium. Pressure and temperature estimates from major element thermobarometry were re-calculated here to avoid any discrepancy in calculation across the literature datasets. Major element equilibrium was assessed following the criteria suggested by Nimis and Grütter (2010) and Ziberna et al. (2016).

To assess REE equilibrium, the recommendation of Sun and Liang (2015) was followed by comparing chondrite normalized REE patterns for cpx and garnet side-by-side with pressure-temperature inversion diagrams (i.e., of $(\ln D_i - A_i)$ vs B_i for the REE

and Y). In addition to these two plots, the partition coefficients for garnet-cpx pairs were normalized to those of Vitim 313-105, an off-craton garnet peridotite xenolith exhumed by basaltic magmatism in Central Asia (Ionov et al., 2005). This sample is a fertile peridotite with a bulk composition near that of primitive mantle and it has been interpreted as having extensively equilibrated with a melt such that garnet and cpx appear to be in major and trace element equilibrium (Ionov et al., 2005) and was used successfully by Luchs et al. (2013) to evaluate trace element equilibrium between cpx and garnet in peridotites from the Gibeon kimberlite field, Namibia. It must be noted that (1) basalt-borne xenoliths do not experience the same secondary enrichment processes as kimberlite-borne xenoliths and (2) this sample represents equilibration under a specific pressure and temperature (1034℃ and 2.1 GPa; Ionov et al., 2005). Hence, it is not considered in isolation as an indication for equilibrium but rather in conjunction with the two plots proposed as equilibrium indicators by Sun and Liang (2015).

Two samples (HBR-2 and HBR-4) are shown to illustrate relative equilibrium and disequilibrium, respectively, in Figure 5.1a - f, plots for all other samples are provided in Appendix D. Where one or more element(s) were seen to be out of garnet-cpx equilibrium (as defined by temperature inversion diagrams (elements in equilibrium should define a straight line whilst those out of equilibrium will deviate from the general trend) and normalization to Vitim 313-105) it was excluded from the regression calculation. A sample was rejected for use in REE-based thermobarometry calculations if it was found to have 6 or more elements that exhibited disequilibrium in both the temperature inversion plot and the $D_{gt/cpx}$ normalization to Vitim 313-105. Normalization of cpx-garnet REE and Y partition coefficients to those of Vitim 313-105 was performed in addition to the suggested equilibrium tests of Sun and Liang (2015) because when the normalized REE graphs and temperature inversion diagrams are used in isolation, it is often not

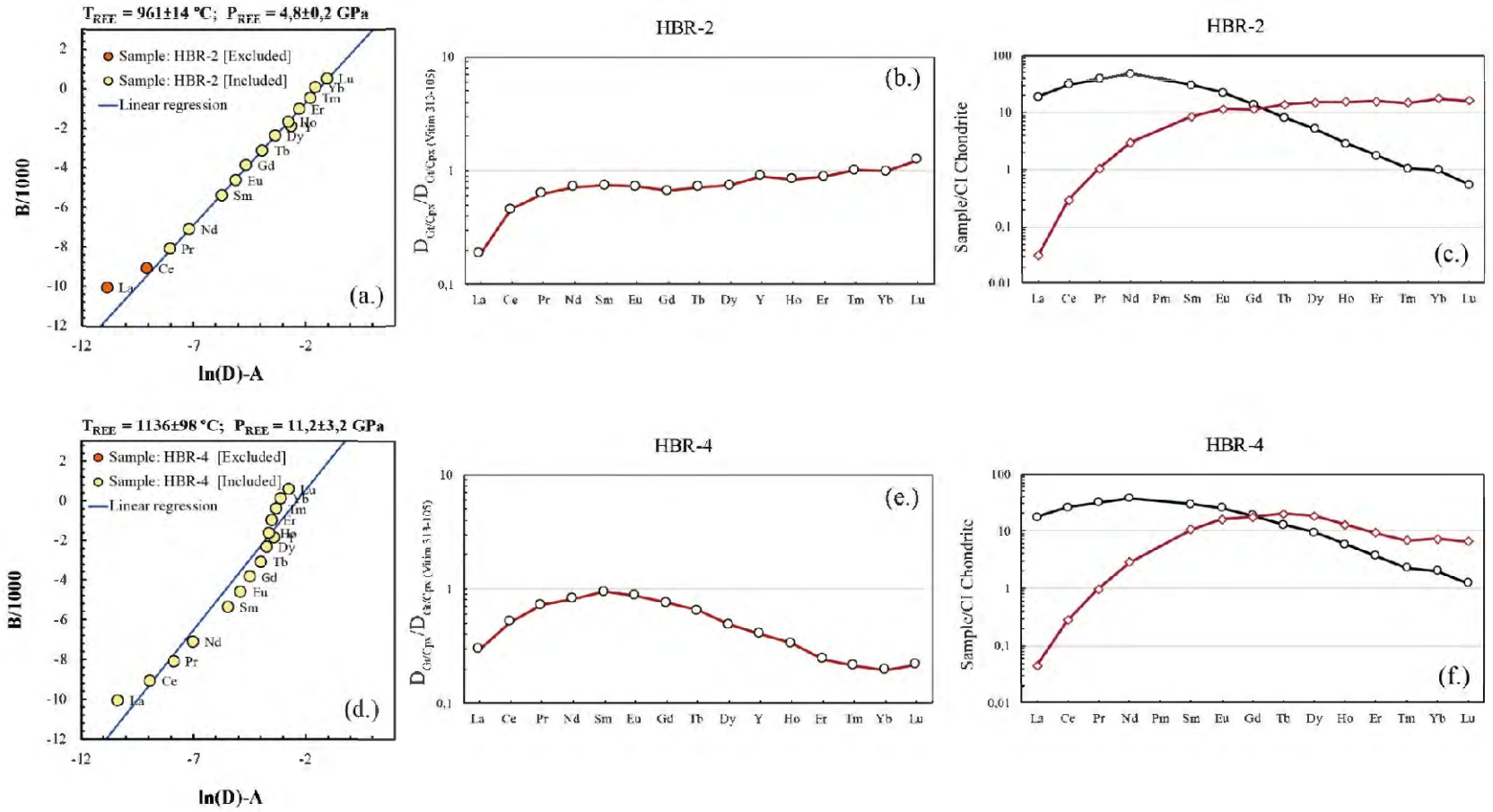

Figure 5.1: (a) Temperature inversion plot, (b) $(D_{Gt/Cpx})/D_{gt/Cpx(Vitim\ 313\text{-}105)}$ and (c) CI chondrite normalized REE patterns for a well equilibrated garnet-cpx pair (HBR-2) and (d), (e), and (f) for a poorly equilibrated sample (HBR-4).

clear which elements are out of equilibrium. HBR-2 is used as an example of a sample exhibiting equilibrium between all REE apart from La and Ce (Figure 5.1a – c). Whilst HBR-4 (Figure 5.1d – f) is an example of poor equilibrium and emphasises the importance of using all three plots (temperature inversion diagram, normalization to Vitim 313-105 and chondrite normalized REE patterns) when assessing equilibrium. On the temperature inversion plot (Figure 5.1d) one could easily assume that the HREE are out of equilibrium whilst the remaining elements fit a "relatively" straight line. However, when using normalization of $D_{gt/cpx}$ values to those of Vitim peridotite 313-105 as a guide to the extent of trace element equilibration (Figure 5.1e), it is clear that virtually all of the REE are significantly out of equilibrium between these two minerals. Admittedly, a precise quantitative parameterization of cpx-garnet REE equilibrium in kimberlite-borne xenoliths, which accounts for the wide range of temperatures and pressures from which they may be derived remains elusive, and the above method for testing for equilibrium may only provide a crude guide. However, in the absence of more sophisticated models, it is still useful. In future, it may be useful to develop a more refined set of mineral-mineral partition coefficients using other data sources, such as megacryst intergrowths, which are interpreted to be crystallization products of kimberlite-related melts at the base of the lithosphere (Bell and Moore, 2004).

5.4 Major element-based thermobarometry

5.4.1 An overview of the available major element-based thermobarometers

A large number of thermometers and barometers applicable to natural mantle assemblages have been proposed since the pioneering work of Boyd (1973). Discrepancies of several hundred degrees Celsius and tens of kilobars between thermobarometry methods has resulted in several studies which extensively assessed the reliability of various methods and attempted to determine which were most reliable (Finnerty and Boyd, 1984; Brey and Kohler, 1990; Taylor, 1998; Nimis and Grütter, 2010; Ziberna et al., 2016).

In their review of the available thermometers for garnet peridotites and pyroxenites, Nimis and Grütter (2010) concluded that the two-pyroxene thermometer of Taylor (1998) and single cpx thermometer of Nimis and Taylor (2000) (hereafter TA98 and NT00, respectively) and the Al-in-orthopyroxene barometer of Nickel and Green (1985) and Cr-in-cpx barometer of Nimis and Taylor (2000) (hereafter NG85 and NT00, respectively) best reproduced experimental results. The authors suggested that the most reliable thermobarometer combinations application to mantle systems were T_TA98 P_NG85 and T_NT00 P_NT00.

The widely used two-pyroxene thermometer of Brey and Kohler (1990) (hereafter BKN) was found to show an increasing positive bias as Na in cpx increases, due to an over estimate of Na's influence on enstatite activity in the formulation (Nimis and Grütter, 2010). TA98 corrects for this by applying a three site solid solution model, which better reproduces experimental results over a broader compositional range (Taylor, 1998). The NT thermometer reproduced experimental results well and was found to show good agreement with TA98 (± 30℃). However, the authors highlighted that the single mineral thermometer is a simplification of the natural system as it assumes a fixed enstatite in orthopyroxene activity (Nimis and Taylor, 2000; Nimis and Grütter, 2010).

In their evaluation of Fe-Mg exchange thermometers, Nimis and Grütter (2010) found that none of the Fe-Mg thermometers were in good agreement with TA98 and commonly exhibited low precision and large uncertainties. This was found to be particularly bad for cpx-garnet thermometers, which was attributed to Fe^{3+} incorporation in cpx (Canil and O'Neill, 1996; Nimis and Grütter, 2010) which exaggerates the influence of inaccurate Fe^{3+} estimation in Fe-Mg thermometry. The cpx-garnet thermometer of Krogh (1988) (hereafter KR88) was found to show increasing disagreement with the two-pyroxene thermometers at temperatures >900 ℃. The applicability of Fe-Mg exchange thermometers to natural assemblages is complicated both by the accuracy of Fe^{3+} estimation in garnet and cpx, and OH^- loss or addition in

cpx post-equilibration with garnet which will result in Fe^{3+} Mossbauer measurements which do not reflect equilibration compositions (Bell and Rossman, 1992; Mofokeng, 1998).

The NG85 barometer is preferred over the BKN barometer by Nimis and Grütter (2010) because these authors found that NG85 exhibited greater precision over a wide range of compositions at pressures up to 60 kbar, whereas BKN overestimated pressures at P > 50 kbar. The NT00 Cr-in-cpx barometer was found to underestimate pressures above 50 kbar and was found to be susceptible to disequilibrium results from thermal perturbation. Additionally, Ziberna et al. (2016) found that the NT00 barometer was exceedingly sensitive to analytical uncertainty and suggested that analytical conditions should be tailored for specific samples and elements to reduce this error.

In this study, the T_TA98 P_NG85 thermobarometer combination is considered most reliable. The reasons for this are:

- The two-pyroxene thermometry is primarily based on Ca-Mg exchange and so is not susceptible to the Fe^{3+} problem (Canil and O'Neill, 1996).
- The three-site solid solution in the TA98 formulation reduces uncertainty which arises in the BKN method due to an over estimation of the influence of Na in enstatite activity.
- NG85 pressure estimates exhibited greater precision to 60 kbar in comparison to BKN and NT00 which overestimated and underestimated pressures and P > 50 kbar, respectively.
- The thermobarometer combination of T_TA98 P_NG85 best reproduced experimental results (Nimis and Grütter, 2010).

However, in addition to T_TA98 P_NG85, the thermobarometers of T_BKN P_BKN and T_NT00 P_NT00 and the thermometer of KR88 were also used because:

- The BKN thermobarometer is the method most widely adopted in the literature and allows for comparison to T_TA98 P_NG85 results.
- The clinopyroxene NT00 thermobarometer allows for assessment of TP data for those samples for which data is only available for cpx and garnet (i.e. dataset of le Roex and Class 2016)
- Sun and Liang (2015) use T_KR88 to assess the applicability of the REE-based thermobarometer to field samples and found REE-based temperatures show the greatest agreement with T_KR88 temperatures (see Figure 8c in Sun and Liang 2015) in comparison to other cpx-garnet thermometers.
- Comparison of T_KR88 with REE-based temperatures allows for direct comparison of temperatures derived from cpx and garnet.

5.4.2 Major element-based thermobarometry results

The available literature data from peridotite xenoliths exhumed by off-craton kimberlites which erupted through the NNP along the south western periphery of the Kaapvaal craton have been utilised for major element-based PT estimates in an attempt to provide a comprehensive assessment of the geothermal gradient in the region. To perform an independent assessment of temperature estimates, the preferred barometer of NG85 was used to test the agreement between the TA98, BKN and KR88 thermometers. Similarly, pressure estimates were independently assessed for NG85 and BKN using temperature estimates from the preferred thermometer, TA98. For those samples for which no orthopyroxene data is available or present, the NT00 thermometer was used in combination with the NT00 barometer. Table 5.1 compares the temperature and pressure estimates by the methods outlined above. Temperatures from all thermometers range from 600 – 1525 ℃ and pressures from 12 – 79 kbar.

A comparison of temperature estimates of TA98 with BKN, NT00 and KR88 is illustrated in Figure 5.2. Both two-pyroxene thermometers, TA98 and BKN, agree well. BKN yielded temperatures which were systematically higher (apart from one sample which plots on the 1:1 correlation) than TA98, however, the overestimation was not greater than 100 ℃ (Figure 5.2a). An excellent correlation was observed between TA98 and NT00, for which all the samples are within ±50 ℃ (Figure 5.2b).

The Fe^{2+} - Mg cpx-garnet thermometer (KR88) shows a poor correlation with TA98 across the entire temperature range, but this is most evident at lower temperatures which generally suggest an overestimation of temperatures yielded by KR88, apart from a cluster of samples exhumed by the Pofadder kimberlite which yield lower KR88 temperatures (Shiimi (2017) showed through trace element mineral chemistry that garnet and cpx from this locality suggest major disequilibrium which likely resulted from interaction with kimberlitic melts), in relation to TA98 (Figure 5.2c). Most of the samples studied here (excluding the data from Pofadder) yielded temperatures higher than TA98 by ~130 ℃ and the difference between the two thermometers becomes larger as temperatures decrease, apart from GANS-1 for which there is an increase in temperature by 431 ℃.

The disagreement in temperature estimates between Fe^{2+}-Mg exchange thermometers and pyroxene solvus thermometers has been reported by several authors (c.f. Brey and Kohler, 1990; Luth et al., 1990; Mofokeng, 1998; Woodland, 2009; Nimis and Grütter, 2010; Nimis et al., 2015). Fe^{2+}-Mg exchange thermometers assume all Fe to be in the 2+ state, yet the oxidation state of the lithospheric mantle has been shown to be heterogeneous (Woodland and Koch, 2003; Nimis et al., 2015). The effects neglecting versus including Fe^{3+} in thermobarometry calculations for mantle systems can result in temperature differences of up to 300 ℃ for cpx-garnet thermometers which can influence iteratively coupled barometry estimates by up to 13 kbar (Luth et al., 1990; Canil and O'Neill, 1996). Therefore, the uncertainty associated with the influence of Fe^{3+} in Fe^{2+}-

Mg exchange thermometry suggests that temperature estimates from KR88 thermometer may be more inaccurate than the available two-pyroxene thermometers.

A comparison of pressure estimates of NG85 with BKN and NT00 are illustrated in Figure 5.3. Both the orthopyroxene-garnet barometers agree well and all samples apart from two samples at P_NG85 > 46 kbar are within 5 kbar of each other Figure 5.3a. The overestimation of BKN pressures at higher pressures was previously noted by Nimis and Grütter (2010), who found that the BKN barometer increasingly overestimated pressures at pressures greater than 50 kbar. A reasonable correlation was observed between NG85 and NT00, but NT00 yielded results which generally overestimate pressures relative to NG85 Figure 5.3b. However, the overestimation was mainly less than a 5 kbar overestimation except for five samples which do not exceed a 10 kbar overestimation.

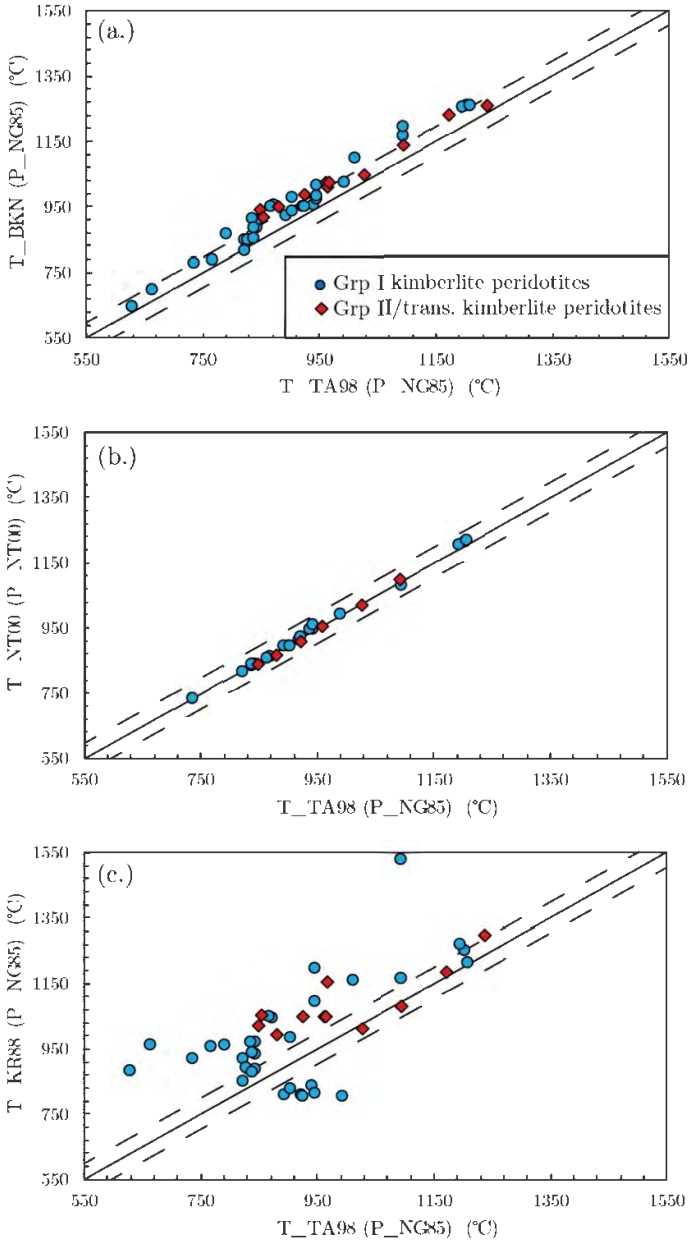

Figure 5.2: Temperature (°C) comparisons of (a) TA98 (P_NG85) vs BKN (P_NG85) which exhibits a good correlation throughout the temperature range but shows an overestimation of temperatures of BKN relative to TA98; (b) TA98 (P_NG85) vs NT00 (P_NT00) which shows an excellent correlation across the entire temperature range within ± 50 °C; (c) TA98 (P_NG85) vs KR88 (P_NG85) which exhibits a poor correlation between the two thermometers, in which KR88 generally overestimates temperatures within the lower temperature range with the exception of a cluster of samples exhumed during the peak of Group I kimberlite magmatism for which KR88 underestimates temperatures in relation to TA98. Solid diagonal line represents the 1:1 correlation and dashed line represents a ± 50 °C envelope. Data sources as for Table 5.1.

Table 5.1: Temperature and pressure estimates calculated using conventional major element-based thermobarometers for peridotite xenolith samples from off-craton kimberlites from the south western margin of the Kaapvaal craton. Data sources are Robey (1981); Janney et al. (2010); le Roex and Class (2016); Shiimi (2017)).

Sample	Locality	two-pyroxene T _BKN (P_NG85)	two-pyroxene T_TA98 (P_NG85)	single cpx T_NT00 (P_NT00)	garnet-cpx T_KR88 (P_NG85)	garnet-orthopyroxene P_BKN (T_TA98)	garnet-orthopyroxene P_NG85 (T_TA98)	single cpx P_NT00 (T_NT00)
		℃	℃	℃	℃	kbar	kbar	kbar
JAR12013	Markt			1050				44
JAR12033	Markt			1101				44
JAR12043	Markt			1004				44
JAR12083	Markt			1005				46
MRK-1	Markt			963				41
JAR-08053	Melton Wold	942	848	841	1020	38	35	40
JAR-08063	Melton Wold	953	880	868	993	40	37	38
JAR-08073	Melton Wold	1049	1025	1020	1012	40	41	43
JAR-08083	Melton Wold	1027	959	955	1049	44	41	44
JAR-08113	Melton Wold	921	853		1053	39	37	
JAR-08123	Melton Wold	991	922	906	1046	41	40	40
MWX-15	Melton Wold			929				40
MWX-18	Melton Wold			964				46

Table 5.1 continued.

Sample	Locality	two-pyroxene T _BKN (P_NG85) ℃	two-pyroxene T_TA98 (P_NG85) ℃	single cpx T_NT00 (P_NT00) ℃	garnet-cpx T_KR88 (P_NG85) ℃	garnet-orthopyroxene P_BKN (T_TA98) kbar	garnet-orthopyroxene P_NG85 (T_TA98) kbar	single cpx P_NT00 (T_NT00) kbar
MWX-19	Melton Wold			928				38
MWX 20	Melton Wold			981				41
MWX-32	Melton Wold			948				40
XMW-7	MeltonWold	1014	963		1048	39	36	
XMW-8	MeltonWold	1260	1237		1297	76	69	
XMW-13	MeltonWold	1143	1092	1097	1081	45	45	51
XMW-19	MeltonWold	1026	964		1152	59	47	
MW-1	MeltonWold	1233	1171		1183	51	46	
UINT-4	Uintjiesberg	894	843	840	884	28	27	30
UINT-8	Uintjiesberg	1015	942	946	1192	34	33	41
UINT-micro	Uintjiesberg	1097	1008		1156	41	36	
JAR09053	Uintjiesberg			841				36
HBR-1	Hebron	853	822	818	916	25	26	31
HBR-2	Hebron	958	870	863	1040	30	27	29
HBR-3	Hebron	886	843		934	24	24	
HBR-4	Hebron	951	864	859	1047	28	26	30
HBR-5	Hebron	909	842		968	26	24	

Table 5.1: continued.

Sample	Locality	two-pyroxene T _BKN (P_NG85) ℃	two-pyroxene T_TA98 (P_NG85) ℃	single cpx T_NT00 (P_NT00) ℃	garnet-cpx T_KR88 (P_NG85) ℃	garnet-orthopyroxene P_BKN (T_TA98) kbar	garnet-orthopyroxene P_NG85 (T_TA98) kbar	single cpx P_NT00 (T_NT00) kbar
HBR-10	Hebron	980	901	895	982	30	28	31
HBR-11	Hebron	850	827		891	21	22	
HBR-12	Hebron	855	837	837	878	24	25	30
JAR-07033	Hebron	914	835		967	26	25	
JAR-07073	Hebron	698	662		958	15	15	
JAR-07143	Hebron	780	736	734	918	18	19	27
JAR-07163	Hebron	889	838	841	938	23	23	29
JAR-07173	Hebron	957	937	945	835	27	27	32
JAR-07183	Hebron	869	789		959	24	22	
GANS-1	Gansfontein	1169	1094		1525	44	39	
GANS-2	Gansfontein	820	822		848	25	27	
GANS-9	Gansfontein	976	943		814	35	33	
GSF-4	Gansfontein			899				30
GSF-5	Gansfontein			780				32
HOD-1	Hoedkop	791	766		954	23	23	
HOD-2	Hoedkop	1262	1202	1213	1251	45	42	47
HOD-3	Hoedkop	1256	1194	1205	1268	48	44	49

Table 5.1: continued.

Sample	Locality	two-pyroxene T _BKN (P_NG85) ℃	two-pyroxene T_TA98 (P_NG85) ℃	single cpx T_NT00 (P_NT00) ℃	garnet-cpx T_KR88 (P_NG85) ℃	garnet-orthopyroxene P_BKN (T_TA98) kbar	garnet-orthopyroxene P_NG85 (T_TA98) kbar	single cpx P_NT00 (T_NT00) kbar
HOD-4	Hoedkop	1262	1206	1219	1211	43	42	46
HOD-5	Hoedkop	983	943	959	1094	29	30	40
HOD-8	Hoedkop			786				28
HOD-9	Hoedkop			600				24
HOD-10	Hoedkop			733				24
HOD-11	Hoedkop	649	627		880	12	13	
JJG 2499-4	Pofadder	1024	990	990	801	34	33	35
JJG 2499-6	Pofadder	924	892	893	805	27	28	33
JJG 2499-7	Pofadder	936	903	896	828	32	32	32
JJG 2499-12	Pofadder	951	920	914	806	31	32	33
JJG 2499-14	Pofadder			876				33
JJG 2499-15	Pofadder	954	922	923	804	29	30	33
JJG 2499-16	Pofadder			913				33
SD-1	Schuitdrift	1198	1093	1081	1163	45	42	38

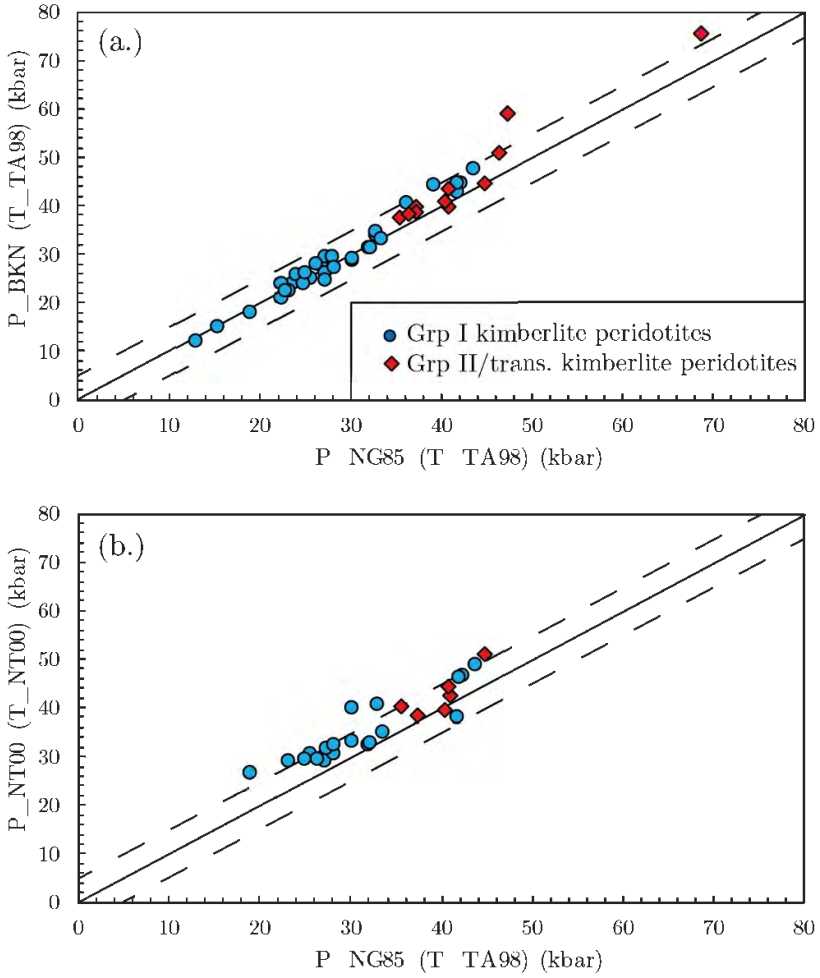

Figure 5.3: Pressure (kbar) comparisons of (a) NG85 (T_TA98) vs BKN (T_TA98) which exhibits a good correlation throughout the pressure range but shows an overestimation of pressures of BKN relative to NG85 at P > 46 kbar (P_NG85); (b) NG85 (T_TA98) vs NT00 (T_NT00) which shows a reasonable correlation but exhibits a general overestimation of the pressures of NT00 relative to NG85. Solid diagonal line represents the 1:1 correlation and dashed line represents a ± 5 kbar envelope. Data sources as for Table 5.1.

5.5 REE-based thermobarometry results

Samples were screened for equilibrium following the procedure outlined above, which resulted in discarding of 35% of the data for the use of REE-based thermobarometry due to lack of sufficient inter-mineral equilibrium for the Sun and Liang (2015) thermobarometer to be meaningful. 76% of the samples exhibited

disequilibrium for one or more elements when comparing $D_{gt/cpx}$ values with those of Vitim 313-105 in conjunction with temperature inversion plots.

Calculated REE-based thermobarometry results yield temperatures in the range of 857 – 1326℃ and pressures ranging from 20 – 105 kbar (Table 5.2). The T_{REE}-P_{REE} values of the samples define a steep geotherm, with far greater scatter than conventional major element-based estimates (Figure 5.4). 95% confidence and prediction intervals calculated for linear regressions fitted to samples exhumed during the Grp II/transitional peak and Grp I kimberlite peak suggest that the data is not resolvable within uncertainties between the two time periods.

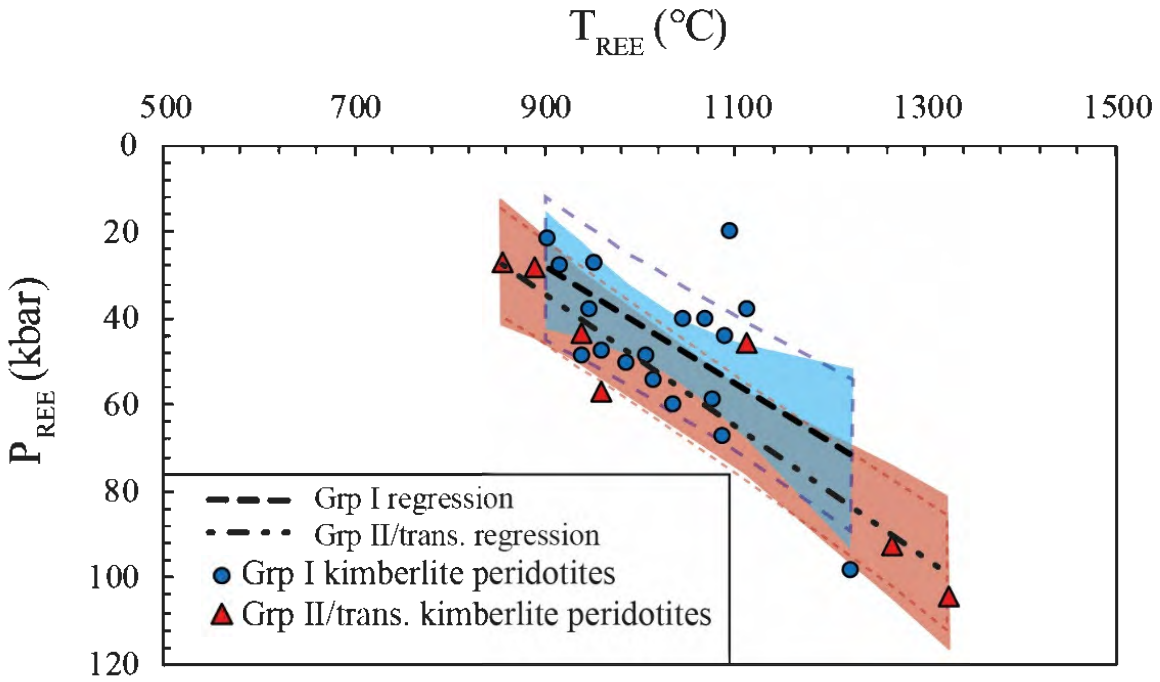

Figure 5.4: T_{REE} vs P_{REE} estimates calculated using the cpx-garnet thermobarometer of Sun and Liang, (2015). Light blue shaded field represents 95% confidence interval and blue dashed region represents 95% prediction interval of the regression model for Grp I kimberlite xenoliths. Red shaded field represents 95% confidence interval and red dashed region represents 95% precision interval of the regression model for samples exhumed during the Grp II/transitional kimberlite peak.

Table 5.2: Temperature (℃), pressure (kbar) and depth (km) estimates for garnet-cpx pairs calculated from Sun and Liang (2015) (T_{REE} and P_{REE}).

Sample	Locality	T_{REE} (℃)	±1σ	P_{REE} (kbar)	±1σ	D_{REE} (km)
HBR-1	Hebron					
HBR-2	Hebron	961	14	48	2,0	147
HBR-3	Hebron	1013	24	54	4,0	167
HBR-4	Hebron					
HBR-5	Hebron	987	16	50	2,0	154
HBR-10	Hebron					
HBR-11	Hebron	1006	27	48	3,8	150
HBR-12	Hebron	1034	36	60	5,6	186
HBX-1	Hebron	1086	26	67	4,7	207
GANS-1	Gansfontein					
GANS-2	Gansfontein	1069	25	40	3,0	124
GANS-9	Gansfontein	948	30	38	3,0	117
UINT-micro	Uintjiesberg	939	21	49	3,6	150
UINT-4	Uintjiesberg					
UINT-8	Uintjiesberg	951	29	27	4,0	83
UBX-1	Uintjiesberg	904	33	22	3,6	67
UBX-18	Uintjiesberg	1221	44	98	11,0	303
HOD-1	Hoedkop	1094	28	20	0,2	62
HOD-2	Hoedkop	1111	24	38	3,0	118
HOD-3	Hoedkop					
HOD-4	Hoedkop	1090	62	44	7,0	136
HOD-5	Hoedkop	1076	28	59	5,0	182
HOD-11	Hoedkop	1046	42	40	6,0	124
SD-1	Schuitdrift	916	52	28	6,0	86
XMW-7	Melton Wold	1265	48	92	8,5	285
XMW-8	Melton Wold	1113	15	46	1,9	142
XMW-13	Melton Wold	1326	47	105	9,9	323
XMW-19	Melton Wold					
MWX-5	Melton Wold					
MWX-10	Melton Wold	939	38	44	5,4	134
MWX-15	Melton Wold	890	25	28	3,9	87
MWX-18	Melton Wold					
MWX-19	Melton Wold	857	20	27	3,2	83
MWX-20	Melton Wold					
MWX-32	Melton Wold					
JAR12013	Markt	959	57	57	9,2	177
JAR12033	Markt					
MRK-1	Markt					

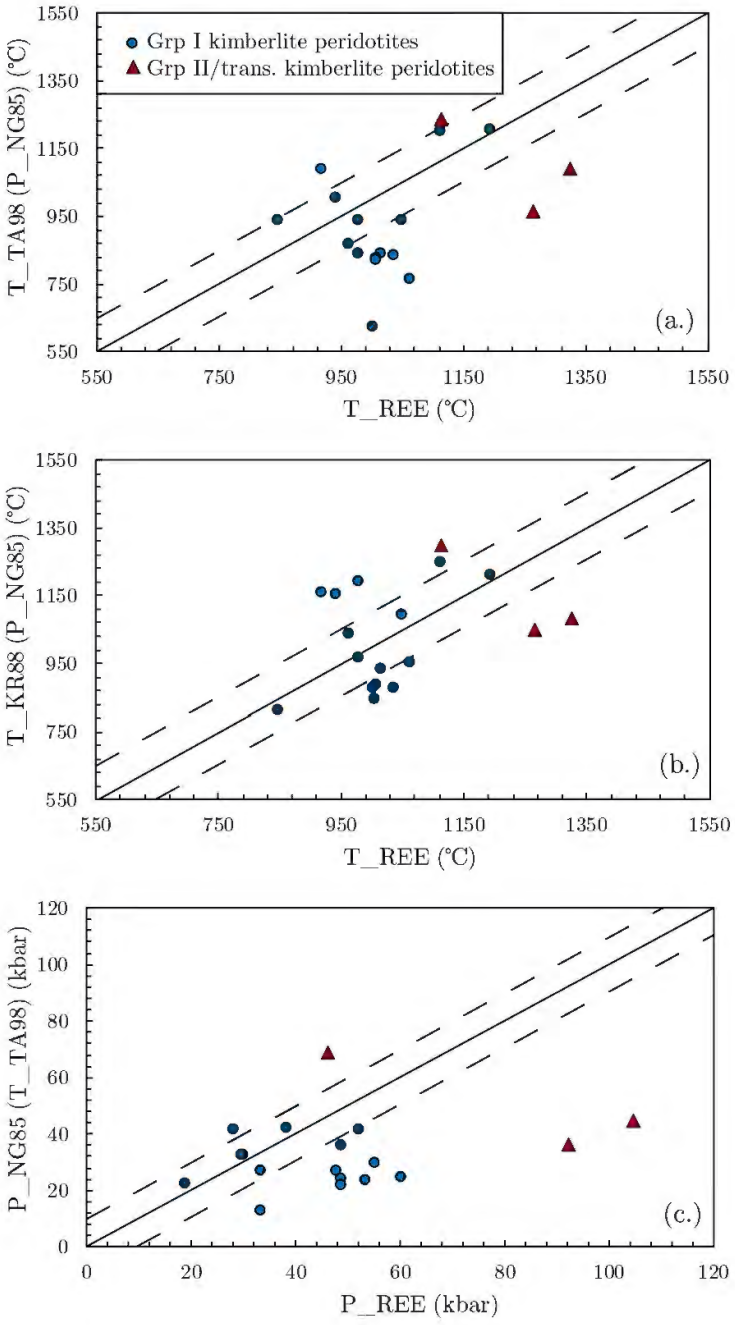

Figure 5.5: Comparisons of (a) temperature estimates calculated from REE-based thermobarometry vs TA98, which show an overestimation of T_REE relative to TA98 for ~50% of the dataset; (b) temperature estimates calculated from REE-based thermobarometry vs KR88, which show scatter throughout the 1:1 correlation and both an over and underestimation in temperatures relative to KR88; (a & b) Solid line represents the 1:1 correlation and dashed line illustrates a ± 100 °C envelope; (c) pressure estimates calculated from REE-based thermobarometry vs NG85, which similarly displays a poor correlation and an increasing overestimation in REE-based pressure estimates as pressure increases. Solid line represents the 1:1 correlation and dashed line illustrates a 10 kbar envelope.

5.6 Comparison of REE-based and conventional TP estimates

A comparison of REE-based temperature and pressure estimates to those calculated from the preferred major element-based thermometer and barometer (TA98 NG85) is illustrated in Figure 5.5.

A poor correlation is observed between REE-based temperatures and pressures in comparison to TA98 and NG85, respectively. Temperatures are overestimated by the REE-based thermometer in nine of the seventeen samples for which there is data, with only six samples falling within the ±100 ℃ envelope Figure 5.5a. The overestimation in temperature occurs across the entire temperature range. Similar to what was found in TA98 vs REE-based temperatures, only six of the samples fall within the ±100 ℃ envelope when compared with the Fe^{2+} - Mg thermometer of KR88 (Figure 5.5b). However, relative to KR88, REE-based temperature estimates exhibit both an over- and an underestimation across the temperature range.

Pressure estimates of the REE-based barometer are overestimated in eleven of the seventeen samples, relative to NG85 (Figure 5.5c). In two samples the overestimation in pressure relative to NG85 is by up to 50 kbar. Four samples plot within the 1:1 ±10 kbar envelope and two samples are underestimated relative to NG85.

5.7 FITPLOT paleogeotherm results

To evaluate the contrasting major element thermobarometry results in the Eastern Namaqualand cluster between Group II and Group I kimberlite emplacement, FITPLOT paleogeotherms have been modelled to the P-T array. Crustal thickness was set at 40 km (Durrheim and Mooney, 1994) and heat production in the upper and lower crust at 1.27 and 0.29 $_{i}Wm^{-3}$ (Rudnick and Fountain, 1995), respectively. Temperature and pressure estimates calculated from TA98 and NG85 (Table 5.1) were used as the input dataset for major element thermobarometry, and for those sample

for which either orthopyroxene is absent or was not analysed, and the compositional parameters of Nimis and Grütter (2010) and Ziberna et al. (2016) were satisfied, NT00 data was also included.

Pressure and temperature estimates and the FITPLOT paleogeotherm results from major element-based thermobarometry are illustrated in Figure 5.6a & b. Lithospheric thickness for Eastern Namaqualand at the time of Group II/transitional kimberlite eruptions is calculated to be 200 ±10 km and corresponds to a "diamond window" (the depth interval along the conductive geotherm between the intersections with the diamond-graphite boundary of Day (2012) and the mantle isentrope) of 70 ± 10 km (Figure 5.6a). Most of the PT data cluster around the 40 mW/m^2 model geotherm of Hasterok and Chapman (2011). Lithospheric thickness for Eastern Namaqualand at the time of Group I kimberlite eruptions (Figure 5.6b) is calculated to be 160 ± 15 km and PT data clusters near the 45 mW/m^2 geotherm of Hasterok and Chapman (2011).

At the time of Group I kimberlite eruptions the "diamond window" which was present within Eastern Namaqualand lithosphere, along the south western periphery of the Kaapvaal craton, during Group II/transitional kimberlite eruptions has been entirely removed. The conductive geotherm in this region appears to have re-equilibrated from a "cratonic" 40 mW/m^2 geotherm (after Hasterok and Chapman 2011) at the time of Group II/transitional kimberlite magmatism (140 – 120 Ma), to a higher, 45 mW/m^2 geotherm (after Hasterok and Chapman 2011) at the time of Group I kimberlite magmatism (100 – 80 Ma).

Pressure and temperature estimates calculated from REE-based thermobarometry (Sun and Liang, 2015) and the resulting FITPLOT (Mather et al., 2011) paleogeotherm are illustrated in Figure 5.7. The lithospheric thickness for Eastern Namaqualand is 210 ± 35 km (1 sigma) and the resulting "diamond window"

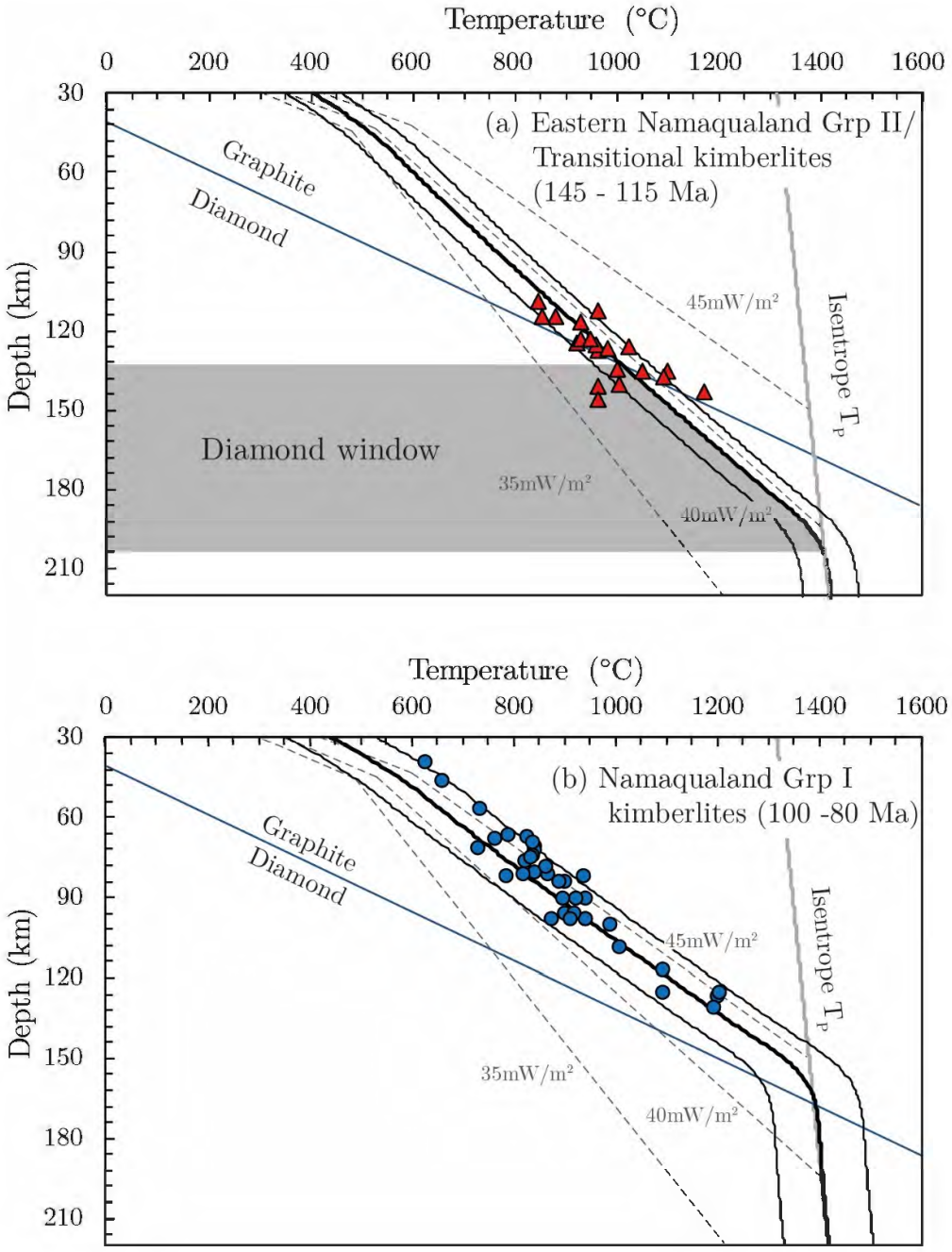

Figure 5.6: Paleogeotherms with error windows (1 sigma) calculated using FITPLOT (Mather et al., 2011) for the lithosphere along the south western periphery of the Kaapvaal craton. PT estimates were calculated after Nickel and Green (1985), Taylor (1998) and Nimis and Taylor (2000). Lithospheric thickness (intersection of the isentrope and the conducting geotherm) for (a) Eastern Namaqualand lithosphere at the time of Group II/transitional kimberlite eruptions is ~200 km, and has a "diamond window" of ~70 km and (b) Eastern Namaqualand at the time of Group I kimberlite eruptions is ~160 km and has no "diamond window". Data sources used for PT calculations are as for Table 5.1. Diamond-graphite transition is from Day (2012). 35, 40 and 45mW/m² geotherms for lithospheric mantle are from Hasterok and Chapman (2011).

(diamond-graphite transition of Day 2012) is 80 ± 35 km (1 sigma) thick. The best-fit geotherm output from FITPLOT clusters nearest to the 40 mW/m² geotherm of Hasterok and Chapman (2011), however, the error window for the resulting FITPLOT geotherm is large (at any given pressure the geotherm error window is 300℃ wide; 1 sigma), and the PT array exhibits large misfit from the FITPLOT geotherm, where the trend produced from the REE-based TP data shows a near vertical geotherm between 800 and 1000℃.

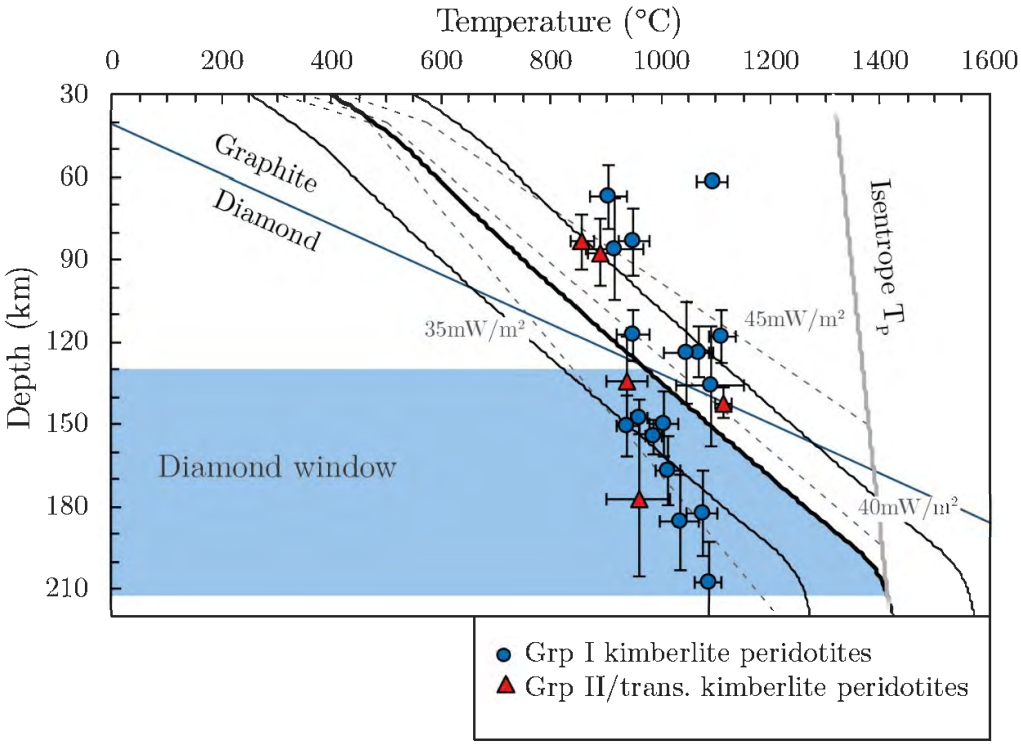

Figure 5.7: Paleogeotherm with error windows (1 sigma) calculated using FITPLOT (Mather et al., 2011) for the Eastern Namaqualand lithosphere along the south western periphery of the Kaapvaal craton. PT estimates with error bars (1 sigma) were calculated after Sun and Liang (2015). Lithospheric thickness is 210 ± 35 km, and the region has a "diamond window" of ~ 80 km. Data used in PT calculations is from this study and le Roex and Class (2016). Diamond-graphite transition is from Day (2012). 35, 40 and 45mW/m² geotherms for lithospheric mantle are from Hasterok and Chapman (2011). Note that PT data for samples exhumed during Group I and Group II/transitional kimberlite magmatism time periods were combined for the FITPLOT input as linear regressions through the datasets are not resolvable within error (c.f. Figure 5.4)

5.8 Summary of thermobarometry results

It has been shown that the TA98 and BKN pyroxene solvus thermometers and the single cpx thermometer NT00 when applied to the peridotite samples investigated in this study display a good correlation across the temperature range. Temperature results for BKN were systematically overestimated relative to TA98, but the overestimation did not exceed 100 ℃ (Figure 5.2). Temperature results obtained by the Fe^{2+} - Mg cpx-garnet thermometer, KR88, display a poor correlation with TA98 and KR88 temperatures are on average 130 ℃ higher than TA98. It is not possible to speculate on the reason for the disagreement between KR88 and TA98 when the influence of Fe^{3+} in both garnet and cpx in the samples investigated here is not known and several studies have shown that inaccurate Fe^{3+} calculation during cpx and garnet stoichiometry, along with the assumption of all Fe being Fe^{2+} in the KR88 formulation and heterogeneity in the oxidation state of continental lithospheric mantle will all significantly influence the accuracy of Fe^{2+} - Mg exchange thermometry (Brey and Kohler, 1990; Luth et al., 1990; Canil and O'Neill, 1996; Mofokeng, 1998; Woodland and Koch, 2003; Woodland, 2009).

Pressure estimates of BKN and NT00 are in good overall agreement with NG85 (Figure 5.3). For NG85 pressures greater than 46 kbar, BKN overestimated pressures relative to NG85, similar to what was found in Nimis and Grütter (2010).

When applied to the peridotites in this study, results obtained through the garnet-cpx REE-based thermobarometer of Sun and Liang (2015) display a large amount of scatter in PT-space. Linear regressions fitted with 95% confidence and prediction intervals suggest that data obtained from Group II/transitional kimberlites cannot be resolved from data obtained from Group I kimberlites (Figure 5.4). Three samples produced pressures greater than 90 kbar (~ 270 km). REE-based temperatures and pressures show a disparity from major element-based results. 35 % of the data

points fall within ± 100 ℃ of the 1:1 correlation with both TA98 (P_NG85) and KR88 (P_NG85; Figure 5.5a & b), and 24 % of the samples fall within ± 10 kbar error window of the 1:1 correlation with pressure estimates from NG85 (T_TA98; Figure 5.5c). The disagreement between major element and REE-based pressures are greater than 40 kbar in two samples, suggesting low accuracy in these results.

Paleogeotherms calculated using FITPLOT (Mather et al., 2011) with major element-based PT estimates suggest that the Eastern Namaqualand lithosphere was ~200 km thick, with a "diamond window" of ~70 km and had a geothermal gradient of 40 mW/m^2 (model geotherm for lithospheric mantle of Hasterok and Chapman 2011) at the time of Group II/transitional kimberlite magmatism (Figure 5.6a). In contrast, at the time of Group I kimberlite magmatism (Figure 5.6b), lithospheric thickness was calculated to be ~160 km with no "diamond window" and the geothermal gradient clusters closer to the 45 mW/m^2 model geotherm of Hasterok and Chapman (2011).

Finally, the FITPLOT (Mather et al., 2011) paleogeotherm calculated using the REE-based thermobarometry results for the samples studied here produces a lithospheric thickness of ~210 km, with a "diamond window" of ~80 km and clusters nearest to the 40 mW/m^2 model geotherm of Hasterok and Chapman (2011). Although the results produce a large amount of scatter in P-T space, with a near vertical geotherm trend, the results from REE-based thermobarometry plot nearest to the Group II/transitional data from major element-based thermobarometry.

6. Discussion

6.1 Validity of REE-based PT estimates with respect to off-craton peridotite xenoliths from the south western periphery of the Kaapvaal craton

A first order observation with respect to the PT estimates obtained from REE-based thermobarometry for the samples studied here is that they produce a steep geothermal gradient which intersects the Moho at an implausible temperature (~750°C), with a large amount of scatter in P-T space which is far greater than that displayed by PT estimates from the conventional thermobarometers (Figure 5.4 & 5.7). For these reasons, the validity of the results and application of the REE-based thermobarometer to the samples studied needs to be investigated.

The REE-based thermobarometer (Sun and Liang, 2015) used in this study is based on REE and Y partitioning between cpx and garnet, which was quantified through a parametrized lattice strain model for cpx-melt (Sun and Liang, 2012) and garnet-melt (Sun and Liang, 2013, 2014) REE and Y partitioning. Sun and Liang (2012) studied REE distribution between cpx and basaltic melt from 43 partitioning experiments to define the influence of pressure, temperature, mineral and melt composition on cpx-melt REE and Y partition coefficients. It was found that REE and Y partitioning in cpx were strongly controlled by Al_2O_3 (X^{T}_{Al} and X^{M1}_{Al}), and MgO (X^{M2}_{Mg}) in cpx. Al^{T} was found to have the greatest influence on REE and Y D_0 (the partition coefficient for strain-free substitution), which was attributed to a charge-balancing substitution of Al and trivalent REE with Si and Ca^{2+} (Sun and Liang, 2012). Whilst X^{M2}_{Mg} and X^{M1}_{Al} were the primary factors found to influence r_0 (The ideal cation size for the lattice site; see section 5.1 above). Sun and Liang (2013, 2014) described garnet-melt REE and Y partitioning through a lattice strain model which principally described X_{Ca}, T and P as the controlling parameters on REE and Y partition coefficients in garnet. Garnet-melt REE partition coefficients were found to

negatively correlate with temperature, pressure and X_{Ca} (c.f. Fig. 6a - d Sun and Liang, 2013). As the influence of melt composition was found to be negligible in the parameterized lattice strain models of Sun and Liang (2012, 2013), Sun and Liang (2014) constructed a mineral-mineral REE and Y partitioning model. Garnet/cpx REE and Y partition coefficients were found to decrease as pressure increased, LREE partition coefficients decreased as temperature decreased, the HREE were found to be insensitive to temperature changes and mineral composition was found to have a strong influence on partitioning, however, the effects of temperature and pressure remained evident within the composition variation studied (c.f. Fig. 4c & d Sun and Liang 2014).

In this section, the relationship between temperature, pressure, mineral stoichiometry and REE content and garnet/cpx D_{REE} will be examined to see how these factors relate to one another in the samples studied here. The aim of this is to establish whether the lattice strain models of Sun and Liang (2012, 2013, 2014) adequately predict REE and Y partitioning between garnet and cpx in these samples with the consequence of their applicability to the REE-based thermobarometer of Sun and Liang (2015).

Only samples which met the equilibrium requirements defined in section 5.3 are used in the analysis below. Temperature and pressure estimates from the preferred thermobarometer combination, TA98 and NG85, are used to assess the influence of mineral composition, temperature and pressure on REE and Y partitioning between garnet and cpx. Problems may arise from temperature and pressure estimates obtained from major element-based thermobarometry as the xenolith samples may record the temperature and pressure at the time of entrainment by the host magma. Major-element based thermobarometry results indicate a lithospheric thermal disturbance southwest of the Kaapvaal craton (Figure 5.6a & b; Bell et al., 2003; Janney et al., 2010) shortly prior to Group I kimberlite magmatism which possibly did not allow for

slower diffusing elements (e.g. the trivalent REE; Van Orman et al., 2001, 2002; Carlson, 2012) to re-equilibrate with the surrounding mantle conditions. However, the chemical zoning which would be predicted from a short-term heating event is not present in the samples studied here.

Ce, Gd, Y and Yb were selected for the purpose of this section, covering the full range of REE and Y whilst avoiding elements which are intrinsically low in either of the two minerals (e.g. La in garnet and Lu in cpx). The four key parameters found to adequately control REE and Y partitioning in garnet and cpx defined by the lattice strain models of Sun and Liang (2012, 2013, 2014) are X^{gt}_{Ca}, $X^{M2,cpx}_{Mg,}$ $X^{M1,cpx}_{Al}$ and $X^{T,cpx}_{Al}$. X^{gt}_{Ca} ranges from 0.3 to 0.55 and shows no apparent correlation with temperature and a weak correlation with pressure (Figure 6.1a & b), suggesting that it is primarily controlled by the bulk composition of the system. $X^{M2,cpx}_{Mg}$ ranges from 0.02 to 0.18, and shows a distinct positive correlation with temperature and pressure (Figure 6.1c & d). The systematics of $X^{M1,cpx}_{Al}$ are more complex than the previously mentioned parameters in that they display moderate correlations in only the Group I samples. There is no obvious correlation between temperature and $X^{M1,cpx}_{Al}$ in the cpx associated with Group II/transitional kimberlite magmatism ($R^2 = 0.095$; Figure 6.1e). Cpx from Group I kimberlites display a broad range in $X^{M1,cpx}_{Al}$ versus temperature with a weak positive correlation with temperature ($R^2 = 0.226$; Figure 6.1e). Cpx from peridotites from Group II/transitional kimberlites shows no correlation between $X^{M1,cpx}_{Al}$ and pressure ($R^2 = 0.019$), and appears to be controlled by bulk composition whereas cpx associated with Group I kimberlite magmatism displays a broad, positive correlation ($R^2 = 0.293$) between $X^{M1,cpx}_{Al}$ and pressure (Figure 6.1f). $X^{T,cpx}_{Al}$ ranges from 0.01 to 0.55 and shows a broad negative correlation with both temperature and pressure (Figure 6.1g & h); this suggests that $X^{T,cpx}_{Al}$ is controlled by bulk composition, pressure and temperature.

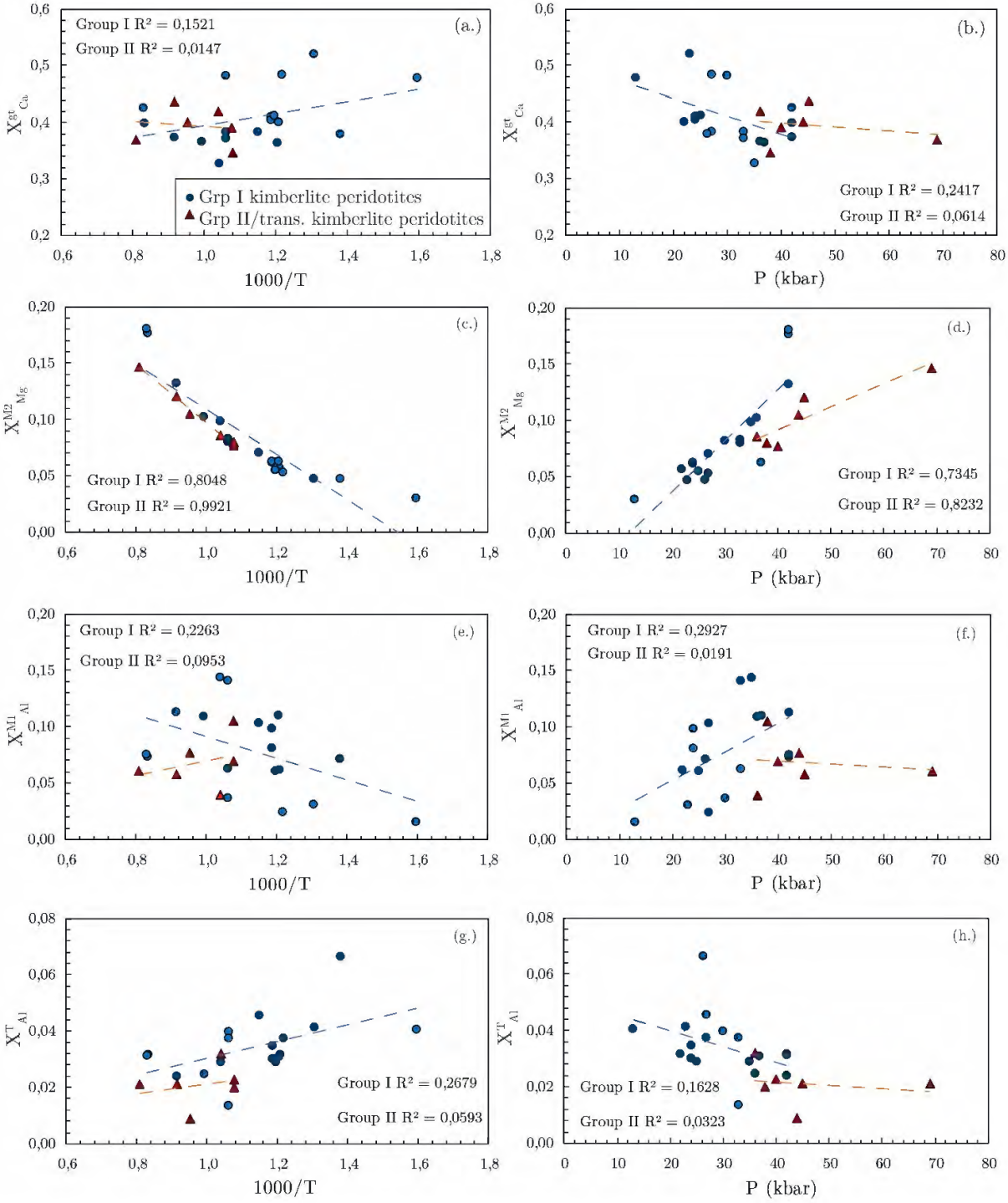

Figure 6.1: Variation in 1000/T (TA98; ℃) and P (NG85; kbar) with key site occupancy variables involved in REE partitioning between garnet and cpx identified in the lattice strain models of (Sun and Liang, 2012, 2013, 2014).

The Ce contents in cpx range from 4 to 52 (ppm) and from <0.1 and 0.84 (ppm) in garnet (Figure 6.2a). There is a good correlation between the Ce content of garnet and X^{gt}_{Ca} (R^2 = 0.326 – 0.618) and a weak correlation between the Ce content of cpx and $X^{M2,cpx}_{Mg}$ and $X^{M1,cpx}_{Al}$ (Figure 6.2b – d). No apparent correlation is evident between Ce in cpx and $X^{T,cpx}_{Al}$ (Figure 6.2e). D_{Ce} (D_i = (concentration of element i in garnet)/(concentration of element i in cpx)) is weakly correlated with temperature (R^2 = 0.215 – 0.278; Figure 6.2f). The samples exhumed during Group I kimberlite magmatism display a broad positive correlation between D_{Ce} and pressure (R^2 = 0.247; Figure 6.2g); There is a poor correlation between D_{Ce} and pressure in the samples exhumed during Group II/transitional kimberlite magmatism (R^2 = 0.170). With the exception of one sample, D_{Ce} in the samples exhumed during Group II/transitional kimberlite magmatism is positively correlated with $X^{T,cpx}_{Al}$ (Figure 6.2g). The samples exhumed during Group I kimberlite magmatism show no dependence of D_{Ce} on $X^{T,cpx}_{Al}$. No correlation is evident between D_{Ce} and X^{gt}_{Ca}, $X^{M1,cpx}_{Al}$ and $X^{M2,cpx}_{Mg}$ (not shown).

Gd in cpx ranges from 0.2 to 4 (ppm) and from 0.2 to 7 (ppm) in garnet (Figure 6.3a). Cpx typically contains slightly more Gd than garnet. There is a weak correlation between Gd in garnet and X^{gt}_{Ca} (R^2 = 0.139 – 0.207; Figure 6.3b). Gd in cpx displays no apparent correlation with $X^{M2,cpx}_{Mg}$ (Figure 6.3c). Gd in peridotitic cpx from Group I kimberlites display a broad positive correlation with $X^{M1,cpx}_{Al}$ (R^2 = 0.435; Figure 6.3d) and Gd in cpx associated with Group II/transitional kimberlite magmatism shows no apparent correlation $X^{M1,cpx}_{Al}$. No clear correlation is noted across the entire sample suite between Gd in cpx and $X^{T,cpx}_{Al}$ (Figure 6.3e). D_{Gd} does not show any correlation with temperature (Figure 6.3f) or pressure (not shown), and no clear correlation is observed with any of the key major element parameters (e.g. Figure 6.3g & h).

Y in cpx ranges from 0.2 to 4 (ppm) and in garnet ranges from 2 to 31 (ppm) (Figure 6.4a). Y in garnet shows weak negative correlation with X^{gt}_{Ca} (Figure 6.4b).

Y in cpx exhibits a weak correlation with $X^{T,cpx}_{Al}$ (Figure 6.4c); there is no correlation between Y in cpx and $X^{M1,cpx}_{Al}$ and $X^{M2,cpx}_{Mg}$ (not shown). There is a positive correlation between D_Y and X^{gt}_{Ca} in samples from Group I kimberlites ($R^2 = 0.498$; Figure 6.4d), and a weak correlation between D_Y and temperature (Figure 6.4e), pressure (Figure 6.4f), and the other key major element parameters (not shown).

Yb contents in cpx range from <0.05 to 0.32 (ppm) and from 0.5 to 11 (ppm) in garnet (Figure 6.5a). Yb in garnets associated with Group II/transitional kimberlite magmatism is negatively correlated with X^{gt}_{Ca} ($R^2 = 0.812$), however, no correlation is apparent in garnets associated with Group I kimberlite magmatism ($R^2 = 0.08$; Figure 6.5b). There is no apparent correlation between Yb in cpx and $X^{M2,cpx}_{Mg}$ and a positive correlation between Yb in cpx from Group I kimberlites and $X^{M1,cpx}_{Al}$ ($R^2 = 0.581$; Figure 6.5c & d). No trend is evident between Yb in cpx from Group I kimberlites and $X^{T,cpxAl}$, whereas a there is a positive correlation in cpx from Group II/transitional kimberlites ($R^2 = 0.738$; Figure 6.5e). D_{Yb} shows a weak correlation with X^{gt}_{Ca} (Figure 6.5f), $X^{M2,cpx}_{Mg}$, $X^{M1,cpx}_{Al}$, $X^{T,cpx}_{Al}$ (not shown), temperature ($R^2 = 0.302 – 0.339$; Figure 6.5g) and pressure ($R^2 = 0.306$ in Group I and 0.004 in Group II/transitional; Figure 6.5h).

REE and Y concentrations in garnet are weakly correlated with X^{gt}_{Ca}. This is in agreement with the lattice strain model of Sun and Liang (2013) and the finding of several other studies (e.g. Gibson et al., 2008; Girnis et al., 2013) that found REE and Y substitution to be largely dependent on Ca contents in the X-cation site of garnet. The effects of temperature and pressure dependent REE and Y partitioning in garnet produced by Sun and Liang (2013) are not reproduced by the samples studied here. Similarly, Girnis et al. (2013) did not identify a temperature or pressure dependence on REE and Y partitioning in the garnets produced in silico-carbonate systems.

The partitioning of REE and Y in cpx is relatively well correlated with the key parameters identified by Sun and Liang (2012). The poor correlations between $X^{T,cpx}_{Al}$ and cpx REE concentrations suggest that the prominent influence of $X^{T,cpx}_{Al}$ involved in charge balance substitution with the REE and Y (Gaetani and Grove, 1995; Lundstrom et al., 1998; Hill et al., 2000) is less important in the samples studied here, suggesting that charge balance may have been satisfied via another mechanism.

There is some indication in samples exhumed during Group II/transition kimberlite magmatism that $X^{T,cpx}_{Al}$ strongly influences D_{Ce} partitioning between garnet and cpx. Among the HREE, minimal compositional effects on mineral-mineral partitioning were noted. Whereas for all other elements there are minimal effects of composition on $D_{REE\&Y}$ between garnet and cpx display minimal influence. The influence of temperature and pressure on $D_{REE\&Y}$ is not immediately evident in the data presented here, it is possible that the importance of crystal chemistry overrides the influence of pressure and temperature or that competing effects between crystal chemistry and temperature and pressure in minimises the influence on variation in $D_{REE\&Y}$ as either variable shifts the parabola in an opposing direction on the Onuma diagram. Although REE and Y substitution in garnet and cpx is reasonably well defined via the key major element parameters identified by Sun and Liang (2012, 2013), the behaviour of the mineral-mineral lattice strain model (Sun and Liang, 2014) fails to describe the variation in $D_{REE\&Y}$ noted in the samples studied here. Thermobarometric equations aim to describe systems of interest in the simplest manner possible whilst maintaining the accuracy of the predicted outcome. The sub-trends present between samples exhumed during Group II/transitional kimberlite magmatism and those exhumed during Group I kimberlite magmatism, as well as the overall scatter in the plots, suggest that localised perturbations of energy and/or mass transfer (such as infiltration by metasomatic fluids or melts) may have affected the composition of the mantle samples studied.

Xenoliths entrained by kimberlites frequently display chemical signatures consistent with interaction with silico-carbonate melts at depth (e.g. Pearson and Wittig, 2008; Shu and Brey, 2015; Giuliani et al., 2016; le Roex and Class, 2016; Tappe et al., 2017; Bussweiler et al., 2018). The lattice strain models used in the REE-based thermobarometer assumes that the mineral of interest is crystallizing in equilibrium with a silicate/basaltic melt where isolated silicate tetrahedra are linked by metal cations (Wood and Blundy, 1997). Whereas, silico-carbonate melts exhibit melt stoichiometry which differ from pyroxene structural units in that silicate tetrahedra are less dominant and many metal cations are linked by $[CO_3]^{2-}$ and $[SiO_4]^{4-}$ groups and therefore mineral-melt partitioning cannot be adequately described by such models (Yaxley and Green, 1998; Hammouda et al., 2009). The experimental studies of trace element partitioning between silico-carbonate melts and silicate minerals of Hammounda et al. (2009) and Girnis et al. (2013) found that cpx-melt partitioning was not adequately described by models calibrated on silicate melts free of CO_2. Additionally, the predicted garnet-melt REE partition coefficients calculated from lattice strain models calibrated against CO_2-free silicate systems were systematically higher than the observed variations in silico-carbonate systems (Dasgupta et al., 2009; Hammouda et al., 2009; Girnis et al., 2013), due to the large temperature effect prescribed in the predictive models of garnet and silicate melts (Draper and van Westrenen, 2007), which is not present in partitioning experiments between garnet and silico-carbonate melts (Girnis et al., 2013). Thus, it is necessary to consider that the uncertainties in REE derived PT data are the result of a metasomatic event(s) by carbonate-bearing melts.

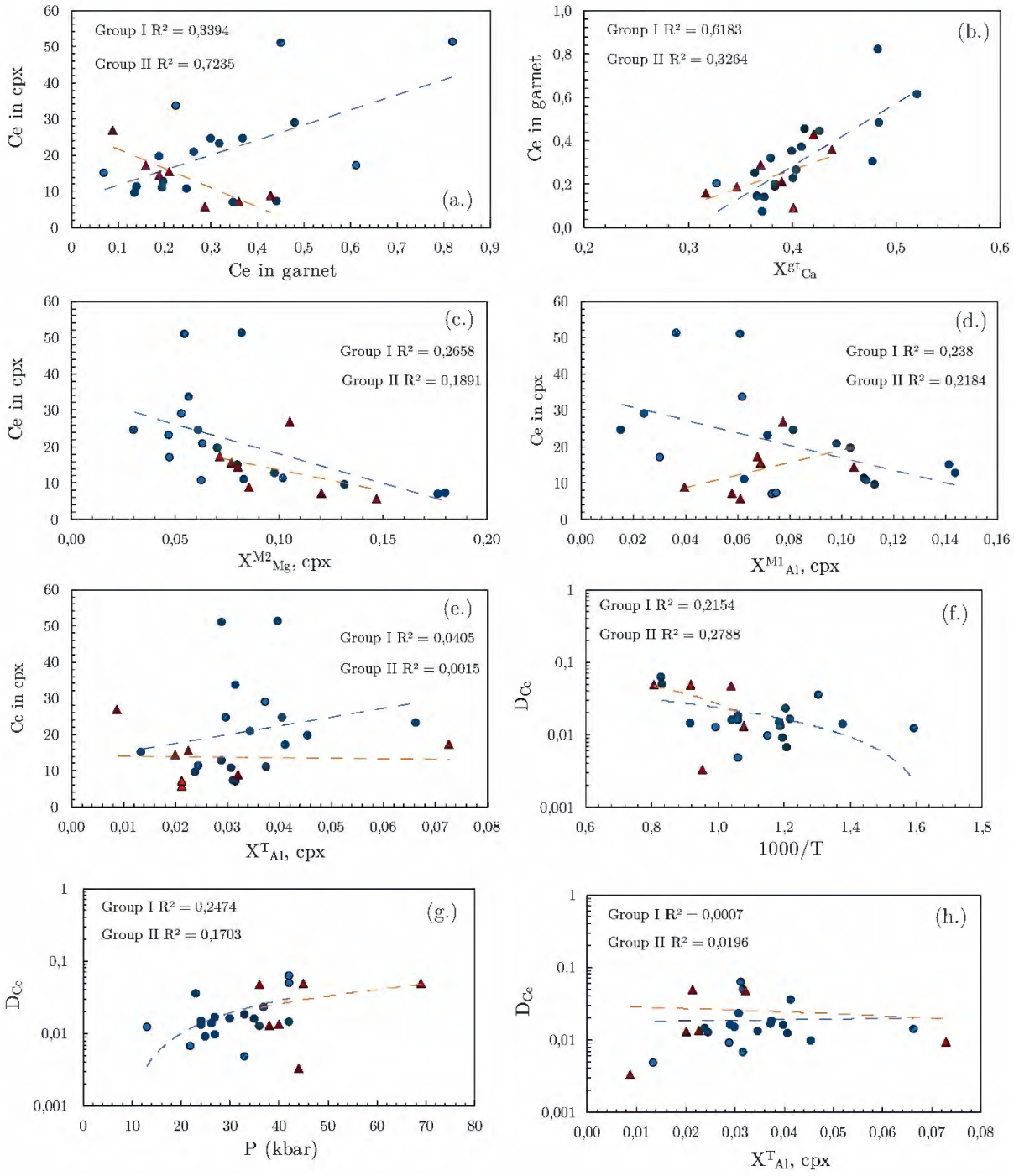

Figure 6.2: Variation Ce (ppm) in garnet and cpx and D_{Ce} (garnet/cpx) with key site occupancy variables and 1000/T (TA98; ℃) and P (NG85; kbar). Symbols as for Figure 6.1.

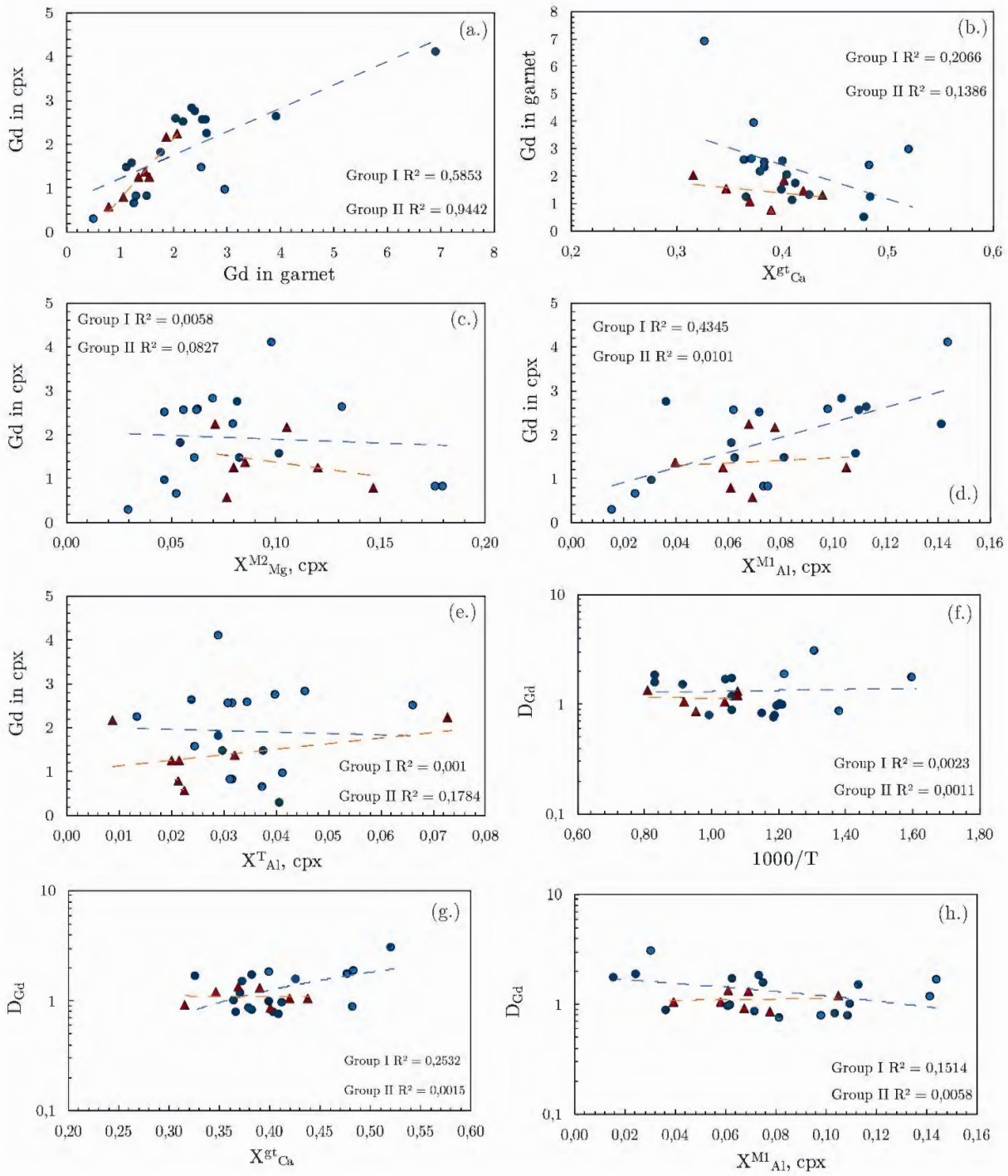

Figure 6.3: Variation in Gd (ppm) in garnet and cpx and D_{Gd} (garnet/cpx) with key site occupancy variables and 1000/T (TA98; ℃). Symbols as for Figure 6.1.

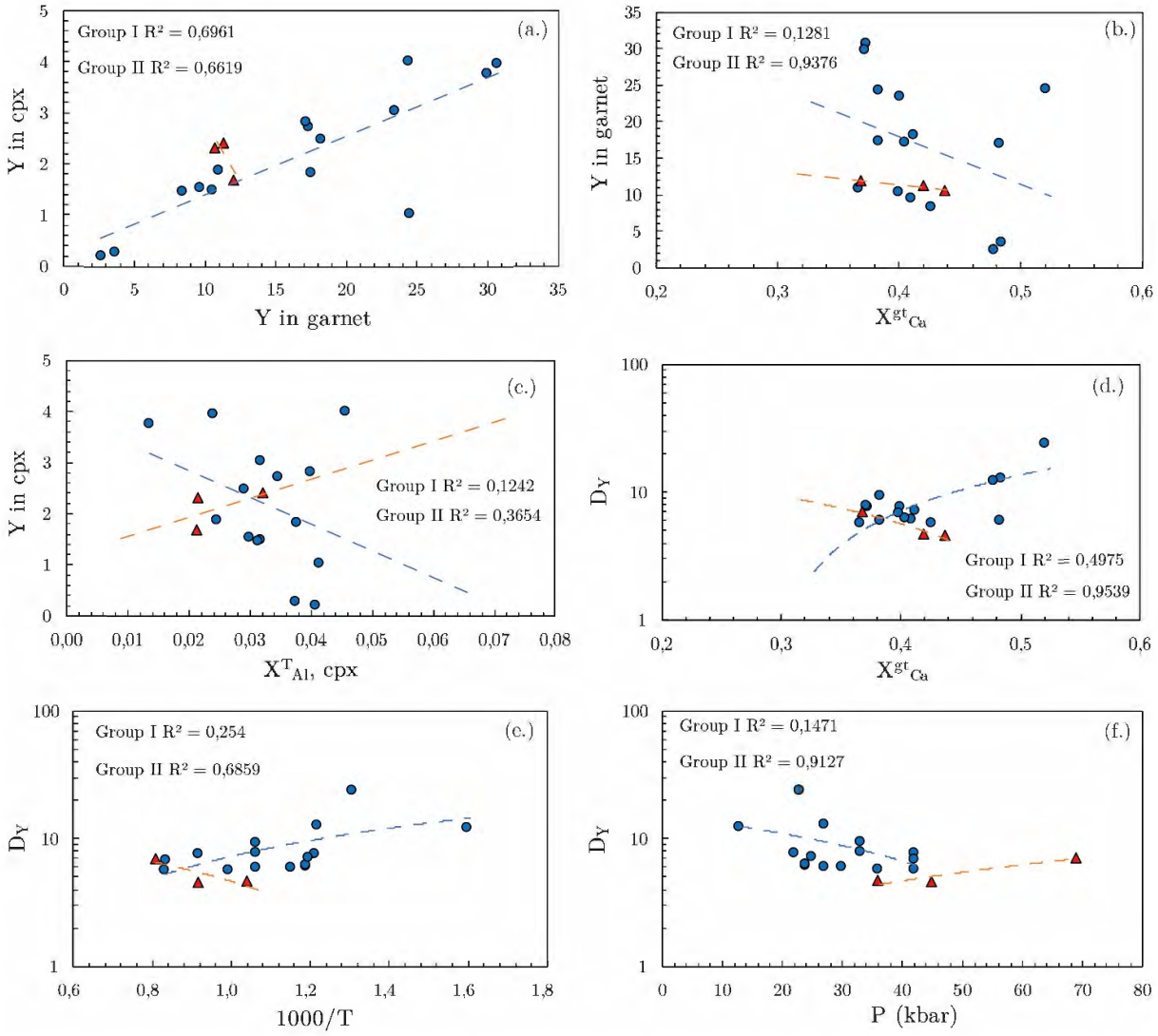

Figure 6.4: Variation in Y (ppm) in garnet and cpx and D_Y (garnet/cpx) with key site occupancy variables and 1000/T (TA98; ℃) and P (NG85; kbar). Symbols as for Figure 6.1.

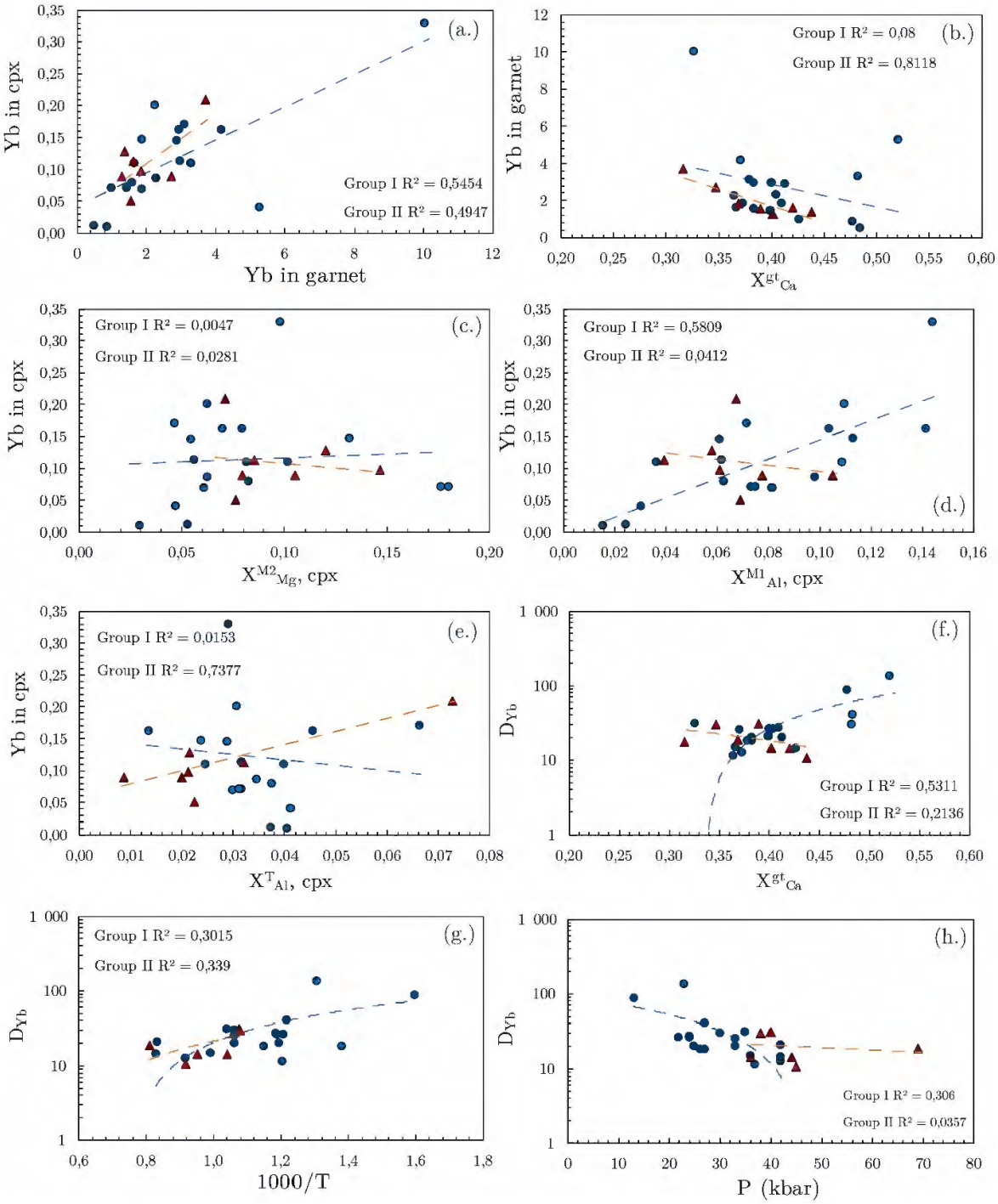

Figure 6.5: Variation in Yb (ppm) in garnet and cpx and D_{Yb} (garnet/cpx) with key site occupancy variables and 1000/T (TA98; ℃) and P (NG85; kbar). Symbols as for Figure 6.1.

6.2 Metasomatism

Trace element abundances in the constituent minerals in mantle xenoliths can be used to determine the nature of secondary processes occurring at depth, prior to kimberlite eruption. Metasomatism is frequently prescribed to account for the chemical and mineralogical signatures of mantle xenoliths and diamond inclusions from the Kaapvaal craton and surrounding Proterozoic lithosphere (e.g. Gregoire et al., 2003; Griffin et al., 2003b; Simon et al., 2007; Kobussen et al., 2008, 2009; Shu and Brey, 2015; le Roex and Class, 2016; Giuliani, 2018; Weiss et al., 2018).

The garnets in the peridotite xenoliths investigated here display a range of garnet REE patterns which could indicate several possible metasomatizing agents or a single agent occurring at varying melt-rock ratios (Figure 4.3). The mode of garnets with "normal" REE patterns fall at lower Cr-numbers than those displaying sinusoidal and humped patterns (Figure 6.6a) indicates that the "normal" garnets are derived from mantle that has experienced lower degrees of melt extraction (Griffin et al., 1999a). However, there is no discernible linear relationship between the degree of sinuosity or slope in MREE to HREE patterns and bulk rock composition inferred from garnet Cr-number (Figure 6.6b), suggesting that the variation in garnet REE patterns was independent of the degree of primary depletion during lithosphere formation. There is no correlation between REE styles and temperature or pressure (not shown).

Garnets that exhibit "normal" REE patterns span the widest range of Ti contents, but 90% of the samples have low Zr contents of less than 50 ppm (Figure 4.3b). In the Y versus Zr discrimination diagram of Griffin et al. (1999b) nearly 60% of the "normal" garnets fall within the melt metasomatized space, with the remaining 40% falling at higher Y contents, either transitional to or falling within the undepleted field (Figure 4.3d). Experimental work on carbonated melts in equilibrium with

garnets has shown that in a carbonate melt system garnet will fractionate Ti from Eu and Zr from Hf, producing a high Zr/Hf and low Ti/Eu signature (Dasgupta et al., 2009; Girnis et al., 2013). Zr/Hf and Ti/Eu systematics can be used to distinguish carbonatitic metasomatism (typified by high Zr/Hf and low Ti/Eu ratios) from silicate metasomatism, such as kimberlitic or basaltic melts (typified by lower Zr/Hf and high Ti/Eu; Yaxley et al., 1991; Shu and Brey, 2015). "Normal" garnets from the samples studied here fall within both the carbonatitic metasomatism field of high Zr/Hf and low Ti/Eu and the kimberlitic/silicate metasomatism field of low Zr/Hf and high Ti/Eu (Figure 4.3f).

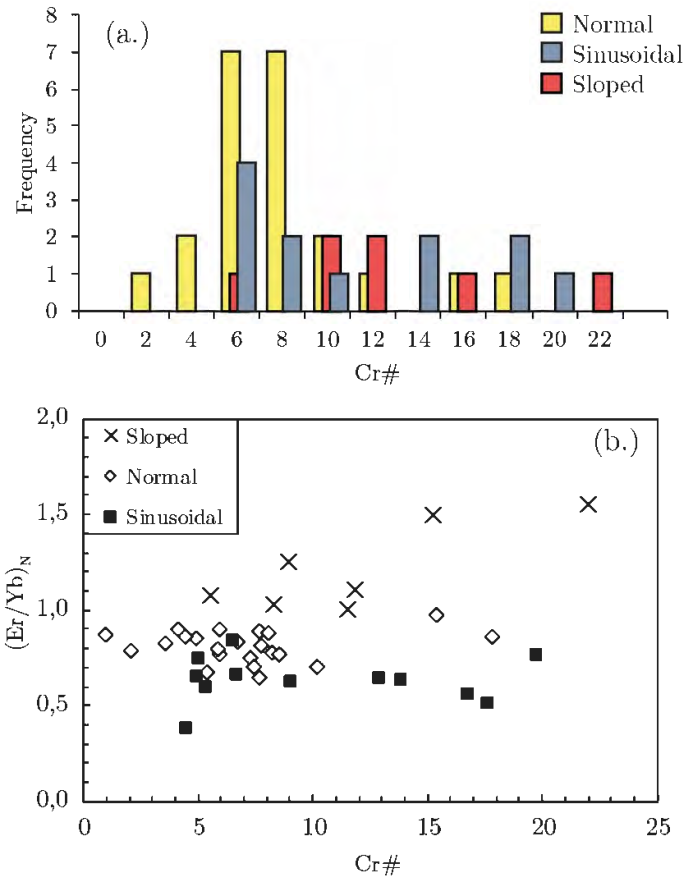

Figure 6.6: (a) Histogram showing frequency distribution of Cr-number (100Cr/(Cr + Al) in garnet with samples plotted by garnet REE style and (b) Cr-number versus $(Er/Yb)_N$ in garnet.

Sinusoidal garnets span a wide range of Y contents at relatibely low Zr (<45 ppm), falling mainly in the melt metasomatized (44%) and depleted (31%) fields (Figure 4.3b & d). One sinusoidal garnet plots within the low temperature metasomatized field of Griffin et al, (1999b). Similar to the "normal" garnets, sinusoidal garnets plot along both the carbonatitic metasomatism trend of low Ti/Eu and high Zr/Hf and the kimberlitic metasomatism trend high Ti/Eu and low Zr/Hf (Figure 4.3f).

The samples that exhibit sloped REE trends plot furthest along the melt metasomatism trend of Griffin et al, (1999b) in Zr-Y space, consistent with higher melt-rock ratios (Figure 4.3d). The higher average Cr-number in sloped garnets may reflect a higher degree of depletion in these samples compared to those with "normal" REE trends, consistent with lower modal garnet and a greater susceptibility to metasomatism with increasing modal cpx. Garnets with sloped REE patterns are distinct in having low Ti contents (<850 ppm) and high Y (>15 ppm) and Zr contents (>60 ppm), giving them the lowest average Ti and highest average Y an Zr contents of any garnet group in the samples studied here. The sloped garnet samples have superchondritic Zr/Hf and subchondritic Ti/Eu ratios (Figure 4.3f) and plot along the carbonatitic metasomatism trend defined by Yaxley et al, (1991) and Shu and Brey (2015).

Most of the garnets plot within, or close to, the 'melt metasomatism' field of Griffin et al, (1999b) in the Y versus Zr diagram (Figure 4.3d), suggesting that their signatures were established at varying degrees of melt-rock ratios. This contrasts with what is commonly found in harzburgitic garnets from cratonic settings which predominantly plot within the 'depleted peridotitic garnet' field, consistent with very low degrees of melt metasomatism (e.g. Stachel and Harris, 2008; Shu and Brey, 2015). The fact that a higher proportion of the off-craton peridotitic garnets in this study fall in the melt metasomatism field compared to harzburgitic cratonic garnets may be

due to the solidus of lherzolite + H_2O (+ CO_2) being crossed at lower temperature for a given pressure in PT space than that of the harzburgite + H_2O + CO_2 solidus (c.f. Fig 6a Weiss et al., 2018). The Zr/Hf versus Ti/Eu diagram provides a more descriptive distinction of the nature of the metasomatizing agent which affected the samples. Garnets exhibiting both "normal" and sinusoidal REE patterns fall along the trends for carbonatitic and kimberlitic/basaltic metasomatism (Figure 4.3f). However, a clearer distinction of the metasomatic history of the samples is evident when grouped by locality rather than by garnet REE patterns (Figure 4.3a, c & e). Samples exhumed during Group II/transitional kimberlite magmatism plot predominantly within the field of silicate/kimberlitic metasomatism and display higher Ti contents, whereas samples exhumed during Group I kimberlite magmatism plot predominantly along the trend for carbonatitic metasomatism and display lower Ti contents (Figure 4.3a & e). The cpx trace element data for the samples studied here display a similar pattern where cpx samples exhumed during the Group II/transitional kimberlite magmatism pulse predominantly fall along the kimberlite/silicate metasomatism trend in the $(La/Yb)_N$ versus Ti/Eu space of Coltorti et al. (1999), and cpx samples exhumed during the Group I kimberlite magmatism pulse exhibit low Ti/Eu ratios and moderate to high $(La/Yb)_N$ ratios, more consistent with a carbonatitic-style metasomatism (Figure 6.7).

Kobussen et al. (2008, 2009) presented a set of garnet xenocryst data from 33 Group II/transitional and 29 Group I kimberlites which erupted along a transect running from the Namaqua-Natal mobile belt southwest of the Kaapvaal Craton to the north eastern portion of the Bushveld Igneous Complex. These authors found that peridotitic garnet xenocrysts from Group I kimberlites that erupted along the south western margin of the Kaapvaal craton and the neighbouring Proterozoic NNP exhibited distinctly elevated Ti, Fe and Zr in comparison to garnet xenocrysts from Group II/transitional kimberlites. These observations were interpreted to be the result

of metasomatism by mafic melts which were linked to the thermal disturbance noted in prior thermobarometry studies to have occurred in the study region (Bell et al., 2003; Kobussen et al., 2008, 2009). In contrast to the findings of Kobussen et al. (2008, 2009), the chemical compositions of garnets from the peridotite xenoliths investigated in this study do not display a distinct change in composition consistent with metasomatism by mafic melts shortly prior to Group I kimberlite magmatism and are more consistent with metasomatism by carbonatitic melts.

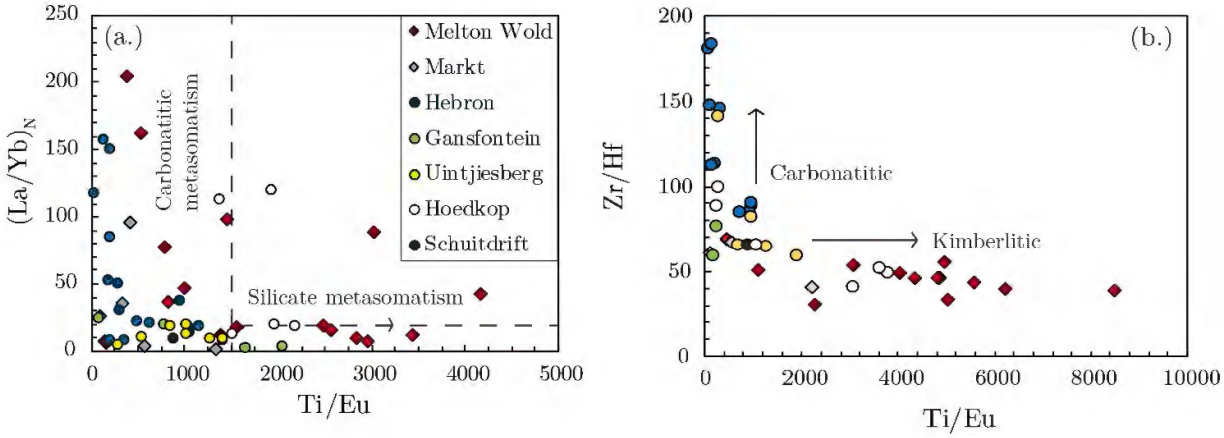

Figure 6.7: (a) $(La/Yb)_N$ versus Ti/Eu in peridotitic cpx and (b) diagram of Zr/Hf versus Ti/Eu in garnet from peridotite xenoliths shown for ease of comparison to the cpx trend. Samples exhumed during the Group II/transitional kimberlite magmatism pulse (~140 – 120 Ma) are plotted as diamonds and samples exhumed during the Group I kimberlite magmatism pulse (100 – 80 Ma) are plotted as circles. Data sources as for Figure 4.4. Compositional trends for (a) are from Coltorti et al. (1999). Compositional trends for carbonatitic and kimberlitic metasomatism in (b) as for Figure 4.3.

However, when plotted here, the distinct elevation in Ti (Figure 6.8b) and Fe (not shown) for garnet xenocrysts from Group I kimberlites is not evident in the data presented in (Kobussen et al., 2008, 2009). In Zr-Y space, both Group II and Group I xenocrysts plot predominantly within the melt metasomatism field of Griffin et al. (1999b). In Zr/Hf versus Ti/Eu space, the xenocryst data from Group I kimberlites plot at low Ti/Eu, more consistent with a carbonatitic style of metasomatism (Figure 6.8f), consistent with the peridotitic xenolith data presented in this study (Figure 6.8a – f).

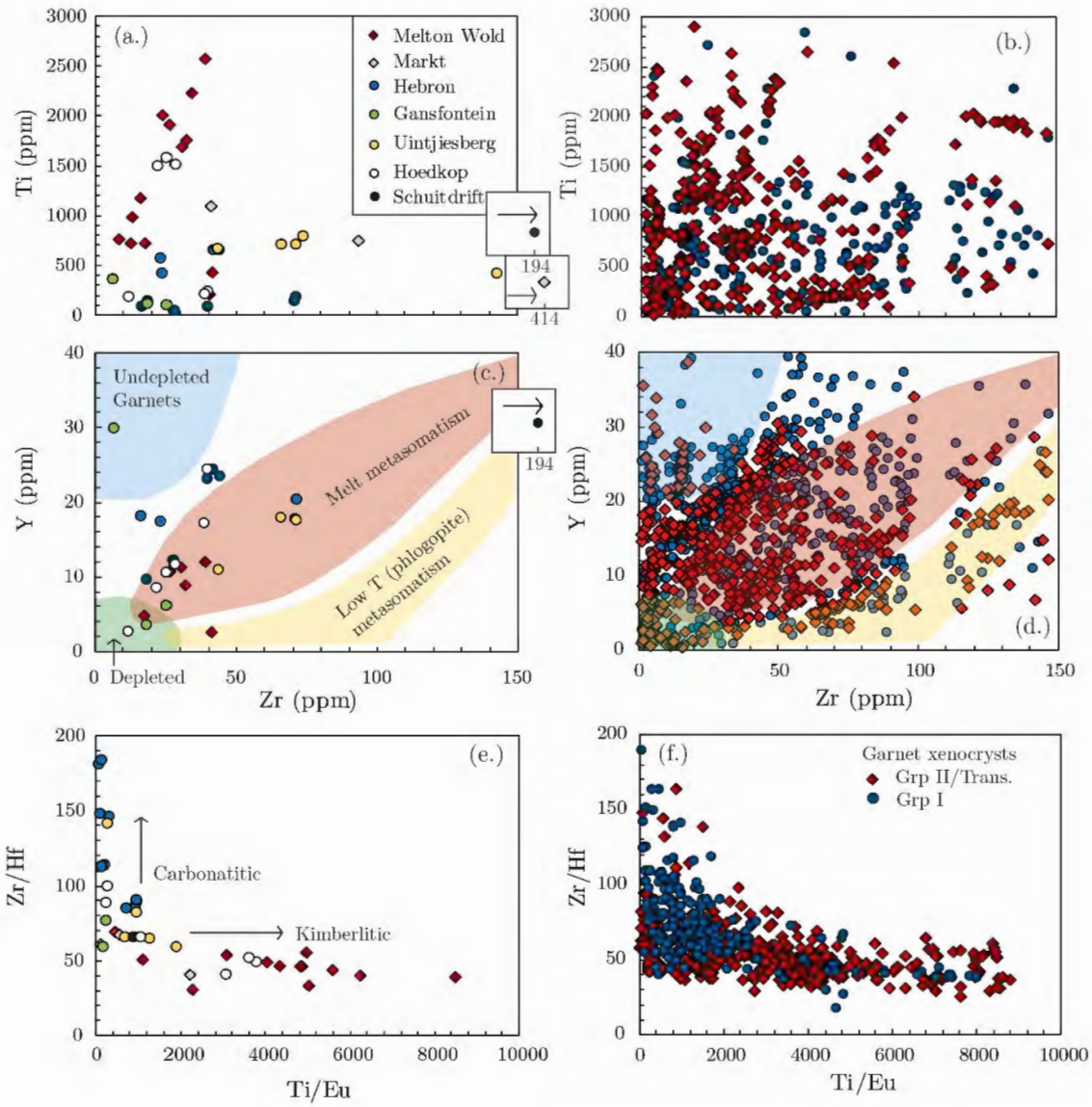

Figure 6.8: Comparison of garnet trace element chemistry for peridotitic garnets from this study (a), (c), & (e) and garnet xenocryst data (b), (d) & (f) for Group I kimberlites Hebron and Uintjiesberg (blue circles) and Group II/transitional kimberlites Melton Wold and Markt (red diamonds) from Kobussen et al. (2008, 2009).

6.3 Melt composition from modelled peridotitic garnet and cpx

Using the partition coefficients of Girnis et al. (2013; reported in Table 6.1) and trace element concentrations in garnet and cpx, the compositions of the melts in equilibrium with garnet and cpx were calculated. Girnis et al. (2013) experimentally

calculated partition coefficients for a large set of trace elements between mantle minerals and silico-carbonate melts at 6 – 12 GPa and 1300 – 1700℃. Fields for Group I southern African kimberlites (light grey) are plotted in all primitive mantle normalized and CI chondrite normalized diagrams for comparative purposes. Where the data exists for the host kimberlite, these are plotted as the dark grey fields on the respective plots. Although the experimental conditions used in the study of Girnis et al. (2013) are at the high range of pressures and temperatures for mantle xenoliths, they were selected for use because they provide an internally consistent set of partition coefficients for both cpx and garnet and, for the majority of the elements, they account for variations in major element composition.

Since partitioning is largely controlled by the composition of the system, as well as melt fraction, pressure and temperature, caution should be applied when making interpretations based on the calculated compositions of equilibrium melts. Given the uncertainties, in the discussion below greater emphasis will be placed on the general patterns of the calculated melt compositions rather than on the magnitude of individual elemental abundances or anomalies.

CI chondrite-normalized REE and primitive mantle-normalized incompatible element patterns of the melts in equilibrium with garnet are plotted in Figure 6.9 and Figure 6.10, respectively. The REE patterns for melts in equilibrium with garnet display depletion in the heavy REE relative to the MREE and LREE (Figure 6.9a – g). For the majority of the localities there is good overlap between the calculated melt in equilibrium and the host kimberlite and/or southern African Group I kimberlites. The melts in equilibrium display a general trend of progressive enrichment in the LREE from melts associated with garnets with sinusoidal REE patterns to melts associated with garnets with sloped and “normal” REE patterns. Several samples display staggered REE trends in the LREE which may be an artefact of the

intrinsically low concentrations of LREE in garnet because of which, any errors in garnet D values or concentrations will be amplified.

Table 6.1: Partition coefficients used to calculate melts in equilibrium with garnet and cpx of (Girnis et al., 2013).

Element	$\mathbf{D^{Gt\text{-}melt}}$	$\mathbf{D^{Cpx\text{-}melt}}$
Rb	0,002	0,002
Ba	0,0002	0,001
Th		
U		
Nb	0,0008	0,0002
Ta	0,002	$0.00013\exp(55.67Al^{T})$
La	0,0005	0,003
Ce	$0.000085\exp(24.8X^{gt}_{Ca})$	$0.0042\exp(22.9Al^{T})$
Pb	0,0003	$0.028\exp(-12.35Al^{T})$
Sr	0,0008	$0.069\exp(-3.614Na)$
Nd	$0.00039\exp(29.23X^{gt}_{Ca})$	$0.0099\exp(20.28Al^{T})$
Sm	$0.0019\exp(28.45X^{gt}_{Ca})$	$0.023\exp(16.63Al^{T})$
Zr	$0.04\exp(16.49X^{gt}_{Ca})$	$0.00044\exp(46.5Al^{T} + 27.4Na)$
Hf	$0.037\exp(20.24X^{gt}_{Ca})$	$0.00042\exp(53.2Al^{T} + 36.5Na)$
Eu	$0.0037\exp(28.33X^{gt}_{Ca})$	$0.025\exp(17.5Al^{T})$
Ti		
Gd	$0.0052\exp(30.17X^{gt}_{Ca})$	$0.03\exp(17.89Al^{T})$
Tb	$0.0126\exp(27.05X^{gt}_{Ca})$	0,04
Dy	$0.0149\exp(30.50X^{gt}_{Ca})$	$0.044\exp(15.42Al^{T})$
Y	$0.0450\exp(21.93X^{gt}_{Ca})$	$0.046\exp(16.25Al^{T})$
Er	$0.0338\exp(30.37X^{gt}_{Ca})$	$0.056\exp(16.2Al^{T})$
Yb	$0.0712\exp(29.01X^{gt}_{Ca})$	$0.06\exp(16.01Al^{T})$
Pr	$0.00013\exp(31.47X^{gt}_{Ca})$	$0.0061\exp(21.42Al^{T})$
Ho	$0.0309\exp(27.13X^{gt}_{Ca})$	0,05
Tm	$0.052\exp(29.14X^{gt}_{Ca})$	0,06
Lu	$0.0973\exp(27.68X^{gt}_{Ca})$	$0.073\exp(12.57Al^{T})$

Al^{T} is the fraction of Al in the tetrahedral site of pyroxene, Na is number of atoms in pyroxene formula on a 6-oxygen basis. X^{gt}_{Ca} = Ca/(Ca + Mg + Fe).

Primitive mantle-normalized incompatible element diagrams for the melts in equilibrium with garnet display sub-parallel trends within each locality, consistent with localized melts of related composition interacting with the samples at each locality. Prominent negative anomalies in Sr, Zr and Hf are present in the melts in equilibrium with garnets from Hebron, Uintjiesberg, Gansfontein and Hoedkop (Figure 6.10a -d). Negative anomalies in Zr and Hf are also present in the melts in equilibrium with garnets from Melton Wold and Markt (Figure 6.10f & g), however these are less pronounced. There is a very good correlation between the patterns of the calculated melts in equilibrium with garnet and the fields for the host kimberlite and/or southern African Group I kimberlites, suggesting an intimate link to carbonated silicate melts.

CI chondrite-normalized REE and primitive mantle-normalized incompatible element patterns of the calculated melts in equilibrium with cpx are plotted in Figure 6.11 and Figure 6.12, respectively. CI chondrite normalized REE patterns for the melts in equilibrium with cpx are enriched in the LREE relative to MREE and HREE (Figure 6.11a – g). The REE patterns of the melts in equilibrium at each locality are subparallel and resemble the patterns for the host kimberlites and/or southern African Group I kimberlites.

Primitive mantle normalized incompatible element diagrams have negative Pb, Zr and Hf anomalies and several localities display a large degree of fractionation in Ta (Figure 6.12a – g). The overall patterns of the incompatible element diagrams for the melts in equilibrium with cpx have similar patterns to the host kimberlite and/or southern African Group I kimberlites and are well correlated with the melts calculated to be in equilibrium with the garnets studied here.

All the calculated equilibrium melts have overall LREE-enriched patterns resembling kimberlitic melts, consistent with silico-carbonate metasomatism at depth. This is in agreement with the findings of le Roex and Class (2016) who provided

evidence through trace element modelling for reactive porous flow of carbonated melts reacting with the surrounding lithosphere to account for the range in trace element signatures noted in peridotitic garnet and cpx from the Eastern Namaqualand kimberlites.

The resemblance of the calculated equilibrium melts to southern African Group I kimberlites and the trace element characteristics discussed in section 6.2 above indicate that the Eastern Namaqualand mantle experienced varying degrees of metasomatism by silico-carbonate melts. These results, combined with the scatter in REE-based thermobarometry and garnet-cpx REE partitioning suggest that the uncertainties in REE-based thermobarometry and mineral-mineral REE partitioning in carbonate-bearing melts render them inaccurate for use in the samples studied here.

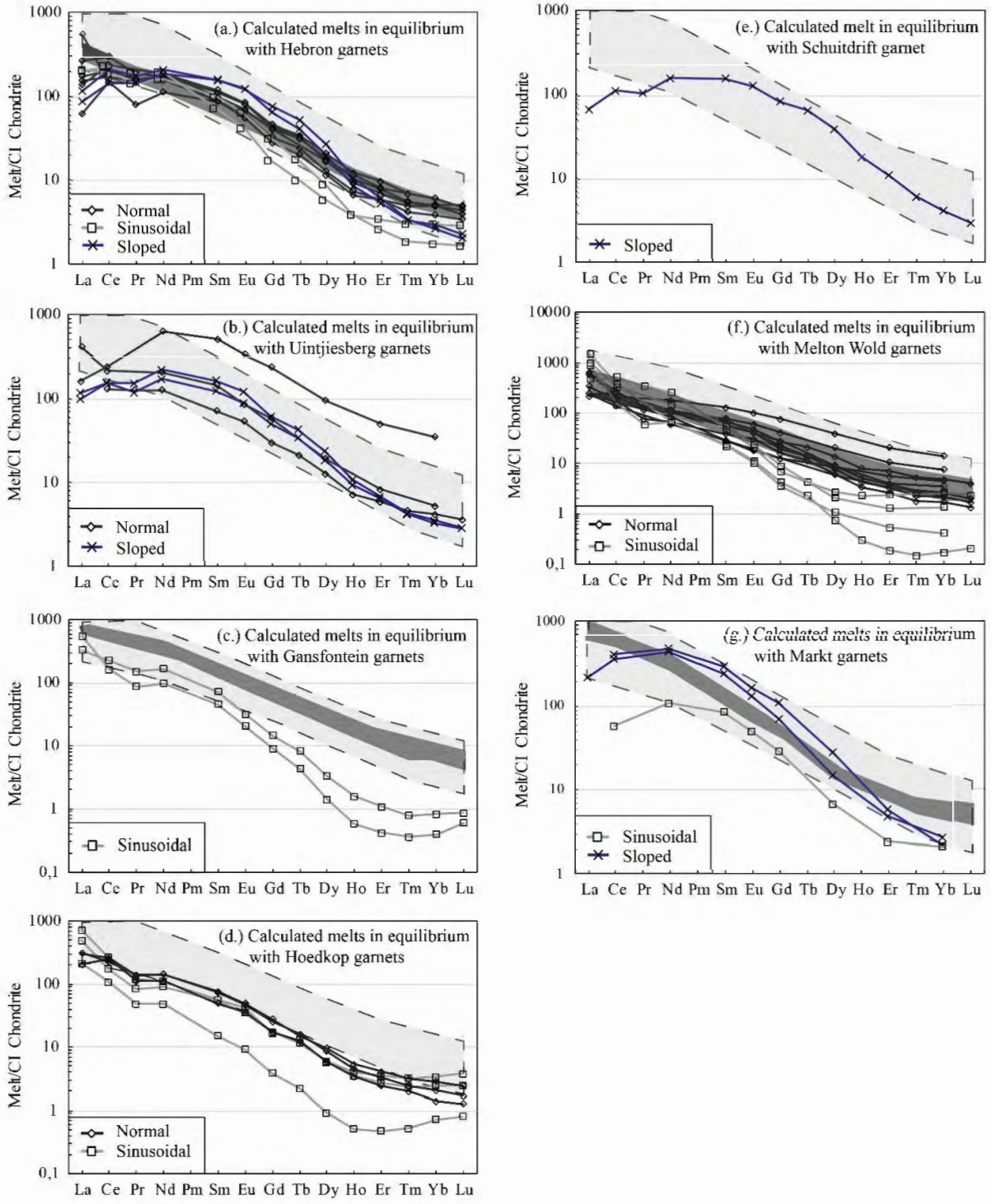

Figure 6.9: CI chondrite-normalized (McDonough and Sun, 1995) *REE patterns for calculated melts in equilibrium with peridotitic garnet (a – g). Partition coefficients for garnet-carbonated melt of Girnis et al. (2013). Light grey field represents southern African Group I kimberlites and dark grey field (where present) represents the host kimberlite* (Becker and Le Roex, 2006). *Symbols represent the garnet REE pattern.*

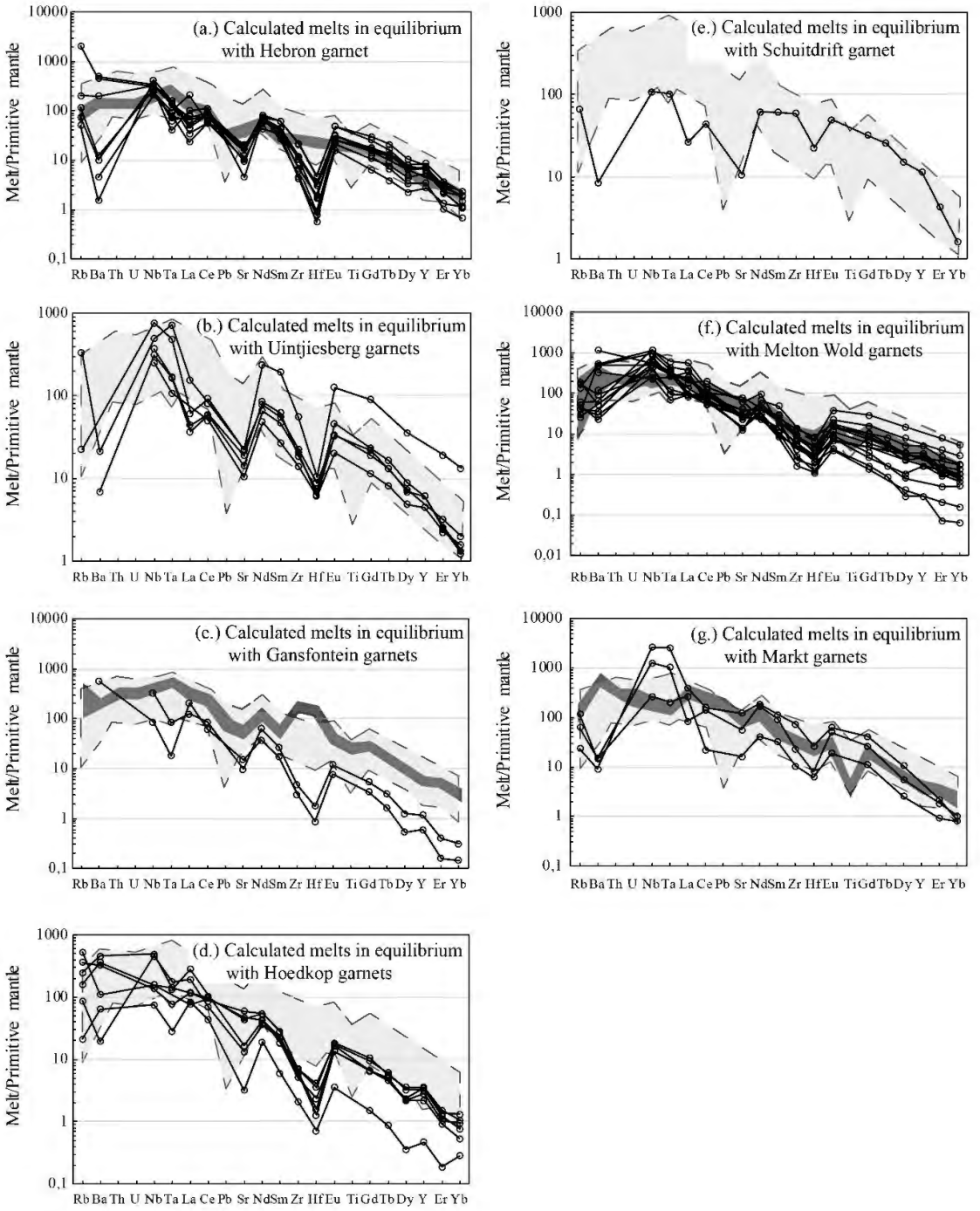

Figure 6.10: Primitive mantle-normalized (McDonough and Sun, 1995) *incompatible element patterns for calculated melts in equilibrium with peridotitic garnet (a – g). Partition coefficients for garnet-carbonated melt of Girnis et al. (2013). Light grey field represents southern African Group I kimberlites and dark grey field (where present) represents the host kimberlite* (Becker and Le Roex, 2006).

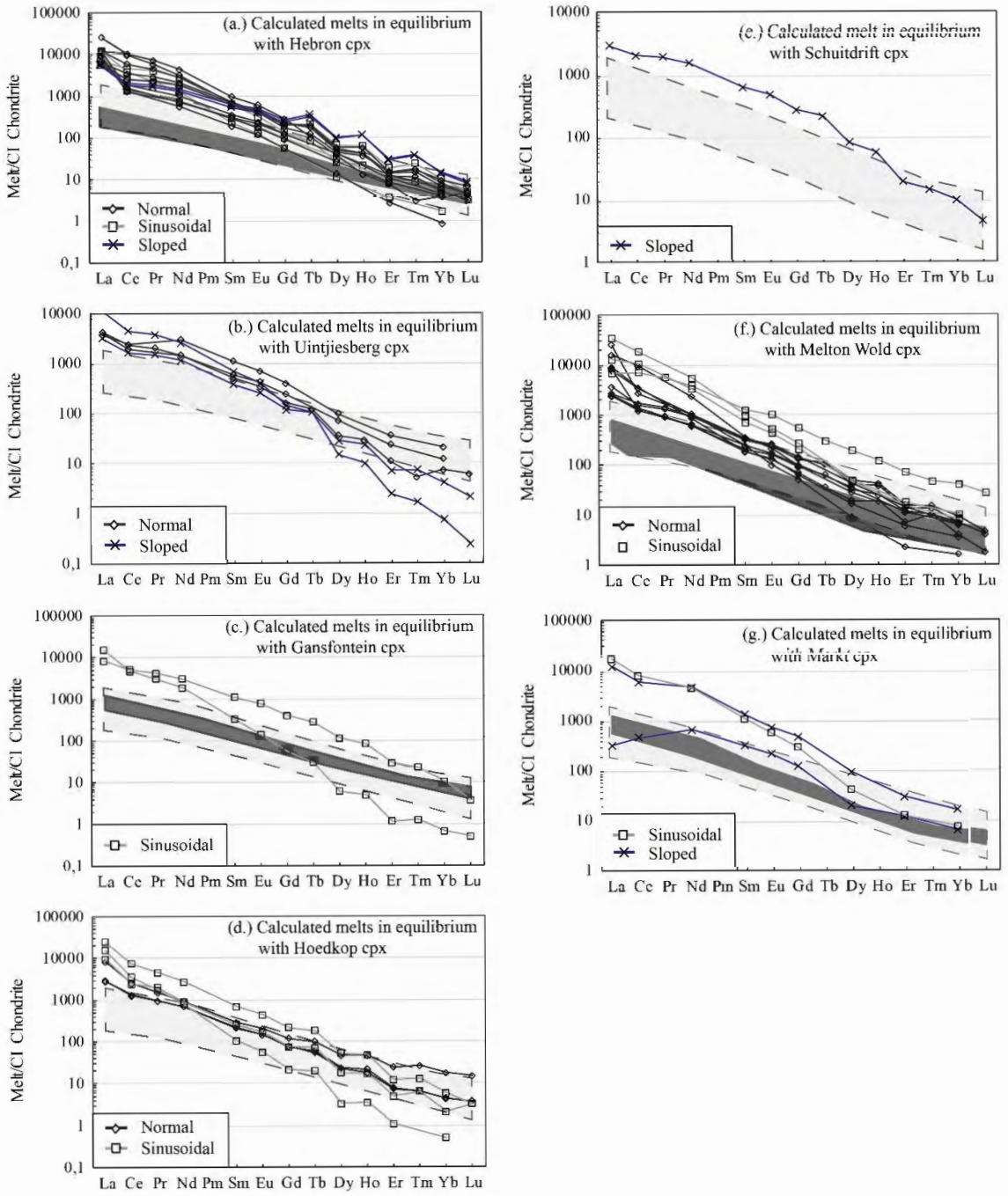

Figure 6.11: CI chondrite-normalized (McDonough and Sun, 1995) *REE patterns for calculated melts in equilibrium with peridotitic cpx (a – g). Partition coefficients for garnet-carbonated melt of Girnis et al. (2013). Light grey field represents southern African Group I kimberlites and dark grey field (where present) represents the host kimberlite* (Becker and Le Roex, 2006). *Symbols represent the REE pattern of garnet in the associated sample.*

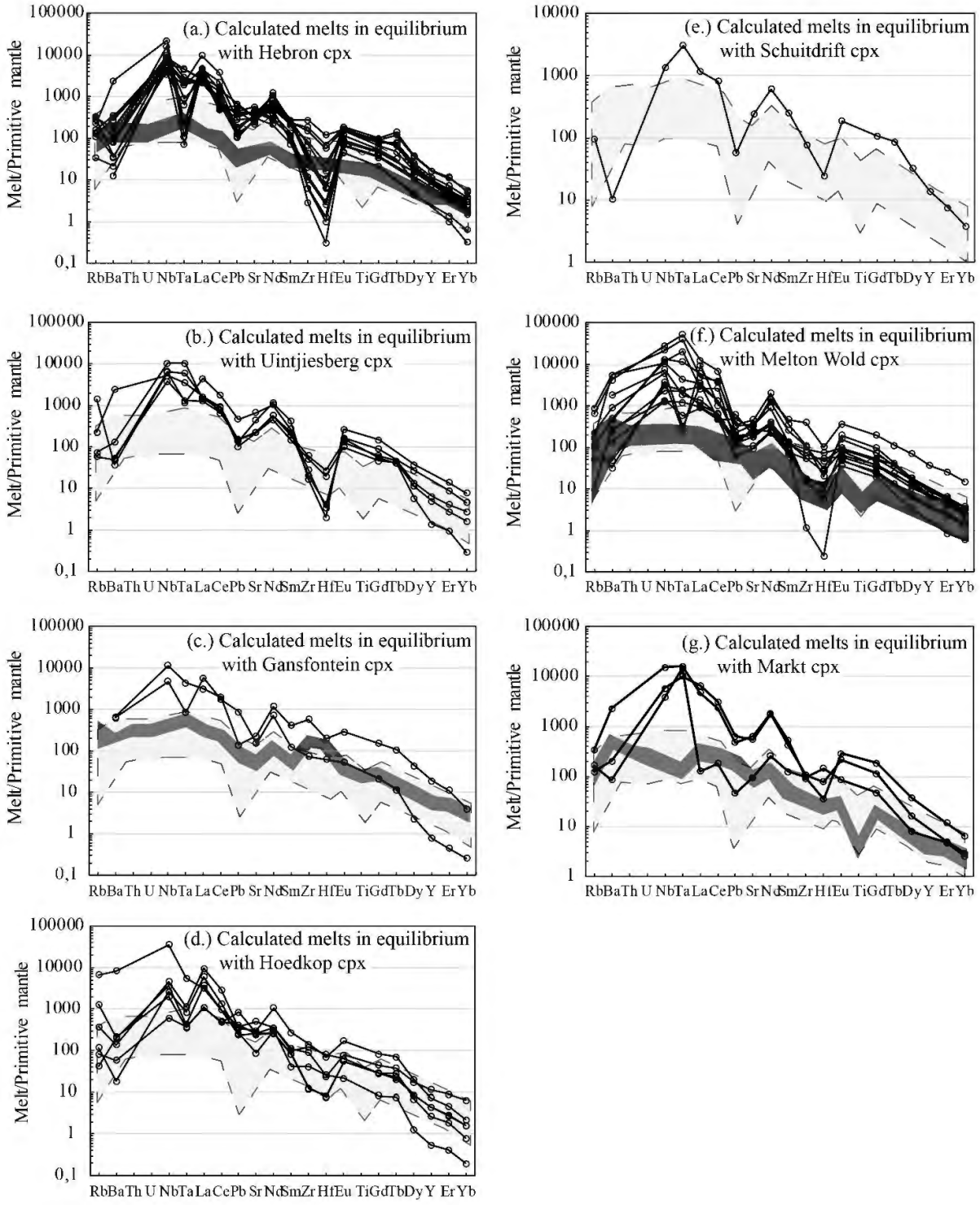

Figure 6.12: Primitive mantle-normalized (McDonough and Sun, 1995) *incompatible element patterns for calculated melts in equilibrium with peridotitic cpx (a – g). Partition coefficients for garnet-carbonated melt of Girnis et al. (2013). Light grey field represents southern African Group I kimberlites and dark grey field (where present) represents the host kimberlite* (Becker and Le Roex, 2006).

6.4 Thermal evolution

Peridotite xenoliths from the Proterozoic NNP, southwest of the Kaapvaal craton document two distinct, temporally constrained thermal states in the off-craton lithosphere. The Group II/transitional Markt and Melton Wold kimberlites which erupted 145 – 115 Ma record an average geotherm (40 mW/m^2 model geotherm for lithospheric mantle of Hasterok and Chapman, 2011) calculated from major element-based thermobarometry resembling that of the Kaapvaal craton lithosphere (Figure 5.6a; Bell et al., 2003; Janney et al., 2010), whereas peridotites from younger 100 – 80 Ma Group I kimberlites display a distinctly shallower geotherm with a higher thermal gradient (~45 mW/m^2 model geotherm for lithospheric mantle of Hasterok and Chapman, 2011), consistent with geophysical evidence for thinner than cratonic lithosphere (Fouch et al., 2004; Priestley et al., 2006; Globig et al., 2016). Although the results from REE-based thermobarometry exhibit a large amount of scatter in P-T space, the geothermal gradient and lithospheric structure determined from FITPLOT more closely resembles cratonic thermal regimes (Figure 5.7). This thermal evolution appears to be distinct for the Eastern Namaqualand region, as a near-cratonic geotherm is recorded in xenoliths exhumed by ~72 Ma Group I kimberlites in the Proterozoic Rehoboth Province to the north (Boyd et al., 2004; Mather et al., 2011; Shiimi, 2017), whereas older (150 – 200 Ma) Group I kimberlites in East Griqualand, southeast of the Kaapvaal craton, record warm conditions similar to those of the xenoliths from Group I kimberlites in Eastern Namaqualand (Bell et al., 2003; Janney et al., 2010). The temporal pattern of this lithosphere-scale thermal perturbation is consistent with the temporal pattern of Gondwana breakup around the margin of southern Africa (i.e., the opening of the Indian Ocean at ~160 Ma in the southeast, followed by the opening of the south Atlantic Ocean along the west coast at ~120 Ma), possibly in conjunction with the 182 Ma Karoo and ~135 Ma

Parana-Etendeka flood basalts (Bell et al., 2003; de Wit, 2007; Kobussen et al., 2008, 2009; Janney et al., 2010).

The calculated FITPLOT paleogeotherms for samples exhumed during the Group II/transition kimberlite peak (150 – 130 Ma) suggest that a thick, cool, lithospheric mantle, capable of hosting diamond, was present within the Eastern Namaqualand region of the Proterozoic NNP prior to the Mesozoic Group I kimberlite eruptions (100 – 70 Ma; Figure 6.13). The mantle geotherm calculated from xenoliths from the Group II/transitional kimberlites Melton Wold and Markt strongly suggests that the lithosphere was ~ 200 km thick with a "diamond window" of ~ 70 km thickness. At the time of Group I kimberlite magmatism the geotherm calculated from xenolith data indicates that the lithosphere may have experienced thinning and heating subsequent to Group II/transitional kimberlite magmatism. The lithosphere was ~ 160 km thick and the "diamond window" was completely removed by the time of Group I kimberlite magmatism (Figure 6.13).

The mantle geotherm at the time of Group II/transitional kimberlite magmatism corresponds to a 40mW/m^2 surface heat flow (Figure 6.13; Hasterok and Chapman, 2011). This is significantly cooler than the geotherm at the time of Group I kimberlite magmatism, which corresponds to 45 mW/m^2 surface heat flow (Hasterok and Chapman, 2011). The depths of samples from Melton Wold and Markt indicate that the kimberlite predominantly sampled xenoliths within the graphite stability field (Figure 5.6a), with only a minor subset of the samples having pressure estimates which fall within the diamond stability field. These results indicate that the peridotite xenoliths sampled by the Group II/transitional Eastern Namaqualand kimberlites were predominantly graphite-stable with only a minor proportion of the samples being diamond-stable, and is consistent with field observations which found these kimberlites to be of low economic importance with minor populations of micro-diamonds (Robey, 1981).

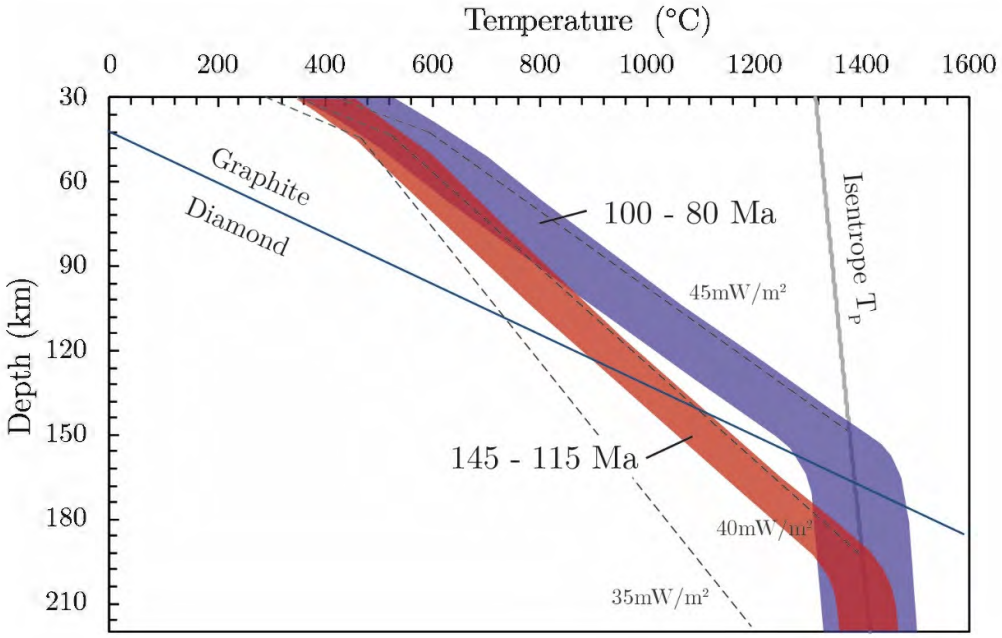

Figure 6.13: Comparison of fitted paleogeotherms calculated using FITPLOT (Mather et al., 2011) *for the Eastern Namaqualand lithosphere at the time of Group II/transitional kimberlite magmatism (145 – 115 Ma) illustrated by the pink field and at the time of Group I kimberlite magmatism (100 – 80 Ma) illustrated by the purple field. The field encompass the 1 sigma error windows. Paleogeotherms were fitted to the major element based thermobarometry results (T_TA98 and P_NG85; Table 5.1). Diamond-graphite transition is from* Day (2012). *35, 40 and 45 mW/m² geotherms for lithospheric mantle are from* Hasterok and Chapman (2011).

There is strong evidence from both the Group I kimberlite xenolith geotherm fitted in this study (Figure 5.6b) and present-day geophysics estimates that the Eastern Namaqualand lithosphere is 150 – 160 km thick (Fouch et al., 2004; Priestley et al., 2006; Globig et al., 2016) and corresponds to an elevated surface heat flow (~45 mW/m²) in comparison to the "cooler" geotherm at the time of Group II/transitional kimberlite magmatism. The timing of the heating and thinning event in the lithospheric mantle sampled by the Eastern Namaqualand Group I kimberlites is synchronous with (U-Th)/He dates for unroofing along the southern African Plateau, onshore fission track analyses and coastal sediment accumulation south of the plateau (de Wit, 2007; Tinker et al., 2008; Stanley et al., 2013). (U-Th)/He data suggest that between the time of Group II kimberlite magmatism and 100 Ma, the Eastern Namaqualand region experienced ~ 800 m of erosion, followed by an additional 1000

– 1500m of erosion by 74 Ma (Stanley et al., 2013; Wildman et al., 2017). Thermochemical thinning of the lithosphere may result in surface uplift (e.g. Hoggard et al., 2016 and references therein), and the intimate temporal constraints of Mesozoic unroofing, coastal sediment accumulation and lithospheric thinning shortly prior to Group I kimberlite magmatism in southern Africa suggests that Mesozoic surface uplift along the southern African Plateau may be linked to mantle-driven processes (de Wit, 2007; Tinker et al., 2008; Stanley et al., 2013).

To investigate the possible contribution to Mesozoic uplift along the southern African Plateau caused by lithospheric thinning the magnitude of air-loaded isostatic uplift was calculated. The air-loaded isostatic uplift, U_l is calculated using equation (2) from Klöcking et al. (2020):

$$U_l = \frac{\alpha T_0}{2(1-\alpha T_0)}\left[\Delta z + \frac{z_c(z_1 z_c - \Delta z)}{z_1 - \Delta z} - \frac{z_c(z_1 - z_c)}{z_1}\right]$$

Where α is the thermal expansivity of mantle material (3×10^{-5}; Hoggard et al., 2016), $T_0 = 1300$ ℃ is the background temperature of the asthenosphere (Hoggard et al., 2016), ΔZ is the amount of lithospheric thinning (calculated here as the thickness of the lithosphere at the time of Group I kimberlite magmatism subtracted from the thickness of the lithosphere at the time of Group II/transitional kimberlite magmatism), Z_l is the original lithospheric thickness (calculated as the thickness of the lithosphere are the time of Group II/transitional kimberlite magmatism) and Z_c is crustal thickness (40 km; Durrheim and Mooney, 1994). The calculation for air-loaded isostatic uplift shows that the uplift associated with lithospheric thinning is 0.7 km, which accounts for a significant proportion of the observed uplift from (U-Th)/He data.

6.5 Melt extraction and depth of melting

Due to the influence of both cryptic and modal metasomatism in the mantle, the whole rock compositions of highly and moderately incompatible elements in

peridotite xenoliths may be susceptible to secondary processes which preclude their use in estimating the primary conditions in the mantle. Olivine Mg-number compositions have been shown to be particularly insensitive to modal metasomatism, possibly providing the most robust signature in estimating the degree of melt extraction (Pearson and Wittig, 2008, 2014). Bernstein et al. (2006) and Pearson and Wittig (2008) have shown that the relationship between olivine Mg-number and the extent of melt extraction from phase equilibria studies provides a relatively robust estimate of the degree of melt extraction experienced in cratonic mantle. The mode of olivine Mg-number for the Eastern Namaqualand xenoliths is 91.5 which translates to 30% melt extraction at 3 GPa and 22% melt extraction at 7 GPa when projected on to Figure 11 of Pearson and Wittig (2008).

The compatibility of HREE in garnet and the resulting "garnet signature" in melts has long been used as an indicator of the depth at which melting occurred in the mantle (Hirschmann, 1996). The application of this has been extended to estimating the depth of melting in cratonic xenoliths, as the differences in the HREE signature of residues of melting in the spinel field are substantially different to residues of melting in the garnet field (Simon et al., 2007; Pearson and Wittig, 2008, 2014; Wittig et al., 2008; Lazarov et al., 2012). It is important to note that the complexity of processes occurring during lithosphere formation such as possible high pressure melting beyond the "garnet out" point, thermal fluctuations, uplift, burial and secondary metasomatic introduction of peridotitic cpx and garnet may hinder the use of these minerals for determining original melt extraction histories (Simon et al., 2007; Aulbach, 2012). The high modal abundance of garnet at high pressure provides further opportunity in utilizing HREE abundances in the residue as the relationship between Lu and Yb is sensitive to both depth and the extent of melting in that residues of high pressure (7 GPa) melt extraction evolve in the opposite direction to residues of

low pressure (3 GPa) melt extraction (Lu is fractionated from Yb when melting occurs in the spinel stability field; Wittig et al., 2008).

Figure 6.14 and 6.15 show CI chondrite normalized reconstructed whole-rock REE patterns for peridotite xenoliths from the Eastern Namaqualand kimberlites with the compositional trends for non-modal fractional melting in the garnet (solid black lines) and spinel (dashed black lines) stability fields compiled by Lazarov et al. (2012). The results show that for all the samples shown in this study, the reconstructed HREE patterns of the whole rocks indicate that melt extraction took place in the spinel stability field. Furthermore, Lu-Yb systematics of the reconstructed whole-rock concentrations show fractionation of Lu from Yb and project along the trend of low-pressure polybaric melting consistent with melting in the spinel stability field (Figure 6.16; Wittig et al., 2008).

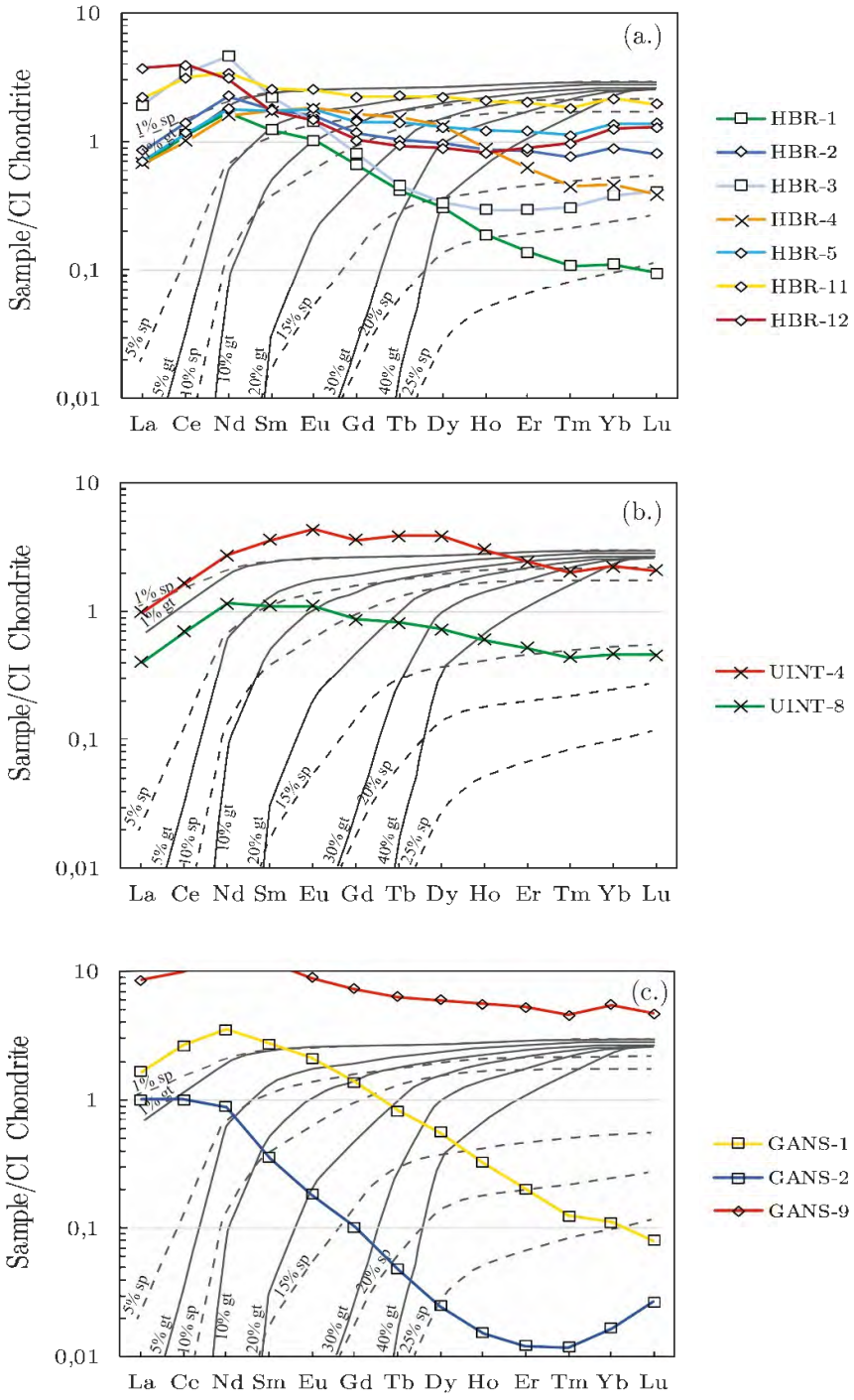

Figure 6.14: CI chondrite-normalized REE patterns for reconstructed whole-rocks calculated from the relative proportions of garnet and clinopyroxene for (a) Hebron, (b) Uintjiesberg and (c) Gansfontein. Samples associated with "normal" garnet REE patterns are indicated by diamond symbols, sinusoidal by square symbols and sloped by cross symbols. Samples illustrated in red are websterites UINT-4 (b) and GANS-9 (c). Non-modal fractional melting curves for melting in the garnet (solid black lines) and spinel (dashed black lines) fields after (Lazarov et al., 2012).

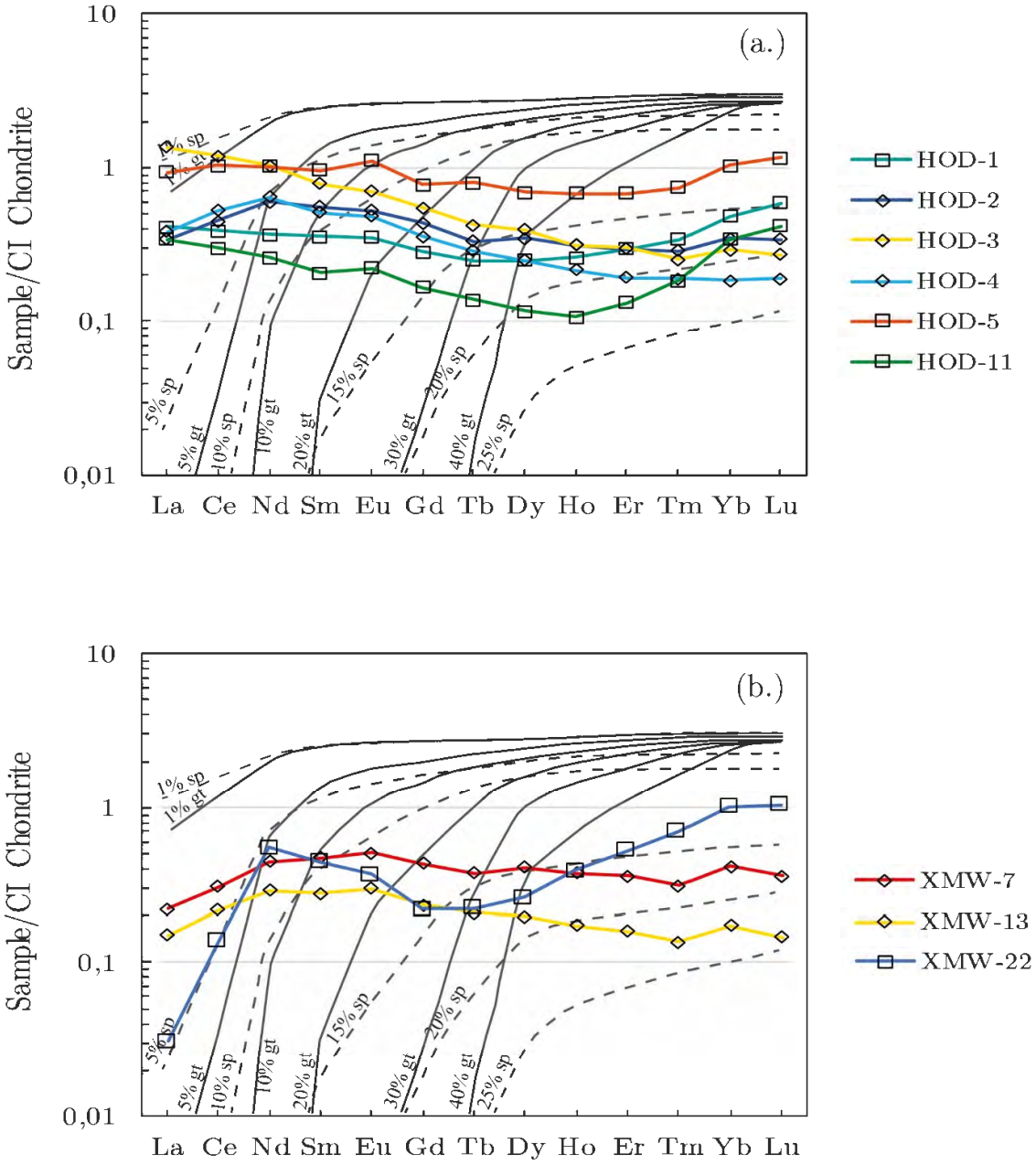

Figure 6.15: CI chondrite-normalized REE patterns for reconstructed whole-rocks calculated from the relative proportions of garnet and clinopyroxene for (a) Hoedkop and (b) Melton Wold. Samples associated with "normal" garnet REE patterns are indicated by diamond symbols, sinusoidal by square symbols and sloped by cross symbols. Non-modal fractional melting curves for melting in the garnet (solid black lines) and spinel (dashed black lines) fields after (Lazarov et al., 2012).

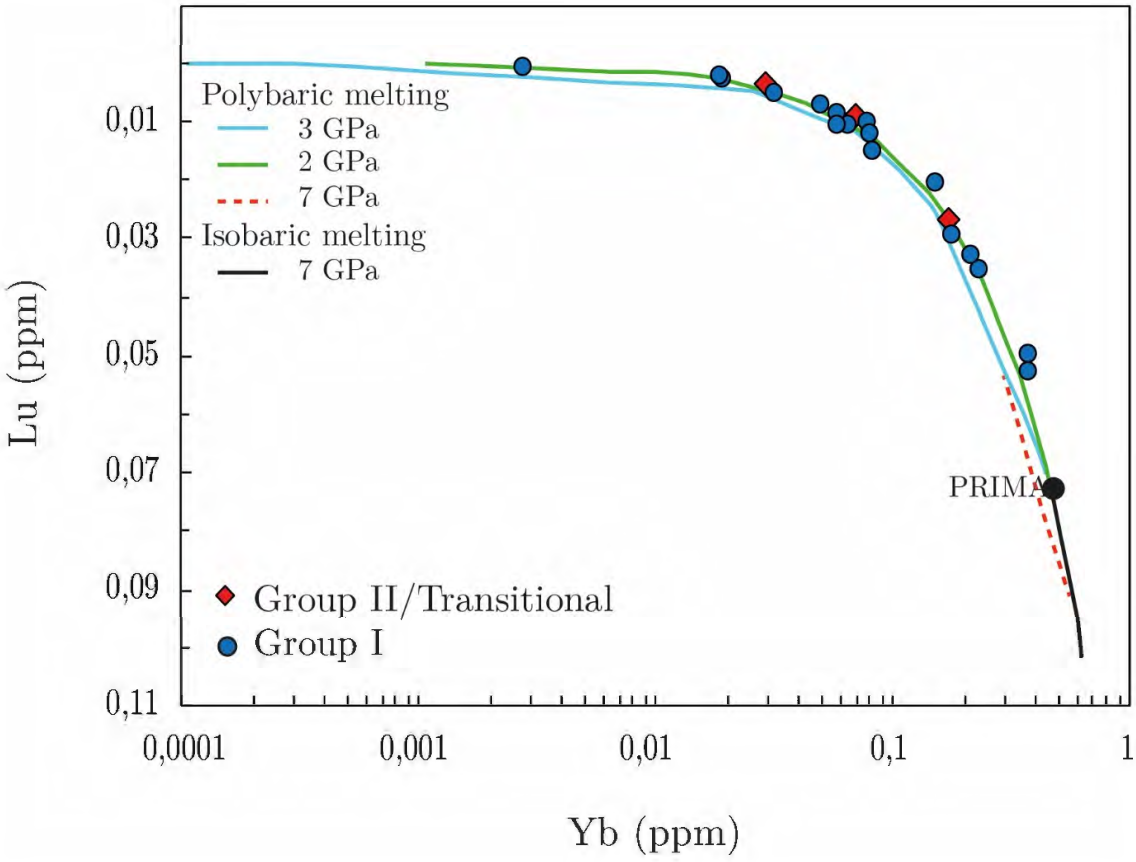

Figure 6.16: Lu versus Yb (ppm) of reconstructed whole-rock peridotites from Eastern Namaqualand kimberlites. Also shown are curves for residual mantle after polybaric fractional melting at 2 GPa, 3 GPa and 7 GPa and isobaric melting at 7 GPa after Wittig et al. (2008). *Note the fractionation of Lu from Yb resulting from low-pressure melting, whereas high-pressure melting in the presence of high modal abundances of garnet, for which the HREE are compatible, results in Lu abundances which would project higher than PRIMA.*

7. Synthesis and concluding remarks

The accuracy in application of thermodynamic equations to natural systems is largely dependent on how well the simplified model of reality represents the key parameters found to control the chemical reaction of interest in the natural system. This study has found that pressure and temperature estimates obtained through application of the garnet and cpx REE-based thermobarometer of Sun and Liang (2015) to peridotite xenoliths from the Eastern Namaqualand kimberlites display a large amount of scatter in P-T space even after rigorous screening for mineral-mineral REE equilibrium. Although differences in diffusion coefficients for divalent and trivalent cations in garnet and cpx (Van Orman et al., 2001, 2002) are expected to result in systematic differences in divalent thermobarometry results and trivalent thermobarometry results, the data presented here do not show any systematic variation in REE-based thermobarometry results from major element-based thermobarometry results, resulting in large uncertainties.

These uncertainties render the application of the REE-based thermobarometer to the samples studied here inaccurate for several reasons. First, the key parameters controlling REE partitioning between cpx and garnet defined by the lattice strain models of Sun and Liang (2012, 2013, 2014) do not correlate well with REE partitioning between cpx and garnet (Figure 6.1 – 6.5). Second, it is likely that lattice strain models parameterized from silicate melt systems, such as the models used in the REE-based thermobarometer, poorly predict the behaviour of trace element partitioning when carbonate is present in the melt (Hammouda et al., 2009; Girnis et al., 2013). Mantle xenoliths exhumed by kimberlites frequently display chemical compositions consistent with metasomatism by silico-carbonate melts such as kimberlites and carbonatites and the samples studied here are no exception. Until a systematic study is carried out on the melt dependence of mineral-mineral REE partitioning in mantle phases and assemblages, the uncertainties in REE-based

thermobarometry results in the samples studied here render them inadequate for interpretation of the thermal history of the mantle sampled by the Eastern Namaqualand kimberlites.

The peridotite xenoliths from the two Group II/transitional and five Group I kimberlites studied here help constrain the thermal and chemical evolution of the Proterozoic NNP lithospheric mantle southwest of the Kaapvaal craton. Peridotite xenolith based major element thermobarometry indicates that the Group II/transitional kimberlite xenoliths originated from a "cool" 200 km thick mantle that had a geothermal gradient of 40 mW/m^2 (model geotherm for lithospheric mantle of Hasterok and Chapman, 2011) with a 60 km "diamond window", akin to cratonic mantle. The presence of a "diamond stable" Proterozoic-age lithosphere at the time of Group II/transitional kimberlite magmatism implies that the exploration for diamond deposits should not be solely guided by *Clifford's Rule* (Clifford, 1966) and the harzburgitic xenolith assemblages (Gurney, 1984).

The peridotite xenoliths from the younger Group I kimberlite record evidence of a Mesozoic thermal perturbation (Bell et al., 2003) which resulted in ~ 60 km of lithospheric thinning (Figure 6.13) and a shift in the thermal regime to a 45 mW/m^2 geotherm (model geotherm for lithospheric mantle of Hasterok and Chapman, 2011) which is consistent with the present-day lithospheric structure as inferred from geophysical data (Fouch et al., 2004; Priestley et al., 2006; Globig et al., 2016). Garnet and cpx trace element concentrations in peridotite xenoliths from Group II/transitional kimberlites record evidence for melt metasomatism by kimberlitic/silicate melts. In contrast, peridotite xenoliths from some of the Group I kimberlites record evidence for carbonatitic metasomatism, indicating that a carbonatitic-style metasomatism affected parts of the mantle sampled by the Group I kimberlites between Group II/transitional and Group I kimberlite magmatism.

The timing of the Mesozoic thermal perturbation is intimately linked to continental breakup of Gondwana, unroofing of the southern African Plateau and offshore sediment accumulation, suggesting that Mesozoic surface uplift may be intimately linked to lithospheric thinning (Bell et al., 2003; de Wit, 2007; Tinker et al., 2008; Stanley et al., 2013; Wildman et al., 2017). Air-loaded isostatic uplift calculations (Klöcking et al., 2020) indicate that the 60 km of lithospheric thinning calculated from FITPLOT paleogeotherms can account for 0.7 km of surface uplift.

HREE concentrations of whole-rock peridotites and olivine Mg-numbers are consistent with lithospheric formation through 30% melt extraction in a shallow melting regime (3 GPa). The lithospheric mantle samples from the Eastern Namaqualand kimberlites are slightly more fertile than cratonic samples from the neighbouring Kaapvaal craton, however, substantially more depleted than global Proterozoic mantle and reflect high degrees of melt extraction (Janney et al., 2010).

8. References

Ashwal, L.D., Wiedenbeck, M. and Torsvik, T.H. 2017. Archean zircons in Miocene Oceanic hotspot rocks establish ancient continental crust beneath Mauritius. Nature communications, 8, 14086.

Aulbach, S. 2012. Craton nucleation and formation of thick lithospheric roots. Lithos, 149, 16–30.

Becker, M. and Le Roex, A.P. 2006. Geochemistry of South African on- and off-craton, group I and group II kimberlites: Petrogenesis and source region evolution. Journal of Petrology, 47, 673–703.

Bell, D.R. and Moore, R.O. 2004. Deep chemical structure of the southern African mantle from kimberlite megacrysts. South African Journal of Geology, 107, 59–80.

Bell, D.R. and Rossman, G.R. 1992. Water in Earth's mantle: The role of nominally anhydrous minerals. Science, 255, 1391–1397.

Bell, D.R., Schmitz, M.D. and Janney, P.E. 2003. Mesozoic thermal evolution of the southern African mantle lithosphere. Lithos, 71, 273–287.

Bernstein, S., Kelemen, P.B. and Hanghoj, K. 2006. Consistent olivine Mg# in cratonic mantle reflects Archean mantle melting to the exhaustion of orthopyroxene. Geology, 35, 459–462.

Bial, J., Büttner, S.H. and Frei, D. 2015. Formation and emplacement of two contrasting late-Mesoproterozoic magma types in the central Namaqua Metamorphic Complex (South Africa, Namibia): Evidence from geochemistry and geochronology. Lithos, 224–225, 272–294.

Boyd, F.R. 1973. A pyroxene geotherm. Geochimica et Cosmochimica Acta, 37, 2533–

2546.

Boyd, F.R. and Gurney, J.J. 1986. Diamonds and the African Lithosphere. Science, 232, 472–476.

Boyd, F.R. and Mertzman, S.A. 1987. Composition and structure of the Kaapvaal lithosphere, Southern Africa. In: Magmatic Processes: Physicochemical Principles. Uinversity Park, PA, USA, Geochemical Society, 13–24.

Boyd, F.R., Pearson, D.G., Hoal, K.O., Hoal, B.G., Nixon, P.H., Kingston, M.J. and Mertzman, S.A. 2004. Garnet lherzolites from Louwrensia, Namibia: Bulk composition and P/T relations. Lithos, 77, 573–592.

Brey, G.P. and Kohler, T. 1990. Geothermobarometry in Four- phase Lherzolites II . New Thermobarometers , and Practical Assessment of Existing Thermobaro .... Geothermobarometry in Four-phase Lherzolites II . New Thermobarometers , and Practical Assessment of Existing Thermobarometers. Journal of Petrology, 31, 1353–1378.

Broecker, W. 2012. The carbon cycle and climate change: Memoirs of my 60 years in Science. Geochemical Perspective, 1, 1–127.

Bussweiler, Y., Pearson, D.G., Stachel, T. and Kjarsgaard, B.A. 2018. Cr-rich megacrysts of clinopyroxene and garnet from Lac de Gras kimberlites, Slave Craton, Canada – implications for the origin of clinopyroxene and garnet in cratonic lherzolites. Mineralogy and Petrology, 112, 583–596.

Canil, D. and O'Neill, Hs. 1996. Distribution of ferric iron in some upper-mantle assemblages. Journal of Petrology, 37, 609–635.

Carlson, W.D. 2012. Rates and mechanism of Y, REE, and Cr diffusion in garnet. American Mineralogist, 97, 1598–1618.

Carlson, R.W., Pearson, D.G. and James, D.E. 2005. Physical, chemical, and

chronological characteristics of continental mantle. Reviews of Geophysics, 43, 1–24.

Clifford, T.N. 1966. Tectono-metallogenic units and metallogenic provinces of Africa. Earth and Planetary Science Letters, 1, 421–434.

Clifford, T.N., Barton, E.S., Stern, R.A. and Duchesne, J. 2004. U-Pb Zircon Calendar for Namaquan (Grenville) Crustal Events in the Granulite-facies Terrane of the O'okiep Copper District of South Africa. Journal of Petrology, 45, 669–691.

Coltorti, M., Bonadiman, C., Hinton, R.W., Siena, F. and Upton, B.G.J. 1999. Carbonatite metasomatism of the oceanic upper mantle: Evidence from clinopyroxenes and glasses in ultramafic xenoliths of Grande Comore, Indian Ocean. Journal of Petrology, 40, 133–165.

Czas, J. 2018. The Quandary of the Sask Craton: Origin and Evolution of the Lithospheric Mantle beneath the Sask Craton. PhD thesis. Uinversity of Alberta, 1–245pp.

Dasgupta, R., Hirschmann, M.M., McDonough, W.F., Spiegelman, M. and Withers, A.C. 2009. Trace element partitioning between garnet lherzolite and carbonatite at 6.6 and 8.6 GPa with applications to geochemistry of the mantle and of mantle-derived melts. Chemical Geology, 262.

Day, H.W. 2012. A revised diamond-graphite transition curve. American Mineralogist, 97, 52–62.

Doucouré, C.M. and de Wit, M.J. 2003. Old inherited origin for the present near-bimodal topography of Africa. Journal of Africa Earth Sciences, 36, 371–388.

Draper, D.S. and van Westrenen, W. 2007. Quantifying garnet-melt trace element partitioning using lattice-strain theory. Contributions to Mineralogy and

Petrology, 154, 731–746.

Durrheim, R.J. and Mooney, W.D. 1994. Evolution of the Precambrian lithosphere: seismological and geochemical constraints. Journal of Geophysical Research, 99.

Eggins, S.M. and Shelley, J.M.G. 2002. Compositional Heterogeneity in NIST SRM 610-617 Glasses. Geostandards and Geoanalytical Research, 26, 269–286.

Eglington, B.M. 2006. Evolution of the Namaqua-Natal Belt, southern Africa - A geochronological and isotope geochemical review. Journal of African Earth Sciences, 46, 93–111.

Eglington, B.M. and Armstrong, R.A. 2004. The Kaapvaal Craton and adjacent orogens, southern Africa: a geochronological database and overview of the geological development of the craton. South African Journal of Geology, 107, 13–32.

Field, M., Stiefenhofer, J., Robey, J. and Kurszlaukis, S. 2008. Kimberlite-hosted diamond deposits of southern Africa : A review Kimberlite-hosted diamond deposits of southern Africa : A review. Ore Geology Reviews, 33–75.

Finnerty, A.A. and Boyd, F.R. 1984. Evaluation of thermobarometers for garnet peridotites. Geochimica et Cosmochimica Acta, 48, 15–27.

Fouch, M.J., James, D.E., van Decar, J.C. and van der Lee, S. 2004. Mantle seismic structure beneath the Kaapvaal and Zimbabwe Cratons. South African Journal of Geology, 107, 33–44.

Gaetani, G.A. and Grove, T.L. 1995. Partitioning of rare earth elements between clinopyroxene and silicate melt Crystal-chemical controls. Geochimica et Cosmochimica Acta, 59, 1951–1962.

Gibson, S.A., Malarkey, J. and Day, J.A. 2008. Melt depletion and enrichment beneath the Western Kaapvaal craton: Evidence from Finsch peridotite xenoliths.

Journal of Petrology, 49, 1817–1852.

Girnis, A. V., Bulatov, V.K., Brey, G.P., Gerdes, A. and Höfer, H.E. 2013. Trace element partitioning between mantle minerals and silico-carbonate melts at 6-12GPa and applications to mantle metasomatism and kimberlite genesis. Lithos, 160–161, 183–200.

Giuliani, A. 2018. Insights into kimberlite petrogenesis and mantle metasomatism from a review of the compositional zoning of olivine in kimberlites worldwide. Lithos, 312–313, 322–342.

Giuliani, A., Phillips, D., Kamenetsky, V.S. and Goemann, K. 2016. Constraints on kimberlite ascent mechanisms revealed by phlogopite compositions in kimberlites and mantle xenoliths. Lithos, 240–243, 189–201.

Globig, J., Fernàndez, M., Vergés, J., Robert, A. and Faccenna, C. 2016. New insights into the crust and lithospheric mantle structure of Africa from elevation, geoid, and thermal analysis. Journal of Geophysical Research:, 5389–5424.

Gregoire, M., Bell, D.R. and le Roex, A.P. 2003. Garnet Lherzolites from the Kaapvaal Craton (South Africa): Trace Element Evidence for a Metasomatic History. Journal of Petrology, 44, 629–657.

Griffin, W.L. and O'Reilly, S.Y. 2007. The Earliest Subcontinental Lithospheric Mantle. In: Earth's Oldest Rocks. Amsterdam, Elsevier, 1013–1035.

Griffin, W.L., O'Reilly, S.Y., Abe, N., Aulbach, S., Davies, R.M., Pearson, N.J., Doyle, B.J. and Kivi, K. 2003a. The origin and evolution of Archean lithospheric mantle. Precambrian Research, 127, 19–41.

Griffin, W.L., O'Reilly, S.Y., Afonso, J.C. and Begg, G.C. 2009. The composition and evolution of lithospheric mantle: A re-evaluation and its tectonic implications.

Journal of Petrology, 50, 1185–1204.

Griffin, W.L., O'Reilly, S.Y., Natapov, L.M. and Ryan, C.G. 2003b. The evolution of lithospheric mantle beneath the Kalahari Craton and its margins. Lithos, 71, 215–241.

Griffin, W.L., O'Reilly, S.Y. and Ryan, C.G. 1999a. The composition and origin of subcontinental lithospheric mantle. In: Y. Fei, C.M. Bertka and B.O. Mysen (Editors) Mantle Petrology: Field Observations and High Pressure Experimentation: A Tribute to Francis R. (Joe) Boyd. Houston, The Geochemical Society, 13–45.

Griffin, W.L., Shee, S.R., Ryan, C.G., Win, T.T. and Wyatt, B.A. 1999b. Harzburgite to lherzolite and back again : metasomatic processes in ultramafic xenoliths from the Wesselton kimberlite, Kimberley, South Africa. Contrib Mineral Petrol, 134, 232–250.

Grütter, H.S., Gurney, J.J., Menzies, A.H. and Winter, F. 2004. An updated classification scheme for mantle-derived garnet, for use by diamond explorers. Lithos, 77, 841–857.

Gurney, J.J. 1984. A correlation between garnets and diamonds in kimberlites. In: J.E. Glover and P.G. Harris (Editors) Kimberlite Occurrence and Origin: A Basis for Conceptual Models in Exploration. Perth, Geol. Dept. & Uinversity Extension, Uinversity of West Australia, 143–166.

Hammouda, T., Moine, B.N., Devidal, J.L. and Vincent, C. 2009. Trace element partitioning during partial melting of carbonated eclogites. Physics of the Earth and Planetary Interiors, 174, 60–69.

Harley, S.L. 1984. An experimental study of the partitioning of Fe and Mg between

garnet and orthopyroxene. Contrib Mineral Petrol, 86, 359–373.

Hasterok, D. and Chapman, D.S. 2011. Heat production and geotherms for the continental lithosphere. Earth and Planetary Science Letters, 307, 59–70.

Hill, E., Wood, B.J. and Blundy, J.D. 2000. The effect of Ca-Tschermaks component on trace element partitioning between clinopyroxene and silicate melt. Lithos, 53, 203–215.

Hirschmann, M.M. 1996. Reading garnet's signature. Nature, 384, 215–217.

Hoggard, M.J., White, N. and Al-Attar, D. 2016. Global dynamic topography observations reveal limited influence of large-scale mantle flow. Nature Geoscience, 9, 456–463.

Ionov, D.A., Ashchepkov, I. and Jagoutz, E. 2005. The provenance of fertile off-craton lithospheric mantle: Sr-Nd isotope and chemical composition of garnet and spinel peridotite xenoliths from Vitim, Siberia. Chemical Geology, 217, 41–75.

Ionov, D.A., Carlson, R.W., Doucet, L.S., Golovin, A. V. and Oleinikov, O.B. 2015. The age and history of the lithospheric mantle of the Siberian craton: Re-Os and PGE study of peridotite xenoliths from the Obnazhennaya kimberlite. Earth and Planetary Science Letters, 428, 108–119.

Jacobs, J., Pisarevsky, S., Thomas, R.J. and Becker, T. 2008. The Kalahari Craton during the assembly and dispersal of Rodinia The Kalahari Craton during the assembly and dispersal of Rodinia. prec, 160, 142–158.

Janney, P.E., Shirey, S.B., Carlson, R.W., Pearson, D.G., Bell, D.R., le Roex, A.P., Ishikawa, A., Nixon, P.H. and Boyd, F.R. 2010. Age, composition and thermal characteristics of South African off-craton mantle lithosphere: Evidence for a multi-stage history. Journal of Petrology, 51, 1849–1890.

Jochum, K.P., Weis, U., Stoll, B., Kuzmin, D., Yang, Q., Raczek, I., Jacob, D.E.,

Stracke, A., Birbaum, K., Frick, D.A., Günther, D. and Enzweiler, J. 2011. Determination of Reference Values for NIST SRM 610-617 Glasses Following ISO Guidelines. Geostandards and Geoanalytical Research, 35, 397–429.

Klöcking, M., Hoggard, M.J., Rodríguez Tribaldos, V., Richards, F.D., Guimarães, A.R., Maclennan, J. and White, N.J. 2020. A tale of two domes: Neogene to recent volcanism and dynamic uplift of northeast Brazil and southwest Africa. Earth and Planetary Science Letters, 547, 116464.

Kobussen, A.F., Griffin, W.L. and O'Reilly, S.Y. 2009. Cretaceous thermo-chemical modification of the Kaapvaal cratonic lithosphere, South Africa. Lithos, 112, 886–895.

Kobussen, A.F., Griffin, W.L., O'Reilly, S.Y. and Shee, S.R. 2008. Ghosts of lithospheres past: Imaging an evolving lithospheric mantle in southern Africa. Geology, 36, 515–518.

Krogh, E.J. 1988. The garnet-clinopyroxene Fe-Mg geothermometer: a reinterpretation of existing experimental data. Contrib Mineral Petrol, 99, 44–48.

Kuehn, S.C., Froese, D.G., Shane, P.A.R. and Participants, I. intercomparison 2011. The INTAV intercomparison of electron-beam microanalysis of glass by tephrochronology laboratories: Results and recommendations. Quaternary International, 246, 19–47.

Lazarov, M., Brey, G.P. and Weyer, S. 2012. Evolution of the South African mantle-a case study of garnet peridotites from the Finsch diamond mine (Kaapvaal craton); Part 2: Multiple depletion and re-enrichment processes. Lithos, 154, 210–223.

Lindsley, D.H. 1983. Pyroxene thermometry. American Mineralogist, 68, 477–493.

Luchs, T., Brey, G.P., Gerdes, A. and Höfer, H.E. 2013. The lithospheric mantle

underneath the Gibeon Kimberlite field (Namibia): A mix of old and young components-Evidence from Lu-Hf and Sm-Nd isotope systematics. Precambrian Research, 231, 263–276.

Lundstrom, C.C., Shaw, H.F., Ryerson, F.J., Williams, Q. and Gill, J. 1998. Crystal chemical control of clinopyroxene-melt partitioning in the Di-Ab-An system: Implications for elemental fractionations in the depleted mantle. Geochimica et Cosmochimica Acta, 62, 2849–2862.

Luth, R.W., Virgo, D., Boyd, F.R. and Wood, B.J. 1990. Ferric iron in mantle-derived garnets: implications for thermobarometry and for the oxidation state of the mantle. Contributions to Mineralogy and Petrology, 140, 56–72.

Macey, P.H., Bailie, R.H., Miller, J.A., Thomas, R.J., de Beer, C., Frei, D. and le Roux, P.J. 2018. Implications of the distribution, age and origins of the granites of the Mesoproterozoic Spektakel Suite for the timing of the Namaqua Orogeny in the Bushmanland Subprovince of the Namaqua-Natal Metamorphic Province, South Africa. Precambrian Research, 312, 68–98.

Macey, P.H., Thomas, R.J., Minnaar, H.M., Gresse, P.G., Lambert, C.W., Groenewald, C.A., Miller, J.A., Indongo, J., Angombe, M., Shifotoka, G., Frei, D., Diener, J.F.A., Kisters, A.F.M., Dhansay, T., Smith, H., Doggart, S., Le Roux, P., Hartnady, M.I. and Tinguely, C. 2017. Origin and evolution of the ~1.9 Ga Richtersveld Magmatic Arc, SW Africa. Precambrian Research, 292, 417–451.

Mather, K.A., Pearson, D.G., McKenzie, D., Kjarsgaard, B.A. and Priestley, K. 2011. Constraints on the depth and thermal history of cratonic lithosphere from peridotite xenoliths, xenocrysts and seismology. Lithos, 125, 729–742.

McCourt, S., Armstrong, R.A., Grantham, G.H. and Thomas, R.J. 2006. Geology and

evolution of the Natal belt, South Africa. Journal of African Earth Sciences, 46, 71–92.

McDonough, W.F. and Sun, S.-S. 1995. The composition of the Earth. Chemical Geology, 120, 223–253.

McKenzie, D., Jackson, J. and Priestley, K. 2005. Thermal structure of oceanic and continental lithosphere. Earth and Planetary Science Letters, 233, 337–349.

McKenzie, D. and Priestley, K. 2008. The influence of lithospheric thickness variations on continental evolution. Lithos, 102, 1–11.

Mofokeng, S. 1998. A comparison of the Nickel and the conventional geothermometers with respect to the Jagersfontein and the Matsoku kimberlite peridotite xenoliths. University of Cape Town, 1–173pp.

Nickel, K.G. and Green, D.H. 1985. Empirical geothermobarometry for garnet peridotites and implications for the nature of the lithosphere, kimberlites and diamonds. Earth and Planetary Science Letters, 73, 158–170.

Nicolaysen, O.L. and Burger, A.J. 1965. Note on an extensive zone 1000 million-year old metamorphic and igneous rock in southern Africa. Sciences de la Terre, 10, 497–518.

Nimis, P., Goncharov, A., Ionov, D.A. and McCammon, C. 2015. Fe3+ partitioning systematics between orthopyroxene and garnet in mantle peridotite xenoliths and implications for thermobarometry of oxidized and reduced mantle rocks. Contributions to Mineralogy and Petrology, 169, 1–18.

Nimis, P. and Grütter, H. 2010. Internally consistent geothermometers for garnet peridotites and pyroxenites. Contributions to Mineralogy and Petrology, 159, 411–427.

Nimis, P. and Taylor, W.R. 2000. Single clinopyroxene thermobarometry for garnet

peridotites . Part I . Calibration and testing of a Cr-in-Cpx barometer and an enstatite-in-Cpx thermometer. Contrib Mineral Petrol, 139, 541–554.

Nyblade, A.A. and Pollack, H.N. 1993. A global analysis of heat flow from Precambrian terrains: implications for the thermal structure of Archean and Proterozoic lithosphere. Journal of Geophysical Research, 98, 12207–12218.

O'Neill, Hs. and Wood, B.J. 1979. An experimental study of Fe-Mg patitioning between garnet and olivine and its calibration as a geothermometer. Contrib Mineral Petrol, 70, 59–70.

Van Orman, J.A., Grove, T.L. and Shimizu, N. 2001. Rare earth element diffusion in diopside: Influence of temperature, pressure, and ionic radius, and an elastic model for diffusion in silicates. Contributions to Mineralogy and Petrology, 141, 687–703.

Van Orman, J.A., Grove, T.L., Shimizu, N. and Layne, G.D. 2002. Rare earth element diffusion in natural pyrope single crystal at 2.8 GPa. Contributions to Mineralogy and Petrology, 142, 416–42.

Pearce, N.J.G., Perkins, W.T., Westgate, J.A., Gorton, M.P., Jackson, S.E., Neal, C.R. and Chenery, S.P. 1997. A compilation of new and published major and trace element data for NIST SRM 610 and NIST SRM 612 glass reference materials. Geostandards Newsletter, 21, 115–144.

Pearson, D.G. and Wittig, N. 2008. Review Formation of Archaean continental lithosphere and its diamonds: the root of the problem. Journal of the Geological Society, London, 165, 895–914.

Pearson, D.G. and Wittig, N. 2014. The Formation and Evolution of Cratonic Mantle Lithosphere - Evidence from Mantle Xenoliths. In: R.W. Carlson (Editor)

Treatise on Geochemistry: Second Edition. Elsevier Ltd., 255–292.

Pettersson, Å., Cornell, D.H., Moen, H.F.G., Reddy, S. and Evans, D. 2007. Ion-probe dating of 1.2 Ga collision and crustal architecture in the Namaqua-Natal Province of southern Africa. Precambrian Research, 158, 79–92.

Priestley, K., McKenzie, D. and Debayle, E. 2006. The state of the upper mantle beneath southern Africa. Tectonophysics, 416, 101–112.

Robey, J. 1981. Kimberlites of the Central Cape Province, R.S.A. University of Cape Town, 234pp.

le Roex, A. and Class, C. 2016. Metasomatic enrichment of Proterozoic mantle south of the Kaapvaal Craton, South Africa: origin of sinusoidal REE patterns in clinopyroxene and garnet. Contributions to Mineralogy and Petrology, 171:14, 1–24.

Rudnick, R.L. and Fountain, D.M. 1995. Nature Crust : and Composition of the Continental Perspective. Reviews of Geophysics, 33, 267–309.

Rudnick, R.L., McDonough, W.F. and O'Connell, R.J. 1998. Thermal structure, thickness and composition of continental lithosphere. Chemical Geology, 145, 395–411.

Ryan, C.G., Griffin, W.L. and Pearson, N.J. 1996. Garnet geotherms: Pressure-temperature data from Cr-pyrope garnet xenocrysts in volcanic rocks. Journal of Geophysical Research, 101, 5611–5625.

Schmitz, M.D. and Bowring, S.A. 2004. Lower crustal granulite formation during Mesoproterozoic Namaqua-Natal collisional orogenesis, southern Africa. South African Journal of Geology, 107, 261–284.

Shiimi, E.T. 2017. A comparison of melt depletion, thermal structure and metasomatism of the Proterozoic mantle lithosphere in the Namaqua-Natal and

Rehoboth Provinces of southern Africa. University of Cape Town, 1–194pp.

Shu, Q. and Brey, G.P. 2015. Ancient mantle metasomatism recorded in subcalcic garnet xenocrysts: Temporal links between mantle metasomatism, diamond growth and crustal tectonomagmatism. Earth and Planetary Science Letters, 418, 27–39.

Simon, N.S.C., Carlson, R.W., Pearson, D.G. and Davies, G.R. 2007. The origin and evolution of the Kaapvaal Cratonic Lithospheric Mantle. Journal of Petrology, 48, 589–625.

Smith, C.B. 1983a. Rubidium-Strontium, Uranium-Lead and Samarium-Neodymium isotopic studies of kimberlite and selected mantle-derived xenoliths. University of Witwatersrand, Johannesburg, 436pp.

Smith, C.B. 1983b. Pb, Sr, and Nd isotopic evidence for sources of African kimberlite. Nature, 304, 51–54.

Smith, C.B., Allsopp, H.L., Kramers, J.D., Hutchinson, G. and Roddick, J.C. 1985. Emplacement ages of Jurassic-Cretaceous South African kimberlites by Rb-Sr method on phlogopite and whole-rock samples. Transactions of the Geological Society of South Africa, 88, 249–266.

Stachel, T., Banas, A., Aulbach, S., Smit, K. V., Wescott, P., Chinn, I.L. and Kong, J. 2018. The Victor Mine (Superior Craton, Canada): Neoproterozoic lherzolitic diamonds from a thermally-modified cratonic root. Mineralogy and Petrology, 112, 325–336.

Stachel, T. and Harris, J.W. 2008. The origin of cratonic diamonds - Constraints from mineral inclusions. Ore Geology Reviews, 34, 5–32.

Stachel, T. and Luth, R.W. 2015. Diamond formation - Where, when and how?

Lithos, 220–223, 200–220.

Stanley, J.R., Flowers, R.M. and Bell, D.R. 2013. Kimberlite (U-Th)/He dating links surface erosion with lithospheric heating, thinning, and metasomatism in the southern African Plateau. Geology, 41, 1243–1246.

Sun, C. and Liang, Y. 2012. Distribution of REE between clinopyroxene and basaltic melt along a mantle adiabat: Effects of major element composition, water, and temperature. Contributions to Mineralogy and Petrology, 163, 807–823.

Sun, C. and Liang, Y. 2013. The importance of crystal chemistry on REE partitioning between mantle minerals (garnet, clinopyroxene, orthopyroxene, and olivine) and basaltic melts. Chemical Geology, 358, 23–36.

Sun, C. and Liang, Y. 2014. An assessment of subsolidus re-equilibration on REE distribution among mantle minerals olivine, orthopyroxene, clinopyroxene, and garnet in peridotites. Chemical Geology, 372, 80–91.

Sun, C. and Liang, Y. 2015. A REE-in-garnet-clinopyroxene thermobarometer for eclogites, granulites and garnet peridotites. Chemical Geology, 393–394, 79–92.

Tappe, S., Romer, R.L., Stracke, A., Steenfelt, A., Smart, K.A., Muehlenbachs, K. and Torsvik, T.H. 2017. Sources and mobility of carbonate melts beneath cratons, with implications for deep carbon cycling, metasomatism and rift initiation. Earth and Planetary Science Letters, 466, 152–167.

Tappe, S., Smart, K., Torsvik, T., Massuyeau, M. and de Wit, M. 2018. Geodynamics of kimberlites on a cooling Earth: Clues to plate tectonic evolution and deep volatile cycles. Earth and Planetary Science Letters, 484, 1–14.

Taylor, W.R. 1998. An experimental test of some geothermometer and geobarometer formulations for upper mantle peridotites with application to the thermobarometry of fertile lherzolite and garnet websterite. N Jb Min Abh, 172,

381–408.

Tinker, J., de Wit, M. and Brown, R. 2008. Mesozoic exhumation of the southern Cape, South Africa, quantified using apatite fission track thermochronology. Tectonophysics, 455, 77–93.

Watson, E.B. and Cherniak, D.J. 2013. Simple equations for diffusion in response to heating. Chemical Geology, 335, 93–104.

Weiss, Y., Navon, O., Goldstein, S.L. and Harris, J.W. 2018. Inclusions in diamonds constrain thermo-chemical conditions during Mesozoic metasomatism of the Kaapvaal cratonic mantle. Earth and Planetary Science Letters, 491, 134–147.

Wildman, M., Brown, R., Persano, C., Beucher, R., Stuart, F.M., Mackintosh, V., Gallagher, K., Schwanethal, J. and Carter, A. 2017. Contrasting Mesozoic evolution across the boundary between on and off craton regions of the South African plateau inferred from apatite fission track and (U-Th-Sm)/He thermochronology. Journal of Geophysical Research: Solid Earth, 122, 1517–1547.

de Wit, M.J. 2007. The Kalahari Epeirogeny and climate change : differentiating cause and effect from core to space. South African Journal of Geology, 110, 367–392.

de Wit, M.J. and Linol, B. 2015. Precambrian Basement of the Congo Basin and Its Flanking Terrains. In: Geology and Resource Potential of the Congo Basin. 19–37.

Wittig, N., Pearson, D.G., Webb, M., Ottley, C.J., Irvine, G.J., Kopylova, M., Jensen, S.M. and Nowell, G.M. 2008. Origin of cratonic lithospheric mantle roots : A geochemical study of peridotites from the North Atlantic Craton , West Greenland. Earth and Planetary Science Letters, 274, 24–33.

Wood, B.J. and Blundy, J.D. 1997. A predictive model for rare earth element partitioning between clinopyroxene and anhydrous silicate melt. Contributions to

Mineralogy and Petrology, 129, 166–181.

Woodland, A.B. 2009. Ferric iron contents of clinopyroxene from cratonic mantle and partitioning behaviour with garnet. Lithos, 112, 1143–1149.

Woodland, A.B. and Koch, M. 2003. Variation in oxygen fugacity with depth in the upper mantle beneath the Kaapvaal craton, Southern Africa. Earth and Planetary Science Letters, 214, 295–310.

Yaxley, G.M., Crawford, A.J. and Green, D.H. 1991. Evidence for carbonatite metasomatism in spinel peridotite xenoliths from western Victoria, Australia. Earth and Planetary Science Letters, 107, 305–317.

Yaxley, G.M. and Green, D.H. 1998. Reactions between eclogite and peridotite: Mantle refertilisation by subduction of oceanic crust. Schweizerische Mineralogische Und Petrographische Mitteilungen, 78, 243–255.

Ziberna, L., Nimis, P., Kuzmin, D. and Malkovet, V.G. 2016. Error sources in single-clinopyroxene thermobarometry and a mantle geotherm for the Novinka kimberlite , Yakutia. American Mineralogist, 101, 2222–2232.

9. Appendix A

Sample summary

Table 9.1: Summary of rock lithologies and mineral assemblages for samples from this study.

Sample	Locality	Min. assemblage	Rock type
HBR-1	Hebron	ol-opx-cpx-gt-sp	gt lherz.
HBR-2	Hebron	ol-opx-cpx-gt-sp	gt-sp lherz.
HBR-3	Hebron	ol-opx-cpx-gt	gt lherz.
HBR-4	Hebron	ol-opx-cpx-gt-sp	gt-sp lherz.
HBR-5	Hebron	ol-opx-cpx-gt	gt lherz.
HBR-10	Hebron	ol-opx-cpx-gt-sp	gt-sp lherz.
HBR-11	Hebron	ol-opx-cpx-gt	gt lherz.
HBR-12	Hebron	ol-opx-cpx-gt-sp	gt-sp lherz.
HBX-1	Hebron	ol-opx-cpx-gt	gt lherz.
HBX-2	Hebron	ol-opx-cpx-gt	gt lherz.
HBX-4	Hebron	ol-opx-cpx-gt	gt lherz.
HBX-6	Hebron	ol-opx-cpx-gt	gt lherz.
HBX-12	Hebron	ol-opx-cpx-gt	gt lherz.
UINT-micro	Uintjiesberg	opx-cpx-gt	unknown
UINT-4	Uintjiesberg	opx-cpx-gt	gt websterite
UINT-8	Uintjiesberg	ol-opx-cpx-gt	gt lherz.
UBX-1	Uintjiesberg	ol-opx-cpx-gt	gt lherz.
UBX-18	Uintjiesberg	ol-opx-cpx-gt	gt lherz.

Table 9.1 continued.

Sample	Locality	Min. assemblage	Rock type
GANS-1	Gansfontein	ol-opx-cpx-gt-sp	gt-sp lherz.
GANS-2	Gansfontein	ol-opx-cpx-gt-sp	gt-sp lherz.
GANS-3	Gansfontein	ol-opx-cpx-sp	spinel lherz.
GANS-9	Gansfontein	ol-opx-cpx-sp	gt websterite
GSF-4	Gansfontein	ol-opx-cpx-gt	gt lherz.
HOD-1	Hoedkop	ol-opx-cpx-gt	gt lherz.
HOD-2	Hoedkop	ol-opx-cpx-gt	gt lherz.
HOD-3	Hoedkop	ol-opx-cpx-gt	gt lherz.
HOD-4	Hoedkop	ol-opx-cpx-gt	gt lherz.
HOD-5	Hoedkop	ol-opx-cpx-gt-sp	gt-sp lherz.
HOD-11	Hoedkop	ol-opx-cpx-gt-sp	gt-sp lherz.
MW-1	Melton Wold	ol-opx-cpx-gt	gt lherz.
XMW-8	Melton Wold	ol-opx-cpx-gt	gt lherz.
XMW-13	Melton Wold	ol-opx-cpx-gt	gt lherz.
XMW-19	Melton Wold	ol-opx-cpx-gt-sp	gt-sp lherz.
XMW-22	Melton Wold	ol-opx-gt	gt harz.
MWX-5	Melton Wold	ol-opx-cpx-gt	gt lherz.

Table 9.1 continued.

Sample	Locality	Min. assemblage	Rock type
MWX-10	Melton Wold	ol-opx-cpx-gt	gt lherz.
MWX-15	Melton Wold	ol-opx-cpx-gt	gt lherz.
MWX-18	Melton Wold	ol-opx-cpx-gt	gt lherz.
MWX-19	Melton Wold	ol-opx-cpx-gt	gt lherz.
MWX-20	Melton Wold	ol-opx-cpx-gt	gt lherz.
MWX-32	Melton Wold	ol-opx-cpx-gt	gt lherz.
JAR12013	Markt	ol-opx-cpx-gt	gt lherz.
JAR12033	Markt	ol-opx-cpx-gt	gt lherz.
MRK-1	Markt	ol-opx-cpx-gt	gt lherz.
JAR12043	Markt	ol-opx-cpx-gt	gt lherz.
JAR12083	Markt	ol-opx-cpx-gt	gt lherz.

ol = olivine; opx = orthopyroxene; cpx = clinopyroxene; gt = garnet; sp = spinel; lherz. = lherzolite; harz. = harzburgite

10. Appendix B

EPMA data

Table 10.1: EPMA results for cpx in peridotite xenoliths. PEJ denotes data reported in Janney et al. (2010) and FC denotes data collected in this study. n.a. denotes not analysed.

Sample	UINT-4 (PEJ)	UINT-4 (FC)	UINT-8 (PEJ)	UINT-8 (FC)	GANS-2 (PEJ)	GANS-2 (FC) cpx (long counts)	GANS-2 (FC) cpx (default counts)	GANS-9 (PEJ)	GANS-9 (FC)
Mineral	cpx	cpx	cpx	cpx	cpx			cpx	cpx
SiO_2	54.54	54.20	54.36	54.43	54.84	54.71	54.96	54.77	54.56
TiO_2	0.02	0.02	0.31	0.13	0.02	0.03	0.04	0.14	0.15
Al_2O_3	2.72	2.54	2.35	3.13	1.46	1.47	1.46	3.62	3.57
Cr_2O_3	1.27	1.14	1.21	2.40	0.45	0.81	0.81	0.21	0.88
FeO	2.08	2.17	2.61	2.27	1.81	1.81	1.67	3.98	4.18
MnO	0.06	0.05	0.08	0.08	0.06	0.07	0.07	0.08	0.07
MgO	16.86	16.91	16.83	16.50	18.07	18.03	17.98	15.16	15.27
CaO	21.29	21.67	20.10	19.21	23.31	22.48	22.18	19.68	19.68
Na_2O	1.66	1.44	1.86	2.26	0.70	0.64	0.62	2.01	1.90
K_2O	n.a.	0.00	n.a.	0.01	n.a.	0.00	0.01	n.a.	0.01
NiO	0.05	n.a.	0.05	n.a.	0.03	n.a.	n.a.	0.05	n.a.
Total	100.55	100.13	99.78	100.42	100.76	100.04	99.79	99.7	100.27
Mg#	93.53	93.29	92.00	92.82	94.68	94.68	95.05	87.16	86.69
Ca#	47.58	47.94	46.19	45.56	48.11	47.26	46.99	48.27	48.10
Cr#	23.85	23.18	25.67	34.01	17.13	27.11	27.10	3.75	14.17

Table 10.2: EPMA results for garnet in peridotite xenoliths. PEJ denotes data reported in Janney et al. (2010) and FC denotes data collected in this study. n.d. denotes not detected and n.a. denotes not analysed.

Sample	UINT-4 (PEJ)	UINT-4 (FC)	UINT-8 (PEJ)	UINT-8 (FC)	GANS-2 (PEJ)	GANS-2 (FC)	GANS-9 (PEJ)	GANS-9 (FC)
Mineral	gt	gt	gt	gt	gt	gt	gt	gt
SiO_2	41.91	41.6	41.85	41.8	41.77	41.6	41.57	40.7
TiO_2	0.01	0.01	0.14	0.14	0.02	0.03	0.06	0.06
Al_2O_3	22.92	23.0	20.97	21.2	21.40	21.5	22.65	22.7
Cr_2O_3	1.98	2.0	4.17	4.2	3.15	3.9	0.32	1.3
FeO	7.79	8.1	6.62	7.0	7.45	7.9	14.74	14.6
MnO	0.36	0.36	0.33	0.33	0.48	0.48	0.45	0.47
MgO	20.58	19.8	21.22	20.4	19.58	18.7	16.26	15.2
CaO	5.10	5.2	5.05	5.2	6.33	6.5	4.80	4.9
Na_2O	0.01	0.01	0.05	0.05	0.01	0.02	0.02	0.03
K_2O	n.a.	n.d.	n.a.	n.d.	n.a.	n.d.	n.a.	n.d.
NiO	0.01	n.a.	0.01	n.a.	0.01	n.a.	0.01	n.a.
Total	100.68	100.08	100.40	100.37	100.21	100.52	100.88	100.03
Mg#	82.48	81.40	85.10	83.87	82.40	80.90	66.28	64.96
Ca#	15.12	15.80	14.61	15.41	18.86	20.04	17.51	18.87
Cr#	5.48	5.51	11.77	11.82	8.99	10.74	0.94	3.72

Table 10.3: EPMA results for orthopyroxene in peridotite xenoliths. PEJ denotes data reported in Janney et al. (2010) and FC denotes data collected in this study. n.a. denotes not analysed.

Comment	UINT-4 (PEJ)	UINT-4 (FC)	UINT-8 (PEJ)	UINT-8 (FC)	GANS-2 (PEJ)	GANS-2 (FC)	GANS-9 (PEJ)	GANS-9 (FC)
Mineral	opx	opx	opx	opx	opx	opx	opx	opx
SiO_2	56.79	56.62	57.02	57.02	57.06	57.24	56.26	55.58
TiO_2	0.01	0.01	0.07	0.06	0.02	0.03	0.04	0.04
Al_2O_3	1.28	1.26	1.29	1.32	1.24	1.18	1.09	1.08
Cr_2O_3	0.28	0.27	0.49	0.51	0.33	0.31	0.04	0.17
FeO	5.00	5.24	4.62	4.72	4.90	4.99	10.95	11.36
MnO	0.10	0.10	0.11	0.11	0.13	0.12	0.14	0.14
MgO	35.53	35.76	35.48	35.74	35.60	35.87	31.39	31.10
CaO	0.37	0.32	0.52	0.52	0.35	0.31	0.44	0.44
Na_2O	0.06	0.06	0.14	0.13	0.03	0.03	0.08	0.09
NiO	0.12	n.a.	0.11	n.a.	0.10	n.a.	0.12	n.a.
Total	99.53	99.63	99.84	100.13	99.75	100.08	100.54	100.00
Mg#	92.68	92.40	93.19	93.10	92.50	92.75	83.63	82.99
Ca#	0.74	0.63	1.04	1.03	0.60	0.62	1.00	1.01
Cr#	12.79	12.58	20.30	20.43	21.20	14.93	2.40	9.58

11. Appendix C

LA-ICP-MS Standards Data

Table 11.1: LA-ICP-MS results for NIST-610 glass collected during Aug 2018 and recommended concentrations of Pearce et al. (1997). Numbering is for individual days.

	NIST-610 (Aug 2018)								
	15-Aug	15-Aug	15-Aug	20-Aug	29-Aug	29-Aug	29-Aug	29-Aug	Pearce et
ppm	a	b	c	a	a	b	c	d	al. (1997)
Sc	447	428	425	445	436	433	461	435	441
Ti	437	419	416	444	423	457	422	401	434
V	457	420	441	439	442	440	437	448	442
Mn	441	392	438	436	423	429	438	432	433
Co	410	379	395	406	400	414	403	409	405
Ni	446	426	418	452	445	454	442	454	444
Cu	431	396	404	427	428	437	434	435	430
Zn	490	597	440	472	509	461	461	465	456
Rb	440	408	424	431	428	428	435	425	431
Sr	509	473	492	504	491	495	500	499	497
Y	465	434	437	458	448	444	462	451	450
Zr	449	426	423	445	434	437	456	439	440
Nb	433	410	409	426	424	419	431	414	419
Ba	435	407	418	432	427	421	427	425	424
La	468	449	447	464	461	454	466	451	457
Ce	460	434	441	452	452	450	451	448	448
Pr	438	407	420	437	428	432	438	430	430
Nd	439	403	414	441	425	430	438	426	431
Sm	461	419	438	462	446	445	458	448	451
Eu	471	428	451	471	459	455	467	458	461
Tb	455	414	432	456	437	438	453	438	443
Gd	431	396	404	430	418	416	431	416	420
Dy	436	395	413	435	416	420	439	428	427
Ho	458	419	435	459	437	445	460	450	449
Er	436	396	410	438	416	422	435	423	426
Tm	429	386	406	433	409	418	434	420	420
Yb	474	425	451	472	451	461	476	459	462
Lu	441	403	420	445	428	433	451	434	435
Hf	431	392	406	427	410	415	429	422	418
Ta	383	354	360	388	370	377	390	375	377
Pb	423	391	411	413	407	416	424	415	413
Th	466	427	436	460	441	448	465	447	451
U	450	425	455	454	452	439	457	459	457

Table 11.2: LA-ICP-MS results for NIST-610 glass collected during Aug 2019 and recommended concentrations of Pearce et al. (1997). Numbering is for individual days.

	NIST-610 (Aug 2019)								
	05-Aug	05-Aug	05-Aug	05-Aug	05-Aug	05-Aug	05-Aug	05-Aug	Pearce et
ppm	a	b	c	d	e	f	g	h	al. (1997)
Sc	441	441	441	441	441	441	441	438	441
Ti	436	435	436	436	436	436	435	431	434
V	442	442	442	442	442	442	442	440	442
Mn	433	433	433	434	433	433	433	434	433
Co	405	405	405	405	405	405	405	394	405
Ni	444	444	444	444	444	444	444	431	444
Cu	430	430	430	430	430	430	430	414	430
Zn	456	456	456	456	456	456	456	455	456
Rb	431	431	431	431	431	431	431	422	431
Sr	498	498	498	499	499	499	498	485	497
Y	451	451	451	451	451	451	451	437	450
Zr	440	440	441	441	441	441	440	422	440
Nb	420	420	420	420	420	420	420	412	419
Ba	424	424	424	424	424	424	424	418	424
La	457	457	457	457	457	457	457	451	457
Ce	448	448	448	448	448	448	448	443	448
Pr	431	431	431	431	431	431	431	423	430
Nd	431	431	431	432	432	432	431	420	431
Sm	451	451	451	452	452	452	451	446	451
Eu	461	461	461	461	461	461	461	461	461
Tb	444	444	444	444	444	444	444	440	443
Gd	421	421	421	421	421	421	421	414	420
Dy	428	428	428	428	428	428	428	419	427
Ho	450	450	450	450	450	450	450	434	449
Er	427	427	427	427	427	427	427	421	426
Tm	421	421	421	421	421	421	421	419	420
Yb	463	463	463	463	463	463	463	455	462
Lu	436	436	436	436	436	436	436	426	435
Hf	419	419	419	419	419	419	418	405	418
Ta	379	379	379	379	379	379	379	369	377
Pb	414	413	413	414	413	414	413	403	413
Th	452	452	452	452	452	452	452	436	451
U	457	457	457	457	457	457	457	445	457

Table 11.2 continued.

	NIST-610 (Aug 2019)								
	05-Aug	05-Aug	05-Aug	05-Aug	06-Aug	06-Aug	06-Aug	06-Aug	Pearce et
ppm	i	j	k	l	a	b	c	d	al. (1997)
Sc	432	431	444	438	441	441	441	441	441
Ti	438	422	438	426	436	436	436	435	434
V	445	434	446	438	442	442	442	442	442
Mn	430	419	431	434	433	433	433	433	433
Co	400	395	406	405	405	405	405	405	405
Ni	447	433	452	437	444	444	444	444	444
Cu	429	422	418	426	430	430	430	430	430
Zn	456	450	470	446	456	456	457	457	456
Rb	431	418	440	426	431	431	431	431	431
Sr	502	485	511	487	499	499	498	498	497
Y	454	429	460	446	451	451	451	451	450
Zr	440	420	450	439	441	441	441	441	440
Nb	422	406	432	417	420	420	420	420	419
Ba	428	422	433	417	424	424	424	425	424
La	465	445	465	451	457	457	457	457	457
Ce	450	445	451	446	448	448	448	448	448
Pr	435	419	432	430	431	431	431	431	430
Nd	429	409	429	428	432	432	431	431	431
Sm	453	430	459	451	452	452	451	451	451
Eu	460	449	461	447	461	461	461	461	461
Tb	441	433	444	432	444	444	444	444	443
Gd	418	408	421	410	421	421	421	421	420
Dy	428	415	424	423	428	428	428	428	427
Ho	459	444	448	451	450	450	450	450	449
Er	431	419	422	422	427	427	427	427	426
Tm	424	412	420	410	421	421	421	421	420
Yb	463	449	460	451	463	463	463	463	462
Lu	440	415	432	429	436	436	436	436	435
Hf	429	399	410	411	419	419	419	419	418
Ta	387	358	375	369	379	379	379	379	377
Pb	418	391	415	399	414	413	413	414	413
Th	451	438	444	440	452	452	452	452	451
U	460	457	449	448	457	457	457	457	457

Table 11.2 continued.

	NIST-610 (Aug 2019)								
	06-Aug	06-Aug	06-Aug	06-Aug	06-Aug	06-Aug	06-Aug	07-Aug	Pearce et
ppm	a	b	c	d	e	f	g	a	al. (1997)
Sc	441	441	441	441	449	422	454	441	441
Ti	435	436	435	436	441	420	462	435	434
V	442	442	442	442	448	433	449	442	442
Mn	433	433	433	433	437	422	429	433	433
Co	405	405	405	405	410	386	407	405	405
Ni	444	444	444	444	442	430	456	444	444
Cu	430	430	430	430	433	420	428	430	430
Zn	457	456	457	457	465	529	552	457	456
Rb	431	431	431	431	442	427	439	431	431
Sr	498	499	498	498	507	497	498	497	497
Y	451	451	451	450	462	445	469	451	450
Zr	440	441	440	440	452	433	464	440	440
Nb	420	420	420	420	426	408	437	420	419
Ba	424	424	424	424	427	419	431	424	424
La	457	457	457	457	455	452	469	457	457
Ce	448	448	448	448	449	446	460	448	448
Pr	431	431	430	430	436	417	435	430	430
Nd	431	431	431	431	440	417	438	431	431
Sm	451	452	451	451	459	437	451	451	451
Eu	461	461	461	461	463	455	452	461	461
Tb	443	444	443	443	441	436	451	443	443
Gd	421	421	421	421	426	422	432	420	420
Dy	428	428	428	427	434	418	425	427	427
Ho	450	450	450	449	453	438	457	449	449
Er	427	427	427	426	436	419	428	426	426
Tm	421	421	421	420	434	426	413	420	420
Yb	463	463	463	462	475	455	455	462	462
Lu	436	436	436	435	445	424	438	435	435
Hf	418	419	418	418	437	419	418	418	418
Ta	379	379	378	378	394	381	375	378	377
Pb	414	413	413	413	415	426	404	413	413
Th	452	452	452	451	450	457	445	451	451
U	457	457	457	457	458	469	446	457	457

Table 11.2 continued.

	NIST-610 (Aug 2019)							
	08-Aug	08-Aug	08-Aug	08-Aug	08-Aug	08-Aug	08-Aug	Pearce et
ppm	a	b	c	d	e	f	g	al. (1997)
Sc	451	426	436	417	445	431	440	441
Ti	443	408	429	424	441	426	435	434
V	444	420	438	440	450	416	454	442
Mn	430	408	427	406	437	402	440	433
Co	404	383	398	385	412	382	413	405
Ni	444	431	436	426	444	423	451	444
Cu	441	413	442	413	429	424	434	430
Zn	471	643	551	598	491	690	458	456
Rb	448	414	437	429	437	421	434	431
Sr	523	475	513	484	502	472	503	497
Y	471	445	471	429	445	452	451	450
Zr	459	435	455	422	436	439	442	440
Nb	436	410	432	418	418	410	425	419
Ba	441	409	445	423	434	414	423	424
La	463	450	478	441	461	479	459	457
Ce	451	445	471	441	458	450	449	448
Pr	440	410	466	410	446	411	432	430
Nd	437	399	469	397	450	403	446	431
Sm	464	411	488	405	461	423	453	451
Eu	475	414	490	414	472	432	456	461
Tb	462	411	458	389	458	421	436	443
Gd	433	400	447	373	434	405	418	420
Dy	442	396	461	371	431	400	436	427
Ho	474	401	483	403	447	423	461	449
Er	440	387	466	381	430	394	430	426
Tm	429	389	448	371	415	381	422	420
Yb	480	433	493	403	461	418	459	462
Lu	461	400	469	382	438	403	436	435
Hf	438	391	451	366	430	394	421	418
Ta	393	351	411	336	392	359	382	377
Pb	425	391	433	382	423	362	420	413
Th	468	426	489	393	475	426	460	451
U	465	422	490	427	488	388	464	457

Table 11.3: LA-ICP-MS results for NIST-612 glass collected during Oct/Nov 2018 and recommended concentrations of Pearce et al. (1997). Numbering is for individual days.

	NIST-612 (Oct/Nov 2018)								
	31-Oct	31-Oct	31-Oct	31-Oct	31-Oct	31-Oct	31-Oct	31-Oct	Pearce et
ppm	a	b	c	d	e	f	g	h	al. (1997)
Sc	33	35	34	37	37	38	36	37	41.1
Ti	35	37	35	35	35	37	36	38	48.1
V	36	37	36	36	37	38	37	38	39.2
Mn	34	35	35	36	36	36	36	36	38.4
Co	33	33	33	33	33	33	33	33	35.3
Ni	33	37	34	36	36	37	34	37	38.4
Cu	33	35	34	36	35	34	34	35	36.7
Zn	36	32	35	34	34	34	35	34	37.9
Rb	31	32	30	31	31	32	32	31	31.6
Sr	68	70	67	69	71	72	69	70	76.2
Y	31	33	33	34	35	35	33	34	38.3
Zr	32	34	33	35	35	35	34	35	36.0
Nb	31	32	30	32	32	32	31	31	38.1
Ba	33	35	34	34	36	36	35	35	37.7
La	32	34	31	32	33	34	32	32	35.8
Ce	34	35	32	33	34	34	33	33	38.4
Pr	32	32	30	31	32	32	31	31	37.2
Nd	32	33	31	32	33	33	33	33	35.2
Sm	33	34	33	34	35	35	34	34	36.7
Eu	32	33	32	32	34	33	33	32	34.4
Tb	31	32	31	32	33	33	33	32	35.9
Gd	31	32	31	32	33	33	32	32	37.0
Dy	29	31	31	32	33	32	32	31	36.0
Ho	31	32	31	33	34	33	33	33	37.9
Er	30	31	30	31	33	32	31	31	37.4
Tm	29	30	30	31	32	32	31	31	37.6
Yb	33	35	34	35	36	36	35	34	40.0
Lu	29	30	30	32	32	32	32	31	37.7
Hf	29	31	30	32	33	33	32	31	34.8
Ta	26	26	26	27	27	27	26	26	39.8
Pb	34	33	33	33	33	34	33	32	39.0
Th	30	28	27	28	29	28	28	28	37.2
U	33	29	28	28	29	29	28	29	37.2

Table 11.3 continued.

	NIST-612 (Oct/Nov 2018)				
	31-Oct	01-Nov	01-Nov	01-Nov	Pearce et
ppm	i	a	b	c	al. (1997)
Sc	39	35	35	35	41.1
Ti	35	36	35	35	48.1
V	37	36	35	36	39.2
Mn	35	35	34	35	38.4
Co	33	33	32	32	35.3
Ni	37	36	35	37	38.4
Cu	35	33	33	35	36.7
Zn	34	34	34	34	37.9
Rb	32	31	30	31	31.6
Sr	68	70	69	69	76.2
Y	34	33	33	32	38.3
Zr	36	34	32	33	36.0
Nb	32	32	31	31	38.1
Ba	36	35	34	35	37.7
La	33	33	32	32	35.8
Ce	34	33	33	33	38.4
Pr	32	30	30	31	37.2
Nd	33	32	32	32	35.2
Sm	35	34	33	34	36.7
Eu	32	32	32	32	34.4
Tb	33	31	31	31	35.9
Gd	32	31	31	31	37.0
Dy	32	31	30	31	36.0
Ho	34	31	31	31	37.9
Er	32	30	30	29	37.4
Tm	32	29	29	29	37.6
Yb	35	34	34	33	40.0
Lu	33	30	31	30	37.7
Hf	32	31	30	30	34.8
Ta	27	25	26	25	39.8
Pb	34	32	32	32	39.0
Th	29	27	27	26	37.2
U	29	28	28	28	37.2

Table 11.4: LA-ICP-MS results for NIST-612 glass collected during Aug 2019 and recommended concentrations of Pearce et al. (1997). Numbering is for individual days.

	NIST-612 (Aug 2019)								
	05-Aug	05-Aug	05-Aug	05-Aug	05-Aug	05-Aug	05-Aug	06-Aug	Pearce et
ppm	a	b	c	d	e	f	g	a	al. (1997)
Sc	37	35	35	35	35	36	37	44	41.1
Ti	35	34	31	34	32	36	34	33	48.1
V	38	37	36	38	37	37	37	37	39.2
Mn	35	34	33	35	34	35	35	34	38.4
Co	34	32	32	33	32	33	33	33	35.3
Ni	37	37	36	35	36	36	35	37	38.4
Cu	35	34	35	36	33	35	35	35	36.7
Zn	33	33	35	35	35	34	35	36	37.9
Rb	31	30	28	28	30	26	27	32	31.6
Sr	67	68	66	66	65	67	68	65	76.2
Y	29	29	29	28	29	30	31	28	38.3
Zr	31	30	30	29	29	31	32	29	36.0
Nb	31	30	29	30	29	30	31	30	38.1
Ba	34	34	33	33	34	34	35	33	37.7
La	31	31	30	31	31	31	32	31	35.8
Ce	34	34	34	34	33	34	35	34	38.4
Pr	31	30	30	30	30	32	32	31	37.2
Nd	31	30	30	29	30	31	31	29	35.2
Sm	32	32	31	30	31	32	32	30	36.7
Eu	31	31	30	31	30	30	31	30	34.4
Tb	29	29	28	28	28	29	30	28	35.9
Gd	29	29	28	28	28	29	29	27	37.0
Dy	28	28	28	27	28	29	29	27	36.0
Ho	29	29	29	28	28	31	30	27	37.9
Er	29	28	28	27	28	29	30	27	37.4
Tm	28	27	26	26	26	27	29	26	37.6
Yb	32	31	31	30	30	32	32	30	40.0
Lu	28	27	27	26	27	28	28	26	37.7
Hf	28	28	27	26	27	29	29	26	34.8
Ta	25	24	23	23	24	26	25	23	39.8
Pb	35	36	33	34	34	34	34	34	39.0
Th	29	29	29	27	28	30	30	27	37.2
U	34	34	34	33	33	34	34	34	37.2

Table 11.4 continued.

	NIST-612 (Aug 2019)								
	06-Aug	06-Aug	06-Aug	06-Aug	06-Aug	06-Aug	06-Aug	07-Aug	Pearce et
ppm	b	c	d	e	f	g	h	a	al. (1997)
Sc	38	35	35	45	34	37	39	30	41.1
Ti	32	32	36	35	32	36	34	36	48.1
V	37	37	37	38	37	38	37	25	39.2
Mn	34	34	35	35	35	36	35	24	38.4
Co	33	33	33	33	33	34	33	23	35.3
Ni	34	36	36	37	36	41	38	30	38.4
Cu	35	35	34	37	33	36	37	27	36.7
Zn	36	29	32	30	34	27	29	27	37.9
Rb	30	30	30	31	29	36	32	24	31.6
Sr	67	67	67	70	65	69	69	40	76.2
Y	30	29	30	33	29	30	33	23	38.3
Zr	29	29	29	33	29	31	34	23	36.0
Nb	29	29	29	31	30	31	31	22	38.1
Ba	33	33	32	34	33	33	33	25	37.7
La	31	30	32	33	31	31	33	23	35.8
Ce	34	34	35	34	34	34	34	21	38.4
Pr	31	31	31	31	32	33	33	22	37.2
Nd	29	30	30	32	30	32	33	21	35.2
Sm	30	32	32	33	30	34	35	22	36.7
Eu	31	32	31	32	31	33	33	21	34.4
Tb	29	30	28	32	29	31	33	22	35.9
Gd	27	29	28	31	28	30	31	21	37.0
Dy	28	28	27	30	27	30	32	21	36.0
Ho	28	30	29	31	28	31	34	22	37.9
Er	28	29	27	31	28	30	34	21	37.4
Tm	27	28	27	29	27	29	33	22	37.6
Yb	30	32	31	34	31	33	36	22	40.0
Lu	28	29	27	30	27	29	33	22	37.7
Hf	27	29	27	30	27	29	33	22	34.8
Ta	24	25	24	26	25	26	29	19	39.8
Pb	34	36	34	34	35	38	35	23	39.0
Th	28	31	28	31	29	31	33	22	37.2
U	34	38	33	34	35	37	36	24	37.2

Table 11.4 continued.

	NIST-612 (Aug 2019)								
	07-Aug	07-Aug	07-Aug	07-Aug	08-Aug	08-Aug	08-Aug	08-Aug	Pearce et
ppm	b	c	d	e	a	b	c	d	al. (1997)
Sc	42	39	40	36	43	39	39	36	41.1
Ti	37	38	36	37	37	35	39	33	48.1
V	40	43	39	40	37	42	39	41	39.2
Mn	38	39	35	38	36	40	37	37	38.4
Co	39	38	35	38	33	39	37	37	35.3
Ni	40	41	38	41	37	43	39	39	38.4
Cu	41	43	34	39	36	41	38	38	36.7
Zn	24	24	34	25	38	24	28	26	37.9
Rb	29	29	32	33	31	38	33	26	31.6
Sr	77	76	70	69	70	77	73	71	76.2
Y	32	31	32	30	32	33	33	29	38.3
Zr	31	30	32	30	32	32	32	28	36.0
Nb	31	31	31	31	31	32	31	30	38.1
Ba	37	36	34	36	35	39	35	36	37.7
La	31	31	32	31	32	32	33	30	35.8
Ce	36	36	34	36	34	36	36	36	38.4
Pr	35	35	31	33	31	35	34	33	37.2
Nd	35	34	31	32	31	35	34	32	35.2
Sm	36	36	33	33	33	39	35	33	36.7
Eu	37	36	31	33	33	38	35	33	34.4
Tb	33	33	29	30	31	35	32	29	35.9
Gd	33	32	29	30	30	34	32	28	37.0
Dy	33	31	30	30	29	35	32	28	36.0
Ho	33	33	31	31	31	35	33	30	37.9
Er	34	32	30	31	30	34	33	29	37.4
Tm	33	31	28	30	28	33	31	28	37.6
Yb	37	35	32	34	32	38	36	32	40.0
Lu	33	31	29	30	29	33	32	27	37.7
Hf	31	30	30	30	29	33	33	27	34.8
Ta	26	26	26	26	25	27	28	25	39.8
Pb	41	41	34	39	34	43	41	39	39.0
Th	32	30	30	31	30	33	33	29	37.2
U	42	40	33	41	35	45	39	42	37.2

Table 11.4 continued.

	NIST-612 (Aug 2019)			
	08-Aug	08-Aug	08-Aug	Pearce et
ppm	e	f	g	al. (1997)
Sc	33	37	32	41.1
Ti	33	33	34	48.1
V	37	36	37	39.2
Mn	35	33	34	38.4
Co	35	32	33	35.3
Ni	38	35	37	38.4
Cu	36	35	38	36.7
Zn	31	33	34	37.9
Rb	30	31	25	31.6
Sr	66	65	66	76.2
Y	28	31	28	38.3
Zr	29	31	29	36.0
Nb	30	29	29	38.1
Ba	33	33	32	37.7
La	31	32	30	35.8
Ce	35	33	33	38.4
Pr	32	31	29	37.2
Nd	31	32	28	35.2
Sm	31	32	30	36.7
Eu	31	30	30	34.4
Tb	29	30	27	35.9
Gd	28	29	26	37.0
Dy	28	29	26	36.0
Ho	29	31	28	37.9
Er	29	30	27	37.4
Tm	27	29	26	37.6
Yb	32	32	29	40.0
Lu	28	29	26	37.7
Hf	29	29	26	34.8
Ta	25	25	23	39.8
Pb	38	34	34	39.0
Th	30	31	28	37.2
U	37	34	34	37.2

Table 11.5: LA-ICP-MS results for in-house cpx standard, CPX JJG-1424, collected during Aug 2018 and recommended concentrations (*). Numbering is for individual days. <d.l. denotes below detectable limits. n.a. denotes not analysed.

	CPX JJG 1424 (Aug 2018)								
	15-Aug	15-Aug	15-Aug	15-Aug	15-Aug	15-Aug	15-Aug	15-Aug	*
ppm	a	b	c	d	e	f	g	h	
Sc	37	35	30	30	31	29	34	28	30
Ti	1216	1187	1095	1113	1116	1037	1082	1090	n.a.
V	565	547	544	543	543	536	445	504	536
Mn	386	378	386	388	381	382	390	354	n.a.
Co	17	16	17	16	15	15	16	14	n.a.
Ni	245	236	256	246	240	242	250	225	226
Cu	0.382	0.413	0.503	0.911	0.186	0.417	0.328	0.188	n.a.
Zn	4.5	6.7	5.5	4.1	4.8	5.2	3.8	5.9	n.a.
Rb	< d.l.	< d.l.	0.18	< d.l.	0.58	< d.l.	< d.l.	< d.l.	1.02
Sr	313	314	287	304	283	292	299	301	303
Y	2.3	2.5	2.3	2.1	2.1	1.8	2.5	1.9	2.4
Zr	43	39	33	35	38	35	33	37	42
Nb	< d.l.	0.01	0.01	0.02	0.03	0.01	0.02	0.02	2.3
Ba	0.04	0.05	0.04	0.07	0.16	0.06	0.04	0.62	4.2
La	22	22	20	21	20	19	19	22	22
Ce	65	64	62	63	61	60	59	63	62
Pr	7.8	7.4	7.3	7.5	7.0	7.1	7.0	7.9	7.1
Nd	30	27	27	27	27	25	25	29	27
Sm	4.1	3.8	3.5	3.8	3.8	3.6	3.5	4.0	3.9
Eu	1.16	1.09	0.99	1.03	1.08	0.98	1.00	1.06	1.1
Tb	0.20	0.20	0.22	0.16	0.23	0.20	0.18	0.22	0.35
Gd	2.2	2.1	1.9	2.0	2.0	1.9	1.7	2.1	2.2
Dy	0.89	0.83	0.74	0.83	0.80	0.82	0.88	0.86	0.93
Ho	0.12	0.11	0.09	0.10	0.10	0.12	0.09	0.09	0.26
Er	0.17	0.18	0.14	0.17	0.17	0.16	0.18	0.14	0.3
Tm	0.01	0.01	0.01	0.03	0.01	0.01	0.02	0.02	0.37
Yb	0.06	0.10	0.06	0.08	0.09	0.07	0.12	0.07	0.29
Lu	0.01	0.01	0.01	0.00	0.00	0.00	0.01	0.01	0.35
Hf	1.9	1.7	1.6	1.7	1.9	1.7	1.5	2.2	2.1
Ta	< d.l.	0.00	< d.l.	< d.l.	< d.l.	0.01	0.00	0.00	0.98
Pb	0.27	0.36	0.26	0.23	0.26	0.52	0.79	0.27	1.17
Th	1.3	1.4	1.1	1.3	1.2	1.1	1.1	1.5	1.47
U	0.06	0.07	0.06	0.07	0.07	0.06	0.09	0.10	0.31

Table 11.5 continued.

	CPX JJG 1424 (Aug 2018)					
	15-Aug	20-Aug	20-Aug	20-Aug	20-Aug	*
ppm	i	a	b	c	d	
Sc	29	40	39	32	30	30
Ti	1198	1394	1908	1435	1387	n.a.
V	508	612	578	605	549	536
Mn	352	455	401	412	358	n.a.
Co	15	17	17	18	16	n.a.
Ni	219	283	252	272	235	226
Cu	0.526	0.472	0.960	0.413	0.263	n.a.
Zn	6.2	3.4	3.7	4.1	4.3	n.a.
Rb	0.73	< d.l.	0.17	< d.l.	0.17	1.02
Sr	302	365	324	323	286	303
Y	2.0	2.6	2.3	2.1	2.1	2.4
Zr	41	43	51	46	46	42
Nb	< d.l.	0.02	0.65	0.01	0.01	2.3
Ba	0.08	0.23	0.05	0.05	<d.l.	4.2
La	23	25	24	21	19	22
Ce	63	70	66	61	54	62
Pr	7.7	8.7	7.9	7.7	6.7	7.1
Nd	28	33	30	30	26	27
Sm	3.9	4.7	4.4	4.2	3.8	3.9
Eu	1.04	1.34	1.21	1.21	1.03	1.1
Tb	0.26	0.23	0.25	0.24	0.20	0.35
Gd	2.0	2.4	2.3	2.3	2.0	2.2
Dy	0.80	1.03	0.91	0.81	0.78	0.93
Ho	0.08	0.12	0.11	0.13	0.10	0.26
Er	0.21	0.20	0.21	0.18	0.12	0.3
Tm	0.01	0.01	0.02	0.02	0.01	0.37
Yb	0.06	0.09	0.09	0.07	0.05	0.29
Lu	0.01	0.02	0.01	0.01	0.01	0.35
Hf	2.2	2.2	2.3	2.4	2.1	2.1
Ta	< d.l.	0.00	0.05	<d.l.	<d.l.	0.98
Pb	0.22	0.38	0.35	0.30	0.37	1.17
Th	1.5	1.4	1.6	1.5	1.4	1.47
U	0.08	0.08	0.15	0.11	0.09	0.31

Table 11.6: LA-ICP-MS results for in-house cpx standard, CPX JJG-1424, collected during Nov 2018 and recommended concentrations (*). Numbering is for individual days. <d.l. denotes below detectable limits. n.a. denotes not analysed.

	CPX JJG-1424 (Nov 2018)					
	01-Nov	01-Nov	01-Nov	01-Nov	01-Nov	*
ppm	a	b	c	d	e	
Sc	26	27	27	28	27	30
Ti	1233	1392	1247	1269	1295	n.a.
V	550	609	499	499	598	536
Mn	383	389	343	334	121	n.a.
Co	17	18	15	14	18	n.a.
Ni	248	272	225	218	276	226
Cu	0.5	0.8	0.4	0.4	0.7	n.a.
Zn	4.2	3.5	4.1	4.8	3.6	n.a.
Rb	0.13	0.12	0.10	0.08	0.05	1.02
Sr	303	316	263	257	323	303
Y	2.0	1.9	2.1	2.1	2.1	2.4
Zr	39	43	42	42	41	42
Nb	<d.l.	0.02	0.01	0.01	0.02	2.3
Ba	1.9	0.93	0.03	0.03	0.56	4.2
La	20	17	19	18	22	22
Ce	57	53	49	49	61	62
Pr	6.7	6.6	6.1	5.9	7.3	7.1
Nd	27	27	25	24	30	27
Sm	3.8	4.0	3.6	3.5	4.1	3.9
Eu	1.06	1.12	0.98	0.93	1.15	1.1
Tb	0.22	0.22	0.21	0.20	0.22	0.35
Gd	2.0	2.1	2.0	2.0	2.2	2.2
Dy	0.84	0.90	0.83	0.81	0.90	0.93
Ho	0.10	0.10	0.10	0.10	0.09	0.26
Er	0.16	0.18	0.16	0.14	0.18	0.3
Tm	0.013	0.011	0.013	0.012	0.014	0.37
Yb	0.08	0.09	0.08	0.07	0.08	0.29
Lu	0.005	0.009	0.007	0.005	0.005	0.35
Hf	2.2	2.1	2.1	2.1	2.1	2.1
Ta	<d.l.	<d.l.	<d.l.	<d.l.	0.001	0.98
Pb	0.23	0.57	0.19	0.18	0.30	1.17
Th	1.2	1.2	1.0	1.1	1.2	1.47
U	0.08	0.07	0.06	0.06	0.07	0.31

Table 11.7: LA-ICP-MS results for in-house cpx standard, CPX JJG-1424, collected during Aug 2019 and recommended concentrations (*). Numbering is for individual days. <d.l. denotes below detectable limits. n.a. denotes not analysed.

	CPX JJG-1424 (Aug 2019)								
	05-Aug	05-Aug	05-Aug	05-Aug	05-Aug	05-Aug	05-Aug	06-Aug	*
ppm	a	b	c	d	e	f	g	a	
Sc	41	34	42	38	41	34	37	37	30
Ti	1620	1334	1453	1505	1757	2428	2565	1315	n.a.
V	713	597	692	676	742	567	712	618	536
Mn	505	417	603	500	526	349	499	473	n.a.
Co	20	16	23	21	22	15	22	20	n.a.
Ni	298	253	335	308	317	236	316	282	226
Cu	0.8	0.3	0.8	1.5	1.0	0.5	1.2	0.6	n.a.
Zn	3.3	4.0	2.6	2.5	2.9	5.5	2.8	3.3	n.a.
Rb	<d.l.	<d.l.	<d.l.	<d.l.	<d.l.	<d.l.	<d.l.	<d.l.	1.02
Sr	386	333	488	402	423	297	388	373	303
Y	2.3	2.3	2.4	2.4	2.5	2.2	2.4	2.6	2.4
Zr	43	38	42	44	52	56	55	38	42
Nb	0.01	0.01	0.01	0.01	0.05	0.90	0.55	<d.l.	2.3
Ba	4.26	0.08	1.02	0.32	3.32	1.32	4.97	0.01	4.2
La	21	24	19	17	19	20	18	23	22
Ce	65	69	55	54	56	55	54	69	62
Pr	8.2	7.8	8.3	7.8	8.4	6.5	8.2	8.6	7.1
Nd	34	30	37	33	35	26	34	35	27
Sm	4.9	3.9	5.6	5.1	5.4	3.8	5.2	4.6	3.9
Eu	1.4	1.1	1.5	1.4	1.5	1.1	1.4	1.2	1.1
Tb	0.27	0.22	0.40	0.32	0.34	0.22	0.32	0.25	0.35
Gd	2.7	2.2	3.7	3.1	3.3	2.0	3.2	2.4	2.2
Dy	1.09	0.89	1.12	1.12	1.17	0.81	1.16	1.05	0.93
Ho	0.13	0.11	0.13	0.13	0.13	0.10	0.15	0.12	0.26
Er	0.27	0.19	0.43	0.33	0.29	0.17	0.31	0.21	0.3
Tm	0.02	0.01	0.02	0.02	0.02	0.02	0.02	0.03	0.37
Yb	0.12	0.09	0.13	0.12	0.12	0.07	0.13	0.10	0.29
Lu	0.01	0.01	0.01	0.01	0.01	0.01	0.00	0.01	0.35
Hf	2.2	1.9	2.2	2.4	2.6	2.3	2.9	1.8	2.1
Ta	<d.l.	<d.l.	0.001	0.001	<d.l.	0.008	0.007	<d.l.	0.98
Pb	0.34	0.27	0.41	0.77	0.55	0.27	0.48	0.30	1.17
Th	1.3	1.4	1.2	1.2	1.4	1.3	1.6	1.3	1.47
U	0.12	0.07	0.09	0.10	0.12	0.13	0.16	0.09	0.31

Table 11.7 continued.

	CPX JJG-1424 (Aug 2019)					
	08-Aug	08-Aug	08-Aug	08-Aug	08-Aug	*
ppm	a	b	c	d	e	
Sc	37	30	32	28	33	30
Ti	1598	1373	1201	1098	1276	n.a.
V	641	547	521	481	531	536
Mn	403	309	364	333	382	n.a.
Co	18	14	15	13	15	n.a.
Ni	266	206	224	211	231	226
Cu	0.5	0.1	0.4	0.4	0.3	n.a.
Zn	3.9	10	8	10	7	n.a.
Rb	<d.l.	<d.l.	<d.l.	<d.l.	<d.l.	1.02
Sr	342	267	306	297	322	303
Y	2.2	1.9	2.4	2.1	2.5	2.4
Zr	49	46	39	36	43	42
Nb	<d.l.	0.01	0.00	0.00	0.02	2.3
Ba	1.65	1.94	0.03	0.11	0.06	4.2
La	18	20	24	23	26	22
Ce	57	55	67	63	67	62
Pr	7.3	6.1	7.8	7.0	7.9	7.1
Nd	29	24	30	26	31	27
Sm	4.4	3.6	4.1	3.4	4.3	3.9
Eu	1.2	1.0	1.1	1.0	1.1	1.1
Tb	0.26	0.20	0.22	0.20	0.24	0.35
Gd	2.3	1.9	2.3	1.9	2.3	2.2
Dy	0.89	0.81	0.96	0.77	0.95	0.93
Ho	0.12	0.09	0.12	0.09	0.12	0.26
Er	0.20	0.14	0.20	0.15	0.22	0.3
Tm	0.01	0.01	0.02	0.02	0.02	0.37
Yb	0.09	0.07	0.10	0.07	0.07	0.29
Lu	0.01	0.00	0.01	0.00	0.01	0.35
Hf	2.7	2.2	1.9	1.7	2.1	2.1
Ta	0.001	<d.l.	0.001	<d.l.	<d.l.	0.98
Pb	0.34	0.26	0.25	0.26	0.38	1.17
Th	1.4	1.4	1.5	1.2	1.5	1.47
U	0.10	0.09	0.08	0.07	0.07	0.31

Table 11.8: LA-ICP-MS results for in-house garnet standard, Gt JJG-1424, collected during Aug 2018 and recommended concentrations (*). Numbering is for individual days. <d.l. denotes below detectable limits. n.a. denotes not analysed.

	Gt JJG 1424 (Aug 2018)					
	20-Aug	20-Aug	20-Aug	20-Aug	29-Aug	*
ppm	a	b	c	d	a	
Sc	67	67	58	58	77	50.89
Ti	387	407	831	434	509	n.a.
V	149	153	170	158	208	155
Mn	2551	2537	2838	2631	2430	n.a.
Co	39	40	43	40	38	23.1
Ni	18	15	16	15	15	14.1
Cu	0.51	0.02	<d.l.	<d.l.	0.25	1.95
Zn	5.8	6.4	4.0	6.3	9.3	5.16
Rb	< d.l.	0.08	< d.l.	0.18	0.06	0.032
Sr	0.07	0.07	0.06	0.12	0.09	0.419
Y	14	14	13	12	16	12.4
Zr	18	19	21	18	26	16.8
Nb	<d.l.	<d.l.	0.49	0.02	<d.l.	0.041
Ba	<d.l.	<d.l.	<d.l.	<d.l.	<d.l.	0.902
La	0.026	0.013	0.016	0.018	0.007	0.068
Ce	0.18	0.20	0.19	0.15	0.20	0.181
Pr	0.069	0.070	0.059	0.047	0.045	0.061
Nd	0.70	0.61	0.48	0.62	0.72	0.518
Sm	0.60	0.66	0.65	0.57	0.77	n.a.
Eu	0.39	0.39	0.40	0.37	0.44	0.467
Tb	0.33	0.35	0.29	0.25	0.40	0.340
Gd	1.4	1.5	1.2	1.2	1.8	1.50
Dy	2.6	2.6	2.3	2.3	2.7	2.41
Ho	0.62	0.61	0.56	0.57	0.62	0.575
Er	1.7	1.7	1.5	1.4	1.8	1.75
Tm	0.22	0.23	0.22	0.21	0.27	0.251
Yb	1.9	1.8	1.7	1.6	2.1	1.751
Lu	0.25	0.24	0.24	0.21	0.32	0.241
Hf	0.17	0.24	0.23	0.35	0.27	0.206
Ta	<d.l.	<d.l.	<d.l.	<d.l.	0.003	0.0103
Pb	0.022	0.014	0.023	<d.l.	0.010	0.0191
Th	0.018	0.004	0.088	0.009	0.011	0.0108
U	0.008	0.010	0.019	0.013	0.006	0.0065

Table 11.8 continued.

	Gt JJG 1424 (Aug 2018)					
	29-Aug	29-Aug	29-Aug	29-Aug	29-Aug	*
ppm	b	c	d	e	f	
Sc	85	66	62	66	69	50.89
Ti	417	1555	447	468	338	n.a.
V	144	190	165	173	137	155
Mn	2546	3106	2529	2504	2603	n.a.
Co	36	46	39	37	39	23.1
Ni	14	16	18	11	15	14.1
Cu	0.12	0.14	<d.l.	1.51	0.35	1.95
Zn	8.7	3.3	5.9	8.9	7.6	5.16
Rb	<d.l.	<d.l.	0.19	0.46	<d.l.	0.032
Sr	0.08	0.02	0.10	0.04	0.04	0.419
Y	20	13	13	14	16	12.4
Zr	23	25	19	21	17	16.8
Nb	<d.l.	0.71	<d.l.	<d.l.	<d.l.	0.041
Ba	0.14	<d.l.	<d.l.	<d.l.	<d.l.	0.902
La	0.011	0.045	0.054	0.022	0.011	0.068
Ce	0.20	0.21	0.17	0.17	0.16	0.181
Pr	0.056	0.111	0.059	0.052	0.061	0.061
Nd	0.81	0.72	0.66	0.69	0.71	0.518
Sm	0.71	0.71	0.64	0.66	0.68	n.a.
Eu	0.43	0.47	0.40	0.42	0.38	0.467
Tb	0.44	0.35	0.35	0.36	0.42	0.340
Gd	1.9	1.6	1.3	1.5	1.5	1.50
Dy	3.3	2.6	2.4	2.6	2.7	2.41
Ho	0.80	0.60	0.53	0.55	0.66	0.575
Er	2.2	1.7	1.4	1.7	1.9	1.75
Tm	0.32	0.23	0.26	0.23	0.29	0.251
Yb	2.5	2.1	1.8	1.8	2.1	1.751
Lu	0.31	0.30	0.24	0.26	0.35	0.241
Hf	0.26	0.41	0.19	0.22	0.22	0.206
Ta	<d.l.	0.005	<d.l.	<d.l.	<d.l.	0.0103
Pb	0.001	0.007	0.027	0.045	<d.l.	0.0191
Th	0.007	0.053	0.006	0.006	0.009	0.0108
U	0.010	0.076	0.008	0.010	0.010	0.0065

Table 11.9: LA-ICP-MS results for in-house garnet standard, Gt JJG-1424, collected during Oct/Nov 2018 and recommended concentrations (*). Numbering is for individual days. <d.l. denotes below detectable limits. n.a. denotes not analysed.

	Gt JJG-1424 (Oct/Nov 2018)								
	31-Oct	31-Oct	31-Oct	31-Oct	31-Oct	31-Oct	31-Oct	31-Oct	*
ppm	a	b	c	d	e	f	g	h	
Sc	84	72	76	80	75	74	80	68	50.89
Ti	589	433	368	472	502	769	1063	436	n.a.
V	230	168	135	151	171	205	211	154	155
Mn	3521	2891	2536	2575	2643	2498	2621	2818	n.a.
Co	55	44	36	37	38	37	37	44	23.1
Ni	18	16	15	15	14	13	13	17	14.1
Cu	0.42	0.12	0.03	0.10	0.07	0.15	<d.l.	0.18	1.95
Zn	4.5	4.1	5.8	6.5	4.8	6.1	7.1	5.1	5.16
Rb	0.09	0.07	0.17	<d.l.	0.24	<d.l.	<d.l.	0.14	0.032
Sr	0.15	0.06	0.07	0.26	0.09	0.09	0.17	0.12	0.419
Y	16	16	19	19	18	15	17	16	12.4
Zr	27	21	19	26	27	29	33	23	16.8
Nb	0.005	0.002	0.001	0.001	0.001	0.058	0.153	0.004	0.041
Ba	0.05	<d.l.	<d.l.	0.38	<d.l.	0.01	0.21	<d.l.	0.902
La	0.011	0.016	0.016	0.028	0.014	0.021	0.021	0.012	0.068
Ce	0.18	0.17	0.18	0.17	0.13	0.15	0.17	0.17	0.181
Pr	0.08	0.06	0.07	0.07	0.06	0.07	0.07	0.08	0.061
Nd	0.9	0.7	0.7	0.8	0.8	0.8	0.9	0.8	0.518
Sm	1.0	0.7	0.6	0.8	0.8	0.7	0.8	0.8	n.a.
Eu	0.56	0.43	0.38	0.47	0.45	0.42	0.43	0.47	0.467
Tb	0.46	0.41	0.40	0.44	0.39	0.35	0.39	0.43	0.340
Gd	1.9	1.9	1.6	1.9	1.8	1.6	1.7	1.9	1.50
Dy	3.6	3.1	3.1	3.3	3.2	2.6	2.9	3.4	2.41
Ho	0.75	0.67	0.71	0.71	0.69	0.56	0.60	0.72	0.575
Er	2.2	1.9	2.0	2.0	2.1	1.8	1.9	2.0	1.75
Tm	0.34	0.28	0.30	0.30	0.32	0.28	0.29	0.30	0.251
Yb	2.6	2.1	2.3	2.3	2.4	2.1	2.3	2.3	1.751
Lu	0.35	0.30	0.32	0.30	0.34	0.30	0.33	0.32	0.241
Hf	0.37	0.26	0.25	0.33	0.48	0.50	0.57	0.29	0.206
Ta	<d.l.	<d.l.	<d.l.	<d.l.	<d.l.	<d.l.	0.001	<d.l.	0.0103
Pb	0.020	0.032	0.002	0.013	0.004	0.003	0.013	0.006	0.0191
Th	0.005	0.006	0.010	0.006	0.005	0.014	0.028	0.007	0.0108
U	0.009	0.008	0.005	0.005	0.005	0.014	0.024	0.004	0.0065

Table 11.9 continued.

	Gt JJG-1424 (Oct/Nov 2018)							
	31-Oct	31-Oct	31-Oct	01-Nov	01-Nov	01-Nov	01-Nov	*
ppm	i	j	k	a	b	c	d	
Sc	62	65	72	83	68	70	66	50.89
Ti	478	384	558	455	432	589	582	n.a.
V	149	146	155	148	176	155	159	155
Mn	2442	2554	2498	2704	2992	2706	2567	n.a.
Co	37	39	37	40	48	41	38	23.1
Ni	13	15	12	15	17	16	14	14.1
Cu	0.36	0.46	0.24	0.04	0.14	1.04	0.21	1.95
Zn	5.6	5.2	7.4	8.8	3.5	4.4	4.8	5.16
Rb	0.13	<d.l.	<d.l.	0.02	0.20	0.21	0.12	0.032
Sr	0.49	<d.l.	0.57	0.09	0.12	0.17	0.09	0.419
Y	14	16	16	19	16	16	14	12.4
Zr	22	20	24	23	21	23	24	16.8
Nb	0.040	0.008	0.077	0.001	0.007	0.167	0.092	0.041
Ba	0.57	<d.l.	1.94	0.01	<d.l.	0.35	0.03	0.902
La	0.036	<d.l.	0.054	0.016	0.023	0.031	0.014	0.068
Ce	0.18	0.65	0.18	0.20	0.21	0.17	0.15	0.181
Pr	0.06	0.08	0.07	0.07	0.06	0.07	0.06	0.061
Nd	0.7	0.8	0.7	0.8	0.7	0.8	0.7	0.518
Sm	0.7	0.7	0.7	0.8	0.7	0.8	0.7	n.a.
Eu	0.42	0.41	0.41	0.43	0.47	0.41	0.43	0.467
Tb	0.38	0.39	0.38	0.42	0.40	0.40	0.36	0.340
Gd	1.5	1.6	1.7	1.9	1.6	1.8	1.7	1.50
Dy	2.7	3.0	2.9	3.5	3.2	3.2	2.7	2.41
Ho	0.59	0.66	0.62	0.74	0.70	0.69	0.57	0.575
Er	1.7	1.8	1.8	2.1	2.0	2.0	1.7	1.75
Tm	0.25	0.26	0.26	0.31	0.28	0.28	0.25	0.251
Yb	2.0	2.2	2.0	2.3	2.3	2.2	2.0	1.751
Lu	0.29	0.29	0.30	0.31	0.29	0.31	0.28	0.241
Hf	0.36	0.32	0.34	0.27	0.30	0.35	0.38	0.206
Ta	<d.l.	0.001	<d.l.	<d.l.	0.001	<d.l.	<d.l.	0.0103
Pb	0.022	0.067	0.033	0.008	0.017	0.024	0.030	0.0191
Th	0.031	0.042	0.022	0.006	0.009	0.031	0.024	0.0108
U	0.010	0.008	0.010	0.008	0.006	0.012	0.009	0.0065

Table 11.10: LA-ICP-MS results for in-house garnet standard, Gt JJG-1424, collected during Aug 2019 and recommended concentrations (*). Numbering is for individual days. <d.l. denotes below detectable limits. n.a. denotes not analysed.

	Gt JJG-1424 (Aug 2019)							
	06-Aug	06-Aug	06-Aug	06-Aug	06-Aug	07-Aug	07-Aug	*
ppm	a	b	c	d	e	a	b	
Sc	73	73	96	90	74	74	78	50.89
Ti	554	553	484	481	419	572	421	n.a.
V	209	217	189	168	148	214	135	155
Mn	2582	2571	3981	4089	3086	2657	2505	n.a.
Co	38	38	55	59	45	39	36	23.1
Ni	14	14	21	23	18	14	14	14.1
Cu	0.07	0.04	<d.l.	0.75	0.31	0.03	0.06	1.95
Zn	8.2	9.3	2.9	1.8	4.3	7.6	12.1	5.16
Rb	0.33	1.40	<d.l.	<d.l.	<d.l.	<d.l.	<d.l.	0.032
Sr	0.111	0.092	0.093	0.113	0.067	0.122	0.083	0.419
Y	15	15	22	19	17	16	18	12.4
Zr	26	25	22	18	17	26	21	16.8
Nb		0.001	0.000	0.006	0.002	0.004	<d.l.	0.041
Ba	<d.l.	<d.l.	0.018	0.058	<d.l.	0.207	<d.l.	0.902
La	0.008	0.016	0.006	0.012	0.018	0.065	0.016	0.068
Ce	0.154	0.187	0.226	0.221	0.212	0.220	0.221	0.181
Pr	0.08	0.06	0.09	0.11	0.08	0.08	0.08	0.061
Nd	0.78	0.74	0.99	1.06	0.80	0.77	0.72	0.518
Sm	0.77	0.76	0.99	0.94	0.66	0.73	0.68	n.a.
Eu	0.44	0.42	0.60	0.59	0.45	0.42	0.43	0.467
Tb	0.32	0.34	0.57	0.50	0.41	0.35	0.38	0.340
Gd	1.6	1.6	2.2	1.9	1.6	1.6	1.7	1.50
Dy	2.6	2.6	4.7	4.3	3.2	2.6	3.1	2.41
Ho	0.57	0.53	1.04	0.94	0.70	0.57	0.69	0.575
Er	1.7	1.6	3.1	2.8	2.1	1.8	1.9	1.75
Tm	0.25	0.25	0.44	0.40	0.31	0.26	0.29	0.251
Yb	1.9	2.0	3.6	3.3	2.4	2.1	2.2	1.751
Lu	0.27	0.29	0.50	0.41	0.34	0.33	0.31	0.241
Hf	0.37	0.37	0.28	0.26	0.21	0.34	0.21	0.206
Ta	<d.l.	<d.l.	0.001	0.001	<d.l.	0.006	<d.l.	0.0103
Pb	0.008	0.007	0.003	0.116	0.012	0.277	0.020	0.0191
Th	0.006	0.006	0.011	0.002	0.010	0.015	0.012	0.0108
U	0.005	0.006	0.017	0.009	0.010	0.012	<d.l.	0.0065

Table 11.10 continued.

	Gt JJG-1424 (Aug 2019)					
	07-Aug	07-Aug	07-Aug	08-Aug	08-Aug	*
ppm	c	d	e	a	b	
Sc	80	72	81	79	78	50.89
Ti	472	635	441	426	444	n.a.
V	142	212	139	135	165	155
Mn	2504	2633	2584	2355	2699	n.a.
Co	37	39	37	35	40	23.1
Ni	13	14	15	14	15	14.1
Cu	<d.l.	0.83	0.16	0.13	0.38	1.95
Zn	12.6	9.3	9.6	16.6	5.6	5.16
Rb	<d.l.	<d.l.	<d.l.	0.45	<d.l.	0.032
Sr	0.097	1.245	0.076	0.171	0.096	0.419
Y	20	14	19	20	18	12.4
Zr	23	24	22	23	22	16.8
Nb	0.000	0.029	0.003	0.079	0.018	0.041
Ba	0.017	1.8	<d.l.	0.116	0.022	0.902
La	0.023	0.193	0.016	0.120	0.037	0.068
Ce	0.210	0.358	0.207	0.334	0.196	0.181
Pr	0.06	0.08	0.08	0.15	0.09	0.061
Nd	0.75	0.78	0.77	0.81	0.73	0.518
Sm	0.71	0.73	0.72	0.72	0.73	n.a.
Eu	0.44	0.45	0.43	0.50	0.42	0.467
Tb	0.44	0.38	0.43	0.46	0.38	0.340
Gd	1.7	1.6	1.7	1.8	1.6	1.50
Dy	3.2	2.6	3.3	3.2	3.0	2.41
Ho	0.73	0.56	0.74	0.69	0.64	0.575
Er	2.1	1.8	2.1	2.0	1.9	1.75
Tm	0.30	0.27	0.28	0.31	0.27	0.251
Yb	2.3	2.1	2.3	2.1	2.1	1.751
Lu	0.33	0.32	0.33	0.36	0.34	0.241
Hf	0.28	0.36	0.27	0.30	0.32	0.206
Ta	<d.l.	<d.l.	0.001	0.091	0.008	0.0103
Pb	0.015	0.754	0.008	0.104	0.035	0.0191
Th	0.010	0.037	0.009	0.070	0.027	0.0108
U	0.006	0.018	0.005	0.100	0.029	0.0065

12. Appendix D

REE-based thermobarometry PT inversion diagrams and equilibrium assessment diagrams

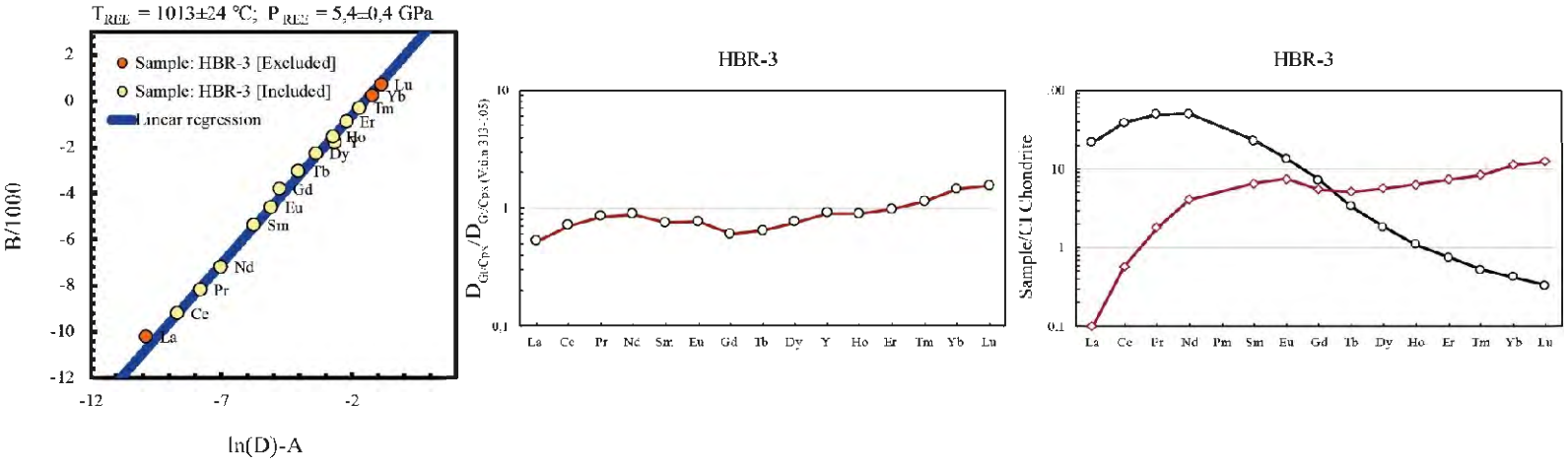
T_REE = 1013±24 °C; P_REE = 5,4±0,4 GPa
Sample: HBR-3 [Excluded]
Sample: HBR-3 [Included]
Linear regression
B/1000
ln(D)-A
HBR-3
HBR-3
Sample/CI Chondrite

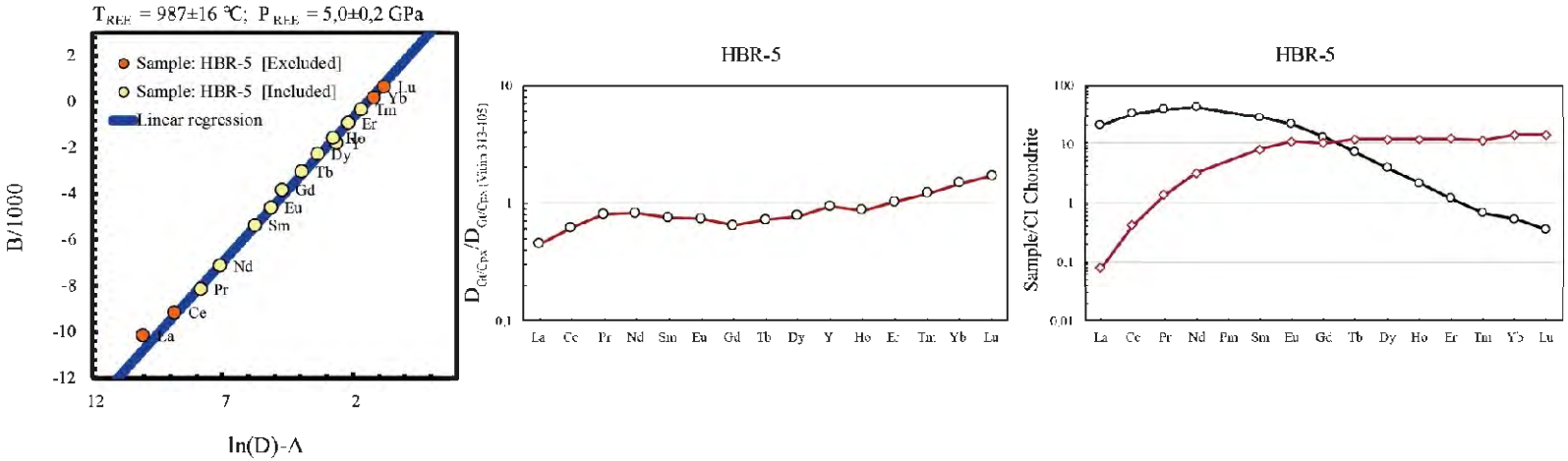
T_REE = 987±16 °C; P_REE = 5,0±0,2 GPa
Sample: HBR-5 [Excluded]
Sample: HBR-5 [Included]
Linear regression
B/1000
ln(D)-A
HBR-5
HBR-5
Sample/CI Chondrite

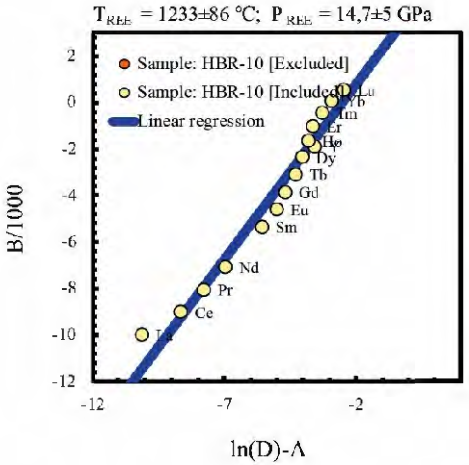
T REE = 1233±86 °C; P REE = 14,7±5 GPa
Sample: HBR-10 [Excluded]
Sample: HBR-10 [Included]
Linear regression
Lu
Yb
Tm
Er
Ho
Dy
Tb
Gd
Eu
Sm
Nd
Pr
Ce
La
B/1000
ln(D)-A
2
0
-2
-4
-6
-8
-10
-12
-12
-7
-2

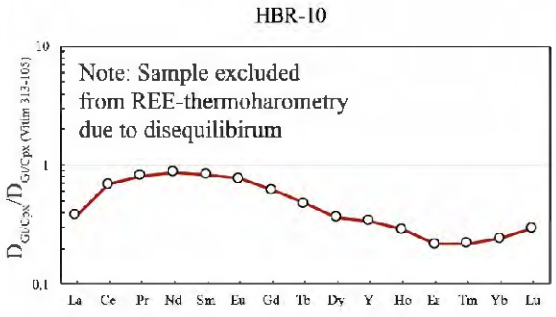
HBR-10
Note: Sample excluded
from REE-thermoharometry
due to disequilibirum
D Gt/Cpx /D Gt/Cpx (Vitim 313-105)
10
1
0,1
La Ce Pr Nd Sm Eu Gd Tb Dy Y Ho Er Tm Yb Lu

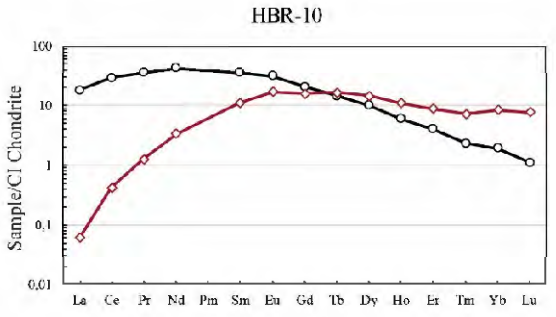
HBR-10
Sample/C1 Chondrite
100
10
1
0,1
0,01
La Ce Pr Nd Pm Sm Eu Gd Tb Dy Ho Er Tm Yb Lu

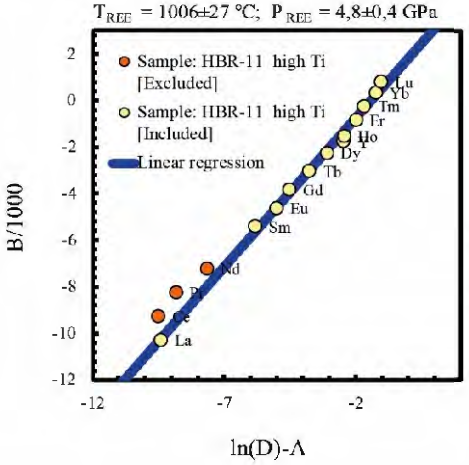
T REE = 1006±27 °C; P REE = 4,8±0,4 GPa
Sample: HBR-11 high Ti
[Excluded]
Sample: HBR-11 high Ti
[Included]
Linear regression
Lu
Yb
Tm
Er
Ho
Dy
Tb
Gd
Eu
Sm
Nd
Pr
Ce
La
B/1000
ln(D)-A
2
0
-2
-4
-6
-8
-10
-12
-12
-7
-2

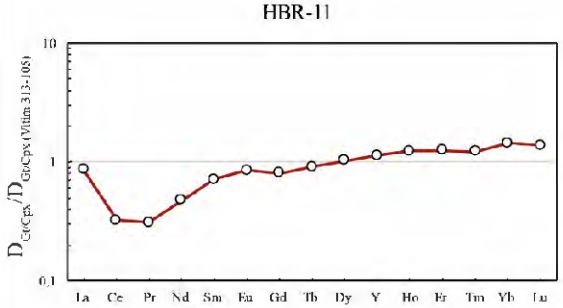
HBR-11
D Gt/Cpx /D Gt/Cpx (Vitim 313-105)
10
1
0,1
La Ce Pr Nd Sm Eu Gd Tb Dy Y Ho Er Tm Yb Lu

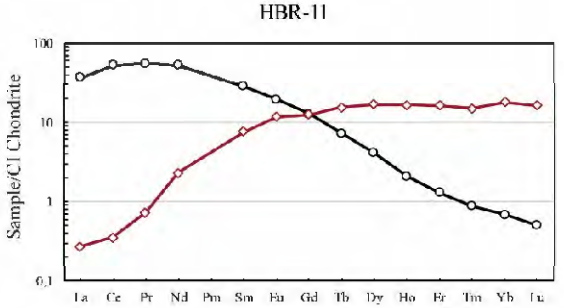
HBR-11
Sample/C1 Chondrite
100
10
1
0,1
La Ce Pr Nd Pm Sm Eu Gd Tb Dy Ho Er Tm Yb Lu

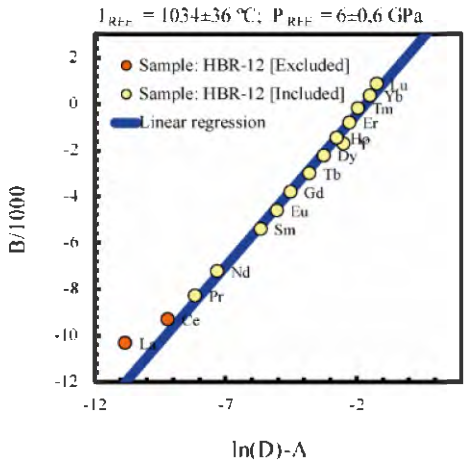
T_{REE} = 1034±36 °C; P_{REE} = 6±0,6 GPa
Sample: HBR-12 [Excluded]
Sample: HBR-12 [Included]
Linear regression
B/1000
ln(D)-A
La
Ce
Pr
Nd
Sm
Eu
Gd
Tb
Dy
Ho
Er
Tm
Yb
Lu

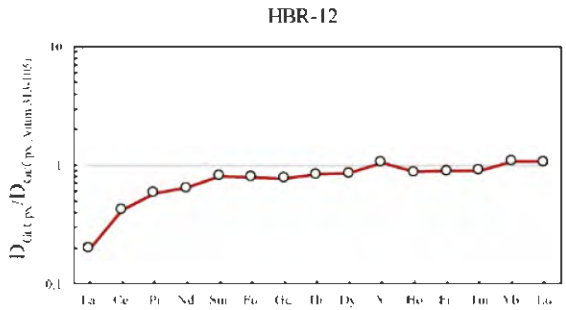
HBR-12

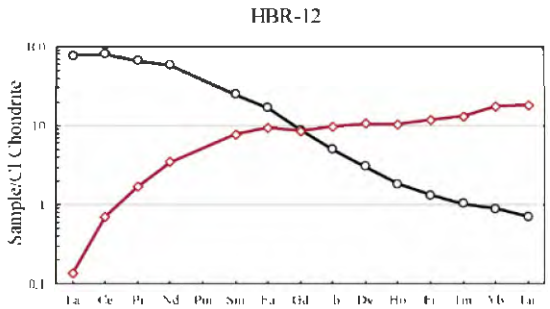
HBR-12
Sample/CI Chondrite

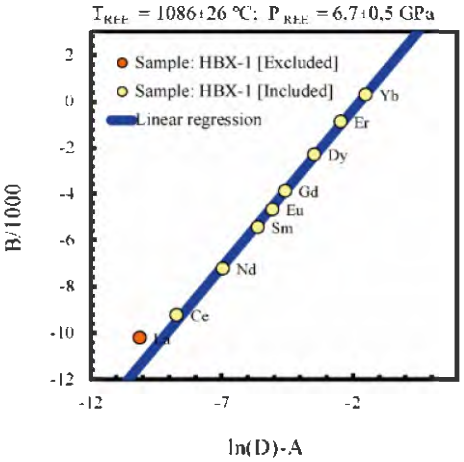
T_{REE} = 1086±26 °C; P_{REE} = 6,7±0,5 GPa
Sample: HBX-1 [Excluded]
Sample: HBX-1 [Included]
Linear regression
B/1000
ln(D)-A
La
Ce
Nd
Sm
Eu
Gd
Dy
Er
Yb

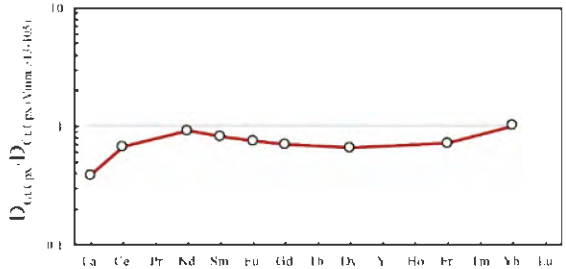
HBX-1

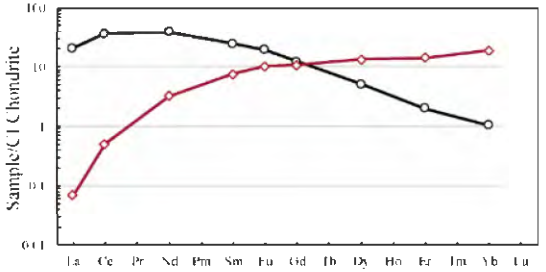
HBX-1
Sample/CI Chondrite

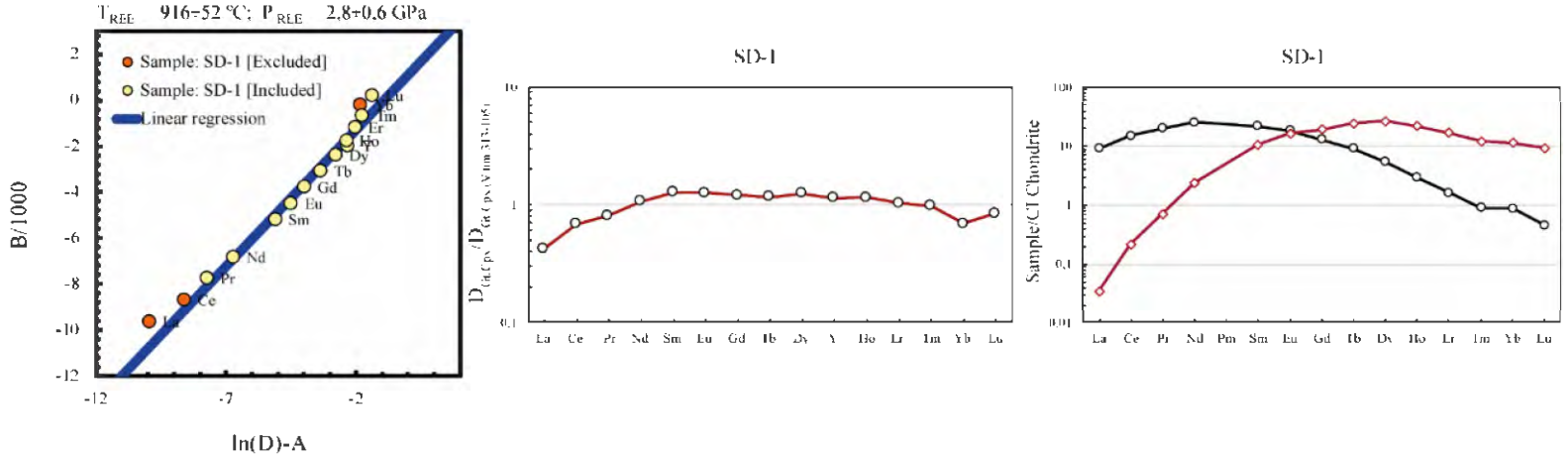
T REE 916±52 ℃; P REE 2.8±0.6 GPa
Sample: SD-1 [Excluded]
Sample: SD-1 [Included]
Linear regression
B/1000
ln(D)-A
SD-1
SD-1
Sample/CI Chondrite

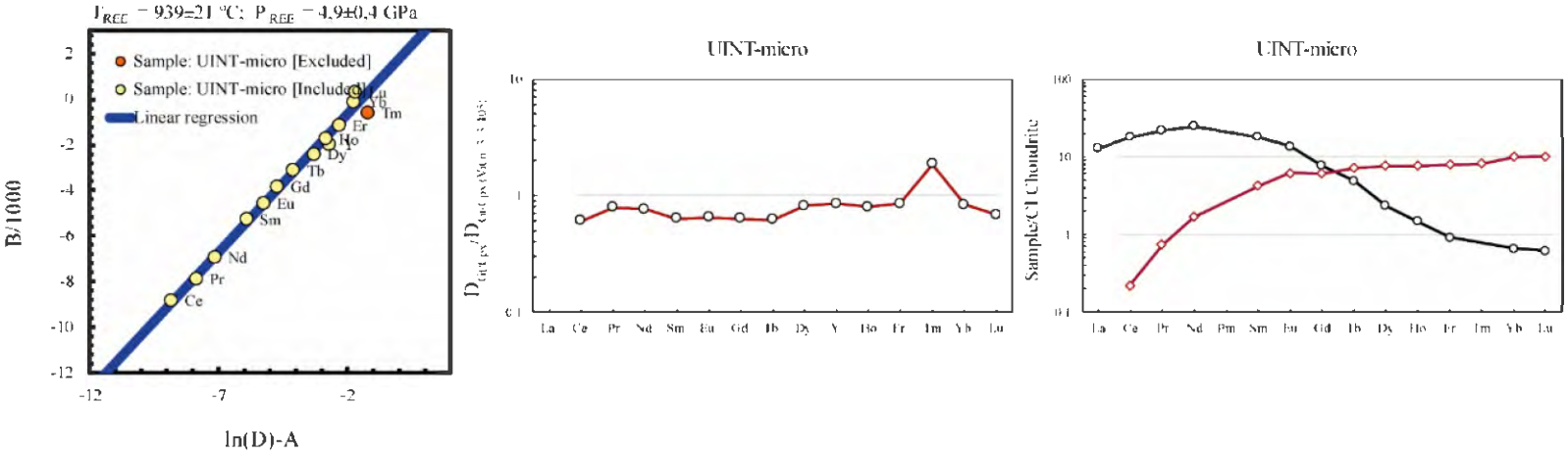
T REE = 939±21 ℃; P REE = 4.9±0.4 GPa
Sample: UINT-micro [Excluded]
Sample: UINT-micro [Included]
Linear regression
B/1000
ln(D)-A
UINT-micro
UINT-micro
Sample/CI Chondrite

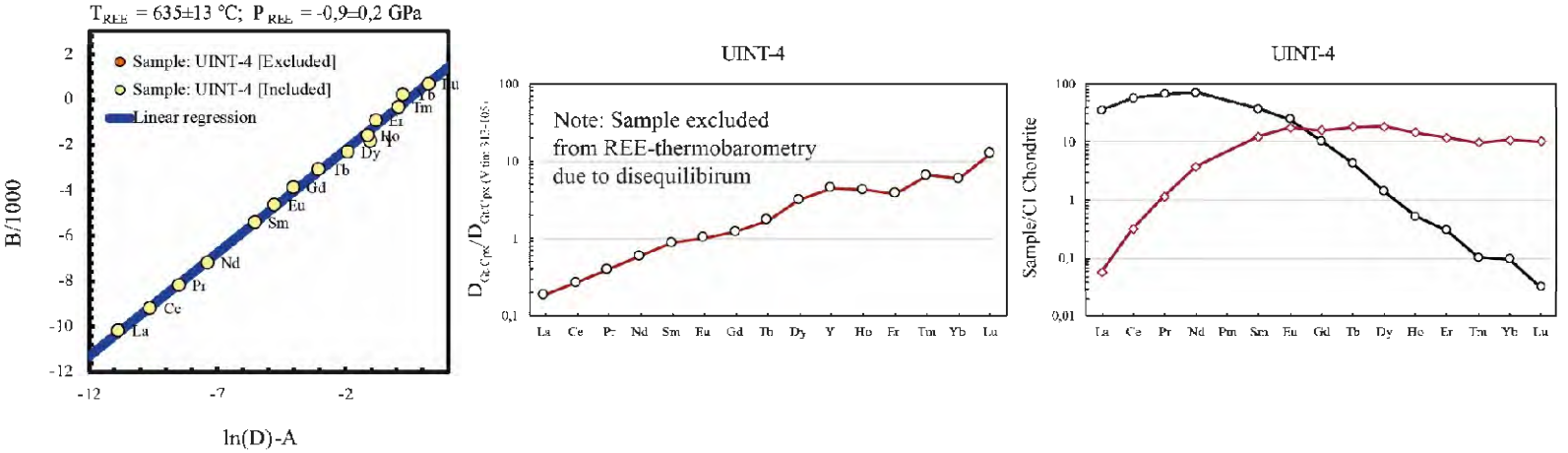
T_REE = 635±13 °C; P_REE = -0,9±0,2 GPa
Sample: UINT-4 [Excluded]
Sample: UINT-4 [Included]
Linear regression
B/1000
ln(D)-A
UINT-4
Note: Sample excluded
from REE-thermobarometry
due to disequilibirum
UINT-4
Sample/CI Chondrite

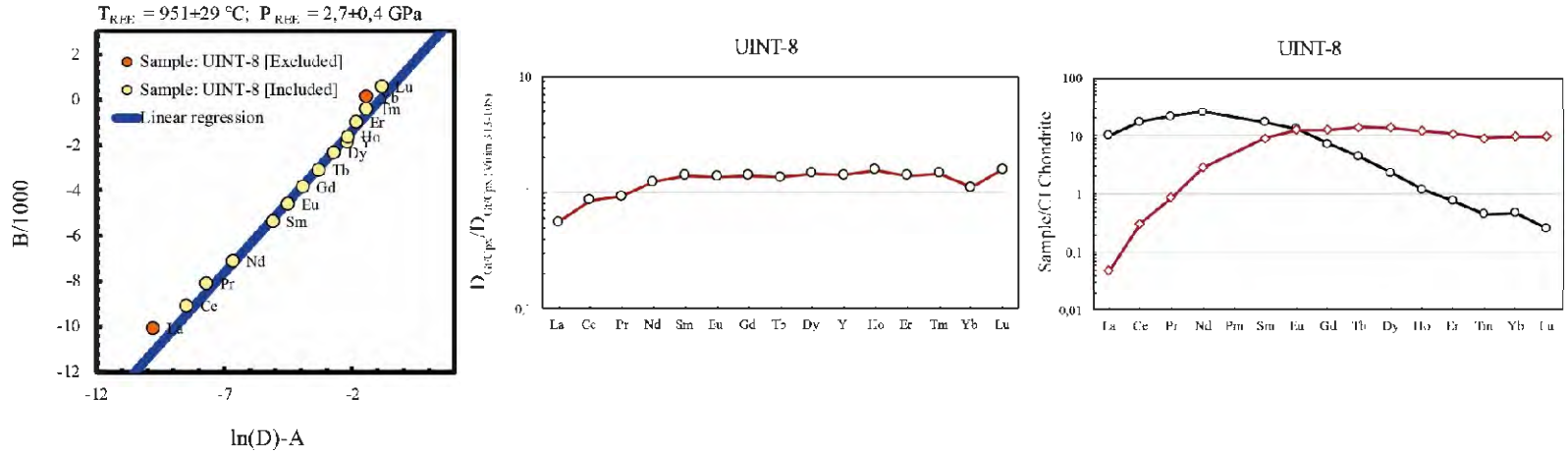
T_REE = 951±29 °C; P_REE = 2,7±0,4 GPa
Sample: UINT-8 [Excluded]
Sample: UINT-8 [Included]
Linear regression
B/1000
ln(D)-A
UINT-8
UINT-8
Sample/CI Chondrite

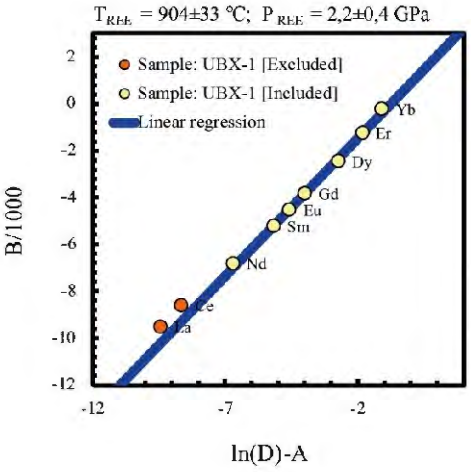
T_{REE} = 904±33 °C; P_{REE} = 2,2±0,4 GPa
Sample: UBX-1 [Excluded]
Sample: UBX-1 [Included]
Linear regression
Yb
Er
Dy
Gd
Eu
Sm
Nd
Ce
La
B/1000
ln(D)-A

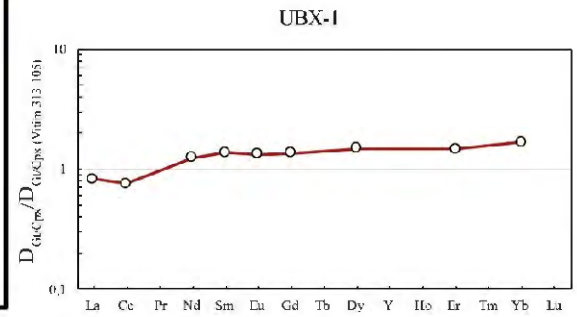
UBX-1
La Ce Pr Nd Sm Eu Gd Tb Dy Y Ho Er Tm Yb Lu

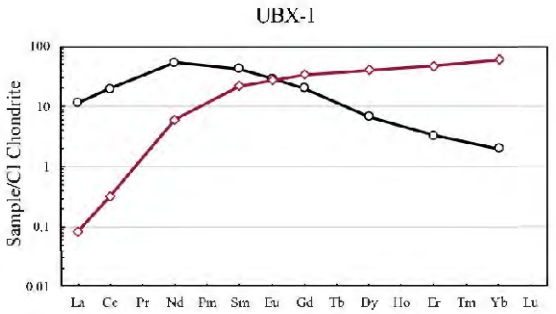
UBX-1
Sample/CI Chondrite
La Ce Pr Nd Pm Sm Eu Gd Tb Dy Ho Er Tm Yb Lu

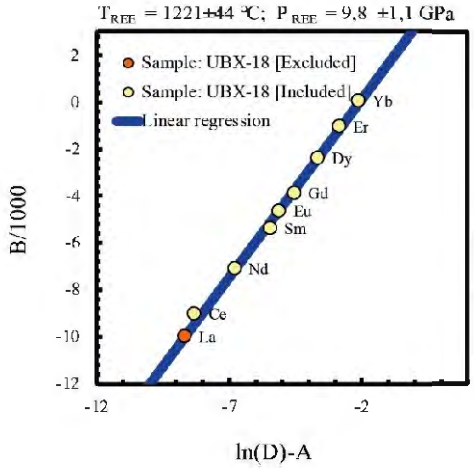
T_{REE} = 1221±44 °C; P_{REE} = 9,8 ±1,1 GPa
Sample: UBX-18 [Excluded]
Sample: UBX-18 [Included]
Linear regression
Yb
Er
Dy
Gd
Eu
Sm
Nd
Ce
La
B/1000
ln(D)-A

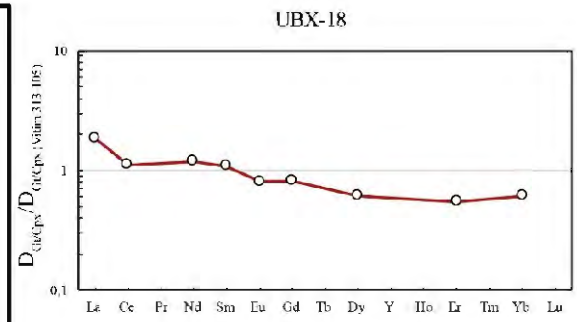
UBX-18
La Ce Pr Nd Sm Eu Gd Tb Dy Y Ho Er Tm Yb Lu

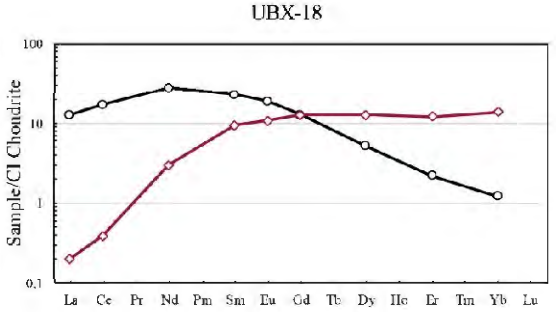
UBX-18
Sample/CI Chondrite
La Ce Pr Nd Pm Sm Eu Gd Tb Dy Ho Er Tm Yb Lu

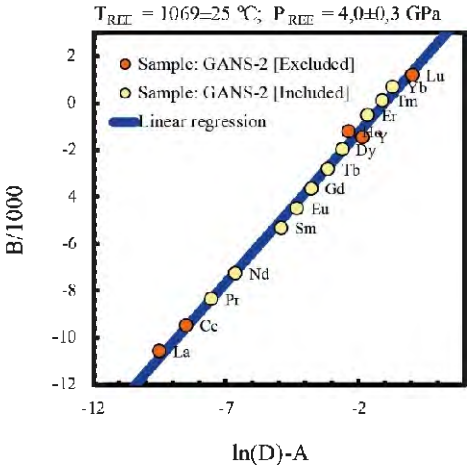
T_REE = 1069±25 °C; P_REE = 4,0±0,3 GPa
Sample: GANS-2 [Excluded]
Sample: GANS-2 [Included]
Linear regression
B/1000
ln(D)-A

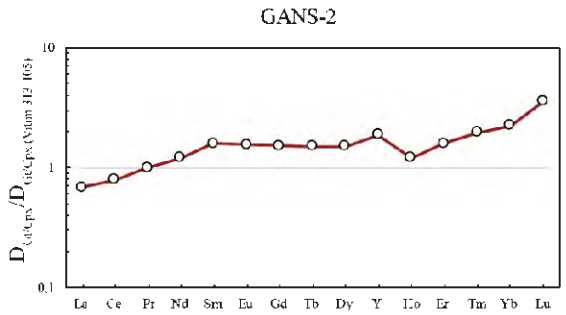
GANS-2

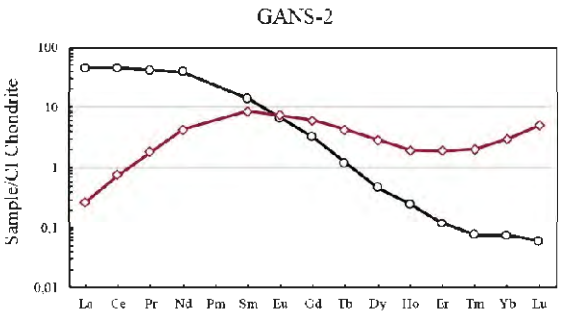
GANS-2
Sample/CI Chondrite

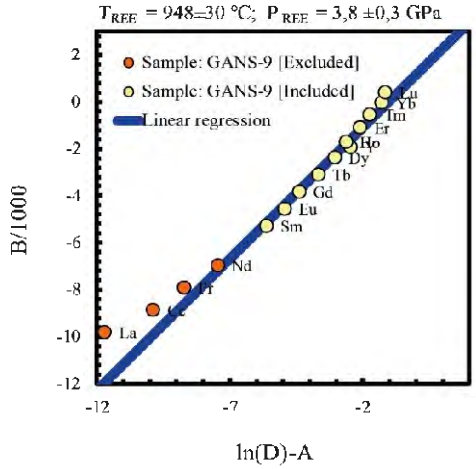
T_REE = 948±30 °C; P_REE = 3,8 ±0,3 GPa
Sample: GANS-9 [Excluded]
Sample: GANS-9 [Included]
Linear regression
B/1000
ln(D)-A

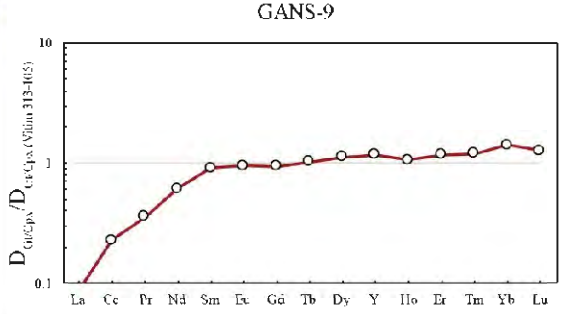
GANS-9

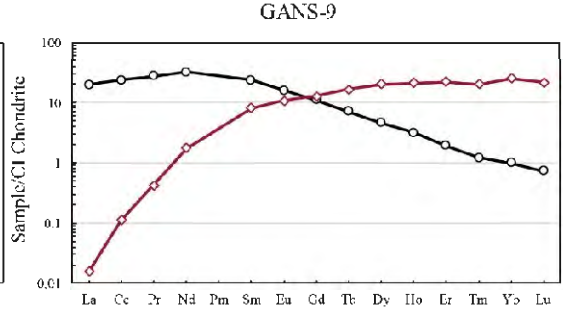
GANS-9
Sample/CI Chondrite

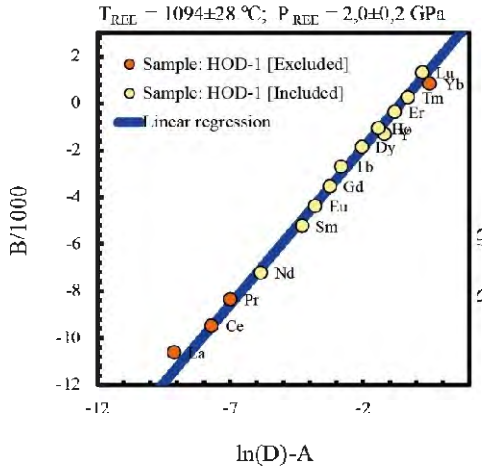
T REE = 1094±28 °C; P REE = 2,0±0,2 GPa
Sample: HOD-1 [Excluded]
Sample: HOD-1 [Included]
Linear regression
B/1000
ln(D)-A

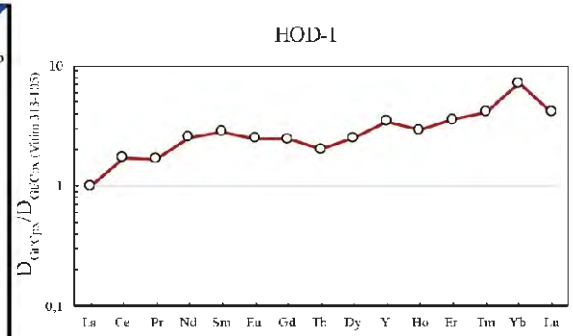
HOD-1

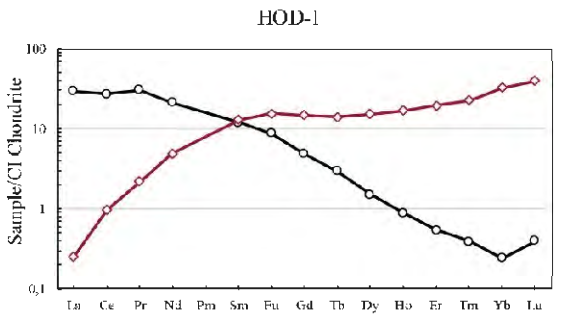
HOD-1
Sample/CI Chondrite

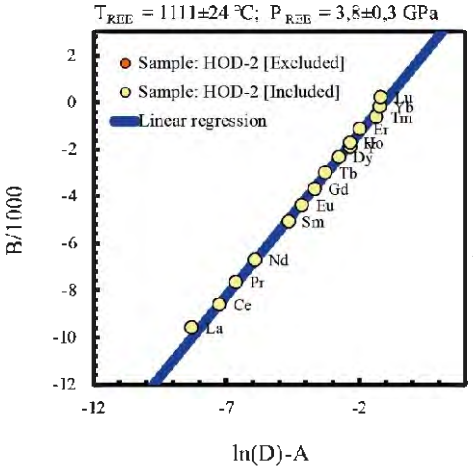
T REE = 1111±24 °C; P REE = 3,8±0,3 GPa
Sample: HOD-2 [Excluded]
Sample: HOD-2 [Included]
Linear regression
B/1000
ln(D)-A

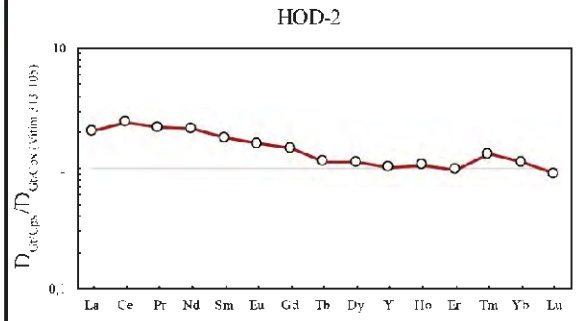
HOD-2

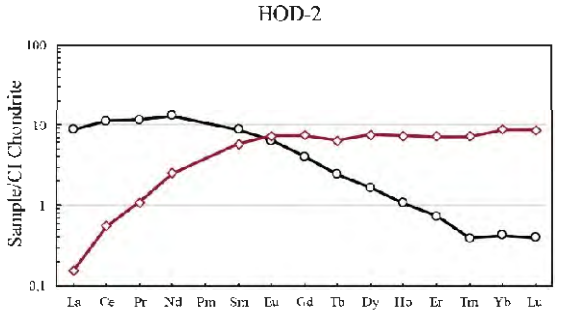
HOD-2
Sample/CI Chondrite

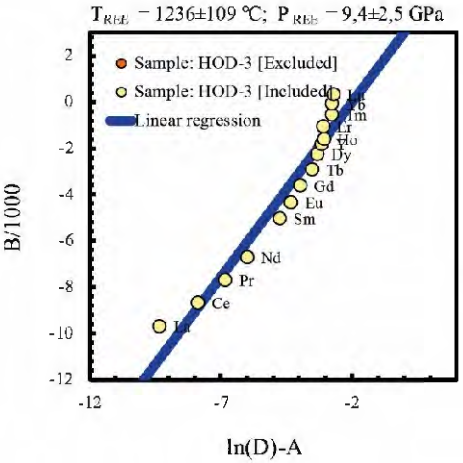
T_REE = 1236±109 °C; P_REE = 9,4±2,5 GPa
Sample: HOD-3 [Excluded]
Sample: HOD-3 [Included]
Linear regression
Lu
Yb
Tm
Er
Ho
Dy
Tb
Gd
Eu
Sm
Nd
Pr
Ce
La
B/1000
ln(D)-A

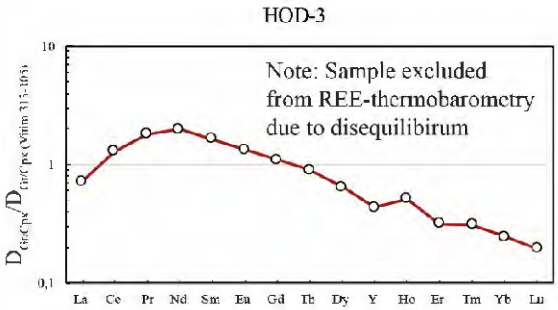
HOD-3
Note: Sample excluded
from REE-thermobarometry
due to disequilibirum
La Ce Pr Nd Sm Eu Gd Tb Dy Y Ho Er Tm Yb Lu

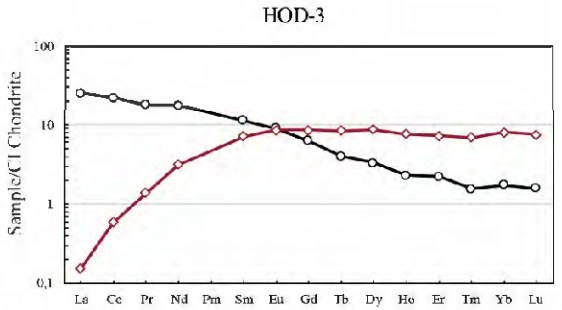
HOD-3
Sample/C1 Chondrite
La Ce Pr Nd Pm Sm Eu Gd Tb Dy Ho Er Tm Yb Lu

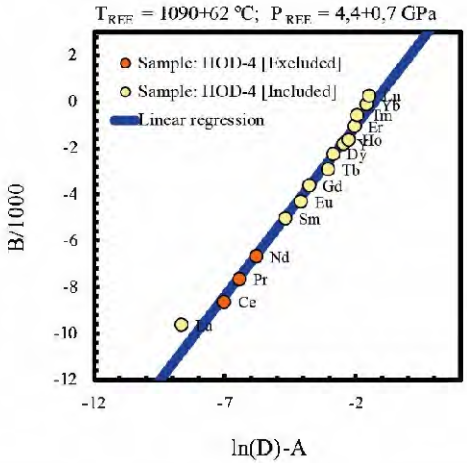
T_REE = 1090+62 °C; P_REE = 4,4+0,7 GPa
Sample: HOD-4 [Excluded]
Sample: HOD-4 [Included]
Linear regression
Lu
Yb
Tm
Er
Ho
Dy
Tb
Gd
Eu
Sm
Nd
Pr
Ce
La
B/1000
ln(D)-A

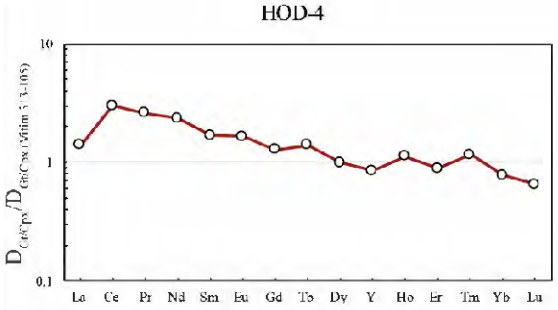
HOD-4
La Ce Pr Nd Sm Eu Gd Tb Dy Y Ho Er Tm Yb Lu

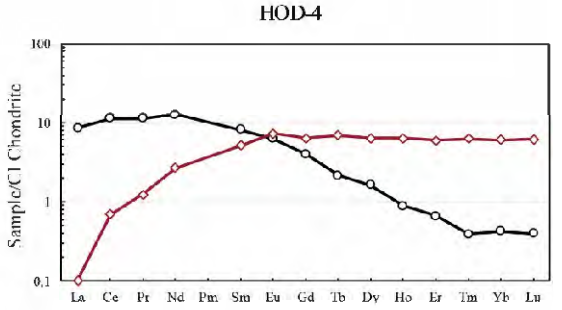
HOD-4
Sample/C1 Chondrite
La Ce Pr Nd Pm Sm Eu Gd Tb Dy Ho Er Tm Yb Lu

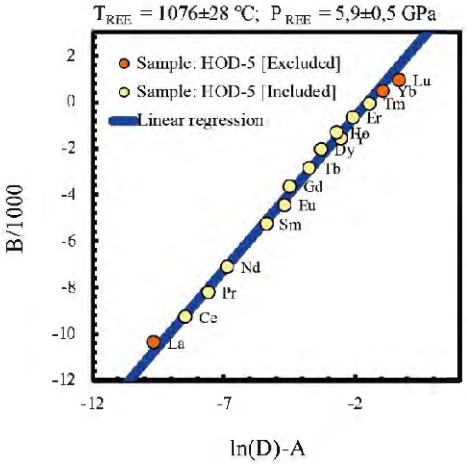
T REE = 1076±28 °C; P REE = 5,9±0,5 GPa
Sample: HOD-5 [Excluded]
Sample: HOD-5 [Included]
Linear regression
B/1000
ln(D)-A
La
Ce
Pr
Nd
Sm
Eu
Gd
Tb
Dy
Ho
Er
Tm
Yb
Lu

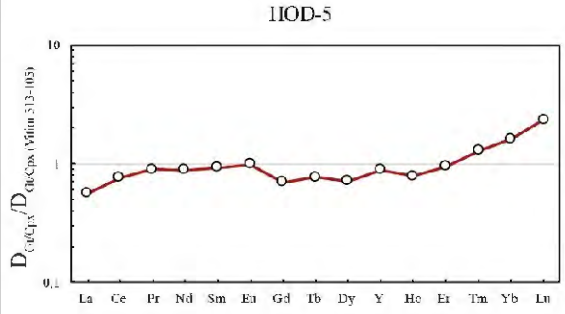
HOD-5
La Ce Pr Nd Sm Eu Gd Tb Dy Y Ho Er Tm Yb Lu

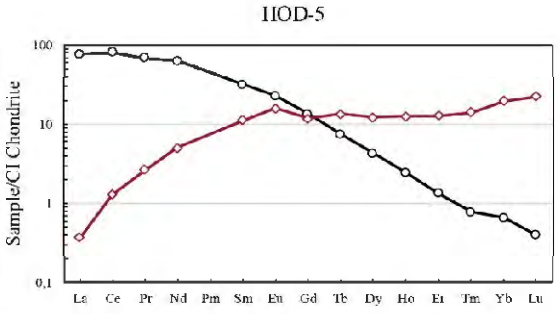
HOD-5
Sample/CI Chondrite
La Ce Pr Nd Pm Sm Eu Gd Tb Dy Ho Er Tm Yb Lu

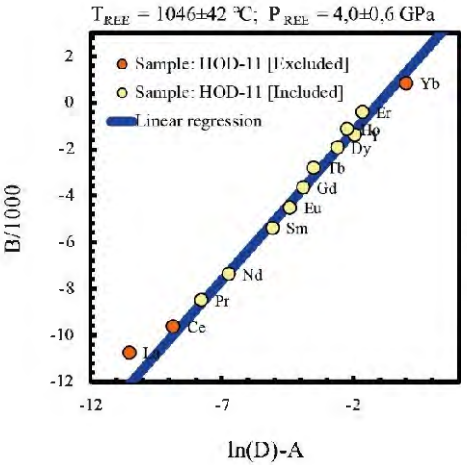
T REE = 1046±42 °C; P REE = 4,0±0,6 GPa
Sample: HOD-11 [Excluded]
Sample: HOD-11 [Included]
Linear regression
B/1000
ln(D)-A
Ce
Pr
Nd
Sm
Eu
Gd
Tb
Dy
Ho
Er
Yb

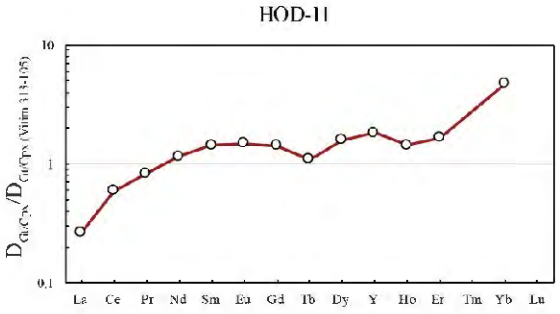
HOD-11
La Ce Pr Nd Sm Eu Gd Tb Dy Y Ho Er Tm Yb Lu

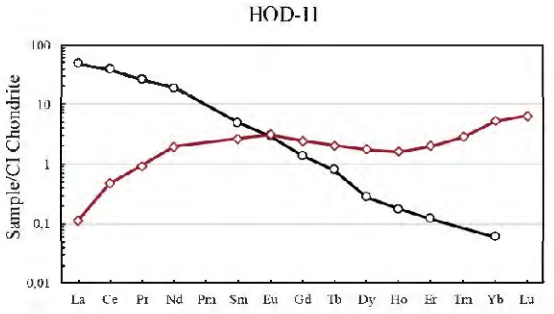
HOD-11
Sample/CI Chondrite
La Ce Pr Nd Pm Sm Eu Gd Tb Dy Ho Er Tm Yb Lu

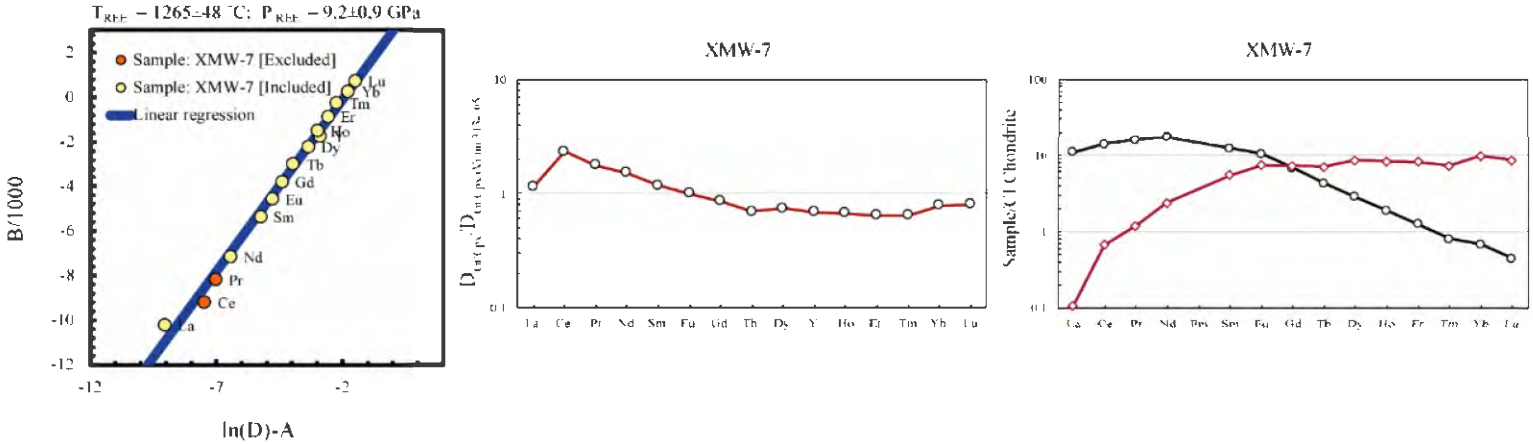
T_REE = 1265±48 °C; P_REE = 9.2±0.9 GPa
Sample: XMW-7 [Excluded]
Sample: XMW-7 [Included]
Linear regression
B/1000
ln(D)-A
XMW-7
XMW-7
Sample/C1 Chondrite

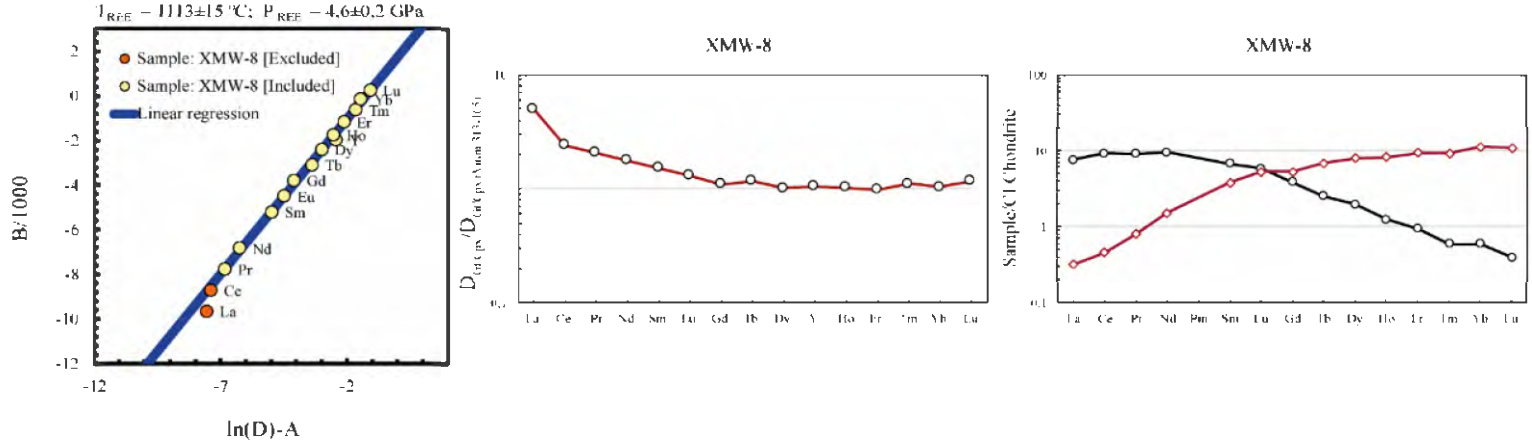
T_REE = 1113±15 °C; P_REE = 4.6±0.2 GPa
Sample: XMW-8 [Excluded]
Sample: XMW-8 [Included]
Linear regression
B/1000
ln(D)-A
XMW-8
XMW-8
Sample/C1 Chondrite

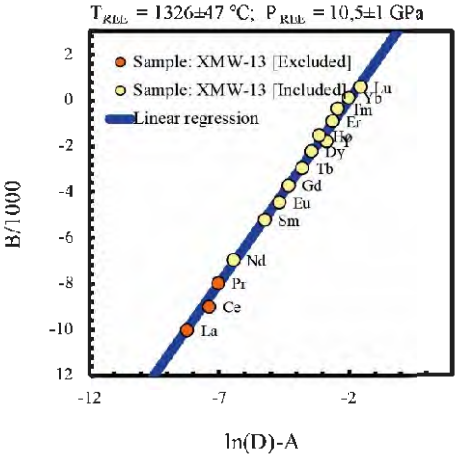
T_REE = 1326±47 °C; P_REE = 10,5±1 GPa
Sample: XMW-13 [Excluded]
Sample: XMW-13 [Included]
Linear regression
Lu
Yb
Tm
Er
Ho
Dy
Tb
Gd
Eu
Sm
Nd
Pr
Ce
La
B/1000
ln(D)-A

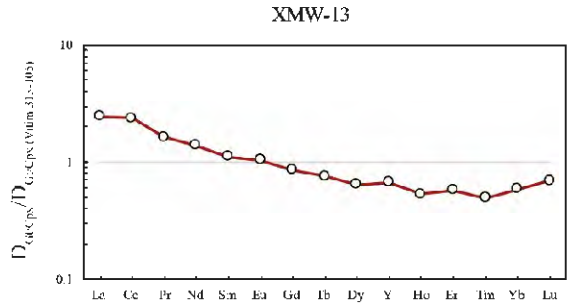
XMW-13
La Ce Pr Nd Sm Eu Gd Tb Dy Y Ho Er Tm Yb Lu

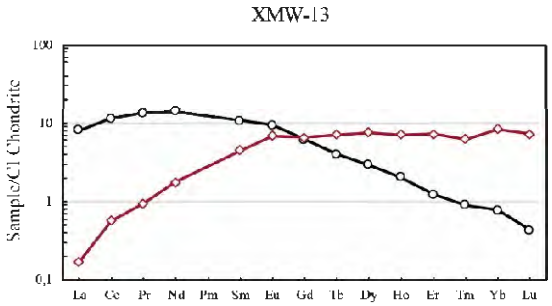
XMW-13
Sample/C1 Chondrite
La Ce Pr Nd Pm Sm Eu Gd Tb Dy Ho Er Tm Yb Lu

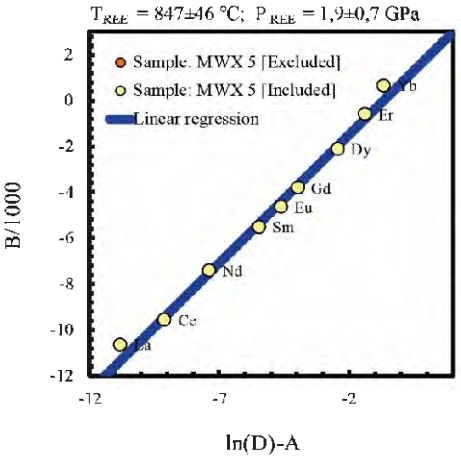
T_REE = 847±46 °C; P_REE = 1,9±0,7 GPa
Sample: MWX 5 [Excluded]
Sample: MWX 5 [Included]
Linear regression
Yb
Er
Dy
Gd
Eu
Sm
Nd
Ce
La
B/1000
ln(D)-A

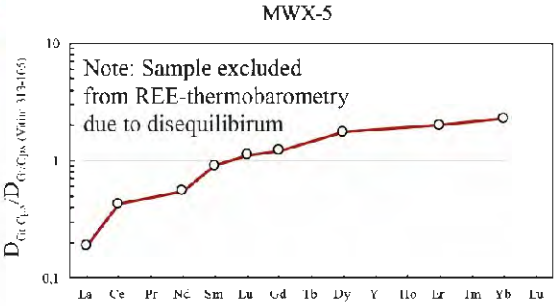
MWX-5
Note: Sample excluded
from REE-thermobarometry
due to disequilibirum
La Ce Pr Nd Sm Eu Gd Tb Dy Y Ho Er Tm Yb Lu

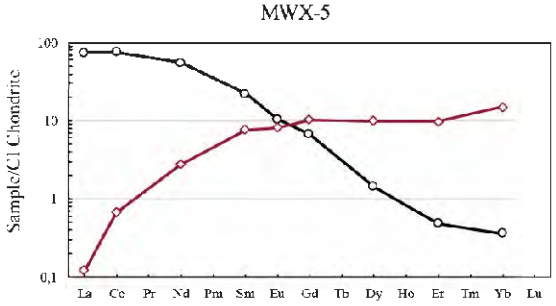
MWX-5
Sample/C1 Chondrite
La Ce Pr Nd Pm Sm Eu Gd Tb Dy Ho Er Tm Yb Lu

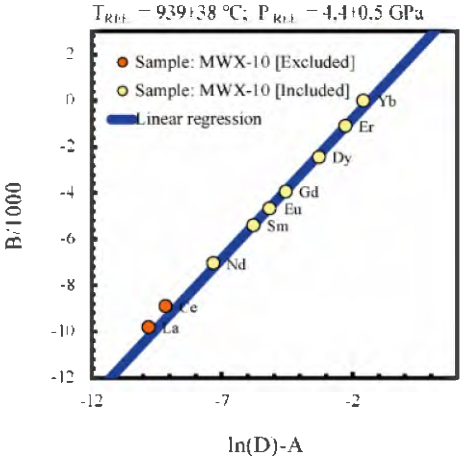
T_{REE} = 939±38 °C; P_{REE} = 4.4±0.5 GPa
Sample: MWX-10 [Excluded]
Sample: MWX-10 [Included]
Linear regression
Yb
Er
Dy
Gd
Eu
Sm
Nd
Ce
La
B/1000
ln(D)-A

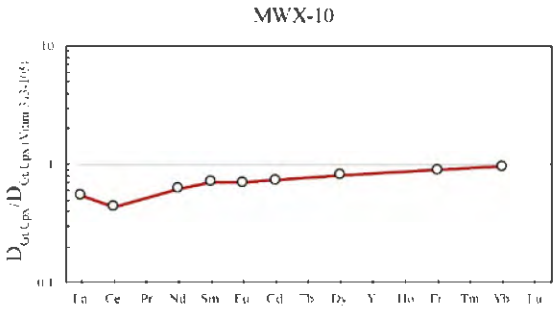
MWX-10

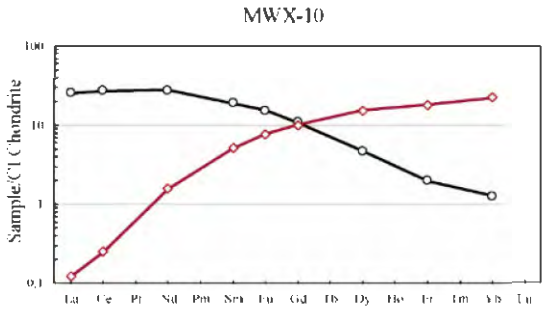
MWX-10
Sample/C1 Chondrite

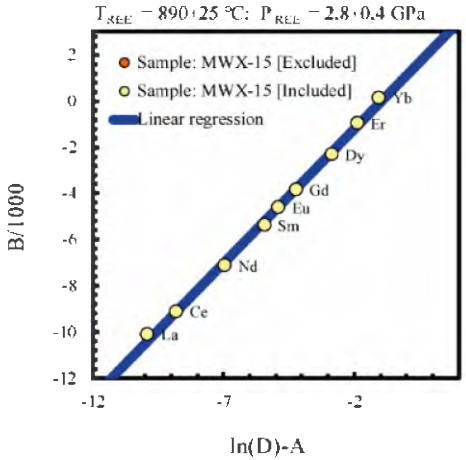
T_{REE} = 890±25 °C; P_{REE} = 2.8±0.4 GPa
Sample: MWX-15 [Excluded]
Sample: MWX-15 [Included]
Linear regression
Yb
Er
Dy
Gd
Eu
Sm
Nd
Ce
La
B/1000
ln(D)-A

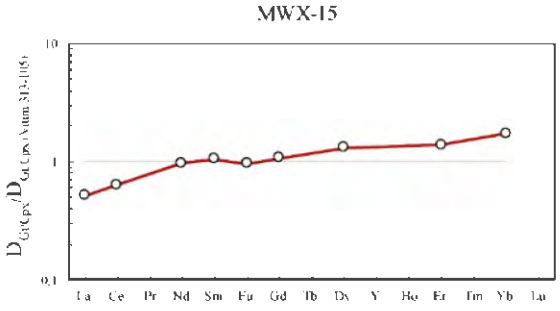
MWX-15

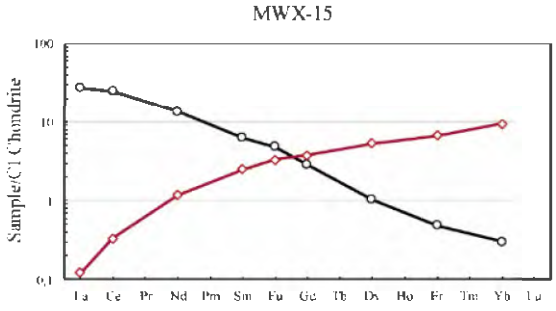
MWX-15
Sample/C1 Chondrite

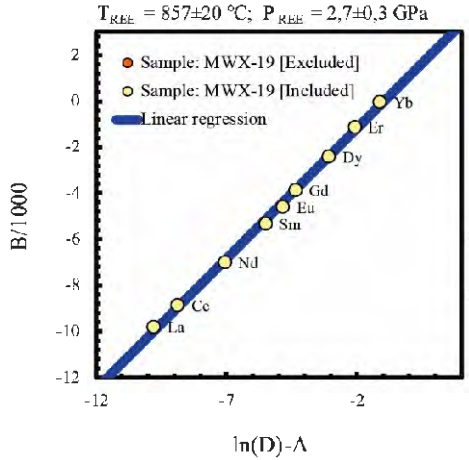
T_REE = 857±20 °C; P_REE = 2,7±0,3 GPa
Sample: MWX-19 [Excluded]
Sample: MWX-19 [Included]
Linear regression
Yb
Er
Dy
Gd
Eu
Sm
Nd
Ce
La
B/1000
ln(D)-A

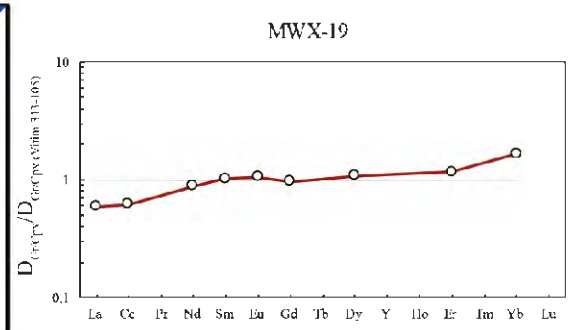
MWX-19
La Ce Pr Nd Sm Eu Gd Tb Dy Y Ho Er Tm Yb Lu

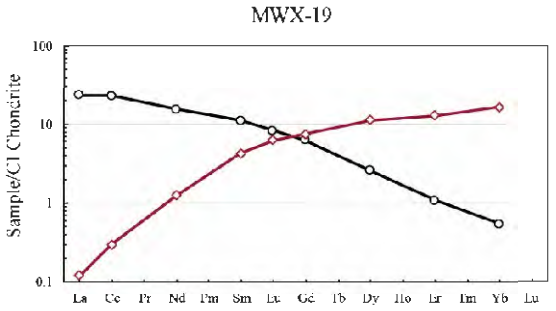
MWX-19
Sample/Cl Chondrite
La Ce Pr Nd Pm Sm Eu Gd Tb Dy Ho Er Tm Yb Lu

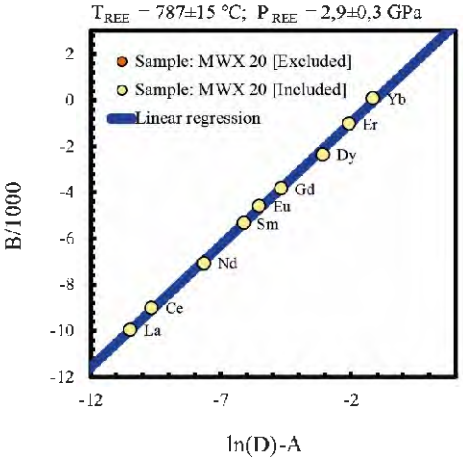
T_REE = 787±15 °C; P_REE = 2,9±0,3 GPa
Sample: MWX 20 [Excluded]
Sample: MWX 20 [Included]
Linear regression
Yb
Er
Dy
Gd
Eu
Sm
Nd
Ce
La
B/1000
ln(D)-A

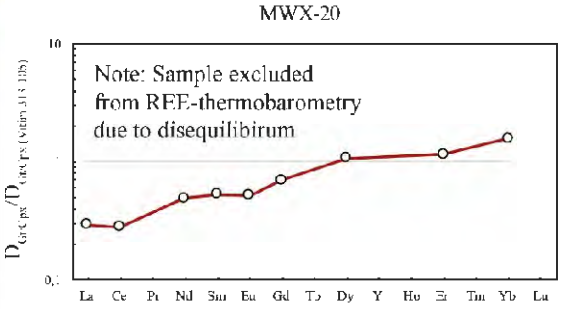
MWX-20
Note: Sample excluded
from REE-thermobarometry
due to disequilibirum
La Ce Pr Nd Sm Eu Gd Tb Dy Y Ho Er Tm Yb Lu

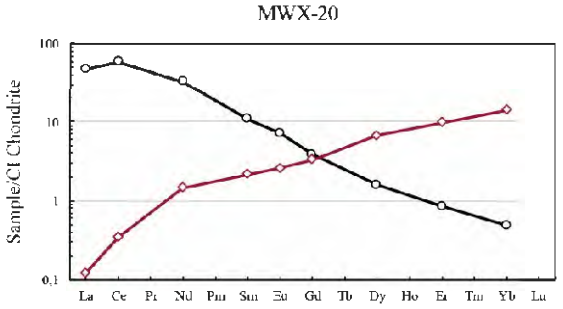
MWX-20
Sample/Cl Chondrite
La Ce Pr Nd Pm Sm Eu Gd Tb Dy Ho Er Tm Yb Lu

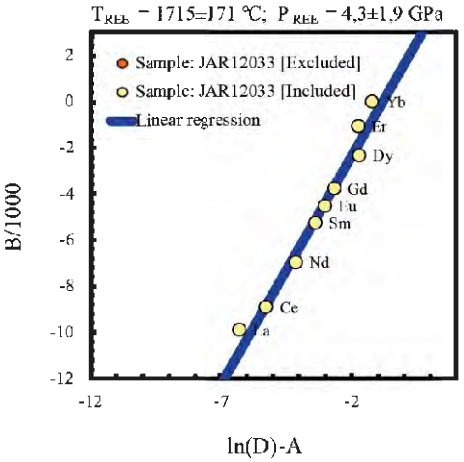
T_REE = 1715±171 °C; P_REE = 4,3±1,9 GPa
Sample: JAR12033 [Excluded]
Sample: JAR12033 [Included]
Linear regression
Yb
Er
Dy
Gd
Eu
Sm
Nd
Ce
La
B/1000
ln(D)-A

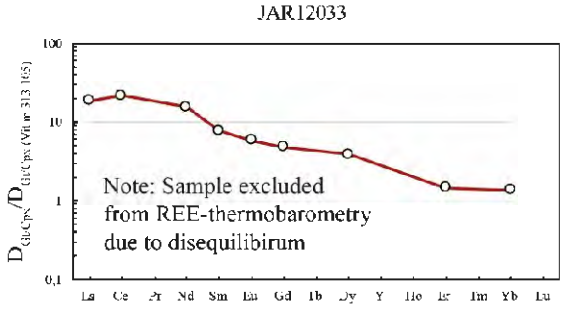
JAR12033
Note: Sample excluded
from REE-thermobarometry
due to disequilibirum

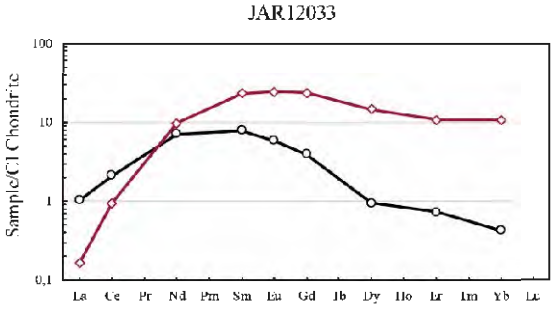
JAR12033
Sample/C1 Chondrite

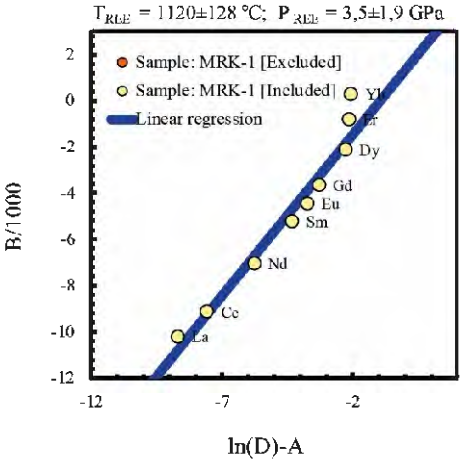
T_REE = 1120±128 °C; P_REE = 3,5±1,9 GPa
Sample: MRK-1 [Excluded]
Sample: MRK-1 [Included]
Linear regression
Dy
Gd
Eu
Sm
Nd
Ce
La
B/1000
ln(D)-A

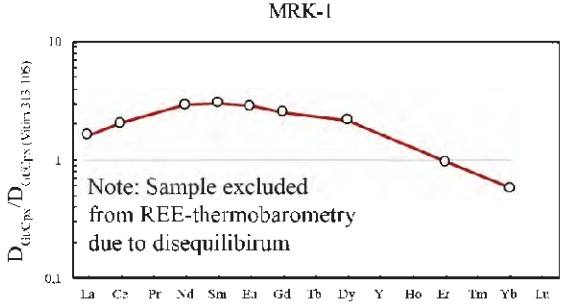
MRK-1
Note: Sample excluded
from REE-thermobarometry
due to disequilibirum

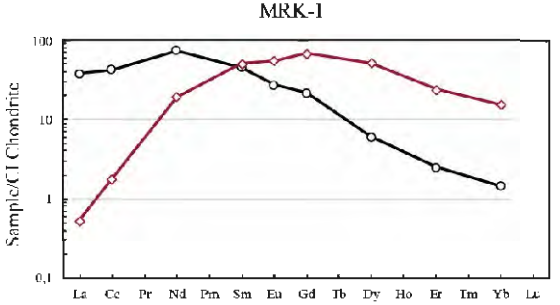
MRK-1
Sample/C1 Chondrite

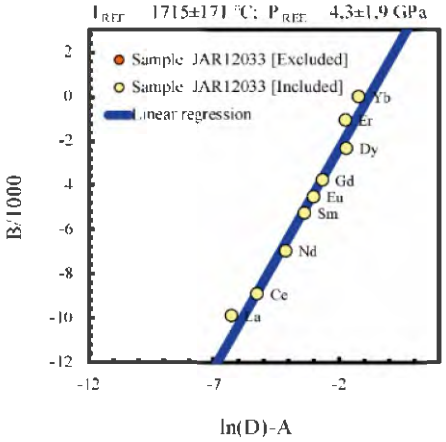
Sample JAR12033 [Excluded]
Sample JAR12033 [Included]
Linear regression
Yb
Er
Dy
Gd
Eu
Sm
Nd
Ce
La
B/1000
ln(D)-A


JAR12033

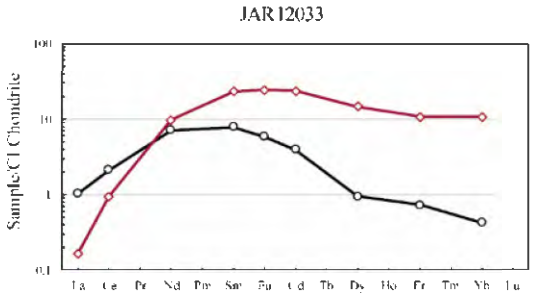
JAR12033
Sample/CI Chondrite

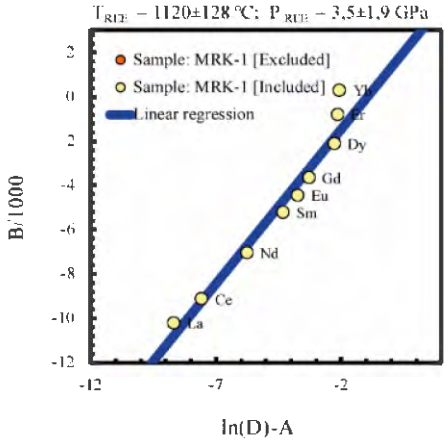
Sample: MRK-1 [Excluded]
Sample: MRK-1 [Included]
Linear regression
Dy
Gd
Eu
Sm
Nd
Ce
La
B/1000
ln(D)-A

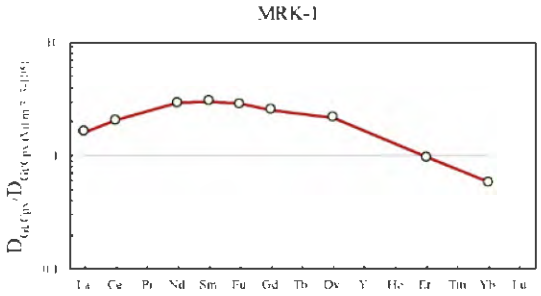
MRK-1

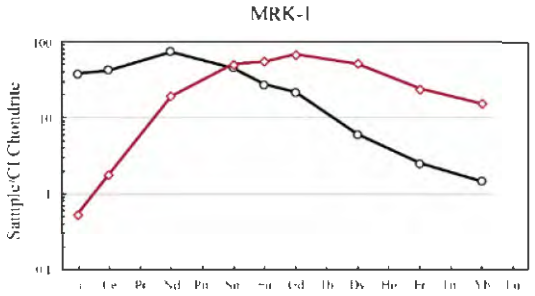
MRK-1